5-2009

DEVELOPMENT, PARAMETERIZATION AND VALIDATION OF DYNAMIC MATERIAL MODELS FOR SOIL AND TRANSPARENT ARMOR GLASS

Bhaskar Pandurangan
Clemson University, bpandur@clemson.edu

DEVELOPMENT, PARAMETERIZATION AND VALIDATION OF DYNAMIC MATERIAL MODELS FOR SOIL AND TRANSPARENT ARMOR GLASS

A Dissertation
Presented to
the Graduate School of
Clemson University

In Partial Fulfillment
of the Requirements for the Degree
Doctor of Philosophy
Mechanical Engineering

---

by
Bhaskar Pandurangan
May 2009

Accepted by:
Dr. Mica Grujicic, Committee Chair
Dr. Paul F. Joseph
Dr. Yong Huang
Dr. Rajendra Singh
Dr. Nicole Coutris

ABSTRACT

Despite the signing of several mine ban treaties in the 1990's, it is widely recognized that there is a landmine crisis. The following are some of the main aspects of this crisis: (a) Millions of unexploded landmines remain deployed all over the world; (b) Thousands of civilians are killed or maimed every year by unintended detonations of the mines; (c) The cost of medical treatment of landmine injuries runs into the millions; (d) the ability of the international community to provide the humanitarian relief in terms of medical services, safe drinking water and food, etc., is greatly hampered by landmine contamination of the infrastructure in mine affected countries; and so on. To address the aforementioned landmine crisis, the research community around the world has taken upon itself the challenge of helping better understand the key phenomena associated with landmine detonation and interaction between detonation products, mine fragments and soil ejecta with the targets (people, structures and vehicles). Such improved understanding will help automotive manufacturers to design and fabricate personnel carriers with higher landmine-detonation survivability characteristics and a larger level of protection for the onboard personnel. In addition, the manufacturer of demining equipment and personnel protection gear used in landmine clearing are expected to benefit from a better understanding of the landmine detonation-related phenomena.

The landmine detonation-related research activity can be broadly divided into three main categories: (a) shock and blast wave mechanics and dynamics including landmine detonation phenomena and large-deformation/high-deformation rate constitutive models for the attendant materials (high explosive, air, soil, etc.); (b) the kinematic and structural response of the target to blast loading including the role of target design and use of blast attenuation materials; and (c) vulnerability of human beings to post-detonation phenomena such as high blast pressures, spall fragments and large vertical and lateral accelerations.

The present work falls primarily into the category (a) of the research listed above since it emphasizes the development of a large-deformation/high-deformation rate material model for soil. It is generally recognized that the properties of soil, into which a landmine is buried, play an important role in the overall effectiveness/lethality of the landmine regardless of the nature of its deployment (fully-buried, flush-buried or ground-laid). Therefore, in the present work, a series of continuum-level material models for soil of different types has been derived (using available public-domain data and various basic engineering concepts/principles), parameterized and validated against experimental results obtained from standard mine-blast testing techniques. Special attention is paid to improving the understanding of the effects of moisture, clay and gravel content on the different aspects of soil material behavior under blast loading conditions. Specifically, the effect of these soil constituents/conditions on the equation of state, strength and failure modes of the material response is investigated.

The results obtained clearly revealed that: (a) the moisture clay and gravel contents of soil can substantially affect the response of soil under blast loading conditions as well as the extent of detonation-induced impulse transferred to the target structure/personnel; (b) over all, the models developed in the present work, when used in transient non-linear dynamics analysis of landmine detonation and detonation product/mine-fragment/ soil-ejecta interaction with the target structures/personnel, yielded results which are in reasonably good agreement with their experimental counterparts.

Keywords: Material modeling; Landmine; Blast; Impulse; Compaction; AUTODYN; Soil; Sand; Clay; Gravel; Non-linear Dynamics.

DEDICATION

This thesis would have been impossible without the unwavering love and support from my father, Mr. V. P. Rangan, my mother, Mrs. Uma Rangan and my brother Mr. Sudhakar Pandurangan, to whom this thesis is dedicated.

ACKNOWLEDGEMENTS

I wish to express my sincere gratitude to my advisor, Dr. Mica Grujicic for his continuous encouragement, supervision and useful suggestions throughout this research endeavor. His extensive knowledge and timely suggestions have been helpful in providing elegant solutions to the problems encountered throughout this research project.

My sincere thanks is also due to my advisory committee members Dr. Paul .F. Joseph, Dr. Yong Huang, Dr. Rajendra Singh and Dr. Nicole Coutris for their valuable suggestions during the course of this research project. Other faculty members of the department of Mechanical Engineering at Clemson University and the administrative staff are also greatly acknowledged for their support. I would also like to thank the Mechanical Engineering department at Clemson University for providing me with the much needed financial assistance, though a teaching assistantship, during the first two years of the research.

This acknowledgement will not be complete without the mention of my colleagues at Clemson University; in particular Dr. Balajee Ananthasayanam, Mr. Cameron Bell, Mr. Guruprasad Arakere, Mr. Hamid Marvi, Mr. Hemanth Nallagatla, Dr. Tao He, and Mr. Vijay Sellappan among numerous others, whose valuable support and insightful discussions have helped mold this research into its existing form.

I also want to thank my parents and my brother for their continuous support during the whole tenure of my research.

Finally, I would like to thank all who directly or indirectly supported me in the completion of this research/thesis.

TABLE OF CONTENTS

Page

LIST OF TABLES

LIST OF FIGURES

List of Figures (Continued)

Figure Page

List of Figures (Continued)

Figure Page

List of Figures (Continued)

Figure Page

List of Figures (Continued)

Figure Page

CHAPTER 1

INTRODUCTION

1.1. Background

Despite the signing of several treaties banning the use of land-mines, millions of unexploded landmines remain buried in more than 60 countries throughout the world. The presence of these mines leads to more than 30,000 civilian deaths in various regions of the world every year and also disrupts the ability of the international community in providing the necessary medical and humanitarian support to affected countries and regions. To address this crisis, the research community around the world has taken upon itself the challenge of helping better understand the key phenomena associated with landmine detonation and interaction between detonation products, mine fragments and soil ejecta with the targets (people, structures and vehicles). It is also recognized that such improved understanding will help automotive manufacturers to design and fabricate personnel carriers with higher landmine-detonation survivability characteristics and a larger level of protection for the onboard personnel.

The landmine detonation related research activity can be broadly divided into three main categories: (a) shock and blast wave mechanics and dynamics including landmine detonation phenomena and large-deformation/high-deformation rate constitutive models for the attendant materials (high explosive, air, soil, etc.); (b) the kinematic and structural response of the target to blast loading including the role of target design and use of blast attenuation materials; and (c) vulnerability of human beings to post-detonation phenomena such as high blast pressures, spall fragments and large vertical and lateral accelerations.

The present work falls primarily into the category (a) of the research listed above. This research emphasizes the development, parameterization and validation of high-pressure, large-

deformation/high-deformation rate material models for soil with various degrees of water saturation, clay content and gravel content.

1.2. Literature Review

The relevant literature survey for each of the sub-topics covered in the present work is provided in Chapters 2-5 and the Appendix.

1.3. Thesis Objective and Outline

The initial main objective of the present work was to develop dynamic high-pressure, high strain-rate material models for soil. The models to be developed had to be parameterized and validated using available open-literature data for soils with various contents of moisture, clay and gravel. Per request of the sponsor the original plan was amended to also include the development of a material model for ballistic glass. It is expected that the material models developed here will help in improving the ability of computational analyses in predicting real world phenomena, especially in the fields of ballistic testing on glass and the behavior of soil under blast loading. The organization of the present work is as follows:

In Chapter 2, the widely used compaction material model for dry sand is critically assessed. The model is next modified to include the effects of the degree of saturation and the deformation rate on the constitutive response of the soil. This model is validated against open-literature findings in the form of impulse transferred to a target structure and the sand crater morphology. It is found that the degree of saturation and the deformation rate play a critical role in characterizing soil behavior.

In Chapter 3, a material model for soil containing sand with a smaller volume fraction (<15%) of clay is presented. It is presumed that clay forms a coating on the surface of sand and thus contributes considerably to the strength characteristics of the sand-clay system. Validation of

the model is provided by comparing the computed and the corresponding experimental results pertaining to sand overburden height, sand overburden width and overpressures resulting from the explosion of a C4 charge.

In Chapter 4, a dynamic material model is presented for STANAG 4569 sandy gravel type of soil. Sand sieving curves are used to provide the proper particle size distribution for the sandy gravel material and the continuum-level material properties are measured by simulating basic material test conditions. In the absence of a comprehensive set of experimental results needed for the complete validation of the model, a brief description of experimentation necessary to validate the model has been provided.

In Chapter 5, a dynamic material model for clayey sand type of soil (major constituent: clay) is developed. It is recognized that clay structure differs from that of silica sand with respect to the presence of intra-particle water (related to swelling) along with inter-particle moisture. The model is validated by comparing the simulated results with the impulse transfer to the Vertical Impulse Measurement Fixture (VIMF).

In Chapter 6, the major conclusions related to the present work and a few suggestions for future work are presented.

Lastly, in the Appendix A, pertinent modeling work completed during this research project focusing on materials other than soil is presented. Specifically, a dynamic material model for soda lime glass has been developed. The behavior of glass at high strain rate and low strain rate regimes has been discussed. To augment the model, a macro-cracking failure criterion has been introduced. The model has been validated by comparing the computational results with their experimental counterparts obtained in Edge-on-Impact and frontal impact tests found in open-literature.

CHAPTER 2

THE EFFECT OF DEGREE OF SATURATION ASSOCIATED WITH THE DETONATION OF SHALLOW BURRIED AND GROUND-LAID MINES

2.1. Abstract

A new materials model for sand has been developed in order to include the effects of the degree of saturation and the deformation rate on the constitutive response of this material. The model is an extension of the original compaction materials model for sand in which these effects were neglected. The new materials model for sand is next used, within a non-linear-dynamics transient computational analysis, to study various phenomena associated with the explosion of shallow-buried and ground-laid mines. The computational results are compared with the corresponding experimental results obtained through the use of an instrumented horizontal mine-impulse pendulum, pressure transducers buried in sand and a post-detonation metrological study of the sand craters. The results obtained suggest that the modified compaction model for sand captures the essential features of the dynamic behavior of sand and accounts reasonably well for a variety of the experimental findings related to the detonation of shallow-buried or ground-laid mines.

2.2. Introduction

Detonation of the shallow-buried and ground-laid mines and the subsequent interactions of the resulting shock waves, detonation products and the soil ejecta with the surrounding media and structures involve numerous highly non-linear phenomena of a transient nature. In order to maximize the destructive effects of the explosion or to devise means/strategies for minimizing such effects, a large range of diverse physical phenomena must be considered. While, in

principle, one would prefer to study the aforementioned detonation phenomena using an analytical technique, in hope of elucidating the underlying physics of the problem, analytical methods typically entail major simplifying assumptions so that their predictions are often questionable or even contradicted by the experimental observations. Consequently, a better understanding of the explosion phenomena is being gradually gained by combining physical experiments with numerical modeling techniques. This approach is utilized in the present work in which, for example, the experimental results associated with the explosion of shallow-buried and ground-laid C4 mines obtained through the use of an instrumented horizontal mine-impulse pendulum reported in Ref. [2.1] are compared with a detailed numerical modeling of the same physical problem using AUTODYN, a general purpose non-linear dynamics simulation software [2.2].

In our recent work [2.3], a detailed comparison was made between the experimental results reported in Ref. [2.4] and their computational counterparts for a number of detonation-related phenomena such as the temporal evolutions of the shape and size of the over-burden sand bubbles and of the detonation-products gas bubbles, the temporal evolutions of the side-on pressures in the sand and in air, etc. It was found that the most critical factor hampering a better agreement between the experiment and computational analysis is an inadequacy of the current materials models for sand to capture the dynamic response of this material under blast loading conditions. Hence, the main objective of the present work is to improve the compaction materials model [2.5] for sand currently implemented in AUTODYN. Specifically, the new materials model for sand is developed to include the effects of saturation and the deformation rate on the constitutive response of the sand. A review of the literature reveals that the currently available materials model for sand suffers from either an inability to account for the rate-dependence of the material's response in the case of the saturated sand [2.5] or contain a large number of parameters

whose estimation via analytical/numerical analysis and /or experimental measurements is very difficult and cumbersome [2.6-2.10].

The organization of this chapter is as follows. A brief overview of the design, construction and utilization of the instrumented horizontal mine-impulse pendulum is given in Section 2.3. The non-linear dynamics approach, the relevant materials models and the definition of the computational problem investigated are respectively discussed in Sections 2.4, 2.5 and 2.6. The results obtained in the present work are presented and discussed in Section 2.7. The main conclusions resulting from the present work are summarized in Section 2.8.

2.3. Computational Procedure

2.3.1. An Overview of the Horizontal Mine Impulse Pendulum Experiment

Since one of the objectives of the present work is to assess the validity of the newly proposed materials model for sand by comparing the present non-linear dynamics based computational results with their experimental counterparts obtained using an instrumented horizontal mine-impulse pendulum used in Ref. [2.1], a brief overview of the construction and experimental procedure associated with the impulse pendulum is presented in this section. A more detailed account of the design and the construction of the instrumented horizontal mine-impulse pendulum can be found in Ref. [2.11].

The instrumented horizontal mine-impulse pendulum consists of a 5m long horizontal steel arm with a 1200mm x 1200mm square measuring pan placed at the free end of the arm 400mm above the ground. The arm is attached to the base assembly at the other end through a horizontal pivot. The charge, typically consisting of a cylindrically shaped (14.6cm in diameter and 5cm high) C4 mine is placed under the center of the measuring pan and detonated. The mine is either laid on the ground or is buried to different depths. The resultant maximum angular

displacement of the pendulum arm is measured and used to calculate the detonation-induced impulse on the pendulum, see Eq. (2.5). The use of the mine-impulse pendulum enabled an investigation of the effects of the sand type/properties, extent of saturation with water, the target stand-off distance and the mine depth of burial on the total detonation-induced impulse [2.1]. In an earlier design, the measuring pan was constructed of mild steel, however, the initial experiments revealed that such a measuring pan undergoes substantial plastic deformation. Consequently, the central 600mm x 600mm section of the measuring pan was replaced with a 50mm thick Rolled Homogenized Armor (RHA) plate. The deformation of the RHA plate was found to be in the order of 10^{-4} to 10^{-3} which is small and thus justifies the assumption of negligible deformation. The maximum angular deflection of the pendulum was obtained using a combination of the following three methods: (a) a cable potentiometer, (b) a mechanical gage and (c) high speed video recording of a large pointer.

The relationship between the total detonation-induced impulse on the pendulum and the maximum angular displacement of the pendulum mentioned above was derived in Ref. [2.11] under the assumption that both the effect of gravity and that of pendulum displacement during the initial loading phase (the time period over which the momentum is transferred from the detonation-products/sand ejecta to the measuring pan) can be neglected. These were justified by the fact that a typical duration of the initial loading phase is about 1-2ms, while the typical time for the pendulum to reach the maximum angular displacement position is around 300-400ms. A brief overview of the derivation of the impulse vs. maximum angular displacement relation is given below. The derivation of this relation is based on the principle of conservation of the total energy (a sum of the potential and kinetic energies). When applied to the initial position of the pendulum and the position of the pendulum corresponding to the maximum angular displacement, this principle leads to the following equation:

$$\frac{1}{2} I_0 \omega_0^{\,2} = mgr \sin(\theta_{\max}) \tag{2.1}$$

where I_0 is the moment of inertia of the pendulum arm, ω_0 is the initial angular velocity of the pendulum arm, m is the mass of the pendulum arm, g is the gravitational acceleration (9.81m/s^2), r is the distance between the pivot point and center of gravity of the arm and θ_{max} is the maximum angular displacement of the pendulum arm. It should be noted that the potential energy of the pendulum in its initial position is arbitrarily set to zero (the left hand side of Eq. (2.1)), while the kinetic energy of the pendulum associated with the maximum angular displacement is also zero (the right hand side of Eq.(2.1)). Thus the left hand side of Eq. (2.1) defines the initial rotational kinetic energy of the pendulum while the right hand side of the same equation defines the maximum potential energy of the pendulum. It should be noted that it is postulated in Eq. (2.1) that the kinetic energy is initially imparted to the pendulum by the detonation products/soil ejecta without any pendulum movement.

The initial angular velocity of the pendulum, ω_0, is obtained from the following angular impulse relationship:

$$I_0 \omega_0 = \int_{t_0}^{t_f} (RF - mgr \cos(\theta_{\max}))dt \tag{2.2}$$

where F is the detonation-induced normal force acting on the pendulum over a time period between t_0 and t_f, t is the time and R is the distance between the point of application of the force and the pivot point. Since the blast loads act normal to the surface of measuring pan and over a very short time period, R can be considered as a constant. If the effect of gravity is neglected on the right hand side of Eq. (2.2) and a use is made of the definition of the total detonation-induced impulse on the pendulum, J:

$$J = \int_{t_0}^{t_f} F dt \tag{2.3}$$

the initial angular velocity can be defined as:

$$\omega_0 = \frac{JR}{I_0} \tag{2.4}$$

Substitution of Eq. (2.4) in Eq. (2.1) yields

$$J = \sqrt{\frac{2mgrI_0 \sin(\theta_{\max})}{R^2}} \tag{2.5}$$

Thus for a given pendulum with the parameters m (= 1480kg), I_0 (= 14,700kg-m^2), r (= 2.44m) and R (= 4.27m), Eq. (2.5) enables determination of the detonation-induced impulse from the measured values of the maximum angular displacement (θ_{max}) of the pendulum. The values for the pendulum parameters listed above correspond to the ones for the horizontal mine-impulse pendulum used in Ref. [2.1].

2.4. Non-linear Dynamics Modeling of Detonation Phenomena

All the calculations carried out in the present work are done using AUTODYN, a general purpose non-linear dynamics modeling and simulation software [2.2]. In this section, a brief overview is given of the basic features of AUTODYN, emphasizing the aspects of this computer program which pertain to the problem at hand.

AUTODYN is a fully integrated engineering analysis computer code which is particularly suited for modeling explosion, blast, impact and penetration events. Codes such as AUTODYN are commonly referred to as "*hydrocodes*". Within the code, the appropriate mass, momentum and energy conservation equations coupled with the materials modeling equations and subjected to the appropriate initial and boundary conditions are solved. The numerical methods used for the

solution of these equations involve finite difference, finite volume and finite element methods and the choice of the method used (i.e. "*processor*" as referred to in AUTODYN) depends on the physical nature of the problem being studied. The power of AUTODYN is derived mainly from its ability to handle complex problems in which different regions can be analyzed using different methods such as the Lagrange processor (typically used for solid continuum and structures) and the Euler processor (commonly used for modeling gases, liquids or solids subject to large deformations). While the available Euler processor provides multi-material capabilities, an additional Euler-FCT single material processor in which materials are combined to a single material using a Flux Corrected Transport (FCT) approach is available to help handle computationally intensive multi-material blast phenomena.

Additional methods available in AUTODYN include: an ALE (Arbitrary Lagrange Euler) processor capable of carrying out an automatic rezoning of distorted grids; a Shell processor designated for modeling thin structures and a gridless SPH (Smooth Particle Hydrodynamics) processor which does not suffer from a grid tangling problem (typically encountered in Lagrangian processor) and does not entail the use of an unphysical erosion algorithm (removal of highly distorted grids to help the numerical procedure). The authors are not aware of any comprehensive open literature on the study of the effect of solver type on the computational results in problems which can be solved with alternative solvers. AUTODYN reference manual provides a comparison between the results obtained using Euler, Lagrange and ALE solvers for the case of a cylindrical projectile impacting a thick plate and shows that the solver choice has a relatively small effect on the computational results.

In the present work, the Euler-FCT processor was used to represent air and C4 gaseous detonation products. Sand is handled using the Lagrange processor while the various components of the instrumented horizontal mine-impulse pendulum are represented using a shell processor.

The interactions between the different processors are accounted for through the use of the part-interaction options within AUTODYN [2.2].

2.5. Materials Constitutive Models

Hydrodynamic computer programs such as AUTODYN [2.2] are capable of predicting an unsteady, dynamic motion of a material system by solving the appropriate mass, momentum and energy conservation equations, subjected to the associated initial and boundary conditions. However, for the aforementioned boundary value problem to be fully defined, additional relations between the flow variables (pressure, density, energy, temperature, etc.) have to be defined. These additional relations typically involve an equation of state, a strength equation and a failure equation for each constituent material. These equations arise from the fact that, in general, the total stress tensor can be decomposed into a sum of a hydrostatic stress (pressure) tensor (which causes a change in the volume/density of the material) and a deviatoric stress tensor (which is responsible for the shape change of the material). An equation of state then is used to define the corresponding functional relationship between pressure, density and internal energy (temperature), while a strength relation is used to define the appropriate equivalent plastic-strain, equivalent plastic strain rate, and temperature dependences of the equivalent deviatoric stress. In addition, a materials model generally includes a failure criterion, i.e. an equation describing the (hydrostatic or deviatoric) stress and/or strain condition which, when attained, causes the material to fracture and loose its ability to support normal and shear stresses.

In the present work the following four materials are utilized within the computational domain: air, sand, AISI 1006 steel and Rolled Homogenized Armor (RHA). In the following sections, a brief description is given of the models used for each of the four constituent materials. The values of all the material parameters defined in the remainder of the section are available in the AUTODYN materials library [2.2]. The data cannot be disclosed here due to copyright

violation concerns.

2.5.1. Air

Air is modeled as an ideal gas and, consequently, its equation of state is defined by the ideal-gas gamma-law relation as [2.2]:

$$P = (\gamma - 1)\frac{\rho}{\rho_0} E \tag{2.6}$$

where P is the pressure, γ the constant-pressure to constant-volume specific heats ratio (=1.4 for a diatomic gas like air), ρ_0 (=1.225kg/m^3) is the initial air density, and ρ is the current density. For Eq. (2.6) to yield the standard atmosphere pressure of 101.3kPa, the initial internal energy E is set to 253.4kJ/m^3 which corresponds to the air mass specific heat of 717.6J/kg·K and a reference temperature of 288.2K.

Due to the use of a single-material Euler-FCT processor for the gas-phase region, the C4 detonation products are not modeled as a separate material within the gas phase. Rather, C4 detonation products are modeled initially as a cylindrically shaped air region with a high density ρ (=1601kg/m^3), and a high internal energy density, e (= 5.621·10^{6}J/kg). The corresponding detonation products pressure and the fire ball temperature take on values of 18 MPa and 2950 K, respectively.

Since air is a gaseous material and has no ability to support either shear stresses or negative pressures, no strength or failure relations are required for this material.

2.5.2. AISI 1006 Steel

With the exception of the 600mm x 600mm central square section of the measuring pan, the instrumented horizontal mine-impulse pendulum was constructed from medium-carbon AISI 1006 Steel. For inert solid materials like AISI 1006 steel a linear type of equation of state is

typically used which assumed a Hooke's law type relationship between the pressure and the volume change as:

$$P = K\mu \tag{2.7}$$

where K is the bulk modulus of the material and $\mu = \left(\frac{\rho}{\rho_0} - 1 \right)$ is the compression ratio. Within AUTODYN material database, the initial material density ρ_0, the bulk modulus K, the specific heat and the reference temperature are defined for AISI 1006 steel.

To represent the constitutive response of AISI 1006 steel under deviatoric stress, the Johnson-Cook model is used. This model is capable of representing the material behavior displayed under large-strain, high deformation rate, high-temperature conditions, of the type encountered in problems dealing with the interactions of detonation products and solid structures. Within the Johnson-Cook model, the yield stress is defined as:

$$Y = \left[A + B\varepsilon_{pl}^{n} \right]\left[1 + C_1 \log \dot{\varepsilon}_{pl} \right]\left[1 - T_H^m \right] \tag{2.8}$$

where ε_{pl} is the equivalent plastic strain, $\dot{\varepsilon}_{pl}$ is the equivalent plastic strain rate, A is the zero plastic strain, unit plastic strain rate, room temperature yield stress, B is the strain hardening constant, n is the strain hardening exponent, C_1 is the strain rate constant, m is the thermal softening exponent and $T_H=(T-T_{room})/(T_{melt}-T_{room})$ is a room temperature (T_{room}) based homologous temperature while T_{melt} is the melting temperature. All temperatures are given in degrees of Kelvin.

Since the sections of the instrumented horizontal mine-impulse pendulum constructed from the AISI 1006 steel are generally subjected to relatively low stresses, no failure model was used for the AISI 1006 steel in the present work.

2.5.3. Rolled Homogenized Armor (RHA)

As mentioned earlier, the 600mm x 600mm central square section of the measuring pan was constructed from a Rolled Homogenized Armor (RHA) plate material. The same type of materials models (a linear equation of state and a Johnson-Cook strength model) used for the AISI 1006 steel are also used to represent the dynamic response of the RHA plate material. However, the values of the model parameters differ for the two typed of materials.

2.5.4. Sand

Sand has generally a complex structure consisting of mineral solid particles which form a skeleton. The pores between the solid particles are either filled with effectively dry air (this type of sand is generally referred to as *"dry sand"*), with water ("*saturated sand"*) or a two-phase water/air mixture ("*unsaturated sand"*). The relative volume fractions of the three constituent materials in the sand (the solid mineral particles, water and air) are generally quantified by the porosity, α, and the degree of saturation (Saturation Ratio), SR, which are respectively defined as

$$\alpha = \frac{V_p}{V} = \text{porosity} \tag{2.9}$$

and

$$SR = \frac{V_w}{V_p} \tag{2.10}$$

where V_p is the volume of void (pores), V_w is the volume of water and V is the total volume.

Surface roughness and the presence of inorganic/organic binders are generally considered to be the main causes for friction/adhesion at the inter-particle contacting surfaces. Deformation of the sand is generally believed to involve two main basic mechanisms [2.12]: (a) elastic deformations (at low pressure levels) and fracture (at high pressure levels) of the inter-particle

bonds and (b) elastic and plastic deformations of the three constituent materials in the sand. The relative contributions of these two deformation mechanisms as well as their behavior are affected primarily by the degree of saturation of sand and the deformation rate. Specifically, in dry sand the first mechanism controls the sand deformation at low pressures while the second mechanism is dominant at high pressures and the effect of deformation rate is of a second order. In sharp contrast, in saturated sand very low inter-particle friction diminishes the role of the first deformation mechanism. On the other hand, the rate of deformation plays an important role. At low deformation rates, the water /air residing in the sand pores is squeezed out during deformation and, consequently, the deformation of the sand is controlled by the deformation of the solid mineral particles. At high pressures, on the other hand, water/air is trapped within the sand pores and the deformation of the sand is controlled by the deformation and the volume fractions of each of the three constituent phases.

Within AUTODYN, the dynamic response of sand is represented using a compaction materials model which was formulated using the experimental results obtained by Laine and Sandvik [2.5]. A brief description of the compaction materials model is given below.

2.5.4.1 Compaction Materials Model for Sand

The "*compaction*" equation of state for sand is based on a piece-wise linear pressure-density relation schematically shown in Figure 2-1. It should be noted that, since pressure does not depend explicitly on the internal energy, this relation is equivalent to the standard Mie-Gruneisen equation of state in which the Gruneisen gamma parameter, $\Gamma = v\left(\frac{\partial P}{\partial E}\right)_v$ is set to zero. This means that the model would give a more reliable material response under the conditions when either the energy absorbed is not very high (e.g. when the applied pressure levels are not significantly larger than the pressure levels at which the porous material crushes and compacts

into a solid material), when the initial material porosity is small or when the magnitude of the Gruneisen gamma parameter is near zero.

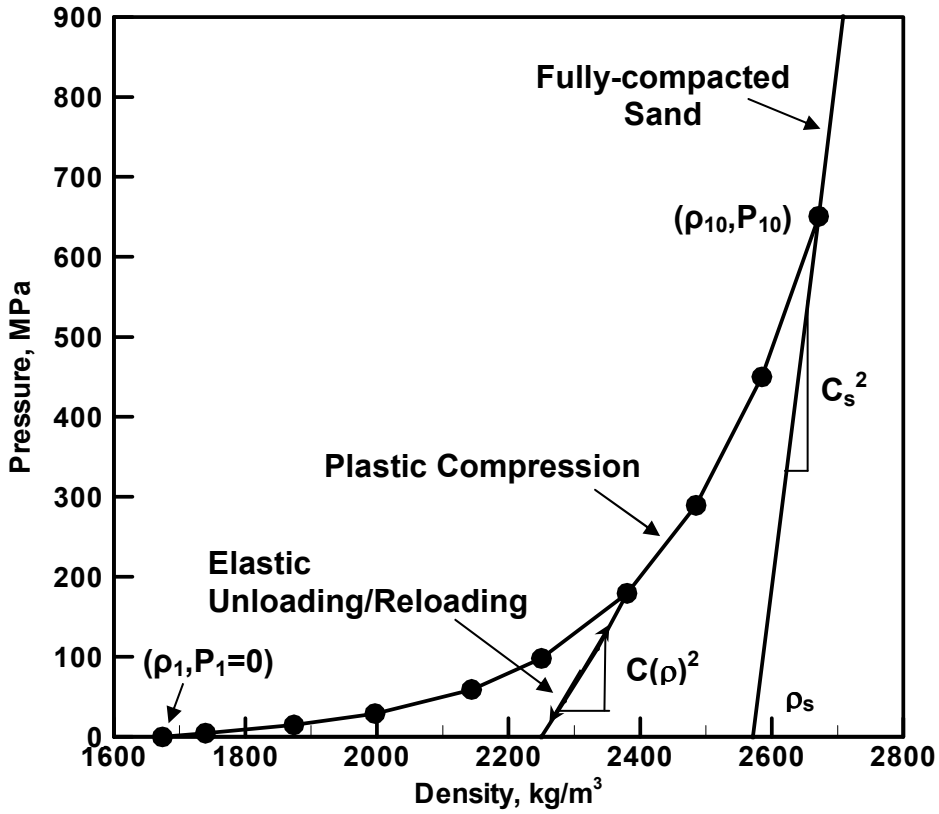

Figure 2-1 Pressure vs. Density Relations for Dry Sand as Defined in the AUTODYN Materials Library [2.2]

Within the AUTODYN computer program [2.2], the initial density of the porous material at a zero pressure level, P_1 is denoted as ρ_1. As the pressure is applied, the relation between the pressure and the density (denoted in Figure 2-1 as "*Plastic Compaction*") is defined using up to ten (ρ, P) pairs of values. This portion of the pressure vs. density relation is associated with a permanent, plastic compaction of sand. Full compaction of the sand corresponds to the last pair of the (ρ, P) values of the plastic compaction curve.

An increase in pressure beyond the point of full compaction is defined by the following elastic loading linear pressure-density relation:

$$P = C_s^2(\rho - \rho_s) \tag{2.11}$$

where C_s is the sound speed in fully compacted sand at zero pressure and ρ_s is the mass density of the fully-compacted sand under a zero applied pressure.

Elastic unloading/reloading of the porous material like sand at any level of compaction is generally governed by the following differential equation:

$$\frac{\partial P}{\partial \rho} = C^2(\rho) \tag{2.12}$$

where C is the sound speed in sand at a density ρ . As indicated in Figure 2-1 by the curves denoted as "*Elastic Unloading/Reloading*", the pressure-density relation during elastic unloading/reloading is not linear which is due to the fact that the sound speed in sand is a function of the material density. Within AUTODYN [2.2], density dependence of the sound speed, C, is defined as a piece-wise linear relation in terms of up to ten (ρ, C) pairs of values.

The "*compaction*" strength model for sand is based on an isotropic, perfectly plastic, rate independent yield-surface approximation and postulates that the yield stress depends explicitly on pressure and not on material density. Within the AUTODYN program [2.2], the relationship between the yield stress, Y, and pressure, P, is defined as a piece-wise linear function consisting of up to ten (P, Y) pairs of values. The yield stress quantifies the resistance of the material to a plastic (irreversible) shape change. The plastic shape change occurs when the magnitude of the second invariant of the deviatoric part of the stress tensor becomes equal to the yield stress.

Unloading (and subsequent reloading) of a previously plastically deformed material is of an elastic (reversible) nature and, in this case, the deviatoric stress is proportional to the

deviatoric strain with the proportionality constant being equal to the shear modulus, G. In a porous material such as sand, the shear modulus is a function of the material density. The "*compaction*" G vs. ρ relation is defined within AUTODYN [2.2] as a piece-wise linear function using up to ten (ρ, G) pairs of data.

The failure behavior of sand is modeled within the AUTODYN materials database by specifying a minimum (negative) value of the hydrodynamic pressure below which, the material fractures, and loses its ability to support any tensile or shear stress. However, if a given "*fractured*" material region is subsequently subjected to positive pressures, it is given an ability to reheal and close up its cracks.

2.5.4.2. Modified Compaction Materials Model for Sand

The compaction materials model for sand described in the previous section does not include two very important factors controlling the dynamic response of sand under the blast loading conditions i.e., the effects of the degree of saturation and the deformation rate. In this section, an attempt is made to modify the original compaction materials model for sand in order to incorporate these two effects. The modifications of the compaction materials model for sand, proposed in the present work, are based on the following set of assumptions:

(a) The average sand particle size, particle size distribution and the presence of inorganic/organic natural matter in sand all have a second order effect on the dynamic constituent response of the sand. This assumption was justified by the experimental observations reported in Ref. [2.1] which clearly showed that the effect of sand type (e.g. prairie sand containing high level of silt and clay, impurity-free -30/+50 sand, etc.), on the detonation-induced momentum transfer to the instrumented horizontal mine-impulse pendulum was small in comparison with the effect of the degree of saturation;

(b) The dynamic mechanical response of the sand at any degree of saturation can be obtained as a linear combination of the corresponding dynamic material behaviors for the dry and the saturated sand;

(c) The dynamic mechanical response of the dry sand is not rate dependent and it can be represented by the original compaction model implemented in AUTODYN [2.2];

(d) The initial density of the saturated sand, $\rho_{1,sat}$, can be calculated using densities of the solid material in the sand, ρ_s , and water, ρ_w , and the known level of sand porosity, α=1-(ρ_1/ρ_s), as:

$$\rho_{1,sat} = \rho_s(1-\alpha) + \rho_w\alpha \tag{2.13}$$

(e) When the saturated sand is subjected to relatively low deformation (compression) rates, water is given enough time to leave the pores and hence the density of the fully compacted sand and the pressure at which full compaction is attained are identical to their counterparts in the dry sand;

(f) When the saturated sand is subjected to very high compression rates, water will be trapped inside the pores and, due to a very low compressibility of the water, the compressibility of the sand is controlled by the compressibility of its solid phase. In other words, the saturated sand behaves as a fully compacted sand under high deformation rates and can only undergo an elastic compaction;

(g) Under intermediate deformation rates, the dynamic material response of the saturated sand can be obtained using a linear interpolation of the high-low-deformation rate behaviors of the saturated sand. A value of $1.0\cdot10^5 s^{-1}$ is used as the "*high*" deformation rate, $\dot{\varepsilon}_{high}$, and a value of $1.0\cdot10^{-3}$ s^{-1} is used as the "*low*" deformation rate, $\dot{\varepsilon}_{low}$. At the deformation rates exceeding $1.0\cdot10^5 s^{-1}$ and at the deformation rates below $1.0\cdot10^{-3}$ s^{-1}, the dynamic behavior of sand

is assumed to be rate independent and to correspond to the dynamic sand behavior at the respective ($1.0 \cdot 10^{5} s^{-1}$ or $1.0 \cdot 10^{-3} s^{-1}$) deformation rates. The linear interpolation of the dynamic sand behavior at the intermediate deformation rates was based on the logarithms of the deformation rates as:

$$\rho = \rho_{high} + (\rho_{low} - \rho_{high}) \left(\frac{\log \dot{\varepsilon} - \log \dot{\varepsilon}_{high}}{\log \dot{\varepsilon}_{low} - \log \dot{\varepsilon}_{high}} \right) \tag{2.14}$$

where the densities ρ, ρ_{high} and ρ_{low} correspond respectively to the deformation rates $\dot{\varepsilon}$, $\dot{\varepsilon}_{high}$ and $\dot{\varepsilon}_{low}$ and are all associated with the same level of pressure. The computational results obtained are found not to be significantly affected by an order of magnitude changes in the values for the high and low deformation rates; and

(h) Since the irreversible plastic deformation of sand is dominated by the plastic deformation behavior of its solid phase, it is assumed to be independent of the degree of saturation and the rate of deformation. In other words, only the equation of state in the original compaction model was modified following the aforementioned procedure. The pressure vs. density relations corresponding to the original compaction model for sand and also for dry sand at a porosity level of 38% is displayed in Figure 2-1. The pressure vs. density relations corresponding to saturated sand in the present formulation with a porosity level of 38% is displayed in Figure 2-2. The new equation of state is implemented in the user subroutine "*mdeosuser.f90*" and interfaced with the AUTODYN computer program [2.2].

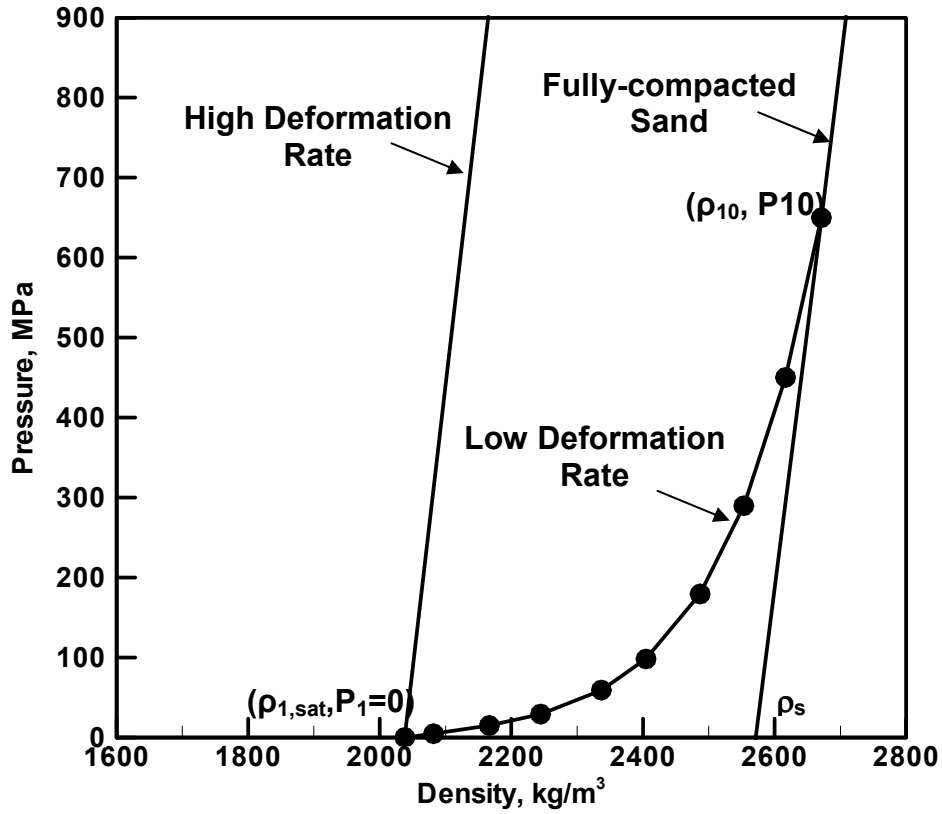

Figure 2-2. Pressure vs. Density Relations for Saturated Sand at Low and High Deformation Rates

2.6. Problem Definition and Computational Analysis

In this section, a brief description is given of the computational model used to simulate the interaction of the detonation-products/soil ejecta resulting from the explosion of a shallow-buried or ground-laid mine and the instrumented horizontal mine-impulse pendulum. The computational modeling of this interaction involved two distinct steps: (a) geometrical modeling of the instrumented horizontal mine-impulse pendulum and (b) a non-linear dynamics analysis of the momentum transfer from the detonation-products/soil ejecta to the pendulum.

Various computational domains used in the present study are shown in Figure 2-3. The geometrical models for the various components of the pendulum were constructed using 50mm x 50mm square shell elements. An advantage was taken of the planar symmetry of the model. In

other words, a vertical plane of symmetry was placed along the length of the pendulum which enabled only a half of the pendulum to be modeled. In accordance with the instrumented horizontal mine-impulse pendulum used in Ref. [2.1], different sections of the pendulum were constructed using AISI 1006 steel and RHA plate material. Welded joints of the different sections of the pendulum were simulated by joining the components in question.

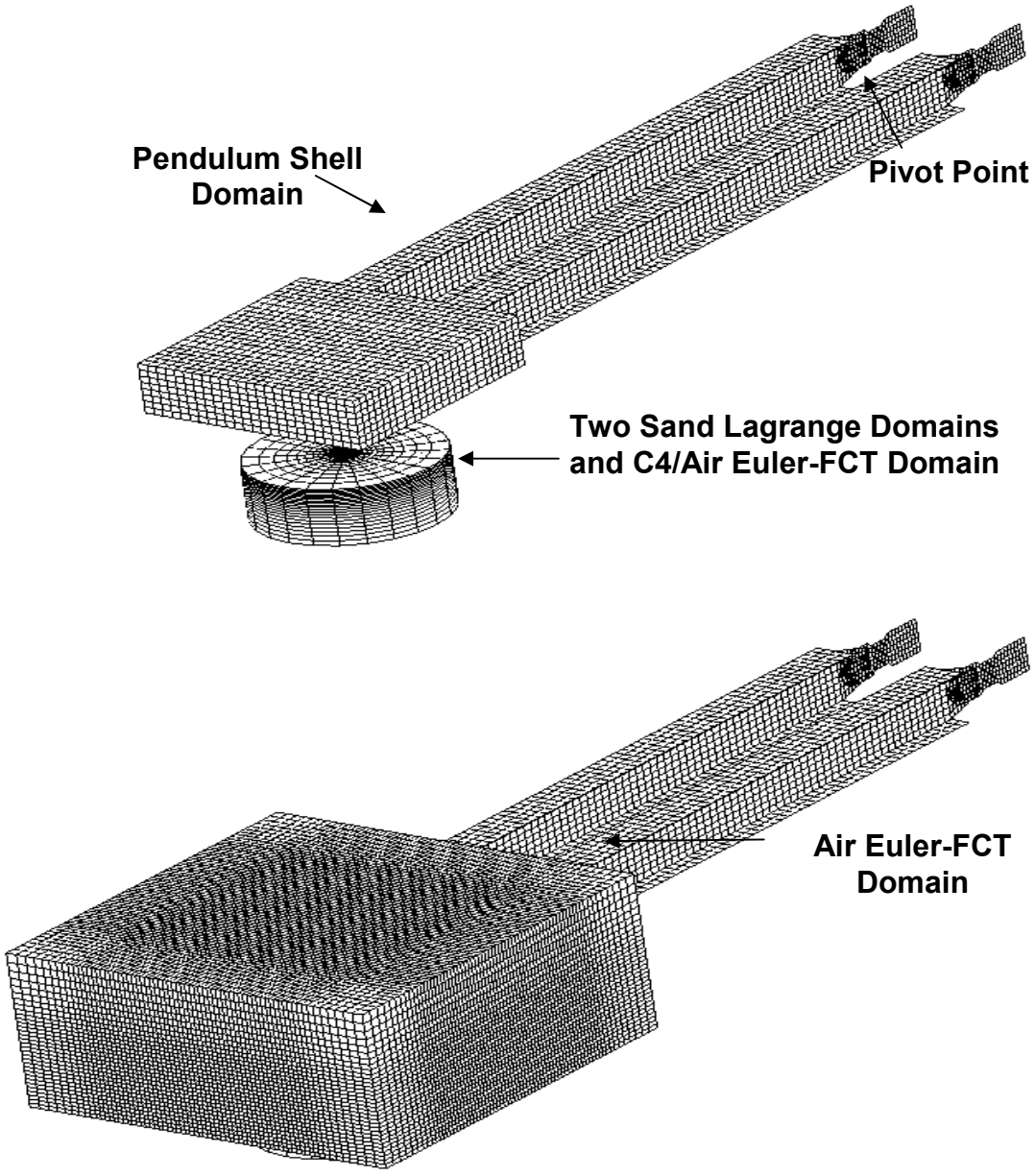

Figure 2-3. Various Computational Domains used in the Non-linear Dynamics Analysis

The head of the pendulum was placed in an Euler-FCT region consisting of 74,000 25mm edge-length cubic cells. In the case of a surface laid mine, the mine was represented by a high-density high-energy cylindrical air region located within the Euler-FCT domain. In the case of a shallow-buried mine, two joined Lagrange domains were used to define a sand region containing a cylindrical cavity whose shape and size match those of the C4 mine. A second Euler-FCT domain overlapping with the two sand domains is defined and the portion of this domain corresponding to the cylindrical sand cavity defined above is initially filled with high-density high-energy air.

The air/sand and air/pendulum interactions are accounted for using the appropriate Euler/Lagrange coupling option with AUTODYN [2.2]. Likewise, the sand/pendulum interactions were modeled through the use of the appropriate Lagrange/Lagrange coupling option.

At the beginning of the simulation, the pendulum is assumed to be at rest (with the gravitational force acting downwards), while the Lagrange and Euler-FCT domains are filled with stationary materials (sand and air, respectively). As explained earlier, the C4 mine was initially modeled as a cylindrical high-density, high-energy sub-domain within the Euler-FCT region.

The motion of the pendulum was constrained to within a vertical plane and a fixed single-point constraint was applied to its pivot point. The *"flow out"* boundary conditions were applied to all the free faces (the faces which do not represent interfaces between the different domains) of the Euler-FCT domain except for the face associated with the vertical symmetry plane. To reduce the effect of reflection of the shock waves at the outer surfaces of the Lagrange domain, *"transmit"* boundary conditions were applied to all the free faces of this domain except for the face associated with the vertical symmetry plane.

To speed up the calculations, all Euler-FCT and Lagrange domains were removed from the analysis after approximately 10ms following detonation when the extent of interaction between the detonation-products/sand ejecta and the pendulum was negligibly small.

2.7. Presentation of Results and Discussion

2.7.1. Validation of the Modified Compaction Equation of State

To validate that the modified compaction equation of state, as described in Section 2.5.4, is correctly implemented in the *mdeosuser.f90* user subroutine and correctly interfaced with AUTODYN [2.2], a series of one cubic-element hydrostatic-compression analyses under different deformation rates is carried out in the present section and the results of these analyses displayed using pressure vs. density plots. The corresponding plots were also generated via numerical integration of the modified compaction equation of state using MATLAB [2.8], a general purpose mathematical package. A perfect agreement was found between the two sets of pressure vs. density plots confirming that the implementation of the modified compaction equation of state was correct.

An example of the results obtained during the validation of the implementation of the equation of state are shown in Figures 2-4(a) and 2-4(b). It should be noted that the results obtained using AUTODYN [2.2] and MATLAB [2.8] are indistinguishable from each other.

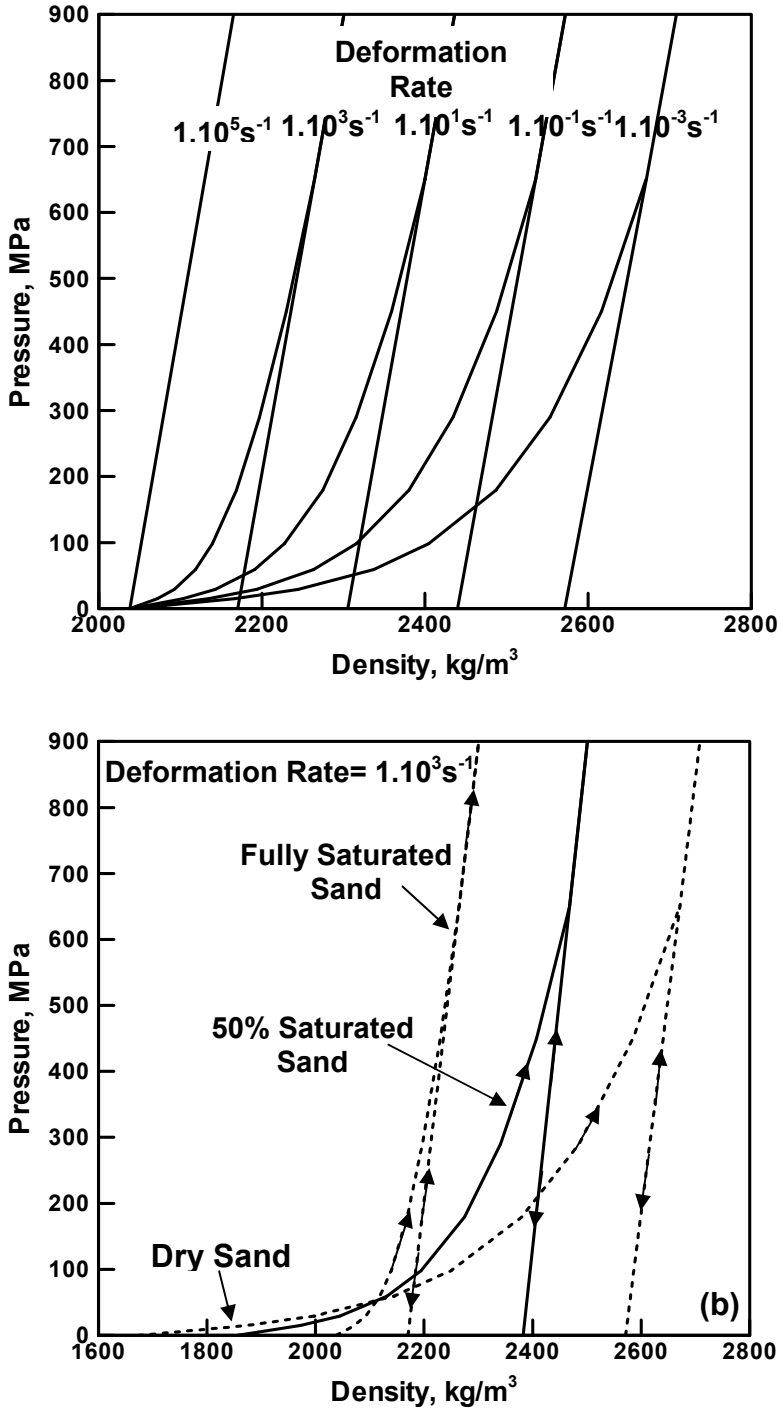

Figure 2-4. Pressure vs. Density Relation for: (a) Fully Saturated Sand with a Porosity Level of 36% at Various Deformation Rates and (b) for Sand at Different Degrees of Saturation and a Deformation Rate of 1.10^3 s^{-1}

2.7.2. Detonation-induced Momentum Transfer to the Pendulum

The non-linear dynamics analysis described in Section 2.6 is carried out in the present section in conjunction with the new materials model for sand described in Section 2.5.4 and Eq. (2.5) to determine the total momentum (impulse) transferred to the horizontal instrumented mine-impulse pendulum by the detonation-products and the sand ejecta. The results obtained are compared with their experimental counterparts as reported in Ref. [2.1].

The effect of the degree of saturation in sand on the total impulse transferred to the pendulum for two types of sand (prairie sand containing high level of silt and clay and impurity-free -30/+50 mesh sand) for the case of a shallow-buried mine at a 5cm depth of burial obtained in Ref. [2.1] is displayed in Figure 2-5. Also displayed in Figure 2-5 are the computational results obtained in the present work using both the original and the modified materials model for sand. The results displayed in Figure 2-5 can be summarized as follows:

(a) The type of sand appears to have a relatively small effect on the impulse transfer;

(b) The degree of saturation of sand has a major effect on the impulse transfer increasing it by 100-150% in saturated sand relative to that in nearly dry sand;

(c) The original compaction model neglects the effect of moisture on the materials response of the sand and hence the total impulse transferred to the pendulum is independent of the degree of saturation;

(d) The modified compaction model, on the other hand, predicts an increase in the total impulse transferred to the pendulum with an increase in the degree of saturation of sand in a qualitative agreement with experimental data reported in Ref. [2.1]; and

(e) The quantitative agreement between the computational total impulse vs. degree of saturation results obtained using the modified compaction model and the experimental results is reasonable considering the fact that the original compaction model (used within the modified

compaction model to represent the behavior of the dry component of sand) also shows a significant disagreement with the experimental results pertaining to dry sand.

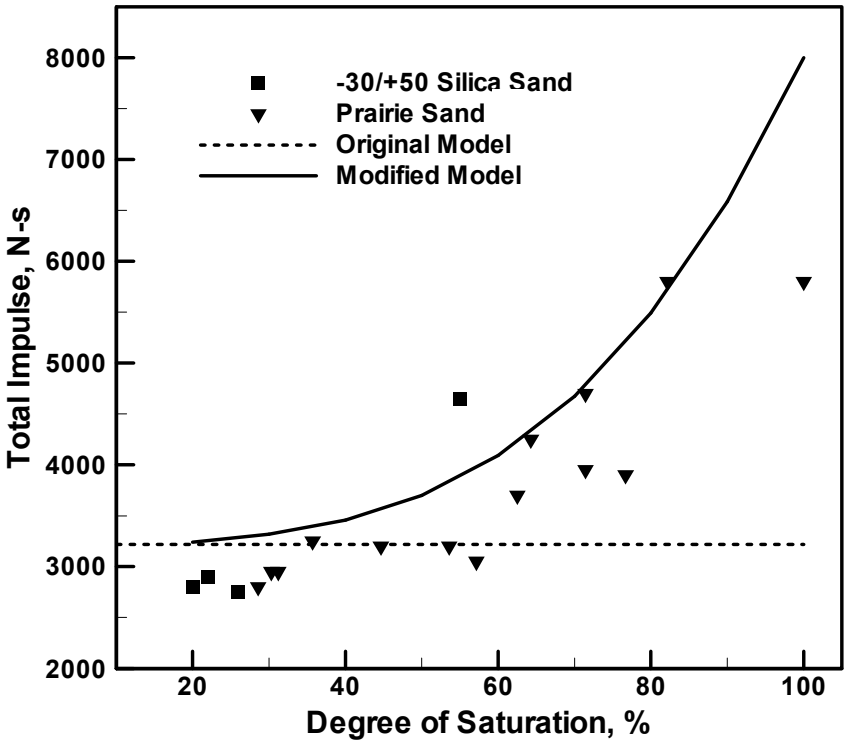

Figure 2-5. The Effect of Degree of Saturation and the Sand Type on the Total Impulse Transferred to the Instrumented Horizontal Mine-impulse Pendulum. Explosive Weight and Type: 1.34kg C4; Depth of Burial: 5cm

The effect of the degree of saturation in sand on the total impulse transferred to the pendulum in the case of the prairie sand containing high level of silt and clay for four different locations of the C4 mine obtained in Ref. [2.1] is displayed in Figures 2-6(a) and 2-6(b). The location of the mine is denoted by the corresponding value of the '*Depth of Burial*' (DOB). A 0cm DOB corresponds to the flush-buried mine while a -5cm DOB corresponds to a ground-laid mine. Also displayed in Figures 2-6(a) and 2-6(b) are the computational results obtained in the present work using the modified materials model for sand. The results displayed in Figures 2-6(a) and 2-6(b) can be summarized as follows:

(a) The lowest value of the impulse transferred to the horizontal instrumented mine-impulse pendulum is obtained in the case of a ground-laid mine, Figure 2-6(a), since this transfer takes place almost exclusively via the interaction of the gaseous detonation products with the pendulum. This is supported by the fact that the impulse transferred to the pendulum is essentially independent of the degree of saturation;

(b) For a flush-buried mine (0cm DOB), Figure 2-6(a), the detonation induced impulse transfer is increased since, in addition to the detonation products, sand ejecta also interact with the pendulum;

(c) The largest impulse transfer occurs in the case of shallow-buried mines (5cm and 10 cm DOB), Figure 2-6(b), where the extent of sand ejection and interaction with the pendulum is the largest;

(d) Since the total impulse transferred to the pendulum is somewhat larger for the case of 5cm DOB than that in the case of 10cm DOB, it appears that there is an optimum DOB which maximizes the lethal effect of detonation of a shallow-buried mine. This can be rationalized by the fact that as the DOB is increased the effects of detonation become more confined within the soil (the *camouflet* effect); and

(e) The overall quantitative agreement between the computational results and their experimental counterparts at different values of DOB is reasonable considering the fact that: (i) as mentioned earlier, the original compaction model is used to represent the behavior of the dry component of the sand and (ii) a significant disagreement between the computational and the experimental results is seen in the -5cm DOB case, Figure 2-6(a), where the choice of the materials model for sand is essentially immaterial since only the gaseous detonation products interact with the pendulum.

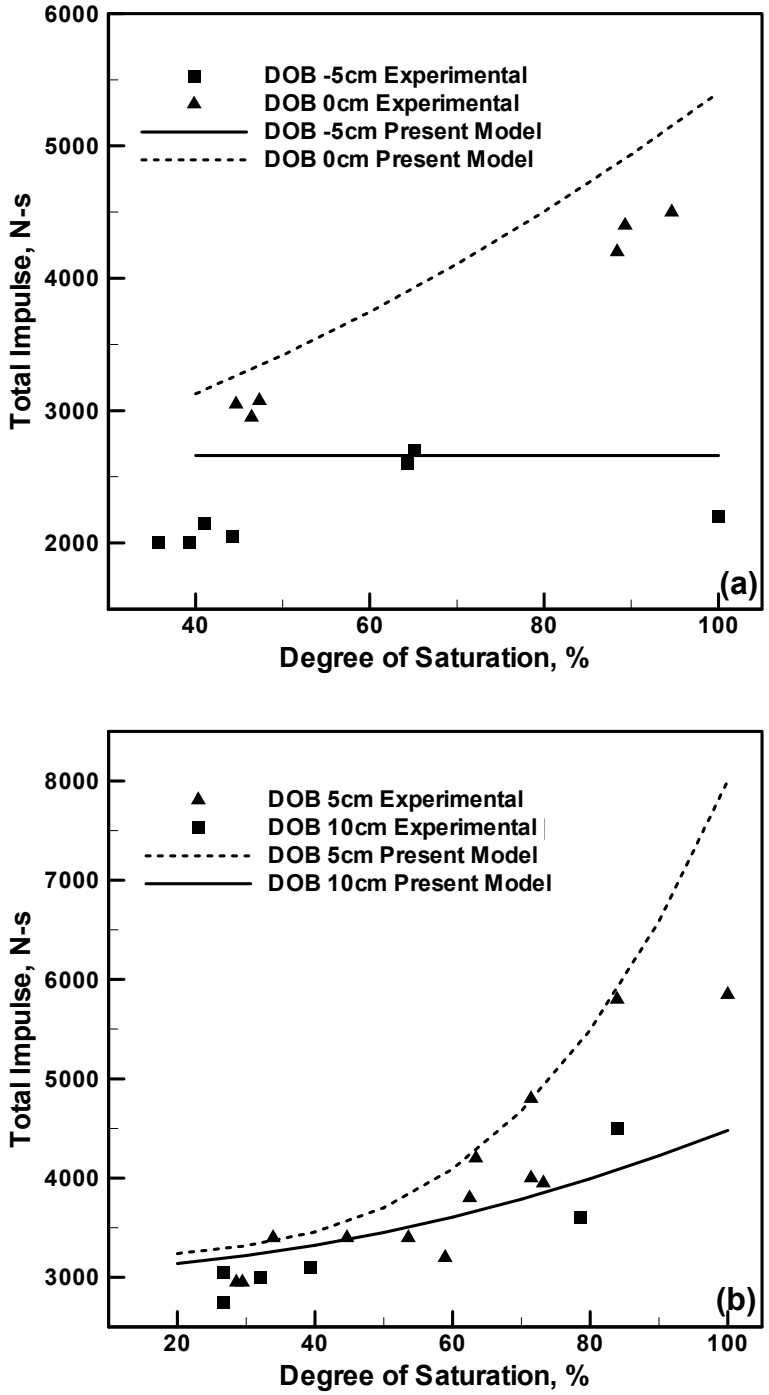

Figure 2-6. The Effect of Degree of Saturation and the Depth of Burial on the Total Impulse transferred to the Instrumented Horizontal Mine-impulse Pendulum. Explosive Weight and Type: 1.34kg C4; Sand Type: Prairie Sand

2.7.3. Blast Wave Propagation in Sand

To further test the validity of the modified compaction model for sand, a non-linear dynamics analysis of the blast wave propagation in sand is carried out and the results obtained compared with their experimental counterparts reported in Ref. [2.7]. The computational analysis carried out in this section follows closely the computational analysis performed in Ref. [2.10] and, hence, only a brief description of the computational model analyzed is given below.

The problem involves an 8kg spherical TNT charge buried at a sufficient depth in sand so that it could be considered as a problem involving a charge buried in an infinitely large sand region. Due to the inherent symmetry of the problem, a two-dimensional axisymmetric analysis was conducted. To minimize the effect of the finite size of the computational domain, the spatial dimension of the computational model is made large enough and the transmit boundary conditions are applied. The transmit boundary conditions enable for the propagation of pressure waves across the main boundaries without reflection, Ref. [2.10]. Since the charge volume is very small in comparison to the volume of the computational domain, the mesh size was increased as a function of the distance from the charge center. To check the adequacy of the mesh size in simulating the blast effects, a convergence study was conducted, whereby trial calculations were performed and the mesh was refined after each analysis until the difference of the results between two consecutive calculations was deemed small. The final mesh used consisted of 35,250 elements, with the smallest element being 25mmx25 mm, and the largest element being 200x200 mm. A series of gage points were defined within the sand domain at the same depth as the buried charge to monitor the blast wave propagation. The TNT charge was represented using the Jones–Wilkins–Lee (JWL) equation of state, Ref. [2.11], while the modified compaction model was used for sand.

The variation of the peak pressure with a scaled distance from the charge center in sand at four different Degrees of Saturation (DOS) obtained experimentally in Ref. [2.10] is displayed using a log-log plot in Figures 2-7(a) and 2-7(b). For comparison, the corresponding computational results obtained in the present work are also shown in Figures 2-7(a) and 2-7(b). The scaled distance is defined as the ratio of the distance from the charge center and the cube root of the charge mass. The results displayed in Figures 2-7(a) and 2-7(b) can be summarized as follows:

(a) At each level of the degree of saturation, the peak pressure decreases monotonically (non-linearly) with the scaled distance;

(b) At any value of the scaled distance, the peak pressure increases with an increase in the degree of saturation of sand;

(c) The trends identified in (a) and (b) are also displayed by the computational results;

(d) The overall quantitative agreement between the computational and experimental results is reasonable considering a significant scatter in the experimental results. It should be noted that the results displayed in Figures 2-7(a) and 2-7(b) are a better indication of the ability of the modified compaction model to account for the dynamic behavior of sand at different levels of the degree of saturation than the results presented in Figures 2-5 and 2-6 since: (i) they include only the effect of charge/sand interactions and (ii) the detonation products are represented by a more realistic (JWL) model.

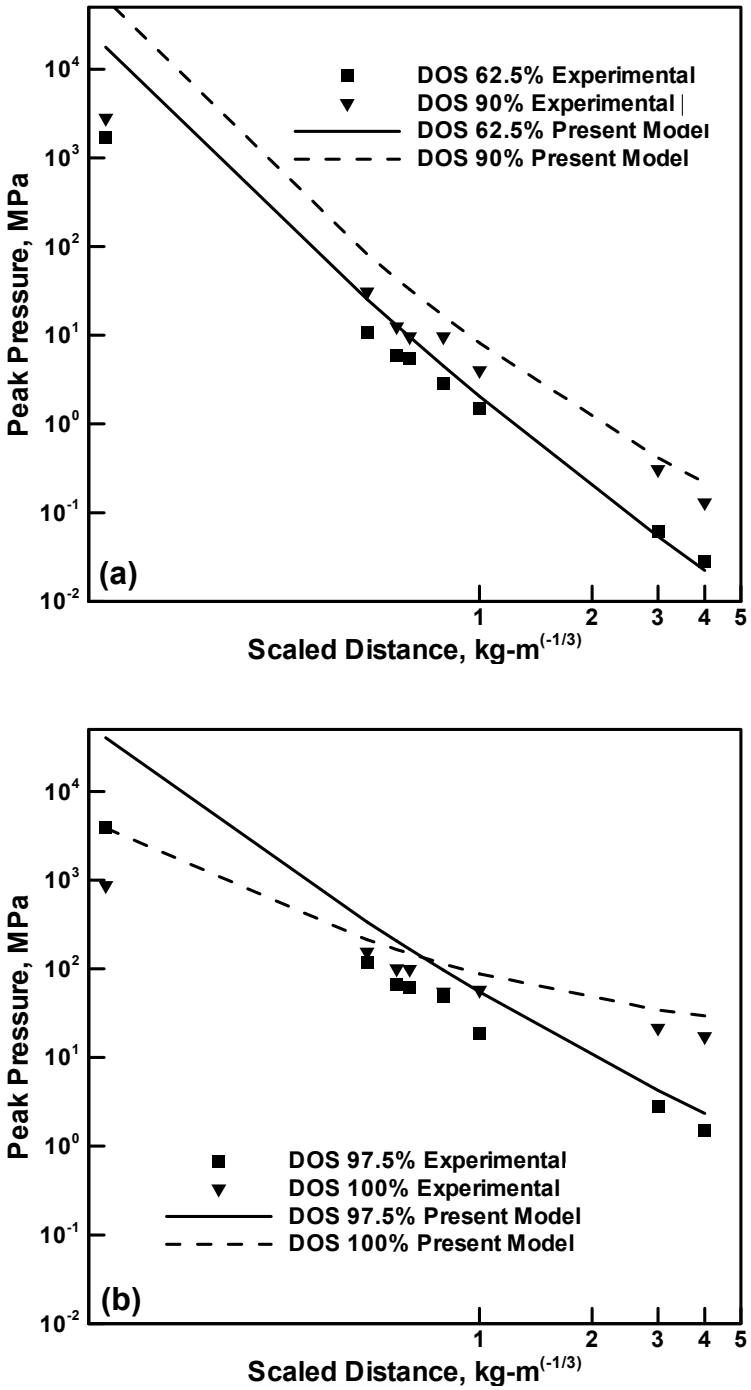

Figure 2-7. Variation of Peak Pressure with the Scaled Distance from the Charge Center and the Degree of Saturation for: (a) 62.5 and 90% DOS and (b) 97.5% and 100% DOS. Explosive Weight and Type: 8kg TNT; Sand Type: Sandy loam

The variation of the specific impulse with a scaled distance from the charge center in sand at four different degrees of saturation obtained experimentally in Ref. [2.10] is displayed in Figures 2-8(a) and 2-8(b). For comparison, the corresponding computational results obtained in the present work are also shown in Figures 2-8(a) and 2-8(b). The results displayed in Figures 2-8(a) and 2-8(b) are obtained by integrating with respect to time the pressure vs. time traces at the location of the pressure transducers/gage points. An analysis of the results displayed in Figures 2-8(a) and 2-8(b) reveals that conclusions similar to those drawn from Figures 2-7(a) and 2-7(b) can be made.

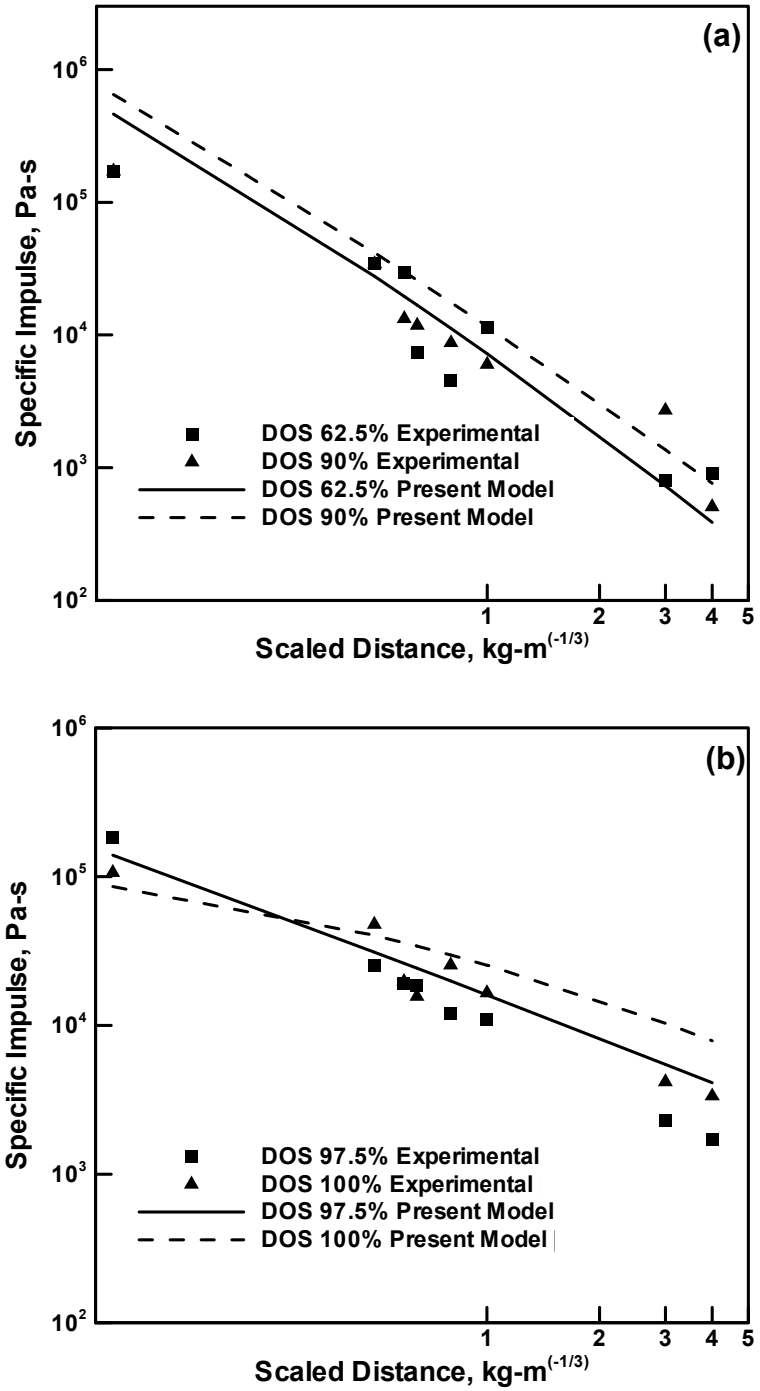

Figure 2-8. Variation of Specific Impulse with the Scaled Distance from the Charge Center and the Degree of Saturation for: (a) 62.5 and 90% DOS and (b) 97.5% and 100% DOS. Explosive Weight and Type: 8kg TNT; Sand Type: Sandy loam

2.7.4. Sand Crater Morphology

The final comparison between the experimental and computational results used to validate the modified compaction model for sand is presented in this section. The experimental results used in this section pertain to the sand crater morphology resulting from the detonation of 0.1kg C4 charges buried in sand (contained in a thick-wall barrel) at different DOBs obtained in Ref. [2.4]. Since a detailed account of the associated computational procedure used is given in our previous work [2.3], such details are not presented here. Rather, only the relevant results are presented and compared with their experimental counterparts.

The final morphology of the craters resulting from detonation of the C4 high-energy explosive at 0cm, 3cm and 8cm DOBs experimentally determined in Ref. [2.4] are displayed in Figures 2-9(a)-(c), respectively. Figures 2-9(a)-(c) can be summarized as follows:

(a) For each of the three values of DOB, the crater width extends up to the diameter of the barrel (barrel walls are denoted as heavy solid lines);

(b) The depth of the crater increases slightly with an increase in the DOB from approximately 16cm, in the case of 0cm DOB, to approximately 17cm, in the case of 8cm DOB; and

(c) For the cases of 0cm and 3cm DOB, the central portion of the crater appears to be nearly flat, Figures 2-9(a)-(b), while for the case of 8cm DOB, Figure 2-9(c), the central portion of the crater contains a minor bulge.

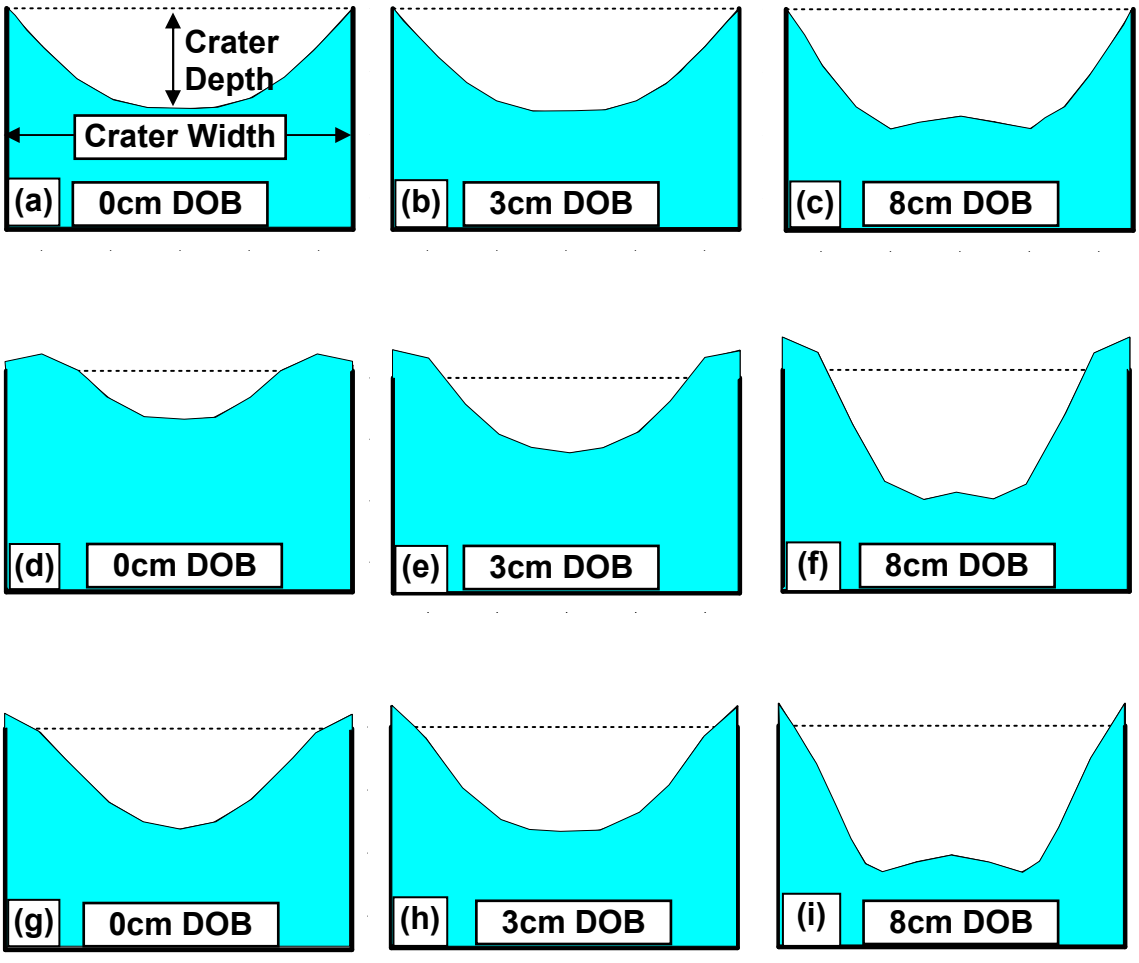

Figure 2-9. Effect of the Depth of Buri1al (DOB) on the Crater Shape obtained: (a)-(c) Experimentally in Ref. [2.4]; (d)-(f) Computationally using Original Compaction Model for Sand; (g)-(i) Computationally using the Modified Compaction Model for Sand. DOS: 7.5%. Explosive Weight and Type: 0.1kg C4; Sand Type:-30/+50 Mesh Silica Sand

The corresponding computational results obtained using the original compaction model for sand is displayed in Figures 2-9(d)-(f). Figures 2-9(d)-(f) differ from their measured counterparts displayed in Figures 2-9(a)-(c) in several respects:

(a) The computed sand craters (defined with respect to the initial position of the sand/air interface) do not extend out to the barrel walls;

(b) The computed results show that some displaced sand remains above the initial position of the sand/air interface (denoted as a dashed line);

(c) While the computed results show an increase in the crater depth with an increase in DOB, in agreement with the measured results, this variation is substantially more pronounced in the case of the computed results;

(d) The computed values of the crater depth at low values of DOB, Figures 2-9(d)-(e), are substantially lower than their measured counterparts, Figures 2-9(a)-(b); and

(e) While the computed crater shape for the largest DOB, Figure 2-9(f), shows a bulge at its bottom in agreement with the corresponding experimentally determined crater shape shown in Figure 2-9(c), the height of the computed bulge is clearly smaller.

The corresponding computational results obtained using the modified compaction model for sand is presented in Figures 2-9(g)-(i). A comparison of the results displayed in Figures 2-9(a)-(c), 2-9(d)-(f) and 2-9(g)-(i), show that the modified compaction model for sand gives a qualitatively better agreement with the experimental results than the original compaction model.

It should be noted that the measured results shown in Figures 2-9(a)-(c) correspond to the final crater shapes while the computed crater shapes displayed in Figures 2-9(d)-(f) and 2-9(g)-(i) are obtained after simulation time of 150ms (at this time, sand velocities are found to be quite small, suggesting that no major subsequent changes in the crater shape should be expected).

To obtain a more quantitative comparison between the measured and computed crater shapes, the corresponding variations in the crater depth and the crater width with the charge DOB are displayed in Figures 2-10(a) and 2-10(b), respectively. It should be noted that the measured crater depths correspond to their final values while the measured crater widths correspond to the time of 12ms following detonation, the time which was matched in the computational analysis. Hence, obtaining a better agreement with respect to the crater width between the experiment and the computational analysis is more critical.

By analyzing Figures 2-9-2-10, the following main observations can be made:

(a) In general, the agreement between the computed sand crater shapes based on the modified sand materials models and their measured counterparts is improved relative to the corresponding agreement based on the original sand materials model;

(b) The improvement is particularly pronounced at smaller values of the DOB; and

(c) The computed sand crater shape and size appear to be fairly sensitive functions of the sand materials model used.

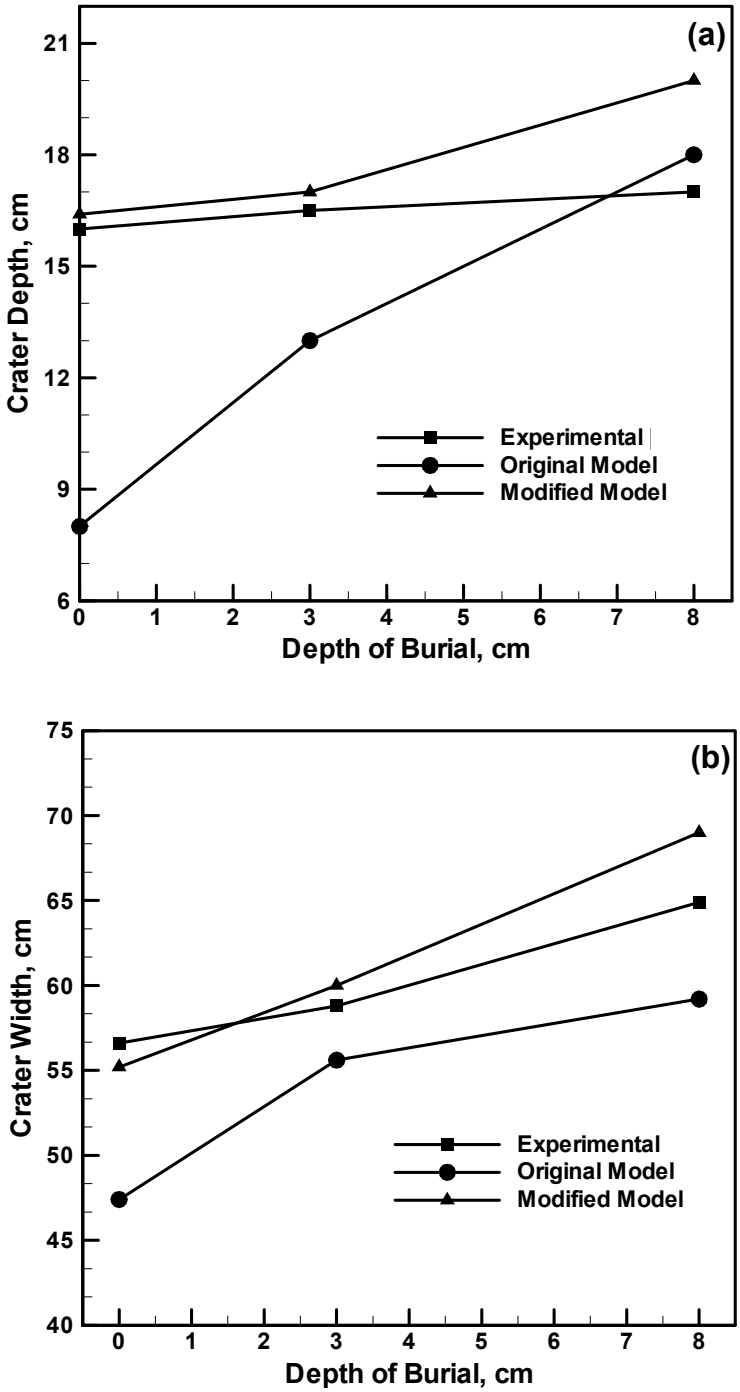

Figure 2-10. Variation of the (a) Final Crated Depth and (b) Final Crater Width (at a Post-detonation Time of 12ms) with Depth of B2urial. DOS: 7.5%; Explosive Weight and Type: 0.1kg C4; Sand Type:-30/+50 Mesh Silica Sand

2.8. Summary and Conclusions

Based on the results obtained in the present work, the following main summary remarks and conclusions can be drawn:

1. Water residing in the pores and the rate of deformation play a critical role in the dynamic material response of sand. In particular, the behavior of dry sand is essentially rate independent and dominated by irreversible energy-absorbing densification processes while the high deformation-rate behavior of saturated sand is predominantly elastic and controlled by incompressibility of water. Consequently, the efficiency of momentum transfer to the target structure/personnel during detonation of a shallow buried mine is higher in the case of saturated sand.

2. The modified compaction materials model for sand developed in the present work appears to capture the essential feature of the effect of the degree of saturation and the rate of deformation on the dynamic materials behavior during its interaction with high-pressure detonation products and the target structures. This conclusion was the result of a comprehensive analysis within which findings of a number of mine-detonation studies were compared with their computational counterparts.

3. In the current rendition of the modified compaction model for sand, the effects of the degree of saturation and the rate of deformation are included only in the volumetric behavior of sand as represented by its equation of state. Since the degree of saturation (and, perhaps, the rate of deformation) can also affect the constituent behavior of sand represented by its strength model, further development of the modified compaction model is planned to account for these potential effects.

2.9. References

2.1 D. Bergeron, J. E. Trembley, "*Canadian Research to Characterize Mine Blast Output*,"16th International MABS Symposium, Oxford, UK, September 2000.

2.2 AUTODYN-2D and 3D, Version 5.0, *User Documentation*, Century Dynamics Inc., 2004.

2.3 M. Grujicic, B. Pandurangan and B. Cheeseman, "*A Computational Analysis of Detonation Phenomena Associated with Mines Shallow-buried in Sand*," Journal of Impact Engineering, submitted for publication, May 2005.

2.4 D. Bergeron, R. Walker and C. Coffey, "*Detonation of 100-gram Anti-Personnel Mine Surrogate Charges in Sand-A Test Case For Computer Code Validation*," Suffield Report No. 668, Defence Research Establishment Suffield, Ralston, Alberta, Canada, April 1998.

2.5 L. Laine and A. Sandvik, "*Derivation of Mechanical Properties for Sand*," Proceedings of the 4th Asia-Pacific Conference on Shock and Impact Loads on Structures, CI-Premier PTE LTD, Singapore, November 2001, 361-368.

2.6 D. Bergeron, S. Hlady and M. P. Braid, "*Pendulum Techniques to Measure Land Mine Blast Loading*," 17th International MABS Symposium, Las Vegas, USA, June 2002.

2.7 J. Henrych, "*The Dynamics of Explosion and Its Use*", Chapter 5, Elsevier Publications, New York, USA, 1979.

2.8 MATLAB, 6th Edition, "*The Language of Technical Computing*," The Math Works Inc., 24 Prime Park Way, Natick, MA, 01760-1500, 2000.

2.9 Z. Wang, H. Hao and Y. Lu, "*A Three-phase Soil Model for Simulating Stress Wave Propagation due to Blast Loading*," International Journal for Numerical and Analytical methods in Geomechanics, 28, 2004, 33-56.

2.10 Z. Wang, H. Hao and Y. Lu, "*Numerical Investigation of Effects of Water Saturation on Blast Wave Propagation in Soil Mass*," Journal of Engineering Mechanics, May 2004, 551-561.

2.11 E. L. Lee, H. C. Hornig and J. W. Kury, "*Adiabatic Expansion of High Explosive Detonation Products*," UCRL – 50422, Lawrence Radiation Laboratory, University of California, 1968.

CHAPTER 3

DERIVATION AND VALIDATION OF A MATERIAL MODEL FOR CLAYEY SAND FOR USE IN LANDMINE DETONATION COMPUTATIONAL ANALYSES

3.1. Abstract

A large-strain/high-deformation rate model for clay-free sand recently proposed and validated in our work [3.1,3.2], has been extended to sand containing relatively small (< 15vol.%) of clay and having various levels of saturation with water. The model includes an equation of state which represents the material response under hydrostatic pressure, a strength model which captures material behavior under elastic-plastic conditions and failure model which defines conditions and laws for the initiation and evolution of damage/failure in the material. The model was validated by comparing the computational results associated with detonation of a landmine in clayey sand (at different levels of saturation with water) with their computational counterparts.

3.2. Introduction

Despite the signing of Mine Ban treaty in 1999, it is widely recognized that there is a landmine crisis. The following are some of the main aspects of this crisis: (a) in excess of 100 Million unexploded landmines remain deployed in over 60 countries or over the world [3.3]; (b) Nearly 30,000 civilians are killed or maimed every year by unintended detonations of the mines [3.4]; (c) the cost of medical treatment of landmine injuries exceed 100 million per year [3.5]; (d) the ability of the international community to provide the humanitarian relief in terms of medical services, safe drinking water and food, etc., is greatly hampered by landmine contamination of the infrastructure in mine affected countries [3.5]; and so on. To address the aforementioned landmine crisis, the research community around the world has taken upon itself the challenge of

helping better understand the key phenomena associated with landmine detonation and interaction between detonation products, mine fragments and soil ejecta with the targets (people, structures and vehicles). Such improved understanding will help automotive manufacturers to design and fabricate personnel carriers with higher landmine-detonation survivability characteristics and a larger level of protection for the onboard personnel. In addition, the manufacturer of demining equipment and personnel protection gear used in landmine clearing are expected to benefit from a better understanding of the landmine detonation-related phenomena.

The landmine detonation related research activity can be broadly divided into three main categories: (a) shock and blast wave mechanics and dynamics including landmine detonation phenomena and large-deformation/high-deformation rate constitutive models for the attendant materials (high explosive, air, soil, etc.); (b) the kinematic and structural response of the target to blast loading including the role of target design and use of blast attenuation materials; and (c) vulnerability of human beings to post-detonation phenomena such as high blast pressures, spall fragments and large vertical and lateral accelerations.

The present work falls primarily into the category (a) of the research listed above since it emphasizes the development of a large-deformation/high-deformation rate material model for clay-containing sand with various levels of water content. It is generally recognized that the properties of soil, into which a landmine is buried, play an important role in the overall effectiveness/lethality of the landmine regarding of the nature of its deployment (fully-buried, flush-buried or ground-laid). The present work, during the material-model validation stage, also addresses briefly the category (b) of the landmine detonation related research.

While there are a variety of soils, it is customary to divide soil into two main categories: (a) Cohesion-less soils (e.g. sand) which consist of relatively coarse particles (average particle size 4.0-4.75mm) which have a negligible tensile strength and derive their shear strength

primarily from the inter-particle friction; and (b) Cohesive soils (e.g. clay) which consist of fine particles (average particle size 50-75μm) which derive their strength and failure properties from the inter- and intra-particle electrostatic and polar forces. In the present work, we address the problem of material model derivation and validation for sand containing minor (< 15vol. %) of clay. Such sand was assumed to have been at some point fully saturated with water which has caused the clay particles to become suspended in water and (upon a subsequent decrease in the water content) form a continuous (bonding) coating over the sand particles. Such sand, as will be discussed in next section, acts as a cohesive soil and displays a combination of properties derived from those of sand and clay. It should be also noted that, in addition to clay, sand may often contain silt with micron-size particles. In such cases, clay would normally act as a binder and promote formation of the agglomerates of silt particles. Such agglomerates are generally smaller than and tend to primarily reside within the sand inter-particle spaces (voids) and, hence, are not expected to have as pronounced effect on the mechanical response of sand as does clay. That is the reason why, in this work, the effect of silt is not considered.

A review of the literature shows that there exists an extensive body of work dealing with the investigation of the detonation of the buried charges. However, much of this work does not focus on the characterization of the blast output of landmines, but rather on cratering effects in soils, with applications towards the efficient utilization of explosives for excavation (i.e. canals, trenches, etc.) or in the survivability of structures subjected to near surface blasts [3.6]. Westine et al. [3.7] carried out experiments on a plate which was mounted above a buried charge comparable is size and power to an anti-tank landmine. The plate contained a number of through-the-thickness holes at incremental distances from the mine, in which, plugs of known mass were placed. The blast accompanying mine detonation caused the plugs to be ejected from the holes and from their initial velocity the impulsive loading on the plate was calculated. Morris [3.8]

used the results of Westine et al. [3.7] to construct a design-for-survivability computer code for lightweight vehicles. More recently, Bergeron et al. [3.9] carried out a comprehensive investigation of the buried landmine blasts using an instrumented ballistic pendulum. From these experiments, the pressure and impulse as a function of time were recorded at several locations in air directly above the mine as well as in the sand surrounding the landmine, along with X-ray radiographs and high-speed photographs of the associated soil cratering and ejecting phenomena.

In our recent computational work [3.10], based on the use of AUTODYN, a general-purpose transient non-linear dynamics explicit simulation software [3.11], a detailed comparison was made between the experimental results of Bergeron et al. [3.12] and their computational counterparts for a number of detonation-related phenomena such as the temporal evolutions of the shape and size of the over-burden sand bubbles and of the detonation-products gas clouds, the temporal evolutions of the side-on pressures in the sand and in air, etc. It was found that the most critical factor hampering a better agreement between the experiment and computational analysis is an inadequacy of the current material model for sand to capture the dynamic response of this material under blast loading conditions. Hence, the main objective of our subsequent work [3.1] was to improve the compaction material model for sand in order to include the effects of the degree of saturation and rate of deformation, the two important effects which were neglected in the original compaction model (proposed by Laine and Sandvik [3.13]) used in AUTODYN [3.11]. The new material constitutive model for sand was subsequently validated for the case of sand with different levels of (water) saturation by comparing the experimental results associated with detonation of the shallow-buried and ground-laid C4 mines obtained through the use of an instrumented horizontal mine-impulse pendulum with their computational counterparts obtained via detailed numerical modeling of the same physical problem using AUTODYN. In our subsequent work [3.2], the ability of the newly developed material model to predict the temporal

evolutions of the blast loads associated with the detonation of mines buried in fully water-saturated sand was tested. This was done by comparing the model predictions with their experimental counterparts obtained in the work of Taylor and Skaggs [3.14] who carried out large-scale experiments using the *Vertical Impulse Measurement Fixture* (VIMF) at the Army Research Laboratory, Aberdeen, MD. All this work culminated in the development of a large deformation/high-deformation rate material model for sand [3.2]. This model for sand is referred to as CU-ARL sand model in the remainder of this manuscript.

As discussed above, the CU-ARL sand model was found to significantly improve the agreement between the transient non-linear dynamics simulations and experimental investigations of several scenarios involving detonation of landmines ground laid or buried in sand to various depths. These improvements were brought about by the inclusion of the effects of water-saturation levels on the compressibility as well as on the cohesive and shear strengths of sand. The objective of the present work is to extend the approach used in our previous work [3.1, 3.2] to the development of a material model for clay-containing sand at different levels of saturation with water. Since this model was jointly developed by Clemson University and the Army Research Laboratory, Aberdeen Proving Ground, MD, it will be referred to, in the remainder of this document, as the CU-ARL clayey-sand model. As will be shown in the next section, the mechanical response of clayey-sand is greatly affected by the phenomena such as clay-coating cohesive and shear strengths, sand inter-particle adhesion, sand inter-particle friction and the adsorption of water by the clay coating and the extent of water in the inter-particles spaces.

The organization of this chapter is as follows. Morphology and microstructure of clay and clayey sand are discussed in Sections 3.3.1 and 3.3.2, respectively. Derivation and parameterization of the CU-ARL clayey sand model are discussed in Section 3.4. The results of the model validation via comparison of the computational and experimental results for a number

of scenarios involving landmine detonation in sand and subsequent interactions of the detonation products, mine fragments and soil ejecta are presented and discussed in Section 3.5. A brief summary and the conclusions obtained in the present work are discussed in Section 3.6.

3.3. Model Derivation and Computational Analysis

3.3.1. Atomic Level Microstructure and Morphology of Clay

As stated earlier, soils are generally classified into two groups: (a) those dominated by sand and (b) those consisting of major fractions of clay. While in both cases, the basic architecture of soil involves a skeleton of solid particles and interconnected spaces (voids) filled with air and/or water, the nature of the inter-particle forces differs in the two cases: (a) In the case of sand, very little adhesion exists between contacting particles which can interact only via mechanical/frictional forces and (b) In clays, particles are finer and more plate-like ensuring large inter-particle contact which in conjunction with the inter-particle electro-chemical forces provides a high cohesive strength and ductile behavior of the material. These properties of clay are closely related to their atomic level structure which is displayed schematically in Figure 3-1.

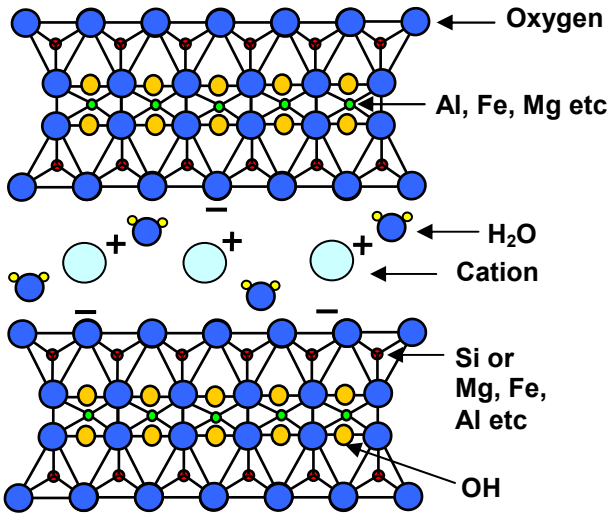

Figure 3-1. A Schematic of the Atomic-level Microstructure of Clay

A simple analysis of the atomic-level microstructure of clay displayed in Figure 3-1 reveals that this material is composed of sheet-like silicate layers with a particular stacking sequence. In natural clay, this sequence involves a central layer consisting mainly of aluminum cations (and oxygen anions) sandwiched between two tetrahedral layers consisting of silicon cations and oxygen anions. Typically, some of the aluminum and silicon ions are replaced by lower valence ions such as Mg^{2+}, Ca^{2+}, Li^{+} etc. creating a negative charge imbalance in each of the 3-layer sheets. The charge imbalance is neutralized by adsorption of Na^{+}, Ca^{2+} and K^{+} cations which tend to have water molecules associated with them. The hydrated Na^{+}, Ca^{2+} and K^{+} cations reside in the interlayer region making clay behave as a pliable material and, at higher water levels, cause the clay to swell.

The atomic structure and properties of clay discussed above are expected to affect the mechanical response of sand whose particles are coated with a thin layer of clay, i.e. the type of clayey sand analyzed in the present work.

3.3.2. Atomic Level Microstructure and Morphology of Clayey Sand

The CU-ARL clayey sand model developed in the present work is aimed at capturing the high-deformation rate behavior of sand containing no more than 15vol.% clay. Under such conditions, clay is most frequently present as a coating on sand particles (rather than being in the form of discrete particles). A schematic of the morphology and microstructure of the CU-ARL sand and the CU-ARL clayey sand is given in Figures 3-2(a)-(b), respectively.

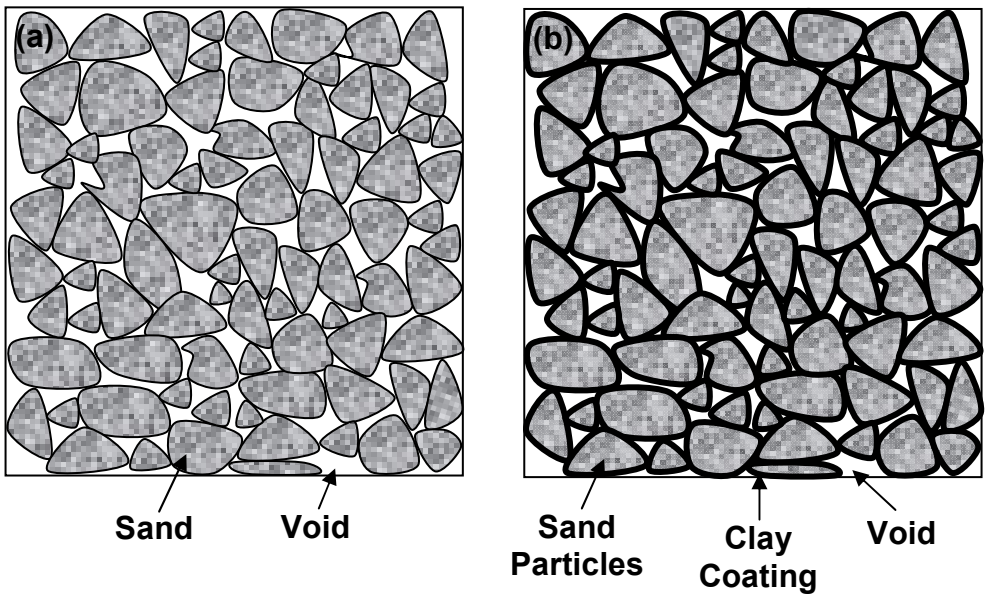

Figure 3-2. A Comparison between Microstructure of: (a) CU-ARL Sand and (b) CU-ARL Clayey Sand

3.4. Material Model Development for Clayey Sand

As discussed earlier, the main objective of the present work is to derive a material for clayey sand with various levels of water content. Such model is needed in computational analyses of various scenarios involving landmine detonation with various types of deployments in soil. Since the computational analyses in question are of a transient, non-linear dynamic nature, the clay model to be developed (the CU-ARL clayey sand model) is primarily required to compute the response of this material under large deformation, high-deformation rate and large pressure conditions. The validity of the model under slow-speed quasi-static conditions is not the subject of this work. As discussed in our previous work [3.1, 3.2], a typical transient non-linear dynamics problem involves numerical simulation of the governing mass, momentum and energy

conservation equations. Spatial coordinates and time are independent variables while mass density, velocities and the internal energy densities are the dependent variables in these equations. Since the stress appears explicitly in these equations, a set of relations (the material model) is needed to establish (for a given material) the relationships between stress and the dependent variables (and/or there integrals). Furthermore, since stress, σ, is generally decomposed into a hydrostatic stress ($-pI$, where p is pressure and I is a second order identity tensor) and a deviatoric stress σ_d, the material model is generally decomposed into: (a) an *Equation of State*, EOS (defines the density and internal energy density dependences of pressure); (b) a strength model (used to express the evolution of deviatoric stress in the elastic and elastic-plastic region of the material) and (c) a failure model (defines the damage/failure response of the material). In addition to these relations, an erosion model is often defined to alleviate numerical difficulties arising in regions experiencing large deformations. Within the erosion model, heavily deformed regions can be removed while conserving their momenta via the retention of the associated nodes as well as the nodal masses and velocities. In the remainder of the section, a brief overview is presented of the derivation of an equation of state, a strength model, a failure model and an erosion model for clayey sand.

For the microstructure of clayey sand proposed in Figure 3-2(b), one would expect that the compaction/compression behavior (as represented by the equation of state) will not be significantly different than that in CU-ARL sand. On the other hand, the shear and failure behavior which are controlled by a low shear resistance and high cohesion strength of clay, respectively, will be significantly affected.

Since the CU-ARL clayey sand material model is intended to include the effects of porosity, degree of saturation and clay content, following parameters are defined to represent the chemical and microstructural state of sand:

$$\alpha = \frac{V_{water} + V_{air}}{V_{total}} \tag{3.1}$$

$$\beta = \frac{V_{water}}{V_{water} + V_{air}} \tag{3.2}$$

and

$$\Omega = \frac{V_{clay}}{V_{clay} + V_{sand}} \tag{3.3}$$

where α is the extent of porosity, β is the degree of saturation, Ω is the solid fraction of clay (clay content), V is volume and the subscripts *sand*, *clay*, *air*, *water* and *total* are self explanatory.

3.4.1. CU-ARL Clayey Sand Equation of State

In this section, the equation of state (EOS) representing the compaction behavior of clayey sand is presented. Table 3-1 contains a list of all parameters appearing in the equation of state for the dry, unsaturated and saturated clayey sands. The equation of state for the CU-ARL clayey sand is defined below as a simple extension of the CU-ARL sand EOS to account for the effect of clay on the model parameters. The CU-ARL sand EOS was originally derived by separately developing the equation of state for dry and fully saturated sand and combining them (using a simple rule of mixture) to define the corresponding relationships for unsaturated sand [3.2].

Dry Sand: The relevant CU-ARL dry sand EOS relations are presented first. The dry-sand pressure dependence on density is defined as [3.1]:

$$P_{dry\ sand} = \begin{cases} 0 & \rho_{dry\ sand} \le \rho_{o,dry\ sand} \\ B_{Pl.Comp,dry\ sand}\left(\rho_{drysand} - \rho_{o,drysand}\right) & \rho_{o,dry\ sand} \le \rho_{dry\ sand} \le \rho^{*}_{dry\ sand} \\ B_{SolidComp,dry\ sand}\left(\rho_{drysand} - \rho_{s,drysand}\right) & \rho_{dry\ sand} > \rho^{*}_{dry\ sand} \end{cases} \tag{3.4}$$

where $B_{Pl.Comp,\ dry\ sand}$ and $B_{SolidComp,\ drysand}$ (=21.68 MPa.m^3/kg [3.2])are respectively the plastic compaction (densification) and the solid-particle compaction moduli, while $\rho_{o,dry,sand} = (1-\alpha_0)\rho_{s,dry\ sand}$ and $\rho_{s,dry\ sand}$ (=2641 kg/m^3) are the initial density of dry sand and the density of the fully compacted sand, respectively and α_o denotes the initial porosity in sand. It should be noted, that the compaction moduli used in Eq. (3.4) are defined as a ratio of the corresponding bulk moduli and mass-densities. The plastic compaction modulus, $B_{Pl.Comp,\ dry\ sand}$, is defined as:

$$B_{Pl.Comp,dry\ sand} = \frac{P_{Comp,dry\ sand}}{\left(\rho^{*}_{dry\ sand} - \rho_{o,dry\ sand}\right)} \tag{3.5}$$

where $P_{Comp,\ dry\ sand}$ (=0.650GPa [3.13]) is the minimum pressure needed for full densification of sand and $\rho^{*}_{dry\ sand}$ is given by;

$$\rho^{*}_{dry\ sand} = \rho_{s,dry\ sand} + \frac{P_{Comp,dry\ sand}}{B_{SolidComp,dry\ sand}} \tag{3.6}$$

To account for the effect of clay in CU-ARL dry clayey sand (specifically that the volumetric-response is controlled by the more compliant clay layer over-coating sand particles), the CU-ARL dry sand EOS model parameters are generalized as:

$$\rho_{o,dry,clayey\ sand} = (1-\alpha)\rho_{s,dry\ clayey\ sand} = (1-\alpha)\left[(1-\Omega)\rho_{s,dry\ sand} + \Omega\rho_{s,clay}\right] \tag{3.7}$$

$$P_{Comp,dry\ clayey\ sand} = (1-\Omega)\,P_{Comp,\,dry\ sand} + \Omega\,P_{Comp,clay} \tag{3.8}$$

$$B_{Pl.Comp,dry\ clayey\ sand} = \frac{P_{Comp,dry\ clayey\ sand}}{\left(\rho^{*}_{dry\ clayey\ sand} - \rho_{o,dry\ clayey\ sand}\right)} \tag{3.9}$$

$$\rho^{*}_{dry\ clayey\ sand} = \rho_{s,dry\ clayey\ sand} + \frac{P_{Comp,dry\ clayey\ sand}}{B_{SolidComp,dry\ clayey\ sand}} \tag{3.10}$$

and

$$B_{solid\ comp,dry\ clayey\ sand} = (1-\Omega)B_{solid\ comp\ dry\ sand} + \Omega B_{solid\ comp\ clay} \tag{3.11}$$

Table 3-1. Parameters appearing in the definition of EOS model for dry, unsaturated and saturated clayey sands with an initial porosity of 0.36 and a clay content of 0.15

Parameter	Symbol	Unit	Value
Dry Clayey Sand			
Initial Density of Dry Clayey Sand	$\rho_{0,dry\ clayey\ \text{sand}}$	kg/m^3	1637.2
Reference Density of Dry Clayey Sand	$\rho_{s,\ dry\ clayey\ sand}$	kg/m^3	2558.2
Dry Clayey Sand Plastic Compaction Modulus	$B_{PlComp,\ dry\ clayey\ sand}$	$MPam.^3kg^{-1}$	581.66
Dry Clayey Sand Solid Compaction Modulus	$B_{SolidComp,\ dry\ clayey\ sand}$	$MPam.^3kg^{-1}$	18453
Minimum Pressure for Full Compaction of Dry Clayey Sand	$P_{Comp,\ dry\ clayey\ sand}$	GPa	0.5531
Saturated Clayey Sand			
Initial Density of Saturated Clayey Sand	$\rho_{0,sat\ clayey\ \text{sand}}$	kg/m^3	1997.2
Saturated Clayey Sand Compaction Modulus	$B_{Comp,\ sat\ clayey\ sand}$	$MPam.^3kg^{-1}$	12584
Minimum Pressure for Full Compaction of saturated Clayey Sand	$P_{Comp,\ sat\ clayey\ sand}$	GPa	0.5531

Saturated Sand: The (high deformation-rate) pressure vs. density curve for saturated clayey sand is defined as a simple extension of the pressure vs. density curve for saturated sand [3.2] and is expressed as:

$$P_{sat\ clayey\ sand} = \begin{cases} 0 & \rho_{sat\ clayey\ sand} \le \rho_{o,sat\ clayey\ sand} \\ B_{sat\ clayey\ sand}\left(\rho_{sat\ clayey\ sand} - \rho_{o,sat\ clayey\ sand}\right) & \rho_{sat\ clayey\ sand} > \rho_{o,sat\ clayey\ sand} \end{cases} \tag{3.12}$$

where $B_{sat\ clayey\ sand}$ is the compaction modulus of saturated clayey sand and is defined using the compaction modulus of dry clayey sand, $B_{SolidComp,\ dry\ clayey\ sand}$ and the compaction modulus of water, B_w, and the fact that both the solid phase and the water-filled porosity form continuous networks, as:

$$B_{sat\ clayey\ sand} = (1-\alpha_0)B_{SolidComp,dry\ clayey\ sand} + \alpha_0 B_w \tag{3.13}$$

while $\rho_{o,\ sat\ clayey\ sand}$ is the initial density of saturated clayey sand and is defined in terms of the density of dry clayey sand, $\rho_{s,dry\ clayey\ sand}$, and the density of water, ρ_w, as:

$$\rho_{o,sat\ clayey\ sand} = (1-\alpha)\rho_{s,dry\ clayey\ sand} + \alpha\rho_w \tag{3.14}$$

Unsaturated Sand: The pressure vs. density curve for unsaturated clayey sand is obtained as a linear combination of the pressure vs. density relations for the dry clayey and the saturated clayey sands, as:

$$P_{unsat\ clayey\ sand}(\alpha_o, \beta, \Omega) = \begin{cases} 0 & \rho_{unsat\ clayey\ sand} \le \rho_{o,unsat\ clayey\ sand} \\ B_{unsat\ clayey\ sand,low}\left(\rho_{unsat\ clayey\ sand} - \rho_{o,unsat\ clayey\ sand}\right); & \\ & \rho_{o,unsat\ clayey\ sand} \le \rho_{unsat\ clayey\ sand} \le \rho^*_{unsat\ clayey\ sand} \\ B_{unsat\ clayey\ sand,high}\left(\rho_{unsat\ clayey\ sand} - \rho^*_{unsat\ clayey\ sand}\right); & \\ & \rho_{unsat\ clayey\ sand} > \rho^*_{unsat\ clayey\ sand} \end{cases} \tag{3.15}$$

where

$$\rho_{o,unsat\ clayey\ sand} = (1-\beta)\rho_{o,dry\ clayey\ sand} + \beta\rho_{o,sat\ clayey\ sand} \tag{3.16}$$

$$\rho^*_{unsat\ clayey\ sand} = (1-\gamma_1)\rho^*_{dry\ clayey\ sand} + \gamma_1\rho^*_{sa\ clayey\ sand} \tag{3.17}$$

$$B_{unsat\ clayey\ sand,low} = \frac{P_{Comp\ dry\ clayey\ sand}}{\left(\rho^*_{unsat\ clayey\ sand} - \rho_{o,unsat\ clayey\ sand}\right)} \tag{3.18}$$

$$B_{unsat\ clayey\ sand,high} = \left[\frac{1}{\frac{(1-\beta)}{B_{SolidComp,\ dry\ clayey\ sand}} + \frac{\beta}{B_{sat\ clayey\ sand}}}\right] \tag{3.19}$$

where

$$\gamma_1 = \beta\left[\frac{1 - \frac{P_{Comp\ dry,alyey\ sand}}{B_{Sat\ clayey\ sand}\rho^*_{sat\ clayey\ sand}}}{(1-\beta)\left(1 - \frac{P_{Comp\ dry\ calyey\ sand}}{B_{Pl.Comp,dry\ clayey\ sand}\rho^*_{dry\ clayey\ sand}}\right) + \beta\left(1 - \frac{P_{Comp,dry\ calyey\ sand}}{B_{sat\ clayey\ sand}\rho^*_{sat\ clayey\ sand}}\right)}\right] \tag{3.20}$$

Eq. (3.19) reflects the fact that the compaction modulus of humid air residing in clayey sand, consisting of dry air and water, is dominated by its more compliant phase (dry air).

Eqs. (3.8)-(3.20) define the pressure vs. density relation during loading which results in (irreversible) compaction of clayey sand. During unloading/elastic-reloading the pressure vs. density relationship is nearly linear with the slope being equal to the (density-dependent) sound speed, C. Thus to fully define the CU-ARL clayey sand EOS model, a C vs. ρ relation must also be specified. The material sound speed is defined as a square-root of the ratio of the bulk modulus and the material mass density.

Dry Sand: The bulk modulus (in GPa) vs. density relationship for CU-ARL dry sand is given as [3.2]:

$$K_{drysand} = \begin{cases} 0 & \rho_{drysand} < \rho_{o,drysand} \\ -15.6302 + 0.0094074\rho_{drysand} & \rho_{o,drysand} < \rho_{drysand} \le 0.8137\rho_{s,drysand} \\ -93.05 + 0.0455\rho_{drysand} & 0.8137\rho_{s,drysand} \le \rho_{drysand} \le 0.9837\rho_{s,drysand} \\ -1873.3 + 0.73074\rho_{drysand} & 0.9837\rho_{s,drysand} < \rho_{drysand} < \rho_{s,drysand} \\ -3.233 + 0.022651\rho_{drysand} & \rho_{drysand} > \rho_{s,drysand} \end{cases} \quad (3.21)$$

To account for the effect of clay in CU-ARL dry clayey sand, the CU-ARL dry sand bulk modulus is modified as:

$$K_{dry,clayey\,sand} = \left[\frac{1}{\frac{(1-\Omega)}{K_{drysand}(\rho_{dry\,sand})} + \frac{\Omega}{K_{clay}}} \right] \quad (3.22)$$

where $K_{dry\,sand}$ is the bulk modulus of dry sand and K_{clay} is the bulk modulus of clay [3.17].

Saturated Sand: The density-dependent bulk modulus in saturated clayey sand is derived following the same procedure as in the case of P vs. ρ relation as:

$$K_{sat,clayeysand} = B_{sat,clayeysand}\rho_{sat,clayeysand} \quad (3.23)$$

Unsaturated Sand: Likewise, the density-dependent bulk modulus for unsaturated clayey sand is defined as:

$$K_{unsat,clayey}(\rho_{unsat,clayey}, \Omega, \alpha_o, \beta) = \left[(1-\beta)K_{dry,\,clayey\,sand} + \beta K_{sat,\,clayey\,sand}\right] \quad (3.24)$$

where

$$\rho_{dry,clayeysand} = \rho_{unsat,clayeysand} - \alpha_0\beta\rho_{water} \quad (3.25)$$

and

$$\rho_{sat,clayeysand} = \rho_{unsat,clayeysat} + \alpha_0(1-\beta)\rho_{water} \quad (3.26)$$

As mentioned earlier, the density dependent sound speed (for dry, saturated and unsaturated clayey sand) is defined as a square root of the ratio of the corresponding bulk moduli and mass densities.

To show the effect of clay on the EOS of sand, a comparison between the EOS relations for CU-ARL sand and CU-ARL clayey sand with 15vol. % of clay is made in Figures 3-3(a)-(b).

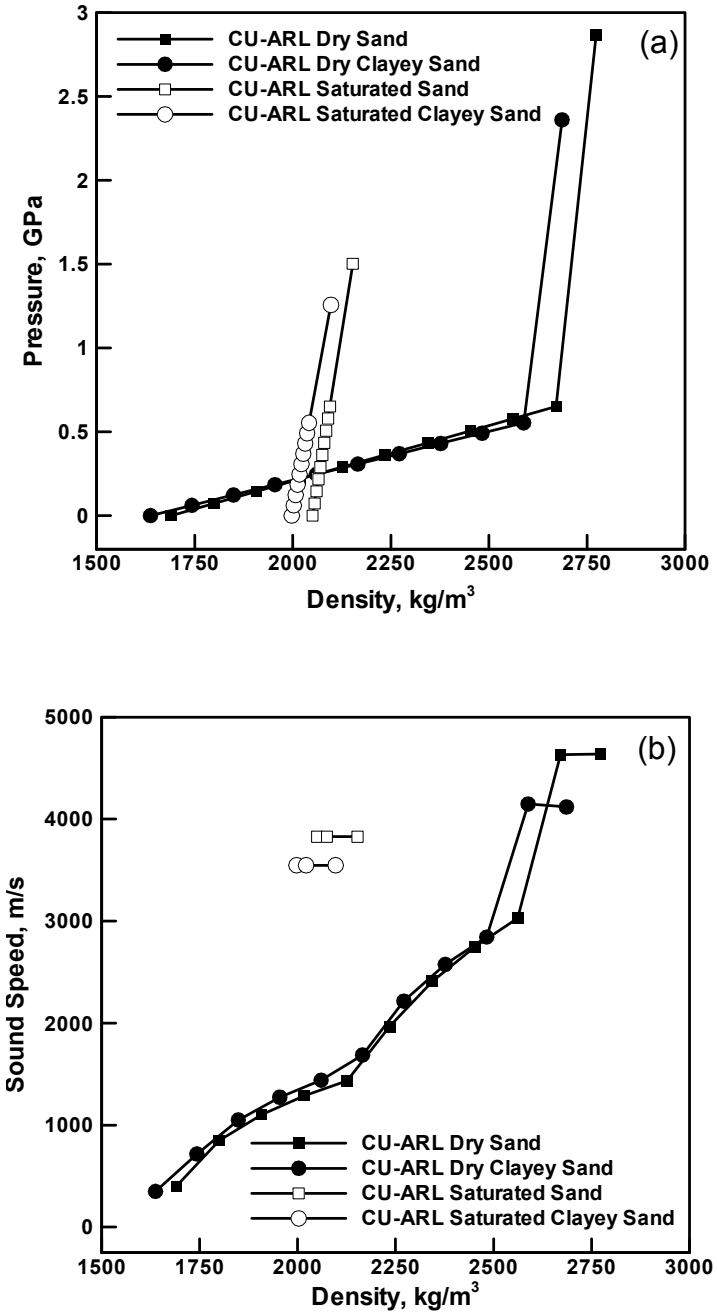

Figure 3-3. (a) Pressure vs. Density and (b) Sound Speed vs. Density Relation for Dry and Saturated CU-ARL and CU-ARL Clayey Sand (15vol. % clay) with a Porosity Level of 36% at Different Degrees of Saturation

3.4.2. CU-ARL Clayey Sand Strength Model

Dry Sand: Since no inter-particle adhesion exists in dry sand, the following inter-particle friction-based, pressure dependent strength model for dry sand was defined within the CU-ARL sand model as [3.2]:

$$\sigma_{y,dry\,sand} = \begin{cases} \mu_{dry\,sand} P_{dry} & 0 < P_{dry} \le P_{MC} \\ \mu_{dry\,sand} P_{MC} & P_{dry} > P_{MC} \end{cases} \tag{3.27}$$

where $\mu_{dry\,sand}$ is the inter-particle friction coefficient for dry sand and is equal to 1.37 [3.13].

The presence of clay over-coat on the sand particles in expected to give rise to inter-particle adhesion while the inter-particle friction coefficient is expected to be reduced. Consequently, the pressure dependent yield strength for CU-ARL dry clayey sand can be defined as:

$$\sigma_{y,dry\,clayey\,sand} = \begin{cases} \sigma_{adhesion} + \mu_{dry\,clayey} P_{dry} & 0 < P_{dry} \le P_{MC} \\ \sigma_{adhesion} + \mu_{dry\,clayey} P_{MC} & P_{dry} > P_{MC} \end{cases} \tag{3.28}$$

where $\sigma_{adhesion}$ is the inter-particle adhesion and $\mu_{dry\ clayeysand}$ is the friction coefficient of dry clayey sand and, in order to account for the fact that inter-particle shear is controlled by the presence of clay, is defined as follows:

$$\mu_{dry\,clayey\,sand} = \frac{\mu_{dry\,sand}\,\mu_{clay}}{(1-\Omega)\mu_{clay} + \Omega\mu_{dry\,sand}} \tag{3.29}$$

where μ_{clay} (= 0.4599, [3.23]) is defined as the slope of the yield strength vs. pressure curve for dry clay.

Saturated Sand: The presence of water in saturated sand reduces the inter-particle friction coefficient and hence, the CU-ARL strength model for saturated sand was defined as:

$$\sigma_{y,sat} = \begin{cases} \mu_{sat\ sand} P_{sat} & 0 \le P_{sat} \le P_{MC} \\ \mu_{sat\ sand} P_{MC} & P_{sat} > P_{MC} \end{cases} \tag{3.30}$$

where the yield-stress-to-pressure proportionality coefficient, $\mu_{sat\ sand}$, is defined as:

$$\mu_{sat\ sand} = \begin{cases} 0.1 + \left(\mu_{dry\ sand} - 0.1\right)\dfrac{P_{sat}}{P_{MC}} & 0 \le P_{sat} \le P_{MC} \\ \mu_{dry\ sand} & P_{sat} > P_{MC} \end{cases} \tag{3.31}$$

in order to account for the effect of pressure on the inter-particle water-layer thickness (i.e. inter-particle friction coefficient). Similarly, to account for the presence of clay over-coat on the sand particles in clayey sand, Eq. (3.30) is modified as:

$$\sigma_{y,sat\ clayey\ sand} = \begin{cases} \sigma_{adhesion} + \mu_{sat\ clayey\ sand} P_{sat} & 0 \le P_{sat} \le P_{MC} \\ \sigma_{adhesion} + \mu_{sat\ clayey\ sand} P_{MC} & P_{sat} > P_{MC} \end{cases} \tag{3.32}$$

where the inter-particle friction coefficient for saturated clayey sand, $\mu_{sat\ clayey\ sand}$, is given by:

$$\mu_{sat\ clayey\ sand} = \begin{cases} 0.1 + \left(\mu_{dry\ clayey\ sand} - 0.1\right)\dfrac{P_{sat}}{P_{MC}} & 0 \le P_{sat} \le P_{MC} \\ \mu_{dry\ clayey\ sand} & P_{sat} > P_{MC} \end{cases} \tag{3.33}$$

Unsaturated Sand: The yield stress vs. pressure relationship for the unsaturated clayey sand can then be defined using a linear combination of the yield-stress/pressure proportionality coefficients in dry clayey and the saturated clayey sand as:

$$\sigma_{y,unsat\ clayey\ sand} = \begin{cases} \mu_{un\ sat\ clayey\ sand} P_{unsat} & 0 \le P_{unsat} \le P_{MC} \\ \mu_{un\ satclayey\ sand} P_{MC} & P_{unsat} > P_{MC} \end{cases} \tag{3.34}$$

where

$$\mu_{unsat\ clayey\ sand} = \left(1 - \beta\right)\mu_{dry\ clayey\ sand} + \beta\mu_{sat\ clayey\ sand} \tag{3.35}$$

The term P_{MC} appearing in Eqs. (3.27) - (3.35) is the Mohr-Coulomb pressure beyond

which the yield stress is pressure insensitive and is defined as:

$$P_{MC} = (1-\Omega)P_{MC,dry\ sand} + \Omega P_{MC,dry\ sand}\frac{P_{Comp,Clay}}{P_{Comp,dry\ sand}} \tag{3.36}$$

where $P_{MC,dry\ sand}$ (=1.864.10^5 kPa) [3.2].

In addition to specifying the yield stress vs. pressure relationship, the compaction strength model entails the knowledge of the density dependent shear modulus. The shear modulus is used to define the relationship between the deviatoric stress and the deviatoric strain components during unloading/elastic reloading.

Dry Sand: The CU-ARL dry sand model shows a relatively modest initial increase in the shear modulus with an increase in density until the moment of full compaction, at which point, the shear modulus becomes a very sensitive function of density. This ($G_{dry\ sand}$ vs. $\rho_{dry\ sand}$) relationship can be found in our previous work [3.2]. To account for the fact that sand particles are coated with a continuous layer of clay the following rule of mixtures is used to define the shear modulus of dry clayey sand:

$$G_{dry,clayey\ sand} = \left[\frac{1}{\frac{(1-\Omega)}{G_{drysand}\left(\rho_{dry\ sand}\right)} + \frac{\Omega}{G_{dry\ clay}}}\right] \tag{3.37}$$

where the shear modulus of dry clay, $G_{dry\ clay}$ is typically equal to 6 GPa [3.24]. Eq. (3.37) is used as follows: From the current level of density of dry clayey sand:

$$\rho_{dry,clayey\ sand} = (1-\Omega)\rho_{dry\ sand} + \Omega\rho_{clay} \tag{3.38}$$

The density of the constituent dry sand, $\rho_{dry\ sand}$ is determined and used in the $G_{dry\ sand}$ vs. $\rho_{dry\ sand}$ relation to assess the $G_{dry\ sand}$ term. Next, $G_{dry\ sand}$ is used in Eq. (3.37) to compute $G_{dry\ clayey\ sand}$.

Unsaturated and Saturated Sand: Next, the effect of water on the shear modulus of unsaturated and saturated clayey sands is defined using a relation analogous to that given in Eq. (3.37) except that the $G_{dry\ clay}$ is replaced with the following expression:

$$G_{sat/unsat\ clay} = (1-\beta)G_{dry\ clay} \tag{3.39}$$

Similarly, the density of unsaturated/saturated clayey sand is defined as:

$$\rho_{sat/unsat\ clayey\ sand} = (1-\beta)\rho_{dry\ clayey\ sand} + \alpha\beta\rho_{water} \tag{3.40}$$

To show the effect of clay on the strength model of sand, a comparison between the strength models for CU-ARL sand and CU-ARL clayey sand with 15vol. % of clay is made in Figures 3-4(a)-(b).

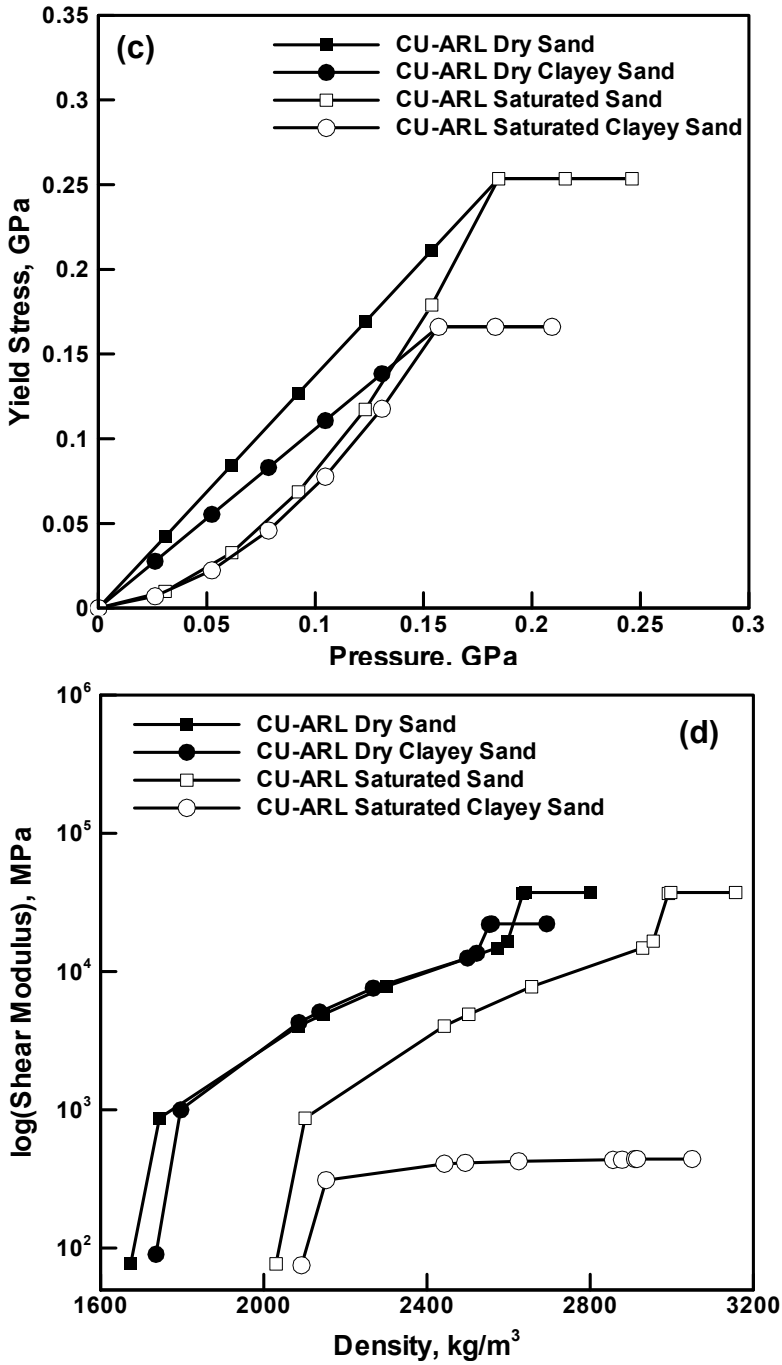

Figure 3-4. (a) Yield Stress vs. Pressure and (b) Shear Modulus vs. Density Relation for Dry and Saturated CU-ARL and CU-ARL Clayey Sand (15vol. % clay) with a Porosity Level of 36% at Different Degrees of Saturation

3.4.3. CU-ARL Clayey Sand Failure Model

The CU-ARL sand failure model developed in our previous work [3.2], is of a "*hydro*" type, according to which failure occurs when the negative pressure falls below a critical value, P_{fail}. After failure, the material looses the ability to support any tensile or shear loads but retains the ability to support compressive loads. To account for the experimentally observed fact that the failure pressure in sand at the saturation level of 0.75 is around 15% of that in saturated sand, the following saturation-level dependent failure pressure relation was proposed:

$$P_{unsatclayeysand,fail} = \beta^5 P_{fail.sat} \tag{3.41}$$

where $P_{fail,\ sat}$ for sand with a negligible amount of silt (which promotes the effect of capillarity and tension) is reported in Ref. [3.18] to be ca. 70 kPa. The CU-ARL sand failure model was adopted in Ref. [3.2] to account for the fact that failure in sand is more likely to take place by decohesion than by shearing. In clayey sand, however, one can expect that shear failure is more likely to take place than decohesion. For this reason, a hybrid "*hydro*" + "*shear*" failure model is adopted for the CU-ARL clayey sand. According to this model, failure will occur when one of the two conditions $P<P_{fail}$ or $\tau<\tau_{fail}$ is reached. To account for the effect of clay content and the effect of saturation on the failure resistance of clayey sand, the following relations are proposed:

$$P_{unsatclayeysand,fail} = (1-\Omega)\beta^5 P_{fail,sat} + \Omega\left[(1-\beta)P_{clay,fail} + \beta P_{fail,sat}\right] \tag{3.42}$$

$$\tau_{fail,claeysand} = \frac{\tau_{fail,clay}\tau_{fail,sat}}{(1-\Omega)\tau_{fail,clay} + \Omega\tau_{fail,sat}} \tag{3.43}$$

The CU-ARL clayey sand parameters appearing in Eqs. (3.42) - (3.43) are listed in Table 3-2.

Table 3-2. Parameters appearing in the definition of the failure model for dry, unsaturated and saturated clayey sands

Parameter	Symbol	Unit	Value
Saturated Sand			
Saturated Sand Tensile Failure Pressure	$P_{fail\ sat\ \text{sand}}$	kPa	70
Saturated Sand Shear Failure Pressure	$\tau_{sat\ sand}$	kPa	350
Clay			
Clay Tensile Failure Pressure	$P_{fail\ clay}$	kPa	20
Clay Shear Failure Pressure	τ_{clay}	kPa	150

3.4.4. CU-ARL Clayey Sand Erosion Model

Erosion of a clayey-sand material element is assumed to take place when geometrical (i.e. elastic plus plastic plus damage/crack) instantaneous strain reaches a maximum allowable value. Our prior investigation [3.10] established that the optimal value for the geometrical instantaneous strain is ~1.0. When a material element is eroded, its nodes are retained along with their masses and velocities in order to conserve momentum of the system.

3.5. Validation of the CU-ARL Clayey Sand Model

The CU-ARL clayey sand model presented in Section 3.3 was developed using simple physical arguments regarding the effects of moisture and minor contents of clay on the dynamic mechanical behavior of sand and parameterized using various material testing results. In this section, an attempt is made to validate the CU-ARL clayey sand model by comparing the available experimental results pertaining to the detonation of shallow-buried landmines in clayey sand with the corresponding transient non-linear dynamics simulations of the same experiments. In order to assess the potential improvements in modeling the behavior of clayey sand, simultaneous non-linear dynamics simulations were also carried out using the original CU-ARL sand model. Such simulations are carried in the present work using the commercial software AUTODYN [3.11]. A brief description of the basics of a typical transient non-linear dynamics analysis is discussed in the next section.

3.5.1. Basics of Transient Non-linear Dynamics Simulations

A transient non-linear dynamics problem is analyzed within AUTODYN [3.11] by solving simultaneously the governing partial differential equations for the conservation of momentum, mass and energy along with the materials constitutive equations and the equations defining the initial and the boundary conditions. The equations mentioned above are solved numerically using

a second-order accurate explicit scheme and one of the two basic mathematical approaches, the Lagrange approach and the Euler approach. Within AUTODYN these approaches are referred to as "*processors*". The key difference between the two basic processors is that within the Lagrange processor the numerical grid is attached to and moves along (and deforms) with the material during calculation while within the Euler processor, the numerical grid is fixed in space and the material moves through it. In our recent work [3.2], a brief discussion was given of how the governing differential equations and the materials constitutive models define a self-consistent system of equations for the dependent variables (nodal displacements, nodal velocities, cell material densities and cell internal energy densities).

In the present work, both the Lagrange and Euler processors are used. The Lagrange processor was used to model the sand and various targets and structural components. High-energy explosives, gaseous mine-detonation products and the surrounding air are modeled using either a single-material FCT (Flux Corrected Transport) or a multi-material Euler processor. Different regions of the mine/air/target/sand model are allowed to interact and self-interact using the AUTODYN interaction options. A brief overview of the parts interactions and self interaction AUTODYN algorithms can be found in our recent work [3.2]. Also a detailed description of the Lagrange, Euler-FCT and multi-material Euler processors as well as of the material models used for air, high explosives and metallic structural materials can be found in our recent work [3.1,3.2].

Throughout this manuscript, terms the "*Depth of Burial*" (DOB) and the "*Stand-off Distance*" (SOD) are used to denote distances between the mine top face and the sand/air interface and between the sand/air interface and the bottom face of the target structure, respectively.

In the remainder of the manuscript, a separate comparison between the computational and experimental results are presented for the total blast-induced momentum transferred to the target

and for the spatial and temporal evolution of the sand overburden bubble and the associated pressure fields.

3.5.2. Total Momentum Transferred to the Target Structure

To assess the ability of the CU-ARL clayey sand model to account for the total momentum transferred to the target structure following detonation of a ground-laid or shallow buried mine at different saturation levels of the sand and different contents of clay, the computational results are compared with their experimental counterparts obtained in Refs. [3.14, 3.16].

3.5.2.1. Dry and Unsaturated Clayey Sand

To assess the ability of the CU-ARL clayey sand model to account for the total momentum transferred to the target structure at different levels of clay content and at low to medium saturation levels, a non-linear dynamics based computational analysis of the interaction of detonation products, mine fragments and sand ejecta with an instrumented horizontal mine-impulse pendulum used in Ref. [3.16], is carried out and the computed results compared with their experimental counterparts. In this section, a brief overview of the- construction and experimental procedure associated with the impulse pendulum is first presented.

The instrumented horizontal mine-impulse pendulum, as shown in Figure 3-5, consists of a 5m long horizontal steel arm with a 1200mm x 1200mm square measuring pan placed at the free end of the arm 400mm above the ground. The arm is attached to the base assembly at the other end through a horizontal pivot. The charge, typically consisting of a cylindrically shaped (14.6cm in diameter and 5cm high) C4 mine is placed under the center of the measuring pan and detonated. The mine is either laid on the ground or is buried to different depths. The resultant maximum angular displacement of the pendulum arm is measured and used to calculate the

detonation-induced impulse on the pendulum. The use of the mine-impulse pendulum enabled an investigation of the effects of the sand type/properties, extent of saturation with water, the extent of clay content, the target stand-off distance and the mine depth of burial on the total detonation-induced impulse. In an earlier design, the measuring pan was constructed of mild steel, however, the initial experiments revealed that such a measuring pan undergoes substantial plastic deformation. Consequently, the central 600mm x 600mm section of the measuring pan was replaced with a 50mm thick Rolled Homogenized Armor (RHA) plate. The maximum angular deflection of the pendulum was obtained using a combination of the following three methods: (a) a cable potentiometer, (b) a scratch gage and (c) high speed video recording of a large pointer.

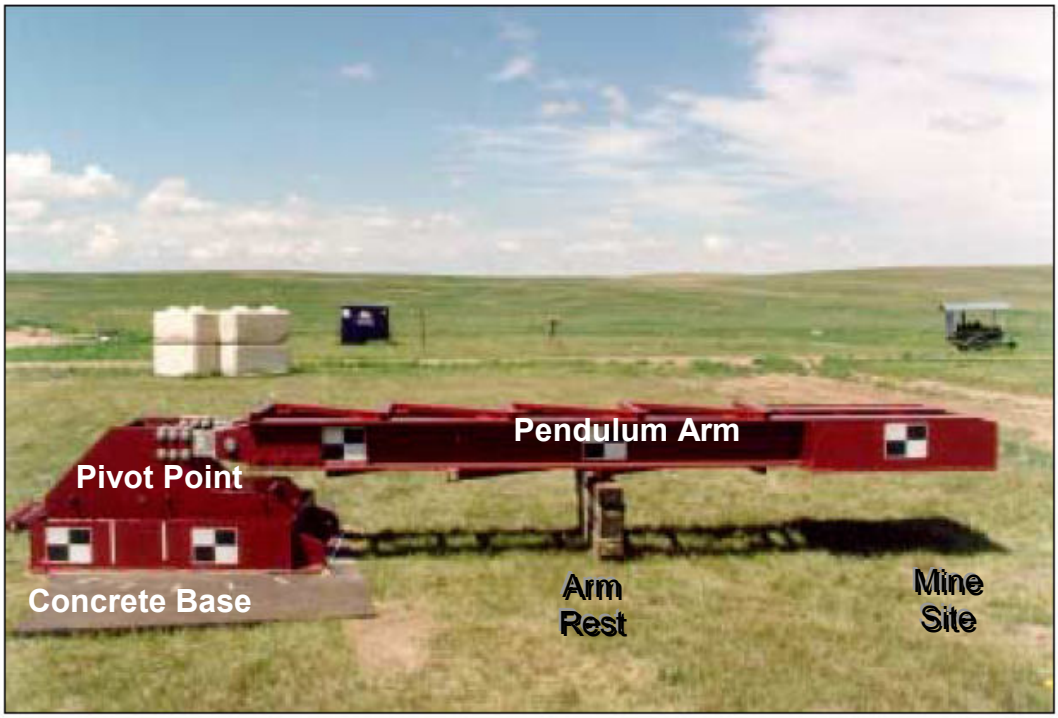

Figure 3-5. Horizontal Mine Impulse Pendulum (MIP) used in Ref [3.16]

Next, a brief description is given of the computational model used to simulate the interaction of the detonation-products/soil ejecta resulting from the explosion of a shallow-buried or ground-laid mine and the instrumented horizontal mine-impulse pendulum. The computational modeling of this interaction involved two distinct steps: (a) geometrical modeling of the instrumented horizontal mine-impulse pendulum and (b) a non-linear dynamics analysis of the momentum transfer from the detonation-products/soil ejecta to the pendulum.

The geometrical models for the various components of the pendulum were constructed using 50mm x 50mm square shell elements. An advantage was taken of the planar symmetry of the model. In other words, a vertical plane of symmetry was placed along the length of the pendulum which enabled only a half of the pendulum to be modeled. In accordance with the instrumented horizontal mine-impulse pendulum used in Ref. [3.16], different sections of the pendulum were constructed using AISI 1006 steel and (Rolled Homogenized Armor) RHA plate material. Welded joints of the different sections of the pendulum were simulated by joining the components in question.

The head of the pendulum was placed in a single-material Euler-FCT region consisting of 74,000 25mm edge-length cubic cells. The Euler-FCT processor is a single material processor in which different materials are represented using a single material model derived using a Flux Corrected Transport (FCT) approach. The Euler-FCT processor was used in place of a multi-material Euler processor in order to reduce the computational cost. Many investigations (e.g. [3.1, 3.2]) showed that the Euler-FCT processor yields results which are quite comparable to their multi-material Euler counterparts. The landmine is modeled using the following procedure: In the case of a surface laid mine, the mine was represented by a high-density high-energy cylindrical air region located within the Euler-FCT domain. In the case of a shallow-buried mine, two joined Lagrange domains were used to define a sand region containing a cylindrical cavity

whose shape and size match those of the C4 mine. A second Euler-FCT domain overlapping with the two sand domains is defined and the portion of this domain corresponding to the cylindrical sand cavity defined above is initially filled with high-density high-energy air.

The air/clayey sand and air/pendulum interactions are accounted for using the appropriate Euler/Lagrange coupling option with AUTODYN [3.11]. Likewise, the sand/pendulum interactions were modeled through the use of the appropriate Lagrange/Lagrange coupling option.

At the beginning of the simulation, the pendulum is assumed to be at rest (with the gravitational force acting downwards), while the Lagrange and Euler-FCT domains are filled with stationary materials (sand and air, respectively). The C4 mine was initially modeled as a cylindrical high-density, high-energy sub-domain within the Euler-FCT region.

The motion of the pendulum was constrained to within a vertical plane and a fixed single-point constraint was applied to its pivot point. The *"flow out"* boundary conditions were applied to all the free faces (the faces which do not represent interfaces between the different domains) of the Euler-FCT domain except for the face associated with the vertical symmetry plane. To reduce the effect of reflection of the shock waves at the outer surfaces of the Lagrange domain, *"transmit"* boundary conditions were applied to all the free faces of this domain except for the face associated with the vertical symmetry plane.

To speed up the calculations, all Euler-FCT and Lagrange domains were removed from the analysis after approximately 10ms following detonation when the extent of interaction between the detonation-products/sand ejecta and the pendulum was negligibly small.

A standard mesh sensitivity analysis was carried out (the results not shown for brevity) in order to ensure that the results obtained are insensitive to the size of the cells used.

The effect of the degree of (water) saturation in clayey sand with 15vol.% of clay [3.16] on the total impulse transferred to the pendulum in the case of sand containing various levels of

moisture for four different DOBs of an 1kg C4 landmine is displayed in Figures 3-6(a)-(d). The 0cm-DOB corresponds to a *"flush-buried"* mine while the -5cm-DOB corresponds to a *"ground-laid"* mine.

An example of the temporal evolution of the distribution of materials involved in the horizontal mine impulse pendulum analysis is displayed in Figures 3-6(a)-(d). It should be noted that only one (longitudinal) half of the computational model is displayed for clarity.

A comparison of the experimental and computational results pertaining to the total impulse transferred to the instrumental horizontal mine-impulse pendulum at different levels of sand saturation with water at four different values of the depth of burial are displayed in Figures 3-7(a)-(d). To assess the extent of the potential agreement-improvement with the experimental results obtained by the use of the CU-ARL clayey sand model, the results obtained using the CU-ARL sand model are also displayed in Figures 3-7(a)-(d).

The results displayed in Figures 3-7(a)-(d) show that, at all the levels of saturation and for all four values of the DOB, the CU-ARL clayey sand model improves somewhat the agreement with the experimental results over that obtained in the case of CU-ARL sand model. However, the overall agreement between the experimental and the present calculation results remains only fair. It should be noted that the experimental results are associated with substantial scatter rendering the CU-ARL clayey sand model validation quite difficult.

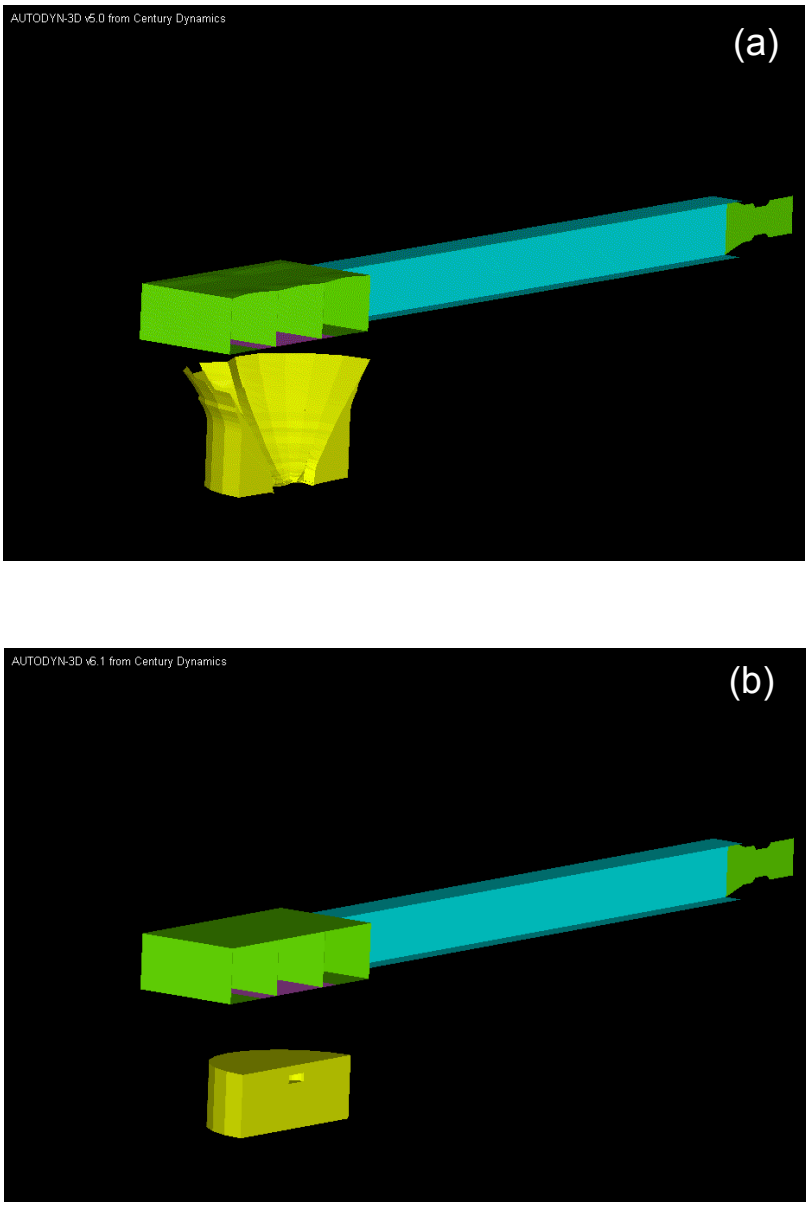

Figure 3-6. Temporal evolution of the material involved in the Horizontal Impact Pendulum experiment Post-detonation times: (a) 0ms; (b) 21ms; (c) 42ms and (d) 65ms

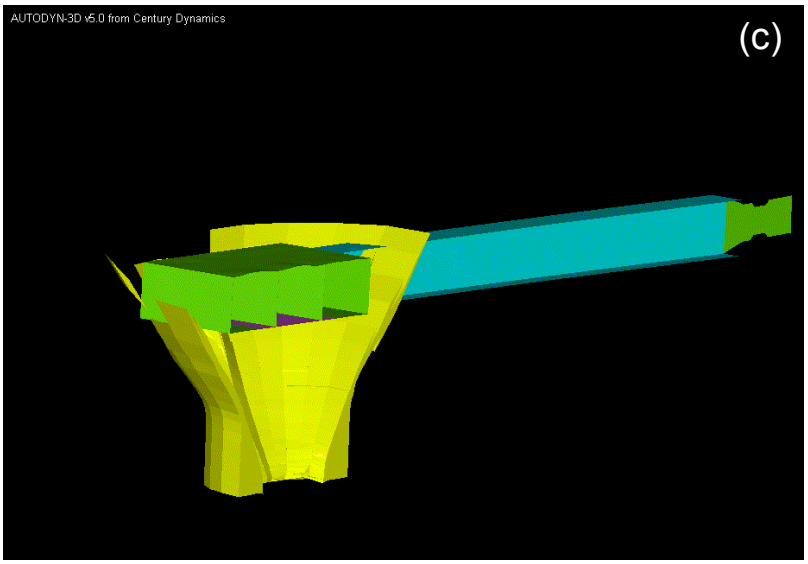

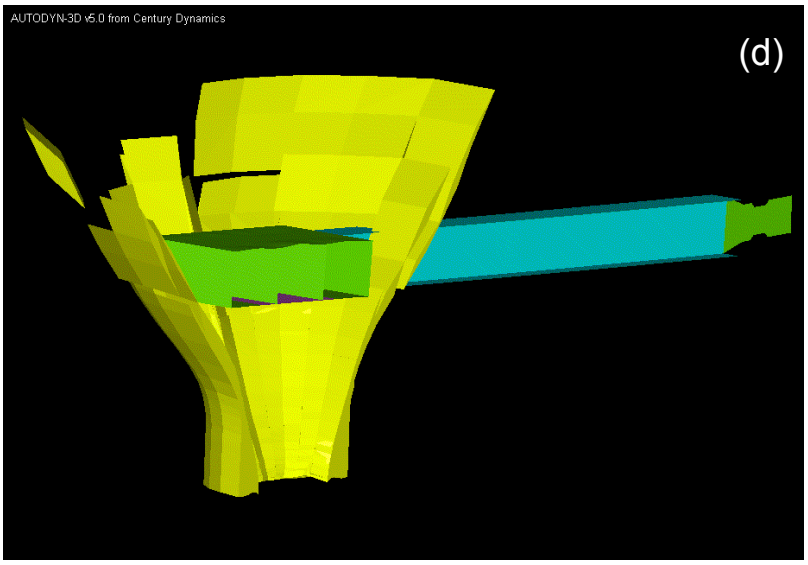

Figure 3-6. Contd…

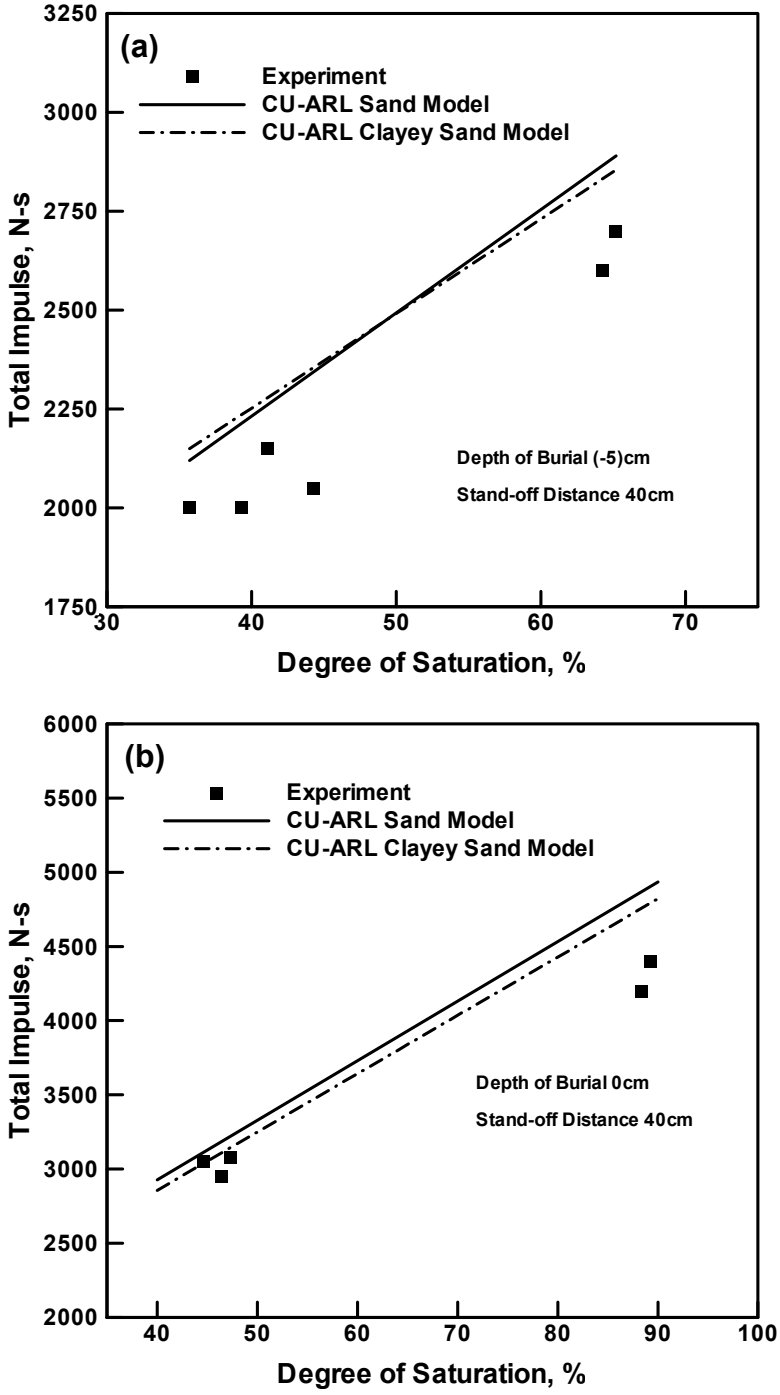

Figure 3-7. The Effect of Degree of Saturation of CU-ARL and CU-ARL Clayey Sand on the Total Impulse Transferred to the Instrumented Horizontal Mine-impulse Pendulum for the Depths of Burial of (a) -5cm; (b) 0cm; (c) 5cm and (d) 10cm

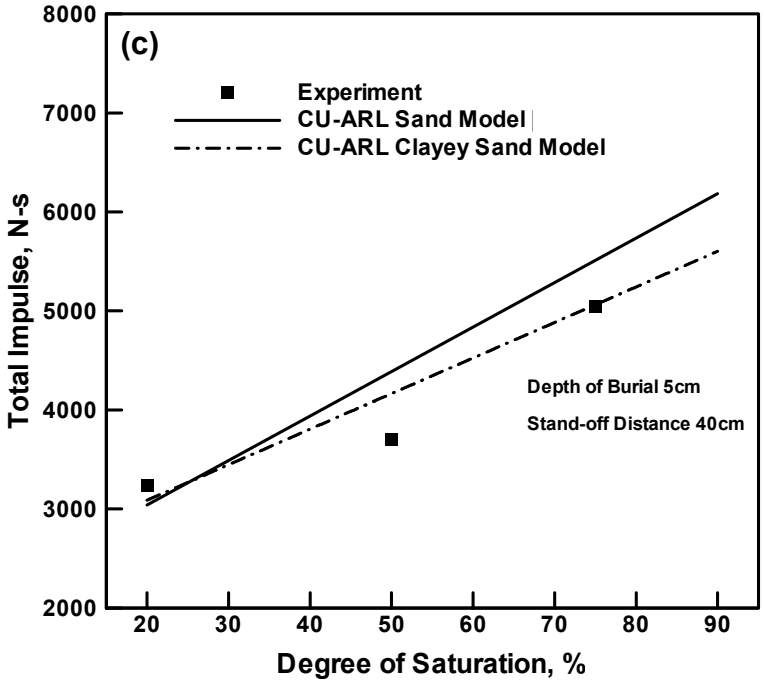

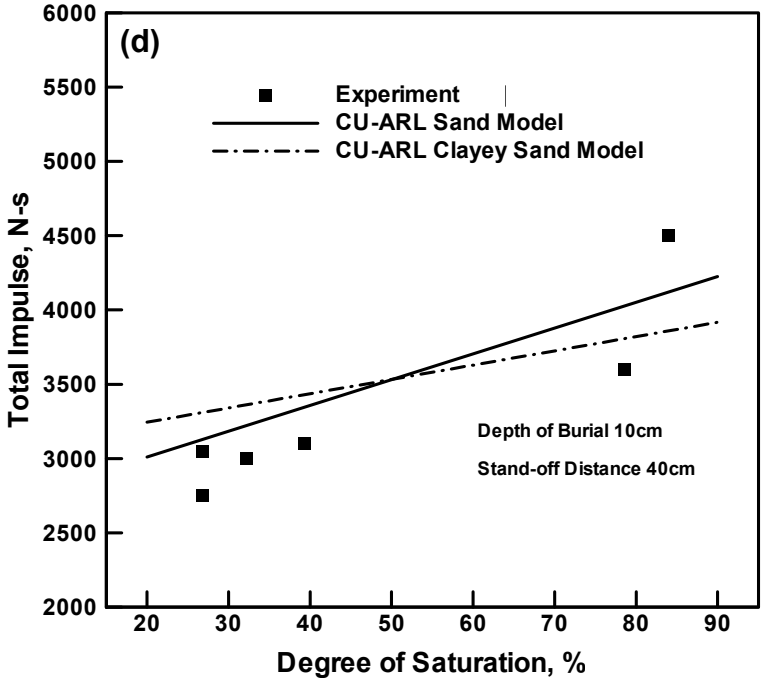

Figure 3-7. Contd…

3.5.2.2. Saturated Clayey Sand

To assess the ability of the CU-ARL clayey sand model to account for the total momentum transferred to the target structure at high saturation levels of the sand, a non-linear dynamics based computational analysis of the interaction of detonation products, mine fragments and sand ejecta with a Vertical Impulse Measurement Fixture used in Ref. [3.14] (Figure 3-8), is carried out and the computed results compared with their experimental counterparts. A brief overview of the construction and experimental procedure associated with the VIMF is presented first.

The VIMF is a structural mechanical device that enables direct experimental determination of the imparted blast-loading impulse via measurements of the vertical displacement of a known fixed-mass vertical guide rail that is capped with a witness plate, which serves as a momentum trap to capture the blast loading of the buried charge. The design and operation of the VIMF has been described in details by Gniazdowski et al. [3.19], and Skaggs et al. [3.20] and Taylor and Skaggs [3.14] and will be only briefly discussed here. To create the required water-saturated sand condition, a cylindrical pit 3.65m in diameter and 1.32m deep is first constructed in the soil within the VIMF test area. To retain water in the sand pit and to keep the sand-water mixture separate from the rest of the sand, the walls of the pit are lined with 0.32cm thick poly-ethylene sheets and the pit floor is built using a commercial swimming pool liner. Once the pit liners are in place, a series of water hoses is placed in pit bottom to allow the introduction of water into the pit from the bottom. Next, approximately 14.2m^3 of commercially available (Quickrete) sand is placed in the pit. The sand typically consists of 94.4wt.% sand, 0.3wt.% gravel, and 5.3wt.% clay. Prior to each test, water is allowed to fill the sand pit until standing water is observed on top of the sand.

Figure 3-8. Vertical Impulse Measurement Fixture used in Ref [3.15]

The basic formulation of the computational problem dealing with the interactions between the detonation products, shell fragments and soil ejecta (all resulting from the explosion of a shallow-buried landmine) and the VIMF is presented next. The computational modeling of this interaction involved two distinct steps: (a) geometrical modeling of the VIMF along with the adjoining mine, air and sand regions, and (b) the associated transient non-linear dynamics analysis of the impulse loading (momentum transfer) from the detonation products, shell fragments and soil ejecta to the VIMF structure. The part (b) of this analysis was performed using a modified version of the technique developed by Fairlie and Bergeron [3.21]. This technique

couples a multi-material Eulerian mesh to three Lagrangian meshes. The Eulerian mesh contained initially a TNT mine (and after mine explosion the resulting high-pressure, high-internal energy-density detonation products) and the (initially stationary, atmospheric-pressure) air. The mesh was constructed in terms of eight node elements. One of the Lagrangian mesh was used to model the soil, the other to represent the VIMF witness plate while the third one was used to model the remainder of the VIMF structure. The soil and the VIMF structure were modeled using eight node solid elements, while the witness plate was modeled using four-node shell elements.

An advantage was taken of the inherent symmetry of the model. In other words, two mutually-orthogonal vertical planes of symmetry were placed along the axis of the VIMF as well as along the axis of the air, mine and sand regions which enabled only a quarter of the computational model to be analyzed. Representative quarter symmetric models for various computational domains used in the present study are shown in Figure 3-9. It should be noted that the lower portion of the Eulerian domain contains the landmine while the rest of the lower portion of the Eulerian domain is occupied by the Lagrangian soil mesh. Likewise, the upper portion of the Eulerian domain which extends above the soil contains initially air and is partially occupied by the Lagrangian VIMF witness-plate and vertical-base meshes.

At the beginning of the simulation, all the Lagrange and Euler domains were activated and the landmine detonated. The (circular-disk shape) mine was detonated over its entire bottom face at the beginning of the simulation.

A standard mesh sensitivity analysis was carried out (the results not shown for brevity) in order to ensure that the results obtained are insensitive to the size of the cells used.

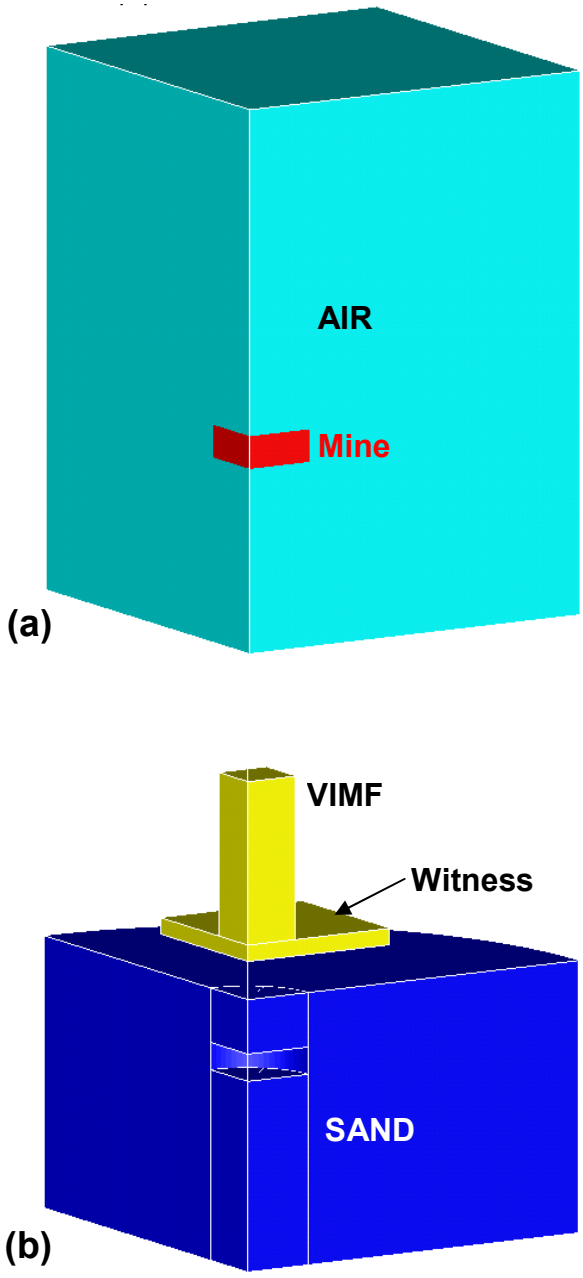

Figure 3-9. Various Computational Domains used in the Present Non-linear Dynamics Analysis of the Interactions of the Detonation Products, Mine Fragments and Sand Ejecta with the VIMF

A comparison between the experimental and the computational results (based both on the use of the CU-ARL sand model and CU-ARL clayey sand model) pertaining to the total impulse transferred to the VIMF are shown in Table 3-3. It should be remembered that all the results displayed in this table correspond to the fully saturated sand. The results displayed in Table 3-3 suggest that in all but one case (case 4) the CU-ARL clayey sand-model based results are in better agreement with their experimental counterparts relative to those between CU-ARL sand and the experimental results.

Table 3-3. VIMF Set-Up and Test Conditions [3.14]

Test No.	Charge Mass (kg)	Charge Diameter (m)	Charge Height (m)	DoB* (m)	HoT** (m)	VIMF Target Total Mass (kg)
1+	4.54	0.254	0.56	0.10	0.40	12,506
3+	4.54	0.254	0.56	0.30	0.40	12,506
4+	4.54	0.254	0.56	0.10	0.20	12,506
4a++	4.54	0.254	0.56	0.10	0.20	11,852
5++	2.27	0.152	0.76	0.80	0	11,852
6++	4.54	0.254	0.56	0.10	0.40	11,852
7++	2.27	0.152	0.76	0.81	0.16	11,535
8++	7.47	0.236	0.86	0.10	0.40	11,535

* DoB = Depth of Burial
** HoT = Height of the Target plate above the soil
\+ Witness plate size: 2.43m by 2.82m by 0.088m
\++ Witness plate size: 1.83m by 3.65m by 0.088m

3.5.3 Temporal Evolution of Sand-overburden Bubble and Pressure Fields

To farther assess the validity of the CU-ARL clayey sand model to account for the spatial and temporal evolutions of the sand-overburden bubble and the pressure fields, following detonation of a ground-laid or shallow buried mine at different saturation levels of the sand, the computational results are compared with their experimental counterparts obtained in Ref. [3.22]. In this section, a brief overview of the experimental set-up and the procedure used in Ref. [3.22] is first presented.

The experiments carried out in Ref. [3.22] can be briefly described as follows: A 1.27cm wall thickness cylindrical barrel with the outer-diameter of 81.6cm and the overall height of 71cm is filled with sand up to its top. A 100g cylindrical-disk shape C4 high-energy explosive (6.4cm in diameter and 2cm in height) is buried into the sand along the centerline of the barrel with its faces parallel with the sand surface. The Depth of Burial (DOB) (defined as the vertical distance between the top face of the explosive and the sand surface) is varied in a range between 0 and 8cm. Thus a 0cm DOB case corresponds to a flush-buried explosive. A set of six pressure transducers is utilized to monitor the pressure in the air following the detonation of the explosive. The designations and the position coordinates of the six transducers are given in Table 3-4. The first number in the Pressure Transducer (PT) designation represents the distance in centimeters of the transducer from the origin of the coordinate system (defined below), while the second number represents the angular relation in degrees between the position vector of the pressure transducer and the axis of symmetry. The location of the six pressure transducers is also shown in Figure 3-10. To be consistent with the definition of coordinate system for the 2D axi-symmetric problem used in AUTODYN [3.11], the y coordinates are measured in the radial direction from the centerline of the barrel, while the x coordinates are measured along the axis of symmetry, with

$x=0$ corresponding to the sand surface and $x<0$ denoting the air region above the ground.

Table 3-4. Measured and Computed Impulse Transferred to the VIMF Witness Plate

Test No.	Measured Total Impulse (N-s)	Computed Total Impulse CU-ARL Sand Model (N-s)	Computed Total Impulse CU-ARL Clayey Sand Model (N-s)
1	71,801	78,014	74,673
3	74,017	64,561	63,656
4	81,125	83,622	95,342
4a	69,644	57,174	66,868
5	77,612	72,448	74,507
6	59,286	64,452	54,582
7	36,938	37,689	34,007
8	94,390	86,042	86,900

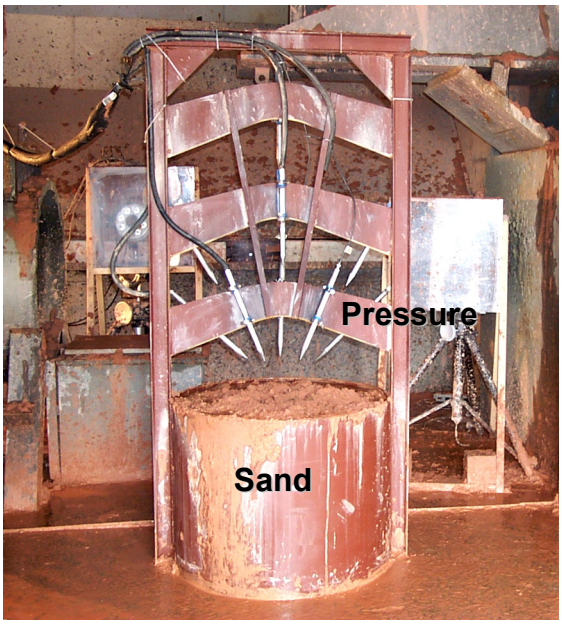

Figure 3-10. The Experimental Setup used in Ref. [3.22] to Study the Effect of Explosion of a Shallow-buried mine

The physical model displayed in Figure 3-10 has been represented using the computational multi-material Euler model shown in Figure 3-11. In Figure 3-12, various portions of the computational domain are filled with one or more of the attendant materials (air, sand, C4 gaseous-detonation products and AISI 1006 mild steel). Due to the inherent axial symmetry of the set-up used in Ref. [3.22], the mine detonation is analyzed as a 2D axi-symmetric problem. The left boundary in Figure 3-11 coincides with the axis of symmetry (x-axis). The horizontal direction (y-axis) corresponds to the radial direction.

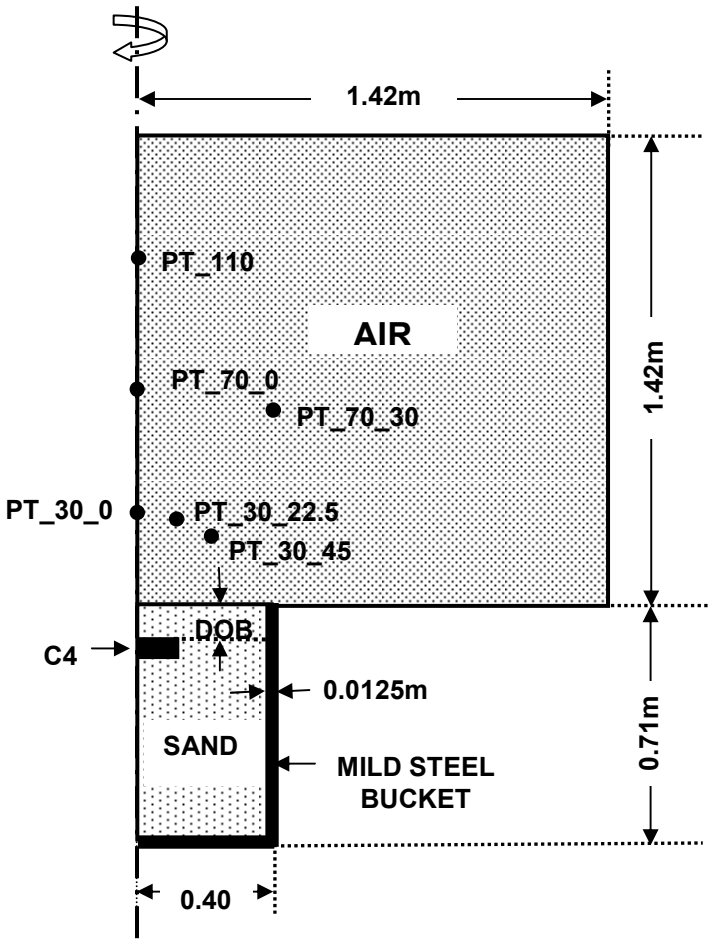

Figure 3-11. A Simple Schematic of the Experimental Setup used in Ref. [3.22] to Study the Effect of Explosion of a Shallow-buried mine

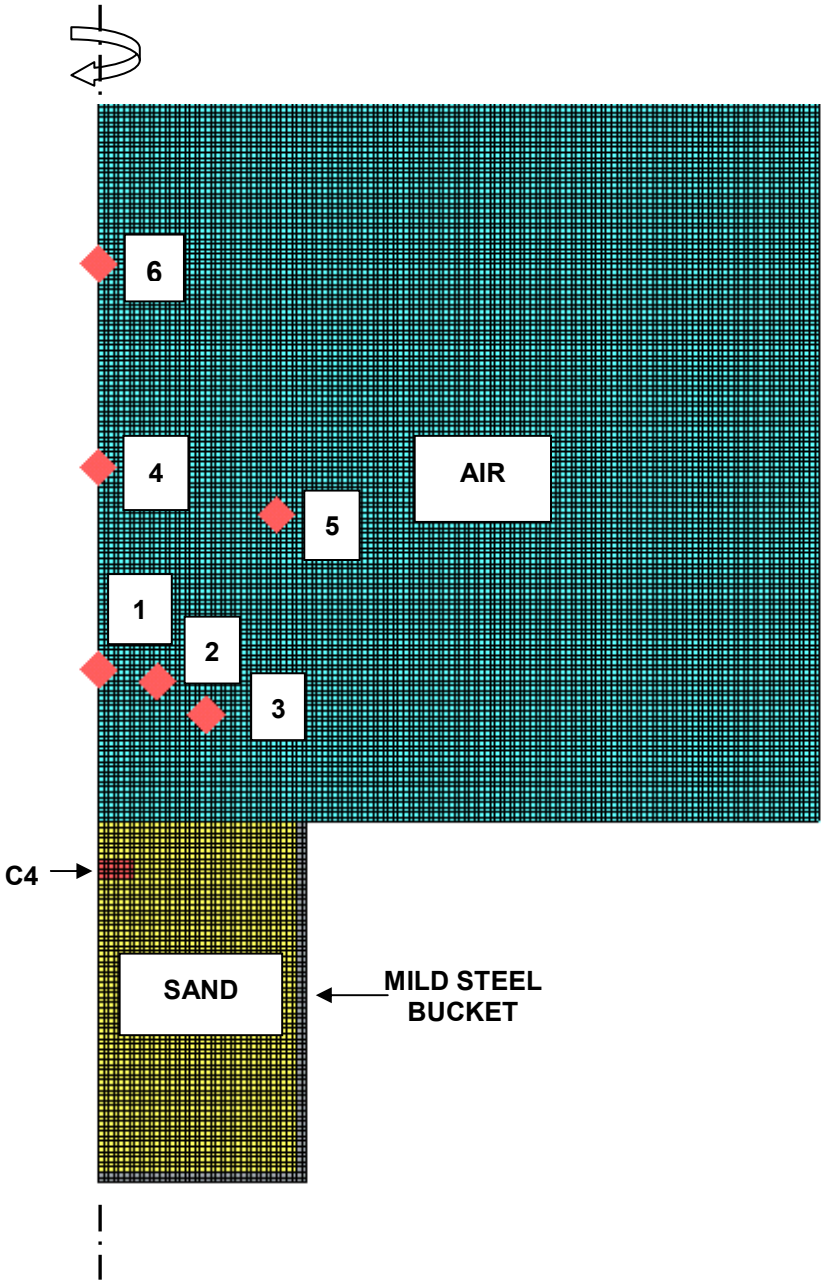

Figure 3-12. Computational Sub-domains Representing the Experimental Setup used in Ref. [3.22] to Study the Effect of Explosion of a Shallow-buried mine

The *"flow-out"* boundary conditions are applied to all the outer boundaries of the computational domain. To mimic the detonation initiation conditions used in Ref. [3.22], detonation is initiated at the central circular portion of the explosive of radius 3.2cm, at the bottom face of the mine. To monitor the temporal evolution of pressure in air, six gage points are introduced whose locations coincide with those of the pressure transducers used in Ref. [3.22].

A standard mesh sensitivity analysis was carried out (the results not shown for brevity) in order to ensure that the results obtained are insensitive to the size of the cells used.

A comparison between the computational results obtained in the present work and their experimental counterparts [3.22] as well as their CU-ARL sand model-based computational results [3.2] for the case of dry and saturated clayey sand are displayed in Figures 3-13(a)-(d) and 3-14(a)-(d), respectively. The results pertaining to the dry clayey sand will be discussed first.

The variation of the peak side-on (static) pressure in air with distance (along the vertical axis) from the sand/air interface at two (3cm and 8cm) DOBs is displayed in Figure 3-13(a). The results displayed in Figure 3-13(a) show that at larger (>60 cm) distances, the CU-ARL clayey sand model clearly shows improved agreement with the experiment over the CU-ARL sand model. At the shorter (30cm) distance, the experimental results show excessive scatter so that a sensible computation-to-experiment quantitative comparison cannot be carried out.

The variation of the blast-wave time of arrival with the distance from the sand/air interface at the same two DOBs is displayed in Figure 3-13(b). A simple analysis of the results displayed in this figure reveals that the agreement between the CU-ARL sand model-based results with the experimental results was already quite good and that level of agreement has not been significantly improved (or worsened) when the CU-ARL model was used.

The variation in the blast-wave time of arrival with offset angle (from vertical axis) at a fixed (30cm) distance from the sand/air interface is displayed in Figure 3-13(c). The results

displayed in this figure show that with the exception of 8cm DOB and zero offset angle, the CU-ARL clayey sand model either improves agreement with the experiment or does not worsen it significantly.

The temporal evolution of the sand bubble height for the cases of 3cm and 8cm DOB is displayed in Figure 3-13(d). The results displayed in this figure show that both the CU-ARL and the CU-ARL clayey sand model yield a reasonable and comparable agreement with the experiment.

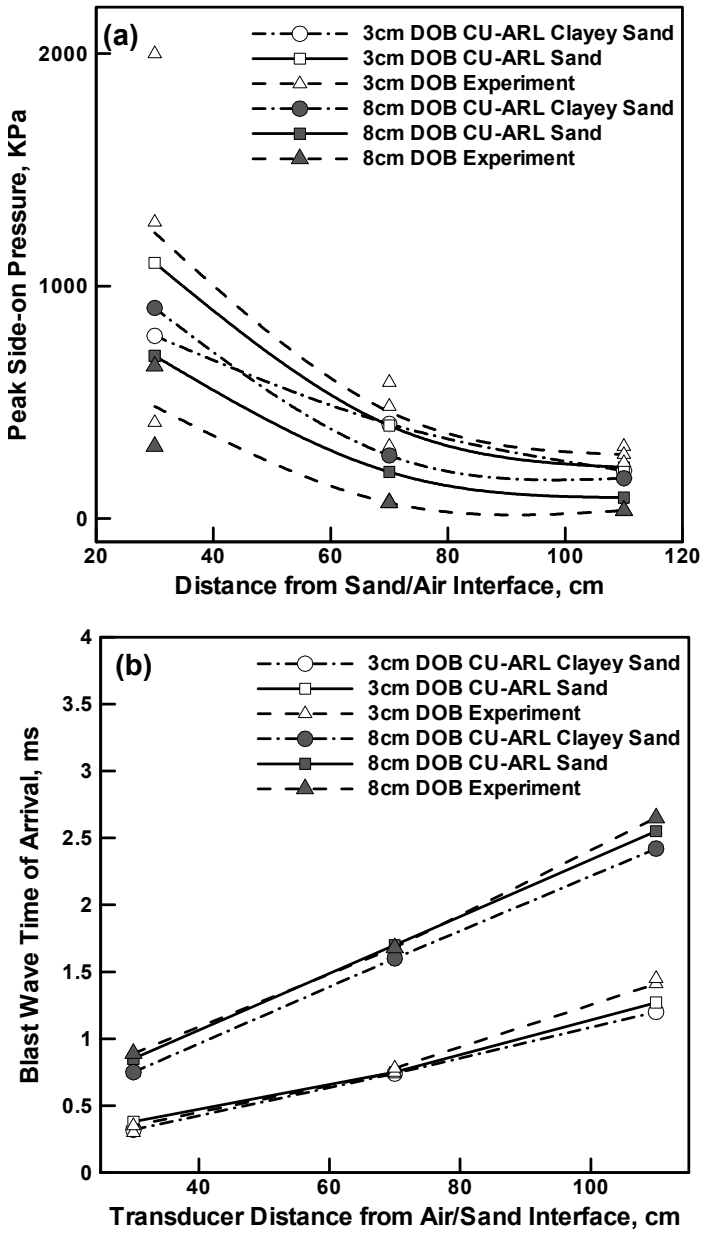

Figure 3-13. A Comparison of the Experimental [3.22] and Computed (present work) Results Pertaining to Various Phenomena Associated with Landmine Detonation in Dry Sand: (a) Side-on Overpressure vs. Transducer Distance from Air/Sand Interface; (b) Blast Wave Arrival Time vs. Transducer Distance from Air/Sand Interface; (c) Blast Wave Arrival Time vs. Transducer Offset Angle from the Symmetry Axis and (d) Sand Bubble Height vs. Landmine Post-detonation Time

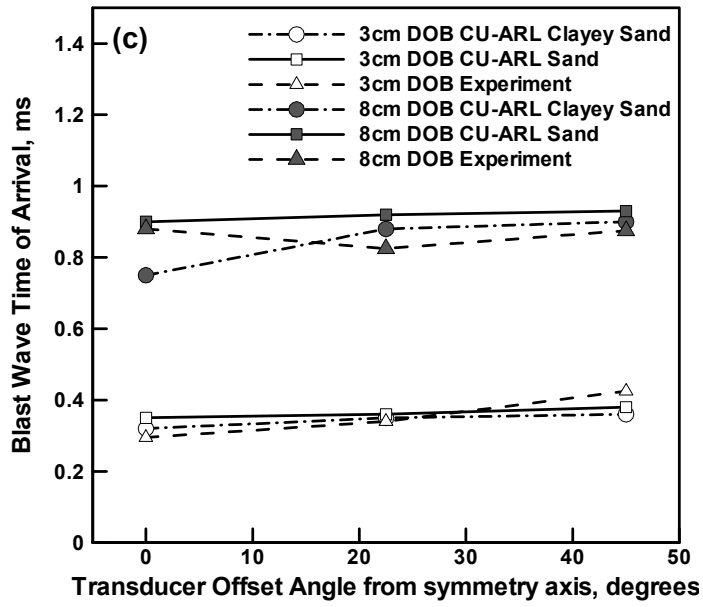

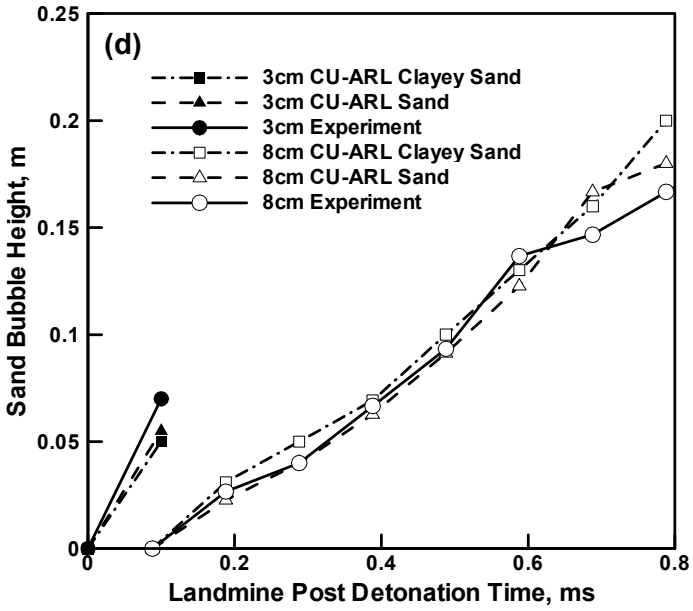

Figure 3-13. Contd…

The computational results and their comparison with the experiment in the case of saturated sand are discussed next.

The results displayed in Figure 3-14(a) show that, in general, the CU-ARL clayey sand model worsens somewhat the agreement with the experimental relative to that observed for the CU-ARL sand. More specifically, the CU-ARL clayey sand model predicted peak pressures are on a higher side. This observation was found to be mainly affected by the choice of the value of the shear modulus of fully –saturated clay (a parameter whose mean value is associated with a considerable amount of uncertainty) in the strength part of the CU-ARL sand model.

The variation of the blast-wave time of arrival with the distance from the sand/air interface at the same two DOBs is displayed in Figure 3-14(b). A simple analysis of the results displayed in this figure reveals that the CU-ARL clayey sand model either improves agreement with the experiment (especially in the case of 8cm DOB) or does not worsen it significantly.

The variation in the blast-wave time of arrival with offset angle (from vertical axis) at a fixed (30cm) distance from the sand/air interface is displayed in Figure 3-14(c). The results displayed in this figure show that except for the case of 3cm DOB with no offset the CU-ARL clayey sand model either improves agreement with the experiment (especially in the case of 8cm DOB) or does not worsen it significantly.

The temporal evolution of the sand bubble height for the cases of 3cm and 8cm DOB is displayed in Figure 3-14(d). The results displayed in this figure show that both the CU-ARL and the CU-ARL clayey sand model yield a reasonable and comparable agreement with the experiment with the CU-ARL clayey sand performing better at later times in the computation cycle.

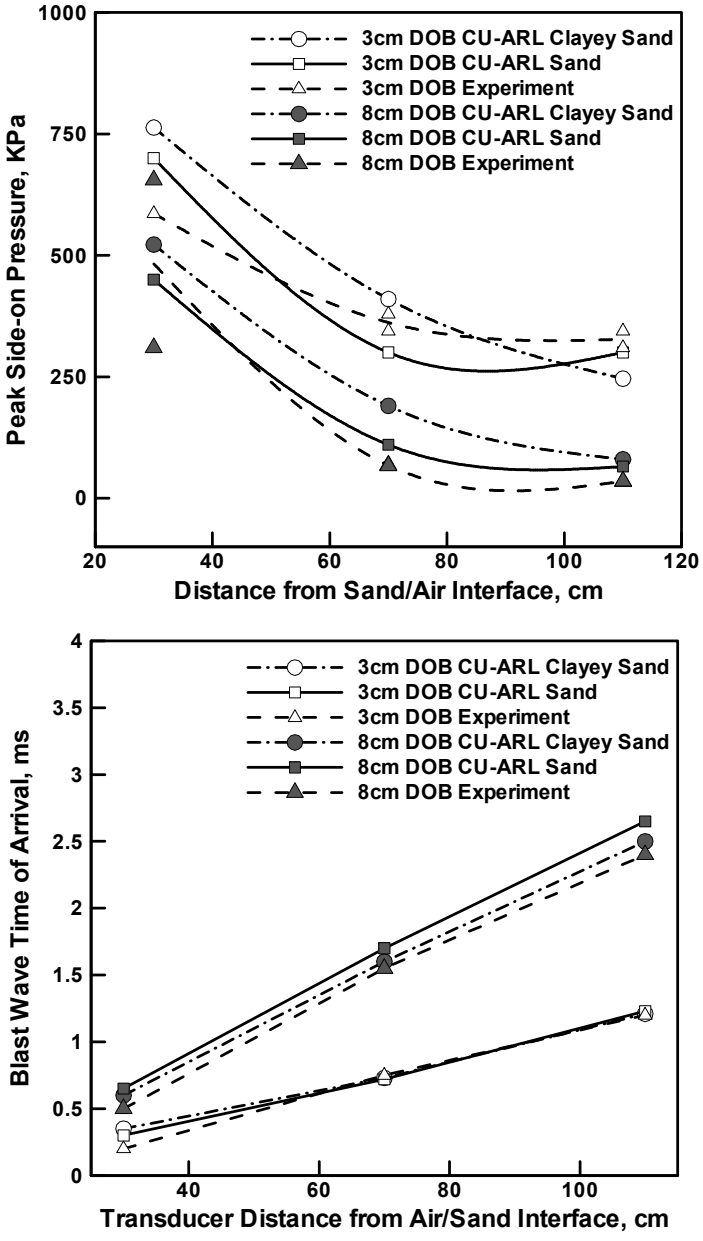

Figure 3-14. A Comparison of the Experimental [3.22] and Computed (present work) Results Pertaining to Various Phenomena Associated with Landmine Detonation in Fully Saturated Sand: (a) Side-on Overpressure vs. Transducer Distance from Air/Sand Interface; (b) Blast Wave Arrival Time vs. Transducer Distance from Air/Sand Interface; (c) Blast Wave Arrival Time vs. Transducer Offset Angle from the Symmetry Axis and (d) Sand Bubble Height vs. Landmine Post-detonation Time

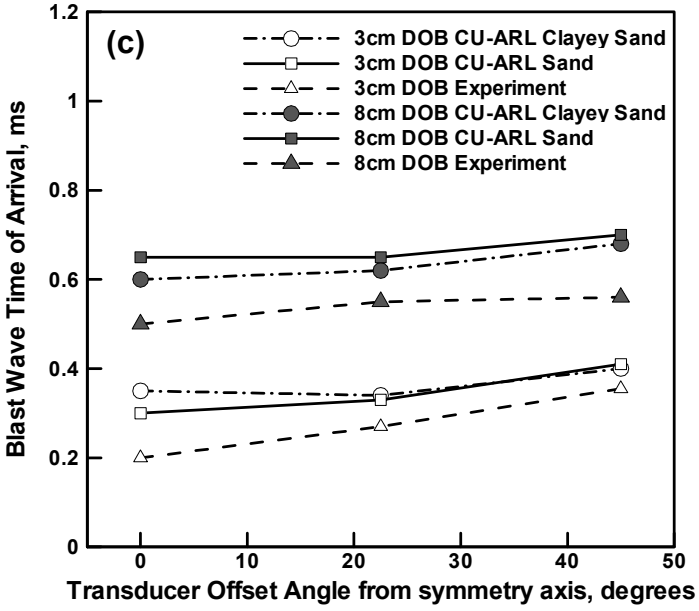

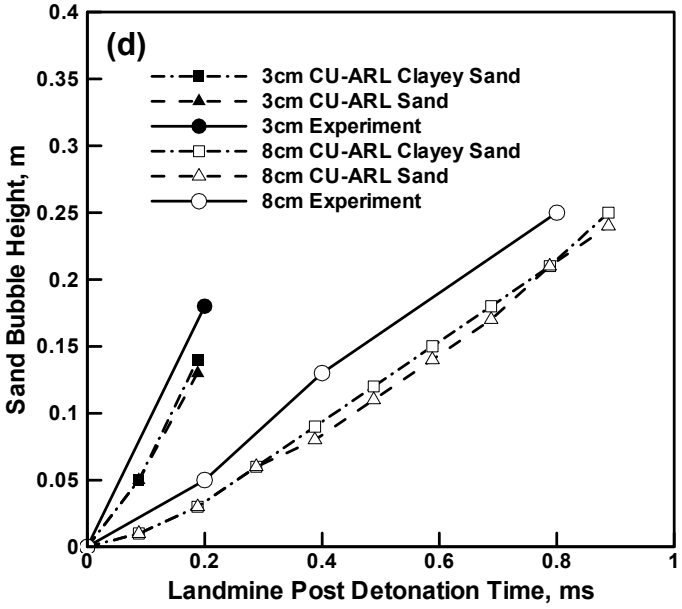

Figure 3-14. Contd…

3.6 Summary and Conclusions

Based on the results obtained in the present work, the following main summary remarks and conclusions can be drawn:

1. Using a simple procedure based on a physics-based analysis and parameter estimation, the previously developed CU-ARL clay-free material model has been expanded to include the effects of clay, as well as the effects of water content.

2. The resulting CU-ARL clayey sand model was tested by comparing the computational results with their experimental counterparts for a number of investigations involving detonation of a landmine (buried in sand) and the interactions of the mine fragments, detonation products and sand ejecta with various target structures.

3. The comparison between the experimental and the computational results (those based on CU-ARL sand model and the CU-ARL clayey sand model) revealed that the CU-ARL clayey sand model shows somewhat better agreement with the experiment. However, in many cases the agreement remained only fair.

3.7. References

3.1 M. Grujicic, B. Pandurangan and B. Cheeseman, *"The Effect of Degree of Saturation of Sand on Detonation Phenomena Associated with Shallow-buried and Ground-laid Mines,"* Shock and Vibration, 13, 2006, 41-61.

3.2 M. Grujicic, B. Pandurangan, B. A. Cheeseman and W. N. Roy, "*Application of the Modified Compaction Material Model to Soil with Various Degrees of Water Saturation*," Shock and Vibration, submitted for publication, July 2006.

3.3 J. Heffernan, *Pentagon announces specific plans to use mines in Iraq*, http://www.banminesusa.org/news/946_pentagon.htm, March 2003.

3.4 M. P. M. Rhijnsburger, "*Overview of the Use of LS-Dyna in Close-in Explosive Problems at TNO-PML*," 11th International Symposium on Interaction of Effects of Munitions with Structures, Manheim, Germany, May 2003.

3.5 Centers for Disease Control (CDC), Landmine Related Injuries, "*Morbidity and Mortality Weekly Report*," 46, 31, August 1997, 724-726.

3.6 K. A. Holsapple and K. R. Housen, *Crater Database and Scaling Tools* http://keith.aa.washinton.edu/craterdata, November 2004.

3.7 P. S. Westine, B. L. Morris, P. A. Cox and E. Polch, "*Development of computer program for floor plate response from landmine explosions*," Contract Report No. 1345, for U.S. Army TACOM Research and Development Center, 1985.

3.8 B. L. Morris, "*Analysis of Improved Crew Survivability in Light Vehicles Subjected to Mine Blast*," Final Report for Contract No. DAAK70-92-C-0058 for the U.S. Army Belvoir RDEC, Ft. Belvoir, VA, 1993.

3.9 D. Bergeron, S. Hlady and M. P. Braid, *Pendulum Techniques to Measure Landmine Blast Loading*, 17th International MABS Symposium, Las Vegas, USA, June 2002.

3.10 M. Grujicic, B. Pandurangan and B. Cheeseman, "*A Computational Analysis of Detonation Phenomena Associated with Mines Shallow-buried in Sand*," Multidiscipline Modeling in Materials and Structures, accepted for publication, January 2006.

3.11 AUTODYN-2D and 3D*, Version 6.1*, *User Documentation*, Century Dynamics Inc., 2006.

3.12 D. Bergeron, R. Walker and C. Coffey, "*Detonation of 100-gram Anti-Personnel Mine Surrogate Charges in Sand-A Test Case for Computer Code Validation*," Suffield Report No. 668, Defence Research Establishment Suffield, Ralston, Alberta, Canada, April 1998.

3.13 P. Laine and A. Sandvik, "*Derivation of Mechanical Properties for Sand*," Proceedings of the 4th Asia-Pacific Conference on Shock and Impact Loads on Structures, CI-Premier PTE LTD, Singapore, November 2001, 361-368.

3.14 L. C. Taylor, R. R. Skaggs and W. Gault, "*Vertical Impulse Measurements of Mines Buried in Saturated Sand*," Fragblast, 9, n 1, March 2005, 19-28.

3.15 M. Grujicic, B. Pandurangan, B. A. Cheeseman, W. N. Roy and R. R. Skaggs, "*Impulse Loading Resulting from Shallow Buried Explosives in Water-saturated Sand*," Journal of Materials: Design and Applications, accepted for publication, October 2006.

3.16 D. Bergeron, J. E. Tremblay, *"Canadian Research to Characterize Mine Blast Output,"* 16th International MABS Symposium, Oxford, UK, September 2000.

3.17 K. T. Spikes and J. P. Dvorkin, "*Gassmann-consistency of velocity-porosity transforms*," The Leading Edge, June 2005, 581-583.

3.18 S. Stein and T. Kim, "*Effect of Moisture on Attraction Force on Beach Sand*," Marine Geosources and Geotechnology, 22, 2004, 33-47.

3.19 N. Gniazdowski, "*The Vertical Impulse Measurement Facility Maintenance and Inspection Manual,*" ARL Technical Report (in submission) 2004.

3.20 R. R. Skaggs, J. Watson, T. Adkins, W. Gault, A. Canami and A. D. Gupta, "*Blast Loading Measurements by the Vertical Impulse Measurement Fixture (VIMF)*,"ARL Technical Report, in submission

3.21 G. Fairlie and D. Bergeron, "*Numerical Simulation of Mine Blast Loading on Structures,*" Proceedings of the 17th Military Aspects of Blast Symposium, Nevada, June 2002.

3.22 J. Foedinger, "*Methodology for Improved Characterization of Landmine Explosions*," SBIR Phase-II Plus Program, Technical Interchange Meeting, Material Science Corporation, June 2005.

3.23 M .K. Jafari and A. Shafiee, "*Mechanical Behavior of Compacted Composite Clays*," Canadian Geotechnical Journal, 41, 2004, 1152-1167.

3.24 M. W. Lee, "*Geophysical Prospecting of the Biot Coefficient in Predicting Shear-wave Velocity in Water-saturated Sediments*," Geophysical Prospecting, 54, 2006, 177-185.

CHAPTER 4

COMPUTER-SIMULATIONS BASED DEVELOPMENT OF A HIGH STRAIN-RATE, LARGE-DEFORMATION, HIGH-PRESSURE MATERIAL MODEL FOR STANAG 4569 SANDY GRAVEL

4.1. Abstract

The NATO Standard Agreement, STANAG 4569, **"***Protection for Occupants of Logistics and Light-armored Vehicles***"** [4.1] defines the make-up and the conditions of sandy-gravel soil which is used for testing the ability of various armor systems to provide the necessary level of protection. In this chapter, an effort is made to develop a high strain-rate, large-strain, high-pressure material model for sandy gravel which can be used in transient non-linear dynamic simulations of the interactions between landmine detonation gaseous products, landmine-casing fragments and soil ejecta and the target military vehicles. The material model for sandy gravel has been developed by extending the CU-ARL sand model [4.2] in order to include the effects of gravel particles on the equation of state, strength, failure and erosion behavior. Parameterization of the sandy gravel soil model has been done by carrying out a series of computational experiments pertaining to the deformation and fracture behavior of the two-phase (sand plus gravel) material. Experimental tests which should be carried out in order to validate the proposed model have been identified and described.

4.2. Introduction

It is well-established that armor used on logistic and light-armored fighting military vehicles must be capable of providing a required level of protection against a variety of battlefield threats. To enable meaningful comparison between such threats, various governing bodies have suggested their classifications and consolidations and have identified specific protection levels

against such threats. For example, in 2004 NATO issued a specification, *STANAG 4569 - "Protection Levels for Occupants of Logistics and Light Armored Vehicles"* [4.1]. In this specification, the common threats used against NATO forces are segregated into five levels of increasing severity and the corresponding lightweight-protection requirements against such threats are specified. Specifically, protection is specified for a range of Kinetic Energy (*KE*) threats such as small arms, and artillery fragments and also for landmines. The STANAG 4569 Annex A defines the level of protection required for KE threats while Annex B the protection required for landmines. Furthermore, STANAG 4569 Annex C specifies the testing and type of approval procedure required to validate a protection system against the KE threat requirements selected from Annex A. Likewise, STANAG 4569 Annex D specifies the testing and type approval required to validate a protection system against the landmine requirements selected from Annex B.

According to the STANAG 4569 Annex D, landmine-threat protection tests shall be conducted using soil with the following specifications: (a) Soil type: sandy gravel; (b) Particle Size Analysis: 100% passing the 40mm sieve, maximum 10% passing 80μm sieve, a typical particle-size distribution curve (*the sieving curve*) for sandy gravel is given in Figure 4-1; (c) Soil total (wet) density: 2200+/-100 kg/m^3; (d) The sandy gravel shall be saturated with water prior to testing. Total soil density shall be calculated using dry density measurement and soil humidity measurement. Standard methods for measuring dry density and humidity are provided in ASTM D2922-01 and ASTM D3017-01. Equivalent methods may be applied: (e) On-site soil measurements, pre-detonation, shall be included in the test report; and (f) The dimensions of the test bed must be at a minimum of 2x2 m^2 area with a minimum depth of 1.5m; and (g) A constant soil quality over the entire test bed should be ensured.

While STANAG 4569 provides the necessary guidance and the requirements for testing the ability of various military vehicles and their armor system to provide the required level of protection for the vehicle occupants, such experiments are generally quite costly (and often cost prohibitive). It is, hence, highly desirable to be able to reduce the number of such experiments by replacing them with the corresponding computational analyses of the threat/target interactions. To carry out such analyses, the availability of high-fidelity material models for all the participating materials is highly critical. Specifically, in the case of the computational simulations of the testing and validation of protection systems against the landmine threats, as specified in STANAG 4569 Annex D, the knowledge of a material model for sandy-gravel soil is imperative. In the present work, an attempt is made to develop a physically-based, mathematically-simple high deformation-rate, large-strain, high-pressure material model for sandy gravel.

Recent advances in numerical analysis capabilities, particularly the coupling of Euler solvers (used to model gaseous detonation products and air) and Lagrange solvers (used to represent vehicles/platforms and soil), have allowed simulations to provide insight into complex loading created by the mine blast event. However, a quantified understanding of the blast phenomena and loadings through computer modeling is still not mature. As discussed in our previous work [4.2], the lack of maturity of computer simulations of the blast event is mainly due to inability of the currently available material models to realistically represent the response of the material involved under high deformation-rate, large-deformation, high-temperature conditions, i.e. the type of conditions accompanying landmine detonation.

The knowledge of the mechanical-response of soil under shock/blast loading conditions is critical in many engineering disciplines and commercial and military endeavors (e.g. mining, construction, design of survivable armored vehicles, etc.). For many years, the common practice

was to develop purely-empirical relations for soil at a given site using a variety of (non-standardized) experimental tests. Such relations are often found to have very little portability and may, when used in soil and test conditions different from the original ones, lead to widely different and unrealistic predictions [4.3,4.4]. To overcome these severe limitations, over the last dozen years, researchers have attempted to develop more general constitutive material models for sand which could include various aspects of sand composition/microstructure and the moisture and organic matter contents [e.g. 4.2, 4.5, 4.10, 4.11].

While there are a variety of soils, it is customary to divide soils into two main categories: (a) *Cohesion-less soils* (e.g. sand) which consist of relatively coarse particles (average particle size 4-5mm) which have a negligible tensile strength and derive their shear strength primarily from the inter-particle friction; and (b) *Cohesive soils* (e.g. clay) which consist of fine particles (average particle size 50-100μm) which derive their strength and failure properties from the inter- and intra-particle electrostatic and polar forces. In the present work, the problem of material model derivation and validation for sandy-gravel soil is addressed. Such soil typically contains low clay content and, hence, can be considered as a cohesion-less type of soil. Furthermore, in the derivation of the material model for sandy gravel it will be assumed that this type of soil can be considered as a mixture of sand and gravel. Consequently, a brief overview of the available dynamic material models for sand is presented below.

Sand has generally a complex structure consisting of mineral solid particles which form a skeleton. The pores between the solid particles are filled with a low-moisture air (this type of sand is generally referred to as *"dry sand"*), with water containing a small fraction of air ("*saturated sand"*) or comparable amounts of water and air ("*unsaturated sand"*). The relative volume fractions of the three constituent materials in the sand (the solid mineral particles, water

and air) are generally quantified by the porosity, , and the degree of saturation (Saturation Ratio), β, which are respectively defined as:

$$\alpha = \frac{V_p}{V} \tag{4.1}$$

and

$$\beta = \frac{V_w}{V_p} \tag{4.2}$$

where V_p is the volume of void (pores), V_w is the volume of water and V is the total volume.

Surface roughness and the presence of inorganic/organic binders are generally considered to be the main causes for friction/adhesion at the inter-particle contacting surfaces. Deformation of the sand is generally believed to involve two main basic mechanisms [4.4, 4.5]: (a) elastic deformations (at low pressure levels) and fracture (at high pressure levels) of the inter-particle bonds and (b) elastic and plastic deformations of the three constituent materials in the sand. The relative contributions of these two deformation mechanisms as well as their behavior are affected primarily by the degree of saturation of sand and the deformation rate. Specifically, in dry sand the first mechanism controls the sand deformation at low pressures while the second mechanism is dominant at high pressures and the effect of deformation rate is of a second order. In sharp contrast, in saturated sand very low inter-particle friction diminishes the role of the first deformation mechanism. On the other hand, the rate of deformation plays an important role. At low deformation rates (of the order of $1.0.10^{-3}$ s^{-1}), the water/air residing in the sand pores is squeezed out during deformation and, consequently, the deformation of the sand is controlled by the deformation of the solid mineral particles. At high deformation rates (of the order of $1.0.10^{5}$

s^{-1}) and pressures (of the order of ca. 1GPa), on the other hand, water/air is trapped within the sand pores and the deformation of the sand is controlled by the deformation and the volume fractions of each of the three constituent phases.

In the areas of soil mechanics and soil dynamics it is often assumed that the solid particles do not undergo plastic deformation and that the water phase is incompressible. The external loading is internally supported by the soil skeleton (via the so-called "*effective stress*" and by the water (via the so-called "*pore pressure*") [4.6]. Furthermore, the deformation of soil is controlled by the effective stress since the water and gas do not support any shear loading and are capable of flowing out through the soil pores. A number of investigators [e.g. 4.4, 4.5] clearly established that the effective stress approach discussed above is correct under the static/quasi-static loading conditions but it becomes deficient under shock loading conditions. The two key deficiencies of the effective stress approach are the inability to account for: (a) deformation of the solid particles under shock loads; and (b) the fact that due to a very short duration of shock loading, water may become trapped in soil pores and provide additional load support.

To overcome these limitations of the effective stress approach, Wang et al. [4.4, 4.5], proposed a so-called "*three-phase soil model*". The model includes an *Equation of State* (based on the conceptual approach presented in [4.6]), a Drucker–Prager type strength model [4.7] and a damage model for degradation of strength and stiffness of the soil skeleton. Despite its physics-based foundation, the three-phase model has not been widely accepted in the military-engineering community, primarily due to its mathematical complexity and difficulties associated with its parameterization.

The most widely used soil material model in the military-engineering community is the so-called "*porous-material/compaction*" model developed by Laine and Sandvik [4.8]. The model was constructed using the experimental results (from a variety of high-rate loading tests) to both

ascertain the nature of the underlying functional relationships and to parameterize the model (via a multi-regression analysis).

As mentioned above, the porous –material/compaction model for sand proposed by Laine and Sandvik [4.8] has been, for quite some time, the sand model which provided the best compromise between the inclusion of essential physical phenomena reflecting material response under dynamic loading and computational simplicity. However, the model of Laine and Sandvik [4.8] was developed essentially for dry and clay-free sand and, as determined by many researchers [e.g. 4.9-4.11], cannot account for the effects of moisture and clay contents. To overcome these deficiencies of the original porous-material/compaction model, Clemson University and the Army Research Laboratory (ARL), Aberdeen, Proving Ground, MD jointly developed [4.14] and subsequently parameterized (using the results of a detailed investigation of dynamic response of sand at different saturation levels, as carried out by researchers at the Cavendish Laboratory, Cambridge, UK [4.12, 4.13]) the new sand model [4.2]. This model is capable of capturing the effect of moisture on the dynamic behavior of sand and was named the CU-ARL sand model. In a subsequent work [4.15], Clemson University and the ARL developed the so-called CU-ARL clayey sand model to include the effect of minor (15vol.%) additions of clay on the mechanical response of sand.

A review of the public-domain literature revealed the lack of a high deformation-rate material model for sandy gravel, suitable for landmine-detonation computational analyses. An experimental method for determining the static strength and deformation behavior of sandy gravel was developed in 1992 by Fragaszy [4.16] and Day [4.19]. Due to the presence of large gravel particles, sandy-gravel soils present serious challenges when tested with conventional laboratory equipment. The new method, *the matrix method*, is based on the assumption that large particles floating in a matrix of finer-grained material do not significantly affect the strength and

deformation characteristics of the mixture. Therefore, the behavior of a prototype soil containing oversized particles can be modeled by testing the matrix portion alone, provided the model specimen is prepared at the density that exists within the prototype soil away from the oversized particles. Results of consolidated-drained triaxial (CDTX) tests performed on prototype and model specimens revealed that the CDTX peak shear strengths for the prototype and model soils are almost identical. Likewise, strengths in the fully saturated state, the stress-strain and the volumetric strain–axial strain behaviors of the prototype and model soils are found to be very similar. The aforementioned observations of Fragaszy [4.16] and Day [4.19] will be used as the foundation of the material model for sandy gravel which is developed in the present chapter. In addition, it will be assumed that the mechanical behavior of the sandy-matrix can be represented using the CU-ARL sand model [4.2].

The organization of the chapter is as follows. A brief overview of the CU-ARL sand material model is presented in Section 4.3. An extension of the CU-ARL sand material model to include the effects of gravel particles and the basic formulation of the CU-ARL sandy-gravel material model are discussed in Section 4.4. Parameterization of the CU-ARL sandy-gravel material model via transient non-linear dynamics analyses of a number of simple mechanical tests is given in Section 4.5. A brief summary and the conclusions obtained in the present work are discussed in Section 4.6.

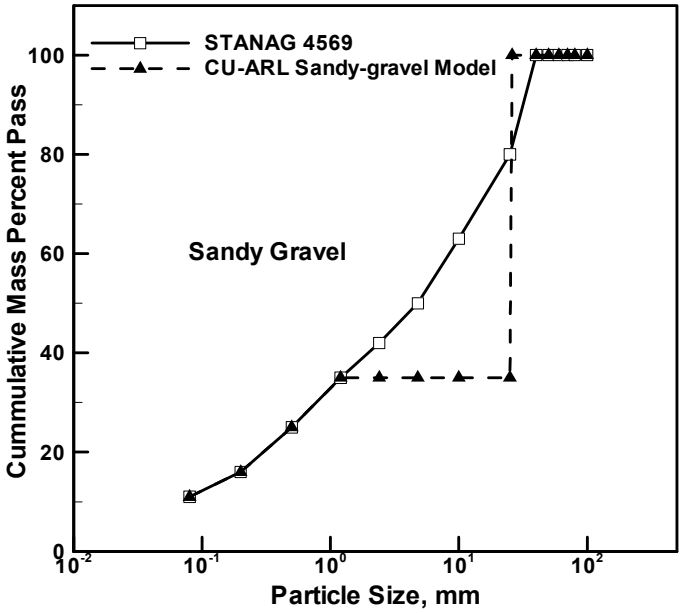

Figure 4-1. Sieving Curves According to the STANAG 4569 and CU-ARL Sandy-gravel Material Model

4.3. CU-ARL Sand Material Model

A complete formulation of the transient non-linear dynamics problem such as the interaction between landmine-detonation products, landmine-casing fragments and soil ejecta with a target structure entails the knowledge of materials models (material-specific relations between pressure, deviatoric stress, mass density, strain, strain rate, internal energy density, etc.). These relations typically involve: (a) an equation of state; (b) a strength equation; (c) a failure equation and (d) an erosion equation for each constituent material. The equation of state defines pressures dependence on mass density and internal-energy density (and, in the case of anisotropic materials, on deviatoric strain.) The strength and failure equations define the evolutions of the deviatoric stress in the elastic regime, elastic-plastic regime, and in the post failure initiation

regime. In other words, the equation of state along with the strength and failure equations (as well as with the equations governing the onset of plastic deformation and failure and the plasticity and failure induced material flow) enable assessment of the evolution of the complete stress tensor during a transient non-linear dynamics analysis. Such an assessment is needed where the governing (mass, momentum and energy) conservation equations are being solved. Separate evaluations of the pressure and the deviatoric stress enable inclusion of the nonlinear shock-effects in the equation of state. The erosion equation is generally intended for eliminating numerical solution difficulties arising from highly distorted Lagrange cells. Nevertheless, the erosion equation is often used to provide additional material failure mechanism especially in materials with limited ductility.

In the remainder of this section, a brief overview is provided of the CU-ARL sand model [4.2]. To facilitate the implementation of the CU-ARL model into commercial and public-domain transient non-linear dynamics codes, the governing model relations are expressed in terms of the following soil-state parameters: mass density at full compaction (referred to as the reference density), ρ_{ref}; (which accounts for the effect of the chemical composition of sand,) the initial soil porosity, $\square_0$, which is primarily controlled by the particles average size and distribution as well as the extent of soil pre-compaction and initial extent of soil water-saturation, β_0, as well as in terms of the model-defining parameters. It should be noted that the CU-ARL model was designated to account for the behavior of sand under high deformation-rate conditions under which the water is trapped in the inter-particles spaces. The CU-ARL sand model is composed of four components; (a) a porous-material/compaction equation of state; (b) a porous-material/compaction strength model; (c) a porous-material/compaction failure model and (d) a porous-material/compaction erosion model. These are presented in the following four sub-sections.

4.3.1. CU-ARL Sand Equation of State

For the CU-ARL sand model, a porous-material/compaction equation of state is used which is a particular form of the Mie-Gruneisen equation of state:

$$P = P_H + \Gamma\rho\left(e - e_H\right) \tag{4.3}$$

in which the second term on the right-hand side of the Eq. (4.3) is omitted. In Eq. (4.3) the following nomenclature is used: P is pressure (a sum of the pore pressure and effective stress in the soil skeleton), ρ the (current) mass density, Γ the Gruneisen gamma parameter, e the internal energy density and the subscript H is used to denote the reference shock-Hugoniot level of a given quantity.

The Hugoniot pressure, P_H, is defined using the following stationary-shock relationship [17]:

$$P_H = \frac{\rho_0 C_0^2 \eta}{\left(1 - s\eta\right)^2} \tag{4.4}$$

where $\rho_0 = \left(1-\alpha_0\right)\rho_{ref} + \alpha_0\beta_0\rho_w$ is the initial material mass density, where C_0 is the speed of sound (in the homogenized sand/pores medium as measured using the standard flyer-plate experiment setup at room temperature [4.12]), $\eta = \left(1 - \frac{\rho_0 - \alpha_0\beta_0\rho_w}{\rho - \alpha_0\beta_0\rho_w}\right) = \left(1 - \frac{(1-\alpha_0)\rho_{ref}}{\rho - \alpha_0\beta_0\rho_w}\right)$ the compressibility ratio, ρ_w the density of water and the parameter s represents a rate of increase of the (average) particles velocity, U_p, with an increase in the shock velocity, U_s and is defined by the relation:

$$U_s = C_0 + sU_p \tag{4.5}$$

In the CU-ARL sand-model equation of state, the aforementioned relations for ρ_0 and η are substituted in Eq. (4.4) to get:

$$P = P_H = \frac{((1-\alpha_0)\rho_{ref} + \alpha_0\beta_0\rho_w)C_0^2\left(1-\frac{(1-\alpha_0)\rho_{ref}}{\rho-\alpha_0\beta_0\rho_w}\right)}{\left(1-s\left(1-\frac{(1-\alpha_0)\rho_{ref}}{\rho-\alpha_0\beta_0\rho_w}\right)\right)^2} \quad , \quad \rho \le \rho_{comp} \tag{4.6a}$$

and

$$P = P_H = P(\rho_{comp}) + C_0^2(\rho - \rho_{comp}) \quad , \quad \rho > \rho_{comp} \tag{4.6b}$$

where $\rho_{comp} = \left(\frac{1-\alpha_0}{1-\alpha_0+\alpha_0\beta_0}\right)\rho_{ref} + \left(\frac{\alpha_0\beta_0}{1-\alpha_0+\alpha_0\beta_0}\right)\rho_w$ is the density of the sand at full compaction. Full compaction is defined as a porosity-free state of sand.

The degree of saturation dependent parameters C_0 and s are obtained by fitting the original U_s vs. U_p results obtained in Refs. [4.12, 4.13] to a low order polynomial in which the coefficients are set to depend on the initial level of porosity and the reference density. The results of this curve fitting procedure can be found in Ref. [4.2], Figures 4-8(a) and 4-8(b), where the C_0 vs. β_0 and the s vs. β_0 functional relations are also given. These relations in conjunction with Eqs. 4.6(a) and 4.6(b) define the dependence of pressure on ρ_{ref}, α_0, β_0 and ρ.

The P vs. ρ relation just derived is valid only during loading and only when such loading gives rise to irreversible/plastic compaction of the porous material. It should be noted that the term loading implies an event within which the pressure is increased (and, in the case of plastic loading, a decrease in material porosity takes place). Conversely, unloading is associated with a decrease in pressure. As shown in our previous work [4.2], during unloading/elastic-reloading, the P vs. ρ relationship is defined as $\frac{dP}{d\rho} = C_0^2(\rho_{ref}, \alpha_0, \beta_0)$, where the $C_0(\rho_{ref}, \alpha_0, \beta_0)$ relation can be found in Ref.[4.2], Figure 4-8(a).

4.3.2. CU-ARL Sand Strength Model

Within the original compaction strength model for dry sand proposed by Laine and Sandvik [4.8], the pressure dependence of yield stress is assumed to be controlled by inter-particle friction and is defined by the following-pressure dependent relation:

$$\sigma_{y,dry} = \phi_{dry} P_{dry} \approx \begin{cases} 1.3732 P_{dry} & 0 < P_{dry} \le P_{MC} \\ 1.3732 P_{MC} & P_{dry} > P_{MC} \end{cases} \tag{4.7}$$

Also, for the saturated sand, as shown in our previous work [4.11], the pressure-dependent yield stress can be defined as:

$$\sigma_{y,sat} = \begin{cases} \phi_{sat} P_{sat} & 0 \le P_{sat} \le P_{MC} \\ \phi_{sat} P_{MC} & P_{sat} > P_{MC} \end{cases} \tag{4.8}$$

where the yield-stress-to-pressure proportionality coefficient, ϕ_{sat}, is defined as:

$$\phi_{sat} = \begin{cases} \left(0.1 + 1.2732 \dfrac{P_{sat}}{P_{MC}}\right) & 0 \le P_{sat} \le P_{MC} \\ 1.3732 & P_{sat} > P_{MC} \end{cases} \tag{4.9}$$

The term P_{MC} (=$1.864 \cdot 10^5$ kPa) appearing in Eqs. (4.7)-(4.9) is the Mohr-Coulomb pressure beyond which the yield stress is pressure insensitive. It should be noted that neither of the Eqs. (4.7)-(4.9) include the effect of strain rate on the yield strength of sand. This was justified in our previous work [4.2], where it was shown that as long as the model is used at high deformation rates (ca. $>1.0 \cdot 10^3 s^{-1}$), the strength and failure behavior of sand can be considered rate independent.

Within the CU-ARL sand strength model, the yield stress vs. pressure relationship for unsaturated sand is defined using a linear combination of the yield-stress/pressure proportionality coefficients in dry and the saturated sands as:

$$\sigma_{y,unsat} = \begin{cases} \phi_{unsat} P_{unsat} & 0 \le P_{unsat} \le P_{MC} \\ \phi_{unsat} P_{MC} & P_{unsat} > P_{MC} \end{cases} \tag{4.10}$$

where

$$\phi_{unsat} = (1 - \beta_o)\phi_{dry} + \beta_o \phi_{sat} \tag{4.11}$$

Defined in this way, Eqs. (4.10) and (4.11) can be also used for dry sand (β= 0.0) and saturated sand (β= 1.0).

In addition to specifying the yield stress vs. pressure relationship, the compaction strength model entails the knowledge of the density dependent shear modulus. Since water has no ability to support shear stresses, the shear modulus, G, of unsaturated sand is dominated by the shear modulus of the solid skeleton of the sand. However, the presence of water changes the density of the sand. Therefore, the original compaction shear modulus vs. density relationship (defined using ten pairs of (G, ρ) points in AUTODYN) was fitted to a polynomial function and modified by: (a) correcting density with a $-\alpha_0\beta_0\rho_w$ term and (b) introducing a moisture-level dependent maximum shear modulus in order to obtain a (deformation-rate independent) shear modulus vs. density relationship for sand at different saturation levels. This procedure yielded the following CU-ARL sand-model shear modulus vs. density functional relationships:

$$G(kPa) = \begin{cases} 5.2175 \cdot 10^{-14} (\rho - \alpha_0\beta_0\rho_w)^6 & \rho(kg/m^3) < (1 - \alpha_0\beta_0)\rho_{ref} + \alpha_0\beta_0\rho_w \\ (1 - \alpha_0\beta_0) G_{Bulk} & \rho(kg/m^3) >= (1 - \alpha_0\beta_0)\rho_{ref} + \alpha_0\beta_0\rho_w \end{cases} \tag{4.12}$$

where G_{Bulk} (=3.73470$\cdot 10^7$) denotes the shear modulus of fully compacted dry sand. Eq. (4.12) correctly accounts for the fact that, at full compaction, the sand density is equal to $(1 - \alpha_0\beta_0)\rho_{ref} + \alpha_0\beta_0\rho_w$.

It should be noted that in the strength model developed in this section, the contribution of water to the material strength was neglected. This can be justified by recognizing the fact that

viscosity of water is typically is around 0.001 Pa.s and at deformation rates of $1.0 \cdot 10^5$ s^{-1}, the contribution of water to the shear strength of the sand is a mere 100Pa.

4.3.3. CU-ARL Sand Failure Model

It is well established that the presence of moisture in sand increases the sand's cohesive strength [4.18]. Therefore, the magnitude of the (negative) failure pressure for sand is expected to increase with the saturation ratio (β). Also, the moisture content should be substantial (β>0.7) before its effect on the cohesive strength of sand becomes significant [4.18]. To account for these two observations, within the CU-ARL sand failure model [4.2], the following expression was proposed for the magnitude of the (negative) failure pressure in unsaturated sand; $P_{fail\ unsat}$:

$$P_{fail,unsat} = \beta_0^5 P_{fail,sat} \tag{4.13}$$

where $P_{fail,sat}$ (set equal to 70kPa) is the failure pressure in saturated sand [4.18]. The relationship given by Eq. (4.13) correctly predicts that the cohesive strength of unsaturated sand with a saturation ratio of 0.7 is around 10-15% of that in the saturated sand.

4.3.4. CU-ARL Sand Erosion Model

Erosion of a porous-material element is assumed, within the CU-ARL sand erosion model, to take place when geometrical (i.e. elastic plus plastic plus damage) instantaneous strain reaches a maximum allowable value. The investigation reported in Ref. [4.9] established that the optimal value for the geometrical instantaneous strain is ~1.0. When a material element is eroded, its nodes are retained along with their masses and velocities in order to conserve momentum of the system. The momentum is conserved by distributing the mass and velocities associated with the eroded cells among the corner nodes of the remaining cells. Despite the fact that some loss of accuracy is encountered in this procedure (due to removal of the strain energy

from the eroded elements) the procedure is generally found to yield reasonably accurate results [4.17].

4.4. Derivation of the CU-ARL Sandy Gravel Material Model

The derivation of the CU-ARL sandy-gravel material model is presented in the present section while the parameterization of this model is deferred until Section 4.5. As mentioned earlier, the sandy-gravel soil is assumed to consist of centimeter-size gravel particles embedded in the sand-matrix at different levels of (water) saturation. The clay content is assumed to be minimal so that cohesion (except at high level of compaction and high saturation levels) can be neglected. Also, the CU-ARL sandy-gravel model is constructed using the four basic model components; (a) an equation of state; (b) a strength model; (c) a failure model; and (d) an erosion model. The derivations of each of these are presented in the following four sub-sections.

In addition to the conditions specified above, the CU-ARL sandy-gravel material model developed in this section is based on the following simplifying assumptions:

(a) The material model for sandy gravel can be derived by combining and integrating the material models for the two constituent materials, sand and gravel;

(b) The dynamic material response of sand can be accounted for using the CU-ARL sand model [4.2];

(c) As for the material model for gravel is concerned, it is assumed that it can be represented by: (i) a linear equation of state, $P=K(1-\rho/\rho_o)$, where K =65GPa is the bulk modulus (considering gravel to be mainly composed of limestone) and the superscript 'o' denotes the initial state; (ii) an elastic strength model, $\sigma_{eq}=2G\varepsilon_{eq}$, where G =39GPa is the shear modulus and the subscript 'eq' denotes the equivalent (stress and strain) quantities; (iii) Since gravel particle can resist fracture much more effectively than sand, no failure criterion for gravel particles is

assumed; and (iv) as in the case of sand, an instantaneous geometrical strain of 1.0 is used as the erosion model for gravel particles since the primary role of the erosion model is to prevent numerical difficulties associated with excessive distortions of the Lagrange cells;

(d) Sandy gravel can be considered as a mixture of a sand matrix and gravel particles of a uniform size. Consequently, the sieving curve for sandy gravel can be simplified as indicated by the dashed line in Figure 4-1. On this curve, the particle size at which the percent pass jumps to 100 is not a significant quantity since the CU-ARL sandy gravel material model developed in this section does not explicitly account for the gravel-particle size dependence. The percent pass at which the simplified sieving curve becomes discontinuous, on the other hand, controls the relative volume fractions of the two constituent materials in the proposed model for sandy gravel and, hence, is a critical model parameter whose assessment is presented in Section 4.5; and

(e) A homogenization procedure can be used to derive the effective (two-phase) sandy gravel material properties in terms of the corresponding properties, volume fractions, morphology and microstructure of the two constituent materials. A schematic of such as homogenization procedure is shown in Figures 4-2(a)-(b).

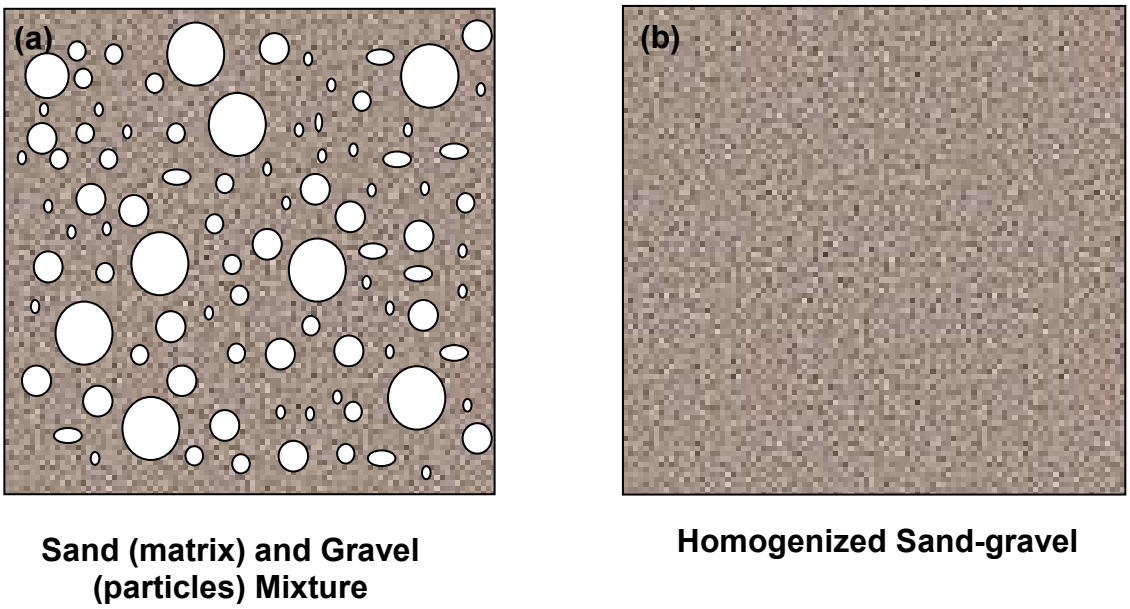

Figure 4-2. (a) Simplified (sand + gravel) Two-phase Model and (b) its Homogenized Single-phase Equivalent

4.4.1. CU-ARL Sandy Gravel Equation of State

As discussed in Section 4.3.1, the equation of state defines a functional relationship between pressure and density. When a representative material element, as the one shown schematically in Figure 4-2(a), is subjected to hydrostatic pressure, compaction takes place almost exclusively within the sand matrix phase while the variation of the pressure throughout the element is minor and can be ignored. In other words, a constant pressure condition can be assumed throughout the element volume.

At a given pressure level P, the corresponding densities of sand and gravel can be obtained by inverting the equations of state for the two materials (i.e. Eq. (4.6) and the relation defined in point (b) in Section 4.4). The problem then is to define the effective density of sandy

gravel, ρ_{sandy_gravel}, in terms of corresponding sand, ρ_{sand} , and gravel, ρ_{gravel},, densities at the same pressure level and in terms of the volume fraction of gravel, f_{gravel} .

Once f_{gravel} is computed, the CU-ARL sandy gravel P vs. ρ relation can be determined using the following relation:

$$\rho_{sandy\_gravel} = \left(1 - f_{gravel}\right)\rho_{sand} + f_{gravel}\rho_{gravel} \tag{4.14}$$

The procedure for determination of the P vs. ρ_{andy_gravel} relation (the CU-ARL sandy gravel equation of state) (during plastic loading) can then be summarized as follows: (a) At a given level of pressure, P, Eq. (4.6) and the $P = K_{gravel}(1-\rho_{gravel}/\rho_{ogravel})$ relation are inverted to get ρ_{sand} and ρ_{gravel}: (b) ρ_{sand}, ρ_{gravel} and f_{gravel} (The procedure used to assess the value of the gravel volume fraction will be presented in Section 4.5) are then used in Eq. (4.14) to compute ρ_{sandy_gravel} corresponding to the given level of pressure, P; and (d). Finally, the resulting (ρ_{sandy_gravel}, P) pairs can be used to construct a piece-wise linear form of the equation of state.

In accordance with the procedure presented above, the sandy-gravel bulk modulus (controls unloading and elastic re-loading behaviors) can be defined using a volumetric rule of mixture applied to the reciprocals of the sand and gravel bulk moduli. Furthermore, the speed of sound for sandy gravel is defined as a square root of the bulk modulus and the density of this material.

4.4.2. CU-ARL Sandy-gravel Strength Model

Determination of the strength model for sandy gravel can be classified as a classical problem of determination of the plastic behavior of a pressure-dependent ideal-plastic matrix material containing elastic inclusions. This problem has been analyzed in many classes of materials (metals, polymers, glasses, etc.) [e.g.4. 17], all these analyses revealed that the nature of the matrix/inclusion interface and its ability to transfer shear loads between the two phases plays a critical role in controlling the effective strength properties of the two-phase material. In the case of sandy gravel, the sand/gravel interface is not expected to possess significant ability to transfer shear loads neither in the case of dry sand (lack of adhesion and low level of friction) or in the case of non-dry sand (moisture acts as an effective friction-coefficient reducer). Therefore, within the CU-ARL sandy-gravel strength model, developed in the previous work, it is assumed that plastic deformation takes place solely within the sand phase and that gravel particles act merely as non-deformable obstacles which force the plastic flow to take place around the particles. This effect causes an increase in the work of plastic deformation. Since the CU-ARL sandy-gravel material model considers a homogenized, single-phase sandy-gravel, the effect of gravel particles can be accounted for only implicitly. This was done by properly increasing the sand-matrix yield strength. Following Ashby [4.20], the resulting effective two-phase material yield strength, σ_{sandy_gravel}, is defined as:

$$\sigma_{sandy\_gravel} = C_{yield}\,\sigma_{sand}\left(1+\frac{1}{16}\left(\frac{f_{gravel}^{1/2}}{1-f_{gravel}^{1/2}}\right)\right) \tag{4.15}$$

Where σ_{sand} denotes the yield strength of CU-ARL sand and C_{yield} is a parameter quantifying the effect of gravel-particle size on the yield strength of sandy gravel.

As in the case of bulk modulus, the sandy-gravel shear modulus (controls unloading and elastic re-loading behaviors) can be defined using a volumetric rule of mixture applied to the reciprocals of the sand and gravel shear moduli. It should be noted that Hardin and Kalinski [4.21] used a special large-scale torsion resonant column apparatus to obtain the values of shear modulus (and its reduction at larger shear strains) for a variety of gravelly soils like: uniform and graded crushed limestone gravel, graded river gravel, standard Ottawa and crushed limestone sands, and gravel–sand–silt mixtures. Their results established several semi-quantitative correlations: (a) The shear-modulus values for relatively clean uniform particle-size and graded particle-size gravels were found to increase with the average particle size, although the effect is relatively weak; (b) The shear modulus in soils with a variety of particle-size gradations was found to be dominated by the particular particle size. This particle size is in the 5-10mm particle-diameter range and is a relatively weak function of the gravelly-soil type (i.e. crushed limestone gravel, river gravel, etc.); and (c) Reduction of the shear modulus at relatively large shear strains is the result of irreversible plastic response of the material and is better handled by using a yield-criterion approach than a non-linear elastic approximation.

4.4.3. CU-ARL Sandy-gravel Failure Model

As discussed in Section 4.3, the CU-ARL sand failure model is a hydro-dynamic type model which defines a minimal (negative) pressure, P_{min}, as condition for the (instantaneous) failure. Past the instant of failure, failed elements cannot support shear or tensile loads while their ability to carry compressive loads is retained. In the case of dry sand, the inter-particle adhesion is practically absent and, hence, P_{min} is set to zero in the CU-ARL sand failure model. The presence of water and the resulting capillary effects in non-dry sand, on the other hand, give rise to inter-particle adhesion. Consequently, P_{min} becomes negative and its magnitude continues to increase with an increase in the saturation level, Eq. (4.13).

The question to be answered next is how the presence of gravel affects the failure behavior of sand at different level of saturation. To answer this question the following physical-level arguments are presented:

(a) In, the absence of water/moisture (and clay), the sandy-gravel soil can be still considered as cohesion-less $(P_{\min} = 0.0)$ since no source of sand/gravel adhesion can be identified;

(b) In the presence of water, the sand/gravel adhesion is present but its origin (capillary) is the same as that for the sand inter-particle cohesion;

(c) Failure of the sandy-gravel soil would take place exclusively by failure of the sand matrix. Consequently the fracture surface (due to presence of un-fractured gravel particles) is expected to be wavier in the case of sandy-gravel in comparison to that in the (gravel-free) sand.

The aforementioned points (a) and (b) suggest that the $P_{\min}$ vs. β_0 relation for the sandy gravel should also be given by Eq. (4.13). However, point (c) suggests that the work of fracture in the sandy gravel should be higher than that in sand. Since the sandy-gravel material model developed in the present work considers this material as a homogenized single-phase brittle material, the work of fracture cannot be readily incorporated. Nevertheless, since pressure and the work of fracture pre unit material volume have identical units, the increased work of fracture in the case of sandy gravel is accounted for by multiplying the $P_{fail,sat}$ parameter in Eq. (4.13) by a gravel-particle size dependent constant, C_{fail}. Except for this change, the CU-ARL sandy-gravel failure model is identical to that for the sand and is given by Eq. (4.13).

4.4.4. CU-ARL Sandy-gravel Erosion Model

Since the erosion model is used primarily to deal with the numerical difficulties associated with excessively distorted Lagrange cells and since the gravel particles (being stiffer

and stronger than sand) are not likely to aggravate the problem of cell distortion, the CU-ARL sand erosion model will be retained. That is, the CU-ARL sandy-gravel erosion model proposed specifies an instantaneous geometrical strain of 1.0 as the condition for the element removal. As discussed In Section II.4, masses and velocities of the freed nodes are retained in order to ensure momentum conservation.

4.5. Parameterization of the CU-ARL Sandy Gravel Material Model

In the previous section, a new material model for sandy gravel, the CU-ARL sandy gravel material model was proposed. The model is an extension of our previously developed CU-ARL sand model [4.2] and contains three additional parameters accounting for the effect of gravel particles in sand. The three parameters are: (a) the (initial) volume fraction of gravel f_{gravel} which was introduced in the equation of state; (b) a gravel-particle size dependent parameter C_{yield} which was introduced in the strength model; and (c) a particle size dependent failure parameter, C_{fail}. In the following subsections, several transient non-linear dynamics analyses have been used to assess these parameters, i.e. to parameterize the CU-ARL sandy-gravel material model. All the calculations carried out in this section were done using AUTODYN, a general purpose non-linear dynamics modeling and simulation software [4.17]. In this section, a brief overview is given of the basic features of AUTODYN, emphasizing the aspects of this computer program which pertain to the problem at hand.

A transient non-linear dynamics problem is analyzed within AUTODYN by solving simultaneously the governing partial differential equations for the conservation of momentum, mass and energy along with the material-model equations and the equations defining the initial and the boundary conditions. The equations mentioned above are solved numerically using a second-order accurate explicit scheme and one of the two basic mathematical approaches, the

Lagrange approach and the Euler approach. Within AUTODYN these approaches are referred to as "*processors*". The key difference between the two basic processors is that within the Lagrange processor the numerical grid is attached to and moves along with the material during calculation while within the Euler processor, the numerical grid is fixed in space and the material moves through it. In our recent work [4.11], a brief description was given of how the governing differential equations and the material-model equations define a self-consistent system of equations for the dependent variables (nodal displacements, nodal velocities, cell material densities and cell internal energy densities).

In the present work, both the Euler and the Lagrange processors were used. The Euler processor was used to construct a material domain which was then subjected to different deformation modes. The results obtained in these computational analyses were next used to carry out parameterization of the CU-ARL sand-gravel material model. Since in the present work two materials (sand or gravel) simultaneously reside within a single Euler computational cell, a multi-material Euler scheme had to be used. A brief overview of the multi-material Euler scheme used is presented in the remainder of this paragraph. Within this scheme, a control volume method is used to solve the integral and finite-difference forms of the mass, momentum and energy conservation equations in order to obtain an accurate and stable solution. The terms appearing in these equations are divided into two groups: Lagrange and transport (convective). A two-step numerical procedure is used to solve the finite-difference form of the governing equations. Within the first step, the Lagrange (cell-deforming) step, the Lagrange form of the governing equations is advanced one time interval. Within the second step, the Euler step, the dependant variables updated in the first step are mapped on to the un-deformed Euler mesh. Multiple materials are handled through a volume fraction technique or an interface technique developed by Youngs [4.22]. All dependent variables are referenced with respect to the center of the cells.

It should be noted that while the Euler formulations are ideally suited for handling large deformations and fluid flow, they suffer from the difficulties in tracking free-surfaces, material interfaces and history-dependent material behavior. The Euler formulation may also be prone to numerical diffusion associated with material convection between cells. To overcome these difficulties interfaces between the two materials in the Euler domain and the interfaces between the Euler and the Lagrange domains were tracked in AUTODYN using the SLIC (Simple Linear Interface Calculation) algorithm developed by Noh [4.23]. Within SLIC, the location of an interface is tracked separately in each coordinate direction. In other words, the position of the interface in a given direction is determined using the (filled/empty) status of the neighboring cell in that direction. Consequently, the representation of the same interface generally appears to be different in different coordinate directions.

As mentioned above, a multi-material Euler processor was used to represent the sandy gravel. In addition, Lagrange processor is used to represent the tooling used in the simulation of sandy-gravel mechanical tests. For example, the initial volume fraction of the gravel f_{gravel} (needed to complete the parameterization of the CU-ARL sandy-gravel equation of state) was determined using a balanced three-dimensional compression test. A schematic of this test is given in Figure 4-3(a). A set of dies in the form of flat platens are used in this test to carry out the compression of sandy gravel. The dies are modeled as Lagrange parts made of tool steel. The interaction between the Euler and the Lagrange parts/domains is done as follows: (a) The Lagrange part occupying a position of the Euler domain prevents sandy gravel from residing in the same region, while the material within Euler region which is in contact with a Lagrange part provides pressure boundary conditions to such a part. No interactions between the Lagrange parts were considered so that the balanced three- dimensional compression test can be carried out using constant–size platens. Furthermore, to prevent merging/coalescence of the contacting gravel

particles, each particle is filled with a "*different*" gravel material, while the properties of different gravel materials are kept identical.

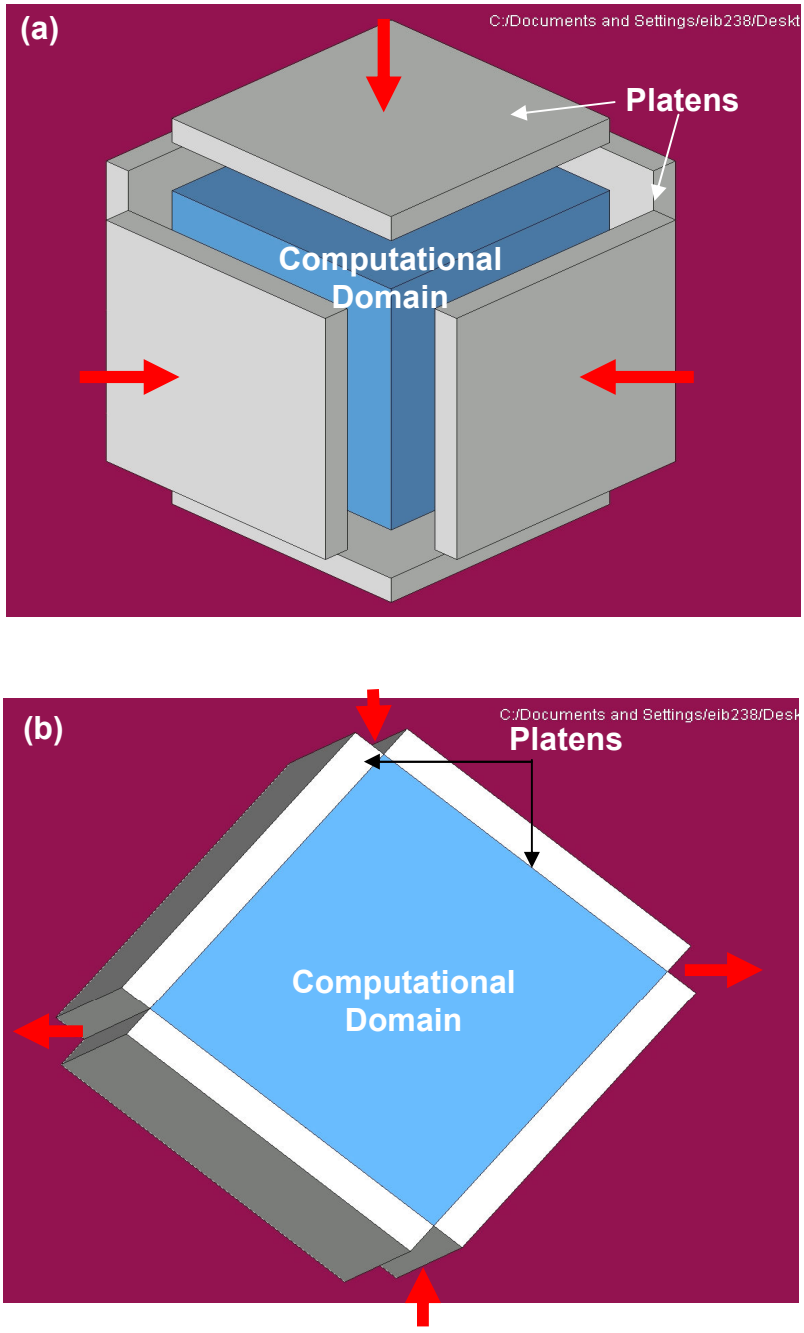

Figure 4-3. (a) Schematics of the computational domain including tooling for pure Hydrostatic compression loading; (b) Pure-shear loading and (c) Pure-hydrostatic tensile loading

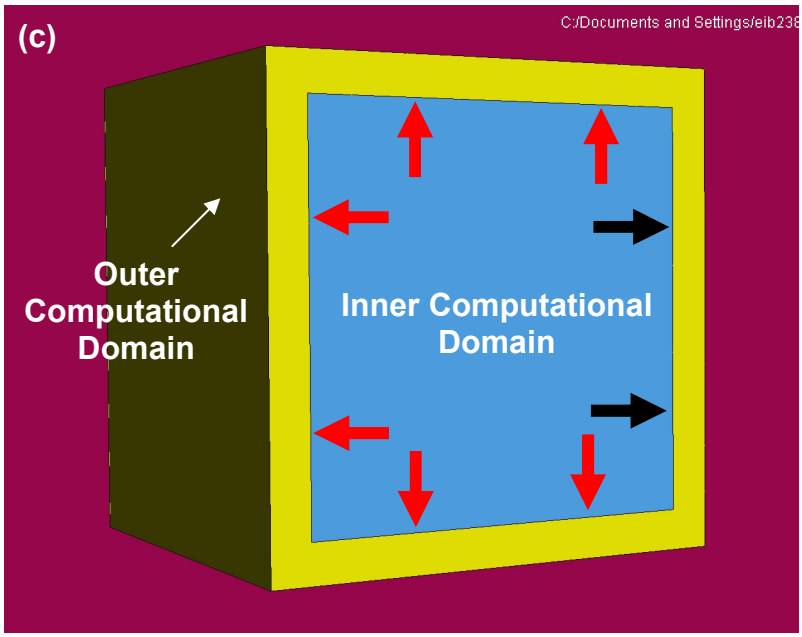

Figure 4-3. Contd…

4.5.1. Parameterization of the CU-ARL Sandy-gravel Equation of State

As mentioned earlier, to complete the parameterization of the CU-ARL sandy gravel equation of state, the initial volume fraction of gravel must be computed. This was done by using a simulated balanced three-dimensional compression test, Figure 4-3(a). The procedure used to fill the Euler computational domain with a sand matrix and gravel particles is described below. To obtain the values of the pressure and density during the test the following procedure is used: (a) pressure is obtained as an average pressure over the surfaces of the platens, while; (b) the associated density is obtained by dividing the total material mass residing in the Euler domain by the current volume occupied by this material.

The procedure used to fill the Euler computational domain with the sand and gravel particles as well as a self-consistent procedure used to determine the initial volume fraction of gravel are presented in the remainder of this section. The procedures were carried out using the following steps:

(a) At the onset, the maximum sand particle size is selected and the corresponding cumulative mass-percent pass read from the sieving curve given in Figure 4-1 (the solid line);

(b). The mass-percent pass obtained in (a) is divided by 100 and divided by the density of sand (ρ_{sand}=1674kg/m^3) while the mass percent not passed is divided by 100 and by the density of gravel (ρ_{gravel}=2100kg/m^3). The resulting (specific) volumes of sand and gravel were next used to compute the corresponding volume fraction of sand (1-f_{gravel}) and gravel f_{gravel}.

(c) The sieving curve displayed in Figure 4-1 (the solid line) is next truncated at its left side to remove the sand part and the remaining curve converted into a cumulative distribution histogram consisting of ten (on the logarithmic scale) equal-width bins, as shown in Figure 4-4(a);

(d) The cumulative mass-percent pass histogram obtained in (c) is then used to construct the mass percent gravel particle size histogram (i.e. the mass percent of gravel particles in each size range), Figure 4-4(b);

(e) The histogram obtained in (d) is then used to construct a gravel particle number fraction vs. gravel particle size histogram (i.e. the number fraction of gravel particles in each size range). An example of this histogram is displayed in Figure 4-5(a);

(f) The histogram obtained in (e) is then used to construct the corresponding cumulative particle-size distribution histogram, Figure 4-5(b);

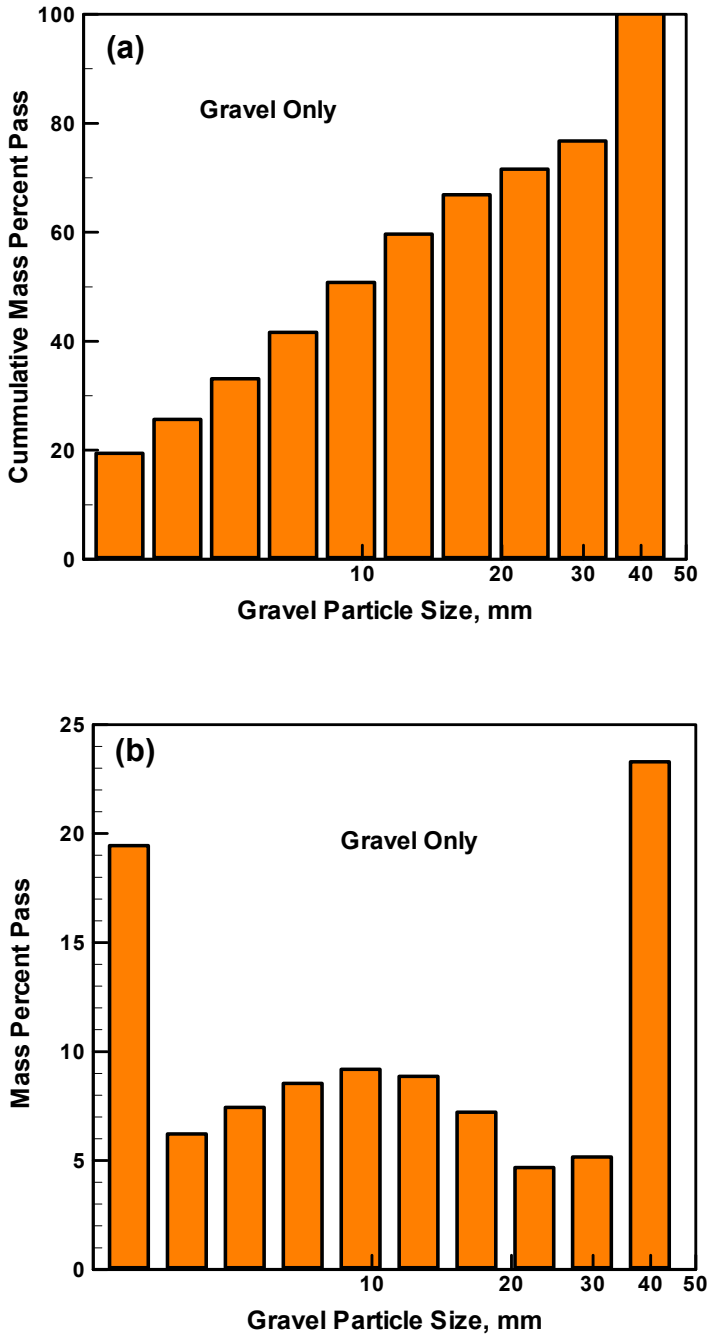

Figure 4-4. (a) Mass-fraction Pass Cumulative Distribution Function for Gravel in the CU-ARL Sandy-gravel Model and (b) Mass-fraction Pass Probability Distribution Function corresponding to (a)

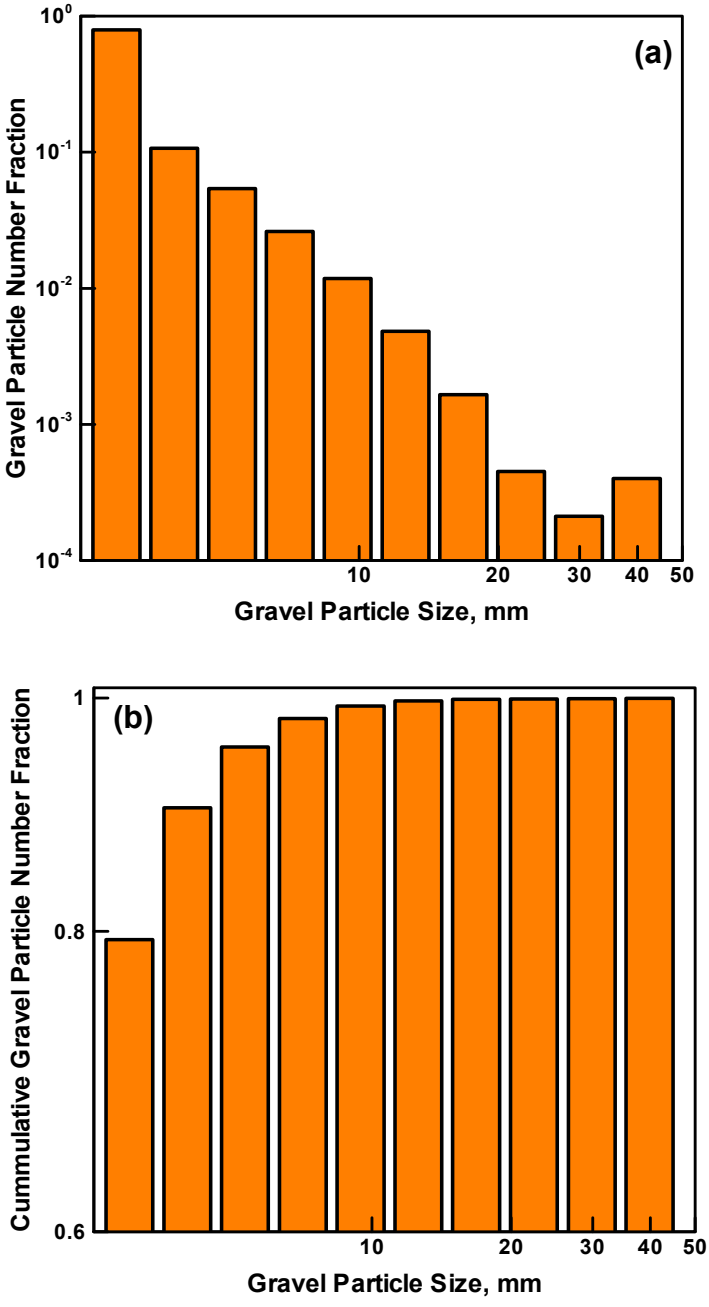

Figure 4-5. (a) Particle Number Density Distribution Function for Gravel in the CU-ARL Sandy-Gravel Model and (b) the corresponding Particle Number Density Cumulative Distribution Function

(g) The histogram obtained in (f) is then used to statistically populate the multi-material Euler computational domain (containing a sand matrix) with gravel particles. This procedure is explained later in this section. The exploded view of a small material element of the resulting multi-material Euler computational domain is displayed in Figure 4-6;

(h) The computational domain is then subjected to a pure-hydrostatic stress state by applying constant inward normal velocities to the platens, Figure 4-3(a) to obtain a second P vs. ρ relationship;

(i) A comparison of the P vs. ρ relationship obtained in (b) and (h) is then used to compute the corresponding sum of squares of the differences between the two relationships;

(j) The procedure is then repeated starting from step (a) using a number of f_{gravel} values and the sum of squares of the difference defined in (i) is computed for each case. The optimum value of f_{gravel} is then defined as the value of the volume fraction for which this sum is minimal; and

(k) The procedure defined in (a)-(j) yielded f_{gravel} = 0.347 for dry sand and f_{gravel}=0.311 for saturated sand. Since the difference between these two is relatively small (~10%), an average value of f_{gravel} =0.33 is assumed, for the subsequent development of the CU-ARL sandy gravel material model as discussed in the following sections.

The procedure used to construct and statistically populate the multi-material Euler computational domain was carried out using the following steps:

(a) At the beginning of the procedure, an edge length of the cube-shaped computational domain is selected. Typically a value of L=40mm is used;

(b) Since the volume fraction of sand, $f_{sand}=1-f_{gravel}$, is known, the computational-domain volume to be occupied by gravel is computed as $f_{gravel}L^3$;

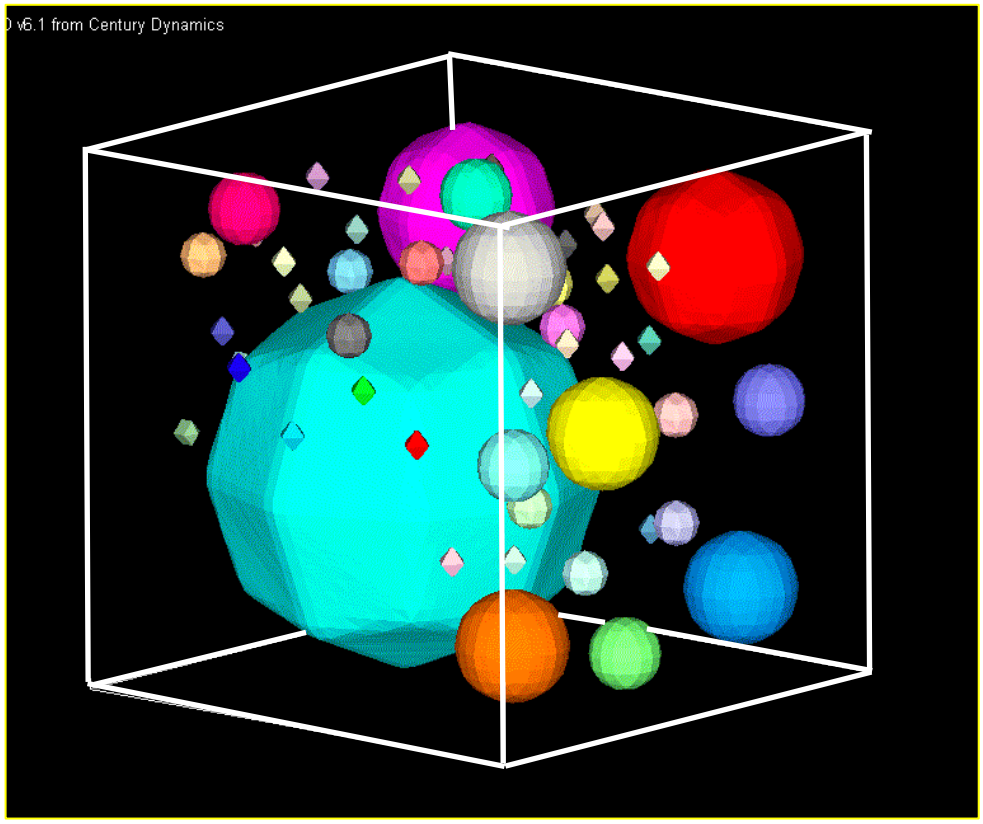

Figure 4-6. Exploded View of a Small Material Element of Sandy-gravel. Please note that the sand matrix is not shown and that the gravel particles are filled with different colors for clarity

(c) A simple gravel-particle sampling procedure is initiated in order to populate the computational domain with the gravel particles. This was done by dividing the 0-1 number range into ten intervals where the dividing number values correspond to the cumulative particle number density values displayed in Figure 4-5(b);

(d) A series of random numbers in the range 0-1 is next generated (one at a time) and the value of the random number is used to select the gravel particle size. For example, if the random number falls in the range N_1 and N_2, where N_1 and N_2 define the boundaries of a cumulative

particle size distribution bin as shown in Figure 4-5(b), then a gravel particle with a diameter equal to the mean diameter of the particles in this bin is used. Once a gravel particle is selected it is placed in the computational domain while ensuring that there is no overlap with other gravel particles already placed in the domain. Typically 410-440 gravel particles would have to be placed in the domain;

(e) Every time a gravel particle is selected, its volume is subtracted from the total remaining volume allotted to the gravel particles in the computational domain; and

(f) The steps (b)-(e) are repeated until the volume of the gravel particles in the computational domain equals the total allowable volume of the gravel particles in the computational domain dictated by the gravel particle volume fraction. A small material region of the resulting computational domain is shown in Figure 4-6. It should be noted that the sand matrix is removed and that particle center-to-center distances have been increased to improve clarity of the image displayed in Figure 4-6.

An example of the results obtained in this section is displayed in Figure 4-7, which shows the evolution of the value of the initial volume fraction of gravel with iteration number.

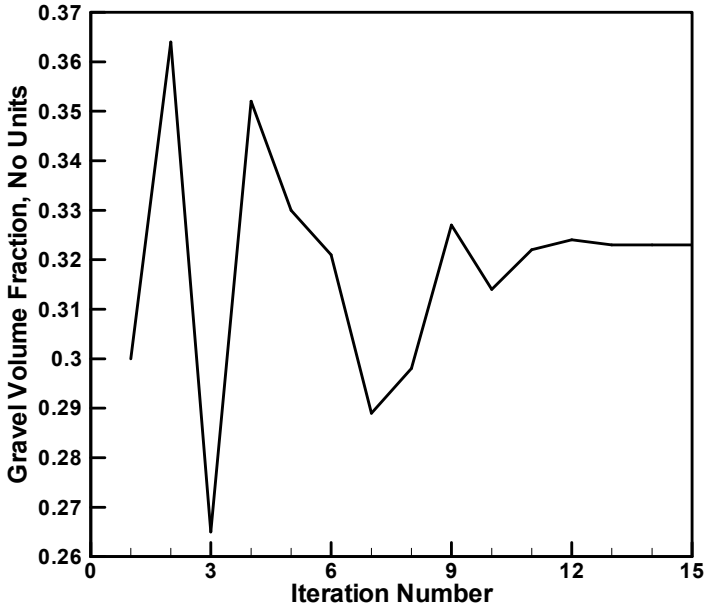

Figure 4-7. A Typical Evolution of the Initial Volume Fraction with Iteration Number

4.5.2. Parameterization of the CU-ARL Sandy-gravel Strength Model

To completely parameterize the CU-ARL: sandy-gravel strength model, the value of the strength parameter, C_{yield}, Eq. (4-15), has to be determined. Toward that end, the same Euler computational domain described in Section 4.4.1 is used and subjected to a pure shear test, Figure 4-3(b). Within such a test, two sets of parallel platens, one on the opposite side of the domain, are pinned at their contact points. The pins are then assigned appropriate velocities to create a balanced compression/tension loading (which produces a pure-shear mode of deformation). It should be noted that in order to ensure that no material leaves the Euler computational domain during the pure-shear test, the two sets of platens are set to lie completely within the original Euler domain. The third set of platens was removed and instead, no-flow boundary conditions were applied to the Euler domain in the respective direction. Furthermore, the sand and gravel

residing outside the region surrounded by the platens were removed so that only forces of interaction between the platens and the enclosed materials would be recorded in the computational analysis. To determine the strength parameter, a series of loading/unloading analysis was carried out and the first instance at which an irreversible shape change has occurred denoted as the moment of yielding. The corresponding yield stress is then computed as $\sigma_y=\sqrt{3}\sigma_n$ where σ_n is the average normal stress acting on the four platens in question. The C_{yield} parameter is then computed from the ratio of the yield stress of sandy gravel and sand.

The procedure described above is repeated for five dry sand and five saturated sand computational domains each containing the same (f_{gravel}=0.33) volume fraction of gravel but with different gravel-particle sizes and locations. The procedure yielded an average value of C_{yield} = 1.23 ± 0.11, where the number following the ± symbol represents one standard deviation.

4.5.3. Parameterization of the CU-ARL Sandy-gravel Failure Model

To complete the parameterization of the CU-ARL sandy gravel model, the third remaining parameter, the fracture parameter, C_{fail}, has to be determined. Again the same Euler computational domain was used but the boundary conditions have been changed in order to apply negative pressure, which is required in the present case.. This turned out to be not an easy task since the boundary conditions can be applied to the external boundaries of an Euler domain and not on the material residing on such boundaries. To overcome this challenge the following procedure was used:

(a) First, a larger cube-shaped Euler domain was created and its central cubic region (of size equal to the Euler domain used in Section 4.4.1 and 4.4.2) filled in the same way as the latter domains;

(b) Since under negative pressure, the linear purely-elastic equation of state ($P=K(\rho/\rho_{ref}-1)$, where K is the bulk modulus and the subscript *ref* represents the reference zero-overpressure quantity) can be used, the initial densities of the two materials (sand and gravel) are increased so that the initial overpressure in both is equal to 500MPa. The peripheral region of the total Euler domain is filled with void material with a zero-overpressure;

(c) Flow-out boundary conditions are applied to all the boundaries of the (outer) computational domain;

(d) A small octahedron-shaped Lagrange part was placed into the very center of the Euler domain. The three axes of the Lagrange part are each set normal to the one of the pair of faces of the Euler domain. The purpose of introducing the Lagrange part was to create a small geometrical perturbation in the sand which would promote fracture. Several sizes of the Lagrange part were explored and within the size range examined no statistically-significant effect of the Lagrange-part size was observed;

(e) The higher pressure in the inner portion of the Euler domain causes the material to flow outward and in the process to reduce density/pressure. When such a pressure drop becomes large enough, a crack nucleates and begins to grow from the lateral surfaces of the octahedron-shaped part. The growth of the crack is quite fast and failure occurs almost instantly. The difference between the pressure at which the crack nucleates and the initial pressure is then defined as the negative failure pressure. The difference in the failure pressure of sand and of sandy gravel is then used to estimate the failure parameter, C_{fail}.

The procedure described above is repeated for five dry sand and five saturated sand computational domains each containing the same (f_{gravel}=0.33) volume fraction of gravel but with different gravel-particle sizes and locations. The procedure yielded a value of C_{fail}= 1.18 ± 0.13.

4.5.4. Parameterization of the CU-ARL Sandy-gravel Material Model

The procedures described in Sections 4.5.1-4.5.3, resulted in the average value of the three parameters which were needed to complete the parameterization of the CU-ARL sandy-gravel model. Thus the parameterization of the model is now complete and can be summarized, as is done in Table 4-1.

To obtain a clearer insight into the CU-ARL sandy gravel material model, the key relations are plotted in Figures 4-8- 4-10 for the cases of dry and fully–saturated sand matrices.

The results pertaining to the equation of state are depicted in Figure 4-8(a)-(c), the ones pertaining to the strength model are depicted in Figures 4-9(a)-(b), while the one associated with the failure model is shown in Figure 4-10. The results displayed in the figures can be readily rationalized. For example, in Figure 4-8(a) the presence of water in saturated sand changes the pressure vs. density relationship into two basic aspects: (a) the initial density is increased, since water replaces air in the inter-particle spaces and the inability of water to be squeezed out under high deformation-rate conditions eliminates the initial plastic compaction of the sand matrix. The remaining results in Figures 4-8(b), 4-9(a)-(b) and 4-10 can be explained in a similar fashion.

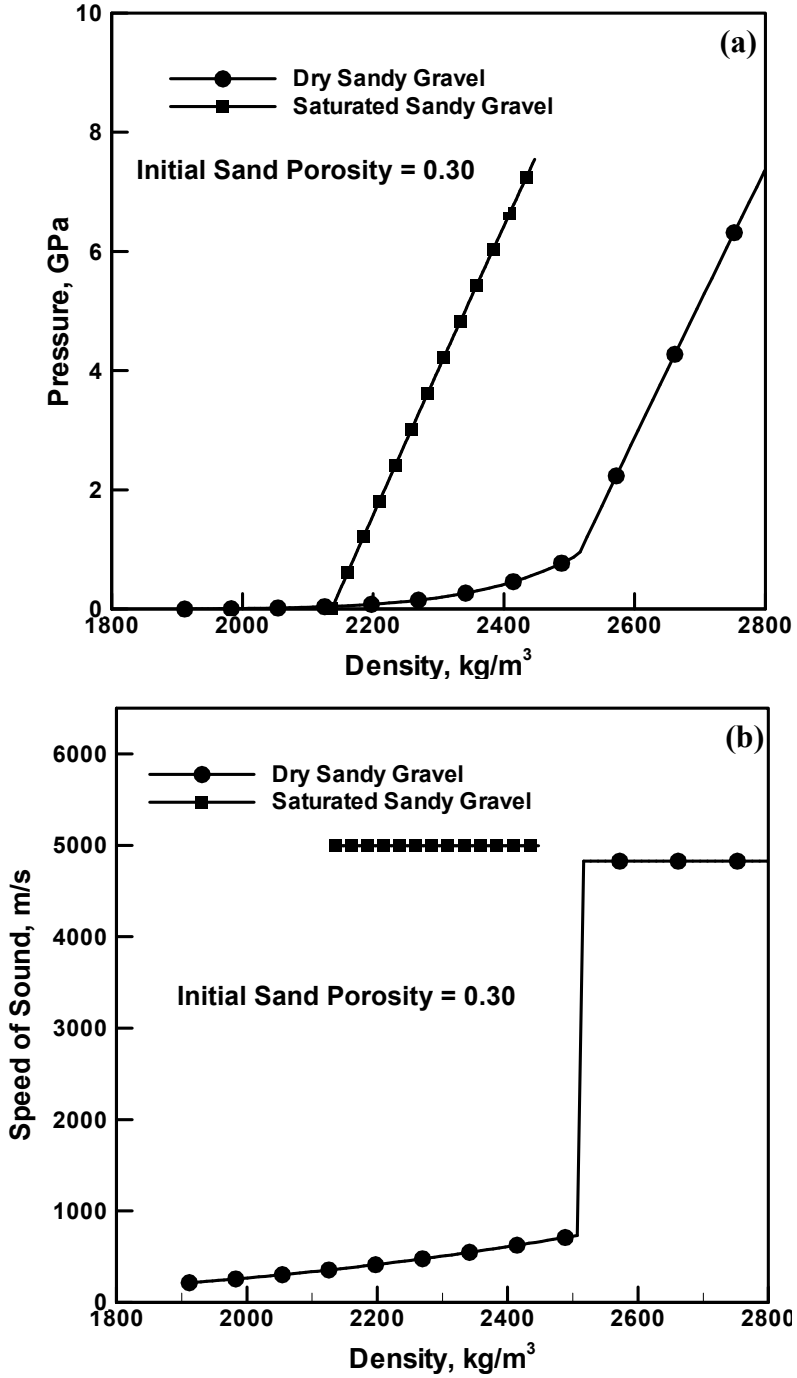

Figure 4-8. (a) Pressure vs. Density; (b) Speed of Sound vs. Density; and (c) Slope of the Shock Speed vs. Particle Speed Line vs. Saturation Ratio for the CU-ARL Sandy-gravel Model in Dry and Fully Saturated Conditions

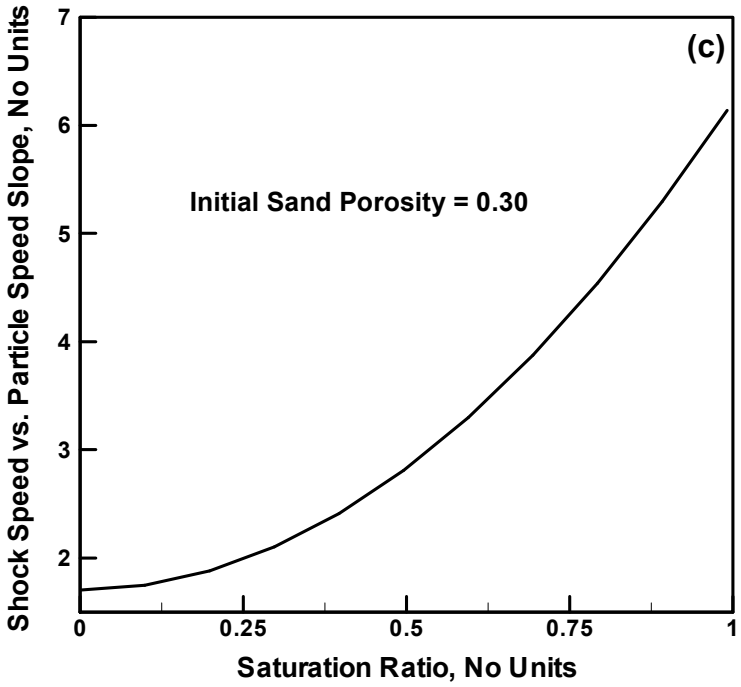

Figure 4-8. Contd…

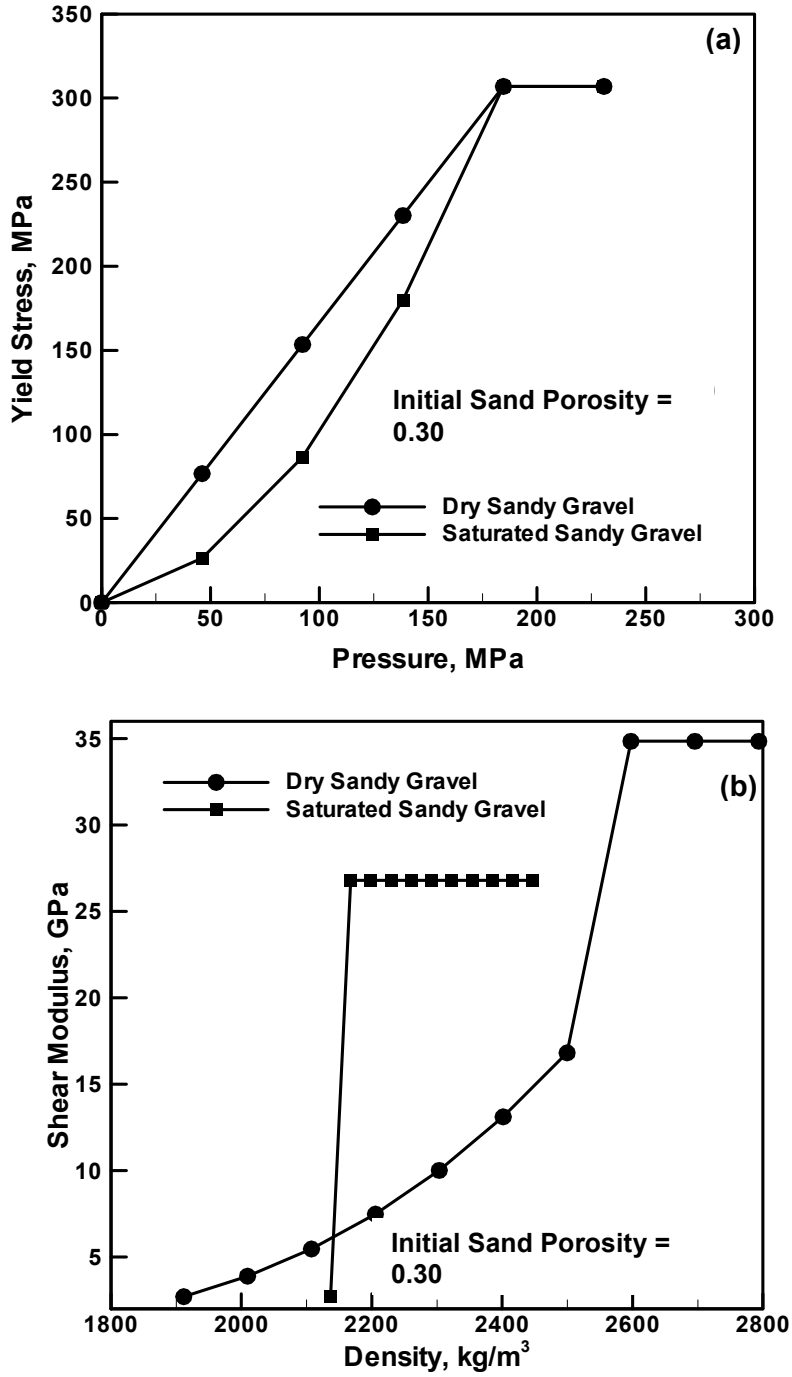

Figure 4-9. (a) Yield Strength vs. Pressure and (b) Shear Modulus vs. Density Relation for the CU-ARL Sandy-gravel Model in Dry and Fully Saturated Conditions

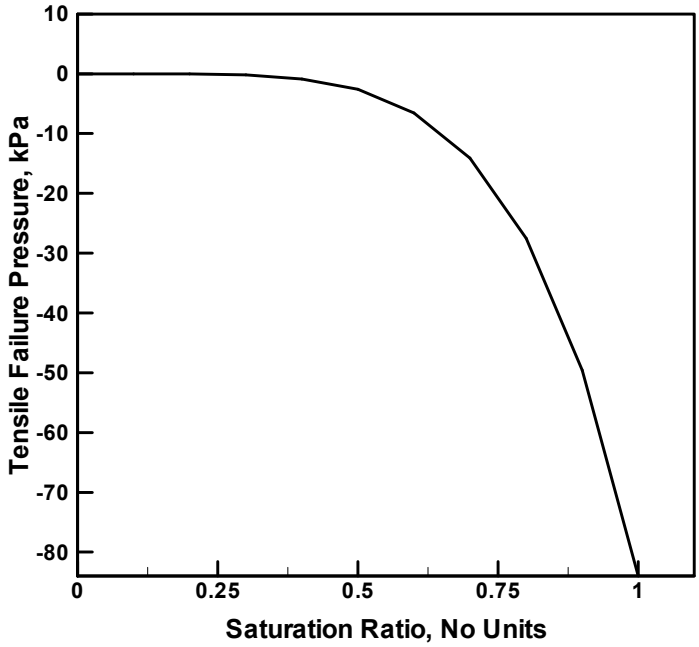

Figure 4-10. Variation of the Tensile Failure Pressure with Saturation Ratio for the CU-ARL Sandy-gravel Model

Table 4-1. Parameters in the CU-ARL Sandy-gravel Material Model

Parameter	Symbol	Unit	Value	Equation Where First Appears
Equation of State				
Density of Full Compaction at Zero Pressure for Dry Sand	ρ_{ref}	g/cm^3	2641	4.6(a)
Initial Volume Fraction of Gravel	f_{gravel}	N/A	0.33 ± 0.034	-
Strength Model				
Dry Sand Yield Strength to Pressure Proportionality Coefficient	ϕ_{dry}	N/A	1.3732	4.7
Mohr-Coulomb Pressure	P_{MC}	kPa	$1.864.10^5$	4.7
Saturated Sand Minimum Yield Strength to Pressure Proportionality Coefficient	ϕ_{sat}	N/A	0.1	4.9
Compacted Dry Sand Shear Modulus	G_{bulk}	kPa	$3.734.10^7$	4.12
Gravel Yield Coefficient	C_{yield}	N/A	1.23 ± 0.11	4.15
Failure Model				
Gravel Failure Coefficient	C_{fail}	N/A	1.18 ± 0.13	-
Erosion Model				
Instantaneous Geometric Strain	-	N/A	1.0	-

4.5.5. Experimental Validation of the CU-ARL Sandy-gravel Model

It should be noted that in a series of our previous studies [4.24-4.26], the CU-ARL sand material model was validated experimentally by comparing its predictions against a number of field-investigations dealing with the detonation of shallow-buried mines. However, no experimental validation of the CU-ARL sandy gravel model has been carried out so far. Such validation is expected to be carried out in the spring of 2008 at the Texas A&M University under a separate project funded by the Army Research Laboratory, Aberdeen, Proving Ground, MD. In the remainder of this section, a brief description is provided of the tests which will be conducted in the planned experimental validation work.

To validate the CU-ARL sandy gravel equation of state both P *vs.* ρ and C_0 *vs.* ρ relations (at different saturation levels of sand matrix) have to be determined. P *vs.* ρ relations will be obtained using constrained uniaxial compaction tests in which the material is placed into a rigid compaction mold and the piston is driven into the mold causing the material to compact [4.27]. The values of pressure and density can be readily obtained by monitoring the load required to advance the piston and the piston displacement. To ensure that a "*high deformation rate*" material response is obtained in the case of a material containing moisture, the material being tested must be enclosed within a polyethylene case to prevent water drainage during the test.

To obtain C_0 *vs.* ρ relationships, a flyer-plate impact test will be carried out using material samples at different levels of compaction and water saturation [4.13]. Within such a test, the granular material being tested is contained between two parallel disc-shaped anvils (typically made of Polymethyl-Methacrylate, PMMA) and surrounded by an aluminum annulus. The flyer-plate is also made up of PMMA and has the same shape as the target anvils. At least two manganin piezoelectric gages are needed to monitor the propagation of the pressure wave. One

of these gages is located at the flyer-plate/front-anvil interface while the other at the sandy gravel/rear-anvil interface. By recording the time of arrival of pressure pulse at these two locations and using the known thickness of the sample and the speed of propagation of sound in the two anvils, the speed of sound propagation in the sandy gravel sample can be determined.

To validate the CU-ARL strength model both the σ_y *vs.* P and the G *vs.* ρ relations (at different levels of water-saturation) must be determined. These will be obtained using *"unconstrained"* uniaxial compression tests in the presence of a surrounding hydrostatic stress. The material sample to be tested will be enclosed in a rubber membrane and subjected to a confining fluid pressure while being loaded axially till failure. As in the case of the equation of state, it is critical that no water drainage takes place in order to mimic the loading conditions encountered during impact loading. If the test described is carried out using material with different levels of pre-compaction and the initial load vs. displacement curve recorded, the G *vs.* ρ relationship can be easily determined (using the corresponding K *vs.* ρ data from the tests used to validate the equation of state).

To validate the CU-ARL sandy gravel failure model, the negative failure pressure must be determined at different levels of saturation of the sand matrix. This will be done using the so-called "*direct tension*" experiment [4.28]. Within this experiment, a "*bow-tie*" shaped sandy gravel sample confined within a mating two-part anvil set up is used. Load is applied in small increments to the parallel ends of the sample in opposite directions until failure occurs. The failure pressure is then obtained from the failure load and the fracture surface area. To ensure that the effect of moisture is retained, the sample will be enclosed in a thin-wall polyethylene casing.

4.6. Summary and Conclusions

Based on the results obtained in the present work, the following main summary remarks and conclusions can be drawn:

1. One of the existing high deformation-rate, large-deformation, high-pressure material models for sand (which includes the effect of moisture) has been expanded to incorporate the effects of gravel particles and to obtain the material model for STANAG 4569 sandy gravel.

2. To parameterize the resulting sandy-gravel material model, a series of computational analyses were carried out in order to simulate the response of this material under simple mechanical tests. While such analyses are not a complete substitute for the experimental validation, they could significantly reduce the effort and the extent of experimental work required.

3. Since no experimental data pertaining to the mechanical response of the STANAG 4569 sandy gravel could be found in the open literature, the tests, needed to validate the model proposed in the present work, have been suggested and briefly described. These tests will be conducted in a follow-up work.

4.7. References

4.1 STANAG 4569- *Protection Levels for Occupants of Logistics and Light Armored Vehicles*.

4.2 M. Grujicic, B. Pandurangan, B. A. Cheeseman, W. N. Roy, R. R. Skaggs and R. Gupta, "*Parameterization of the Porous-Material Model for Sand with Various Degrees of Water Saturation*," Soil Dynamics and Earthquake Engineering, accepted for publication, April 2007.

4.3 Z. Wang, H. Hao and Y. Lu, "*A Three-phase Soil Model for Simulating Stress Wave Propagation due to Blast Loading*," International Journal for Numerical and Analytical Methods in Geomechanics, 28, 2004, 33-56.

4.4 Z. Wang and Y. Lu, "*Numerical Analysis on Dynamic Deformation Mechanisms of Soils under Blast Loading*," Soil Dynamics and Earthquake Engineering, 23, 2003, 705-714.

4.5 B. Loret, N. Khalili, *"A Three-phase Model for Unsaturated Soils,"* International Journal for Numerical and Analytical Methods in Geomechanics, 24, 2000, 893-927.

4.6 J. Henrych, *"The Dynamics of Explosion and Its Use*,*"* Chapter 5, Elsevier Publications, New York, USA, 1979.

4.7 D. C. Drucker and W. Prager, "*Soil Mechanics and Plastic Analysis or Limit Design*," Quarterly of Applied Mathematics, 10, 1952, 157-165.

4.8 P. Laine and A. Sandvik, "*Derivation of Mechanical Properties for Sand*," Proceedings of the 4th Asia-Pacific Conference on Shock and Impact Loads on Structures, CI-Premier PTE LTD, Singapore, November 2001, 361-368.

4.9 M. Grujicic, B. Pandurangan and B. Cheeseman, "*A Computational Analysis of Detonation of Buried Mines,*" Multidiscipline Modeling in Materials and Structures, 2, 2006, 363-387.

4.10 M. Grujicic, B. Pandurangan, B. A. Cheeseman, W. N. Roy and R. R. Skaggs, "*Impulse Loading Resulting from Shallow Buried Explosives in Water-saturated Sand*," Journal of Materials: Design and Applications, accepted for publication, 220, 2006, 1-15.

4.11 M. Grujicic, B. Pandurangan, B. A. Cheeseman and W. N. Roy, "*Application of the Modified Compaction Material Model to Soil with Various Degrees of Water Saturation*," Shock and Vibration, 14, 2007, 1-15.

4.12 A. M. Bragov, A. K. Lomunov, I. V. Sergeichev, K. Tsembelis and W. G. Proud, "*The Determination of Physicomechanical Properties of Soft Soils from Medium to High Strain Rates*," in process of submission, November 2005.

4.13 D. J. Chapman, K. Tsembelis and W.G. Proud, "*The Behavior of Water Saturated Sand under Shock-loading,*" Proceedings of the 2006 SEM Annual Conference and Exposition on Experimental and Applied Mechanics, 2, 2006, 834-840.

4.14 M. Grujicic, B. Pandurangan and B. Cheeseman, *"The Effect of Degree of Saturation of Sand on Detonation Phenomena Associated with Shallow-buried and Ground-laid Mines*,*"* Journal of Shock and Vibration, 13, 2006, 41-61.

4.15 M. Grujicic, B. Pandurangan, N. Coutris, B. A. Cheeseman, W. N. Roy and R. R. Skaggs, "*Derivation and Validation of a material model for clayey sand for Use in Landmine Detonation Computational Analysis*," Multidiscipline Modeling in Materials and Structures, accepted for publication, May 2007.

4.16 R. J. Fragaszy, "*Modeling Strength of Sandy Gravel*," Journal of Geotechnical Engineering, 118, 6, 1992, 920-935.

4.17 AUTODYN-2D and 3D*, Version 6.1*, *User Documentation*, Century Dynamics Inc., 2006.

4.18 S. Stein and T. Kim, "*Effect of Moisture on Attraction Force on Beach Sand,*" Marine Geosources and Geotechnology, 22, 2004, 33-47.

4.19 R. W. Day, "*Discussion of Modeling Strength of Sandy Gravel*," Journal of Geotechnical Engineering, 119, 11, 1993, 1858.

4.20 M. F. Ashby, *Material Selection in Mechanical Design*, 3rd Edition, Butterworth-Heinemann, 2005.

4.21 B. O. Hardin and M. E. Kalinski, *"Estimating the Shear Modulus of Gravelly Soils*" Journal Of Geotechnical And Geoenvironmental Engineering, 131, 2005, 868-880.

4.22 D. L. Youngs, "*Time-dependent Multimaterial Flow with Large Fluid Distortion*," in *Numerical Methods for Fluid Dynamics*, K. W. Morton and M. J. Baines (editors), Academic Press, 1982.

4.23 W. F. Noh, "*A Time-dependent Two-space-dimensional Coupled Eulerian-Lagrange Code*," Methods in Computational Physics, 3, 1962, 117-179.

4.24 M. Grujicic, B. Pandurangan and B. A. Cheeseman, " *The Effect of Degree of Saturation of Sand on Detonation Phenomena Associated with Shallow-buried and Ground-laid mines*," Shock and Vibration, 13, pp. 41-62, 2006.

4.25 M. Grujicic, B. Pandurangan, I. Haque, B. A. Cheeseman and R. R. Skaggs, *" A Computational Analysis of Mine Blast Survivability of a Commercial Vehicle Structure ,"* Multidiscipline Modeling in Materials and Structures, accepted for publication, February 2007.

4.26 M. Grujicic, B. Pandurangan, G. M. Mocko, B. A. Cheeseman, and R. R. Skaggs, "*A Combined Multi-material Euler/Lagrange Computational Analysis of Blast Loading Resulting from Detonation of Buried Landmines*," Multidiscipline Modeling in Materials and Structures, accepted for publication, March 2007.

4.27 Y. M. Tien, P. L. Wu, W. S. Chuang and L. H. Wu, "*Micromechanical Model for Compaction Characteristics of Bentonite-Sand Mixtures*," Applied Clay Science, 26, 489-498, 2004.

CHAPTER 5

DERIVATION, PARAMETERIZATION AND VALIDATION OF A SANDY-CLAY MATERIAL MODEL FOR USE IN LANDMINE DETONATION COMPUTATIONAL ANALYSES

5.1. Abstract

A set of large-strain/high-deformation-rate/high-pressure material models for sand-based soils with different saturation levels and clay and gravel contents recently proposed and validated in our work [5.1-5.3], has been extended in the present work to include clay-based soils of different saturation levels and sand contents. The model includes an equation of state which reveals the material response under hydrostatic pressure, a strength model which captures material elastic-plastic response under shear and a failure model which defines the laws and conditions for the initiation and evolution of damage and ultimate failure of the material under negative pressure and/or shear. The model was first parameterized using various open-literature experimental results and property correlation analyses and, then, validated by comparing the computational results obtained in an ANSYS/Autodyn based [5.4] transient non-linear dynamics analysis of detonation of a landmine buried in sandy-clay with their experimental counterparts.

5.2. Introduction

It is nowadays widely recognized that, despite the signing of the Mine Ban Treaty in 1999, there is an ongoing landmine crisis. The following are some of the main aspects of this crisis: (a) in excess of 100 Million unexploded landmines remain deployed in over 60 countries all over the world [5.5]; (b) Nearly 30,000 civilians are killed or maimed every year by unintended detonations of the mines [5.6]; (c) the cost of medical treatment of landmine injuries

exceed 100 million per year [5.7]; (d) the ability of the international community to provide the humanitarian relief in terms of medical services, safe drinking water and food, etc., is greatly hampered by landmine contamination of the infrastructure in mine affected countries [5.7]; and so on. To address the aforementioned landmine crisis, the research community around the world has taken upon itself the challenge of helping better understand the key phenomena associated with landmine detonation and interaction between detonation products, mine fragments and soil ejecta with the targets (people, structures and vehicles). Such improved understanding will help automotive manufacturers to design and fabricate personnel carriers with higher landmine-detonation survivability characteristics and a larger level of protection for the onboard personnel. In addition, the manufacturer of demining equipment and personnel protection gear used in landmine clearing are expected to benefit from a better understanding of the landmine detonation-related phenomena.

A review of the public-domain literature carried out as a part of the present work revealed that the landmine detonation related research activities can be broadly divided into three main categories: (a) shock and blast wave mechanics/dynamics including landmine detonation phenomena and large-deformation/high-deformation rate constitutive models for the attendant materials (high explosive, air, soil, etc.); (b) the kinematic and structural response of the target to blast loading including the role of target design and use of blast attenuation materials; and (c) vulnerability of human beings to post-detonation phenomena such as high blast pressures, spall fragments and large vertical and lateral accelerations. The present work falls primarily into the category (a) of the research listed above since it emphasizes the development of a large-deformation/high-deformation-rate/high-pressure material model for clay-based soil at different saturation levels and sand contents. It is generally recognized that the properties of soil, into which a landmine is buried, play an important role in the overall effectiveness/lethality of the

landmine regardless of the nature of its deployment (fully-buried, flush-buried or ground-laid). It should further be recognized that the present work, primarily within its material-model validation stage, also addresses briefly the category (b) of the landmine detonation related research.

While there are a variety of soils, it is customary to divide all soils in two main categories: (a) *Cohesion-less soils* (e.g. sand) which consist of relatively coarse particles (average particle size 0.2-2mm) which have a negligible tensile strength and derive their shear strength primarily from the inter-particle friction; and (b) *Cohesive soils* (e.g. clay) which consist of fine particles (average particle size 10-50μm) which derive their strength and failure properties from the inter- and intra-particle electrostatic and polar forces. In the present work, the problem of material model derivation and validation for clay-based soils at various saturation levels and sand contents is addressed (referred to as *the sandy-clay soil* or *sandy clay*, in the remainder of this manuscript).

A review of the open-domain literature carried out as a part of the present work revealed that there exists an extensive body of work dealing with the investigation of the detonation of the buried charges. However, much of this work does not focus on the characterization of the blast output of landmines, but rather on cratering effects in soils, with applications towards the efficient utilization of explosives for excavation (i.e. canals, trenches, etc.) or in the survivability of structures subjected to near surface blasts [5.8]. Westine et al. [5.9] carried out experiments on a plate which was mounted above a buried charge comparable is size and power to an anti-tank landmine. The plate contained a number of through-the-thickness holes at incremental distances from the mine, in which, plugs of known mass were placed. The blast accompanying mine detonation caused the plugs to be ejected from the holes and from their initial velocity the impulsive loading on the plate was calculated. Morris [5.10] used the results of Westine et al. [5.9] to construct a design-for-survivability computer code for lightweight vehicles. More

recently, Bergeron et al. [5.11] carried out a comprehensive investigation of the buried landmine blasts using an instrumented ballistic pendulum. From these experiments, the pressure and impulse as a function of time were recorded at several locations in air directly above the mine as well as in the sand surrounding the landmine. In addition, X-ray radiography and high-speed photography were employed to investigate temporal evolution of the associated soil cratering and soil ejection phenomena.

In our recent computational work [5.12], based on the use of ANSYS/Autodyn, a general-purpose transient non-linear dynamics explicit simulation software [5.4], a detailed comparison was made between the experimental results of Bergeron et al. [5.13] and their computational counterparts for a number of detonation-related phenomena such as the temporal evolutions of the shape and size of the over-burden sand bubbles and of the detonation-products gas clouds, the temporal evolutions of the side-on pressures in the sand and in air, etc. It was found that the most critical factor hampering a better agreement between the experiment and computational analysis is an inadequacy of the current material model for sand to capture the dynamic response of this material under blast loading conditions. Hence, the main objective of our subsequent work was to improve the compaction material model proposed by Laine and Sandvik [5.14] implemented in ANSYS/Autodyn material database [5.4].

Soil is a very complicated material whose properties vary greatly with the presence/absence and relative amounts of various constituent materials (sand, clay, silt, gravel, etc.), and particle sizes and particle size distribution of the materials. In addition the moisture content, the extent of pre-compaction can profoundly affect the soil properties. The so-called *"porous–material/compaction"* model proposed by Laine and Sandvik [5.14] has been, for quite some time, the soil model which provided the best compromise between the inclusion of essential physical phenomena reflecting material response under dynamic loading and computational

simplicity. However, this model was developed essentially for dry sand and, as demonstrated by many researchers [e.g. 5.8, 5.11, 5.15], cannot account for the effects of moisture, clay and or gravel in soil. To overcome these deficiencies of the original porous-material/compaction model, Clemson University and the Army Research Laboratory (ARL), Aberdeen, Proving Ground, MD jointly developed [5.16] and subsequently parameterized (using the results of a detailed investigation of dynamic response of sand at different saturation levels, as carried out by researchers at the Cavendish Laboratory, Cambridge, UK [5.17, 5.18]) the new sand model [5.19]. This model was shown to be capable of capturing the effect of moisture on the dynamic behavior of sand and was named *the CU-ARL sand model*. In a subsequent work [5.2], Clemson University and the ARL developed the so-called *CU-ARL clayey sand model* to include the effect of minor (<15vol.%) additions of clay on the dynamic mechanical response of sand. In the latest publically-reported soil material-model development effort by Clemson University and the ARL, the effect of gravel in sand was accounted for (to comply with the STANAG 4569 material-model requirements [5.20]) and the resulting soil material model named the *CU-ARL sandy gravel* model [5.3].

In the present work, the aforementioned set of the CU-ARL material models for different types of soils is expanded to include the case of clay-based soils at different levels of saturation and various sand contents. Since this model was jointly developed by Clemson University and the ARL, it will be referred to, in the remainder of the document, as the *CU-ARL sandy-clay soil model*. As will be shown in the next section, the dynamic mechanical response of sandy-clay soils is significantly different than that of sand-based soils due to the interplay of a number of physico-chemical phenomena such as electrostatic bonding-enhanced inter-particle adhesion in clay, osmosis-based tendency of clay to absorb and retain water, water-absorption-induced swelling of clay, etc. It should also be noted that in our previous work [5.2], a material model for

sand-based soil containing less than ca. 15 vol.% clay (CU-ARL clayey sand model) was developed, while the model discussed in the present work (the CU-ARL sandy-clay model) pertains to the clay-based soil containing minor additions of sand. A comparison of the basic architecture of the two types of soil is displayed in Figures 5-1(a)-(b). In the case of clayey sand, displayed in Figure 5-1(a), coarser sand particles are coated with a layer of clay while in the case of sandy-clay, Figure 5-1(b), fine clay particles form a continuous matrix within which discrete sand particles are dispersed. In should be also noted that the terms "*sandy clay*" and "*clay-based soils*" have been used interchangeably throughout the manuscript.

The organization of this chapter is as follows. Morphology and microstructure of sand and clay at the atomic and particle/aggregate length scales are compared and contrasted in Sections 5.3.1 and 5.3.2, respectively. The effect of the identified morphological/microstructural differences on the differences in dynamic mechanical response of the two types of soils is discussed in Section 5.3.3. Derivation and parameterization of the CU-ARL sandy-clay material model are discussed in Section 5.3.4. The results of the model validation via comparison of the computational and experimental results for a number of scenarios involving landmine detonation in sand and clay and subsequent interactions of the detonation products, mine fragments and soil ejecta are presented and discussed in Section 5.4. A brief summary and the conclusions obtained in the present work are discussed in Section 5.5.

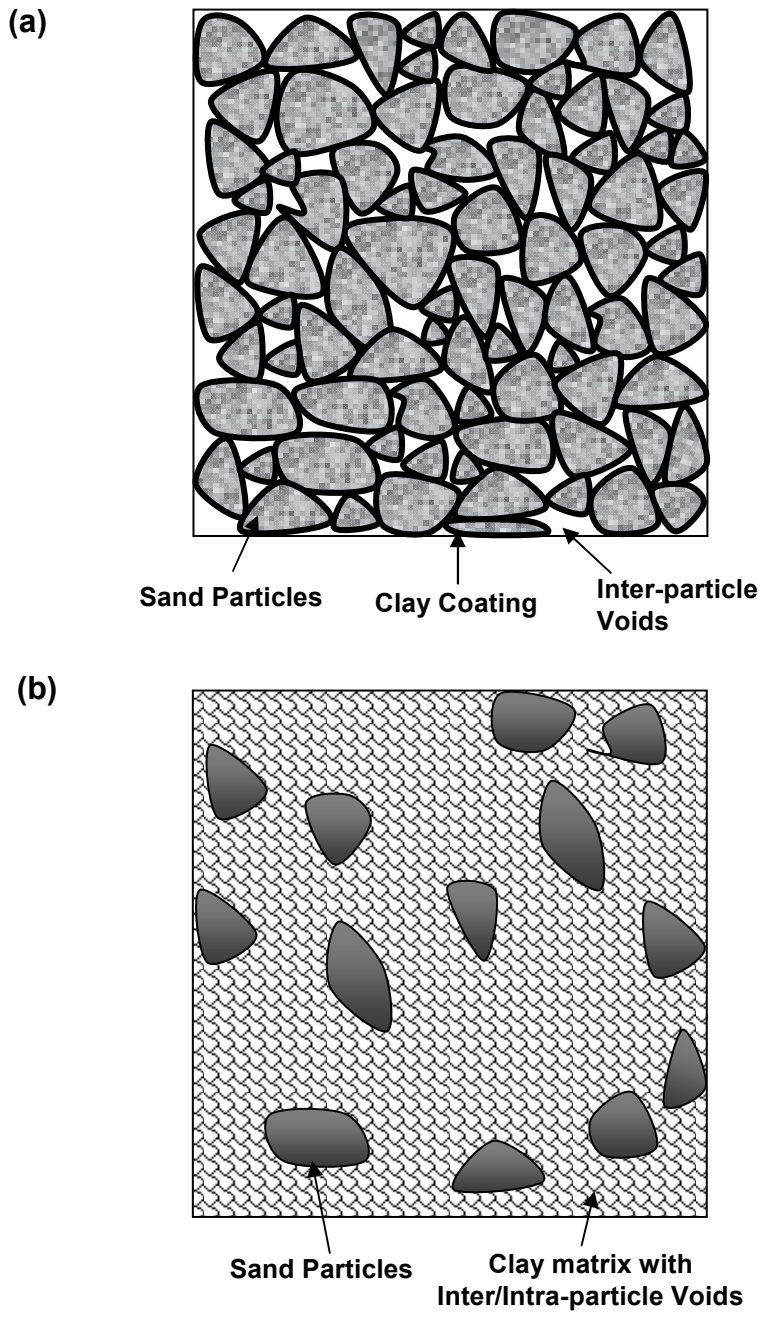

Figure 5-1. Basic Morphology of: (a) the CU-ARL Clayey Sand and (b) the CU-ARL Sandy Clay

5.3. Model Derivation and Computational Analysis

5.3.1. Atomic-level Microstructure and Morphology of Sand and Clay

As stated earlier, soils are generally classified into two groups: (a) those dominated by sand and (b) those consisting of major fractions of clay. While in both cases, the basic architecture of soil involves a skeleton of solid particles and interconnected spaces (voids) filled with air and/or water, significant differences exist in the microstructure of the two types of soil both at the atomic length-scale and the particle/aggregate-length scale. Among these differences the most important ones are outlined in the current and the following section.

In most cases, sand is based on silicon-dioxide (SiO_2). At the atomic length-scale, sand consists of silica-tetrahedrons (SiO_4^{4-}) typically arranged in the form of a quartz allotropic modification, Figure 5-2. Due to the covalent nature of its inter-atomic bonding and its compacted atomic microstructure, quartz behaves as an inert and quite hard material. Consequently, no water absorption by quartz takes place and no significant sand inter-particle adhesion exists.

In sharp contrast, the atomic-level microstructure of clay reveals that this material is composed of sheet-like silicate layers with a particular stacking sequence. In natural clay, this sequence involves a central layer consisting mainly of aluminum cations (and oxygen anions) sandwiched between two tetrahedral layers consisting of silicon cations and oxygen anions. Typically, some of the aluminum and silicon ions are replaced by lower valence ions such as Mg^{2+}, Ca^{2+}, Li^{+} etc. creating a negative charge imbalance in each of the 3-layer sheets. The charge imbalance is neutralized by adsorption of Na^{+}, Ca^{2+} and K^{+} cations which tend to have water molecules associated with them. The hydrated Na^{+}, Ca^{2+} and K^{+} cations residing in the

interlayer region make clay behave as a pliable material and, at higher water levels, cause the clay to swell.

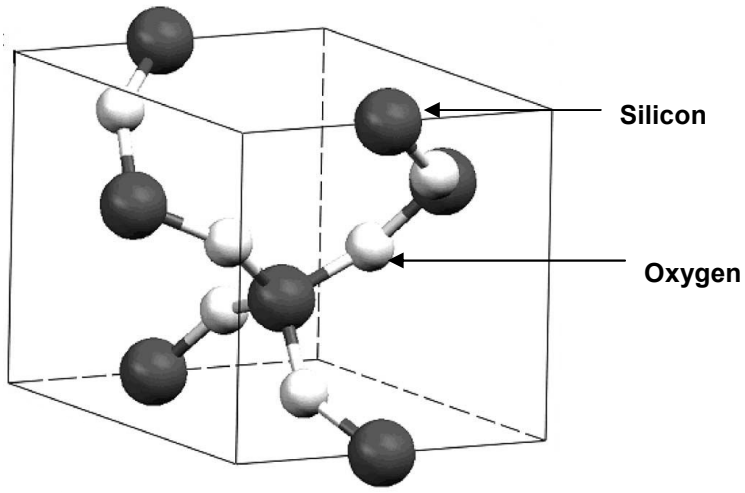

Figure 5-2. A schematic of the atomic-level microstructure of α-quartz

5.3.2. Particle/Aggregate-level Microstructure/Morphology of Sand and Clay

As stated in the previous section, the basic architecture of both sand and clay involves a skeleton of contacting particles and/or aggregates of particles separated by pores/voids. However, the particle/aggregate microstructure of the two types of soils is different in at least two major aspects: (a) Sand particles are typically coarse (average particle size ca. 0.2-2mm), homogeneous, quite rigid and brittle while, clay particles are finer (average particle size ca. 10-50μm) and contain stacks of three-layer sheets, are pliable and ductile; and (b) while air and water may reside in the inter-particle spaces in the case of both sand and clay, intra-particle moisture (moisture residing in the spaces separating adjacent sheets) is present exclusively in clay making it pliable and ductile even in an unsaturated condition. Also, it is the intra-particle water that is believed to be primarily responsible for clay swelling observed at larger saturation levels. This

finding is commonly explained as follows: In unsaturated clay, the exchangeable inter-layer cations are located on the surface of the layers or in the hexagonal holes of the tetrahedral sheets. In this state, the adjacent clay layers lie so close to each other that they are almost in contact. That is the inter-layer distances are quite small (approximately 1nm) and, hence, the negatively charged layers are held together very strongly to the inter-layer cations via ionic and van der Waals forces. After their hydration, the cations tend to position themselves half-way between the clay layers and this leads to the widening of spaces between the layers, i.e. to the swelling of clay. In sharp contrast, since water absorption into inter-particle spaces is mainly a physical phenomena based on capillary effects, sand swelling caused by water absorption is typically not significant.

The removal of intra-particle water generally requires drying/baking of clay resulting in a hard and brittle material containing multiple shrinkage-induced cracks. The behavior of dried/baked clay is not generally relevant in the computational analysis of a landmine detonation and is not considered in the present work

5.3.3. The Effect of Sand/Clay Microstructure on their Mechanical Behavior

Considering the aforementioned differences in the microstructure of sand and clay at the atomic and particle/aggregate length scales, one may anticipate differences in the behavior of these two types of soil when subjected to static and dynamic loading conditions. Among these differences, the main ones can be summarized as follows:

(a) In the case of sand, the strength is controlled by inter-particle friction and, hence, generally increases with an increase in confining pressure, till the point of full compaction. While the presence of moisture in sand reduces the- magnitude of the inter-particle friction coefficient, the strength remains dependent on the magnitude of confining pressure as the saturation-level is increased [5.1]. In sharp contrast, the magnitude of the inter-particle friction coefficient of clay is

generally found to be only weakly affected by the magnitude of confining pressure [5.21], while the saturation level still affects the magnitude of the strength of clay. The latter findings are explained as follows: Due to the relatively tight bonding of the intra-particle water, this water is quite immobile, causing the effective pore pressure to remain essentially constant as the confining pressure is increased. This in turn causes the strength of clay to be controlled by the shear strength of the intra-particle water bonded layers and thus to be less affected by the magnitude of confining pressure. As far as the effect of intra-particle water on clay strength is concerned, it is believed to be associated with the fact that the water molecules tend to orient their negative poles towards positively charged cations and the resulting shielding effect reduces the electrostatic attraction between the negatively-charged clay layers and the positively-charged inter-layer cations. Consequently, while moisture reduces the strength in both sand and clay, this effect is significantly more pronounced in the case of clay [5.21];

(b) Inter-particle cohesion in sand generally increases with an increase in the level of saturation which is attributed to the capillary affects associated with inter-particle voids. In sharp contrast, cohesive strength of clay is generally decreased as the level of saturation is increased, which is attributed to the intra-particle water absorption that leads to an increase in the inter-layer separation and a reduction of the inter-layer bonding strength; and

(c) Stress-rate sensitivity of the deformation behavior of sand and clay at different levels of saturation is also quite different. That is, the deformation of sand is generally believed to involve two main basic mechanisms [5.22-5.24]: (a) elastic deformations (at low pressure levels) and fracture (at high pressure levels) of the inter-particle bonds and (b) elastic and plastic deformations of the three constituent materials in the sand (sand particles, air and water). The relative contributions of these two deformation mechanisms as well as their behavior are affected primarily by the degree of saturation of sand and the deformation rate. Specifically, in dry sand

the first mechanism controls the sand deformation at low pressures while the second mechanism is dominant at high pressures and the effect of deformation rate is of a second order. In sharp contrast, in saturated sand very low inter-particle friction diminishes the role of the first deformation mechanism. On the other hand, the rate of deformation plays an important role. At low deformation rates, the water /air residing in the sand pores is squeezed out during deformation and, consequently, the deformation of the sand is controlled by the deformation of the solid mineral particles. At high pressures, on the other hand, water/air is trapped within the sand pores and the deformation of the sand is controlled by the deformation and the volume fractions of each of the three constituent phases.

The dynamic mechanical behavior of clay, on the other hand, is significantly less sensitive to the rate of deformation at any level of saturation. This behavior of clay is attributed to its ability to easily absorb and retain water within its intra-particles spaces. In other words, while at low deformation-rate conditions, the inter-particle water in clay can still be squeezed out, the intra-particle water is retained giving rise to a low value of compressibility of the clay (similar to that observed at high deformation-rates).

5.3.4. Material Model Development for Sandy Clay

As discussed earlier, the main objective of the present work is to derive a material for clay-based soils with various levels of sand content and water saturation. This model is needed and will be used in the computational analyses of various landmine-detonation scenarios involving various types of deployments in the clay-rich soil. Since the computational analyses in question are of a transient, non-linear dynamic nature, the clay-based soil material model to be developed (*the CU-ARL sandy clay model*) is primarily aimed at the response of this material under large deformation, high-deformation rate and large pressure conditions. The validity of the

model under slow-speed quasi-static conditions (e.g. the loading conditions encountered during tire/soil interactions) is not the subject of the present work.

As discussed in our previous work [5.1-5.3], a typical transient non-linear dynamics problem involves numerical solution of the governing mass, momentum and energy conservation equations. Spatial coordinates and time are independent variables while mass density, velocities and the internal energy densities are the dependent variables in these equations. Since the stress appears explicitly in these equations, a set of relations (the material model) is needed to establish (for a given material) the relationships between stress and the dependent variables (and/or there integrals). Furthermore, since stress, σ, is generally decomposed into a hydrostatic stress ($-pI$, where p is pressure and I is a second order identity tensor) and a deviatoric stress σ_d, the material model is generally decomposed into:

(a) An *Equation of State*, EOS (defines the density and internal energy density dependences of pressure);

(b) A *strength model* (used to express the evolution of deviatoric stress in the elastic and elastic-plastic region of the material) and

(c) A *failure model* (defines the damage/failure response of the material).

In addition to these relations, an erosion model is often defined to alleviate numerical difficulties arising in regions experiencing large deformations. Within the erosion model, heavily deformed regions can be removed while conserving their momenta via the retention of the associated nodes as well as the nodal masses and velocities. In the remainder of the section, a brief overview is presented of the derivation of an equation of state, a strength model, a failure model and an erosion model for sandy clay.

Since the CU-ARL sandy clay material model developed in the present work is intended to include the effects of porosity, inter-particle water saturation content and sand content, the following parameters are defined to represent the physical and chemical state of the soil:

$$\alpha = \frac{V_{water} + V_{air}}{V_{total}} \tag{5.1}$$

$$\beta = \frac{V_{water}}{V_{water} + V_{air}} \tag{5.2}$$

and

$$\Omega = \frac{V_{sand}}{V_{clay} + V_{sand}} \tag{5.3}$$

where α is the extent of porosity, β the degree of saturation, Ω the solid fraction of sand (sand content), V is volume and the subscripts *sand*, *clay*, *air*, *water* and *total* are self explanatory.

CU-ARL Sandy-clay Equation of State

In this section, the equation of state (EOS) representing the compaction behavior of sandy clay under hydrostatic pressure is presented. The equation of state for the CU-ARL sandy clay is derived below following the same procedure which was originally employed to derive the CU-ARL sand EOS. That is the EOS are first separately derived for dry and fully saturated clay containing minor additions (<10 vol.%) of sand. These are next combined (using a simple rule of mixture) to define the corresponding relationships for unsaturated sandy clay. It is also recognized that clay and sand compaction behavior differ in at least two significant respects: (a) clay particles are finer and can more readily be displaced under the soil's own weight to yield a lower level of initial porosity in the soil; and (b) clay particles are deformable which greatly facilitates the compaction of the clay-based soil while, in sharp contrast, in sand-based soils sand-particle fracture is generally required for soil compaction.

Dry Sandy Clay: The relevant CU-ARL dry sandy clay EOS relations are presented first. Following our previous work [5.1-5.3], the dry-clay pressure dependence on mass density is defined using the following three-part piece-wise linear relation:

$$P_{dry\,clay} = \begin{cases} 0 & \rho_{dry\,clay} \le \rho_{o,dry\,clay} \\ B_{Pl.Comp,dry\,clay}\left(\rho_{dryclay} - \rho_{o,dryclay}\right) & \rho_{o,dry\,clay} \le \rho_{dry\,clay} \le \rho^{*}_{dry\,clay} \\ B_{El.Compr,dryclay}\left(\rho_{dryclay} - \rho_{s,dryclay}\right) & \rho_{dry\,clay} > \rho^{*}_{dry\,clay} \end{cases} \tag{5.4}$$

where $B_{Pl.Comp,\ dryclay}$ and $B_{El.Compr,\ dryclay}$ (=12.11MPa.m^3/kg [5.25]) are respectively the plastic compaction and the elastic compression moduli, while $\rho_{o,dryclay} = (1-\alpha_0)\rho_{s,dryclay}$ and $\rho_{s,dryclay}$ (=2005 kg/m^3 [5.26]) are the initial zero-pressure density of dry clay and the density of the fully-compacted clay, respectively and α_o denotes the initial porosity in clay. It should be noted, that the compaction and elastic-compression moduli used in Eq. (5.4) are defined as a ratio of the corresponding bulk moduli and mass densities. The plastic compaction modulus, $B_{Pl.Comp,\ dryclay}$, is defined as:

$$B_{Pl.Comp,dryclay} = \frac{P_{Comp,dryclay}}{\left(\rho^{*}_{dryclay} - \rho_{o,dryclay}\right)} \tag{5.5}$$

where $P_{Comp,\ dryclay}$ (= ca. 0.1GPa [5.26]) is the minimum pressure needed for full densification of dry clay and the corresponding mass density $\rho^{*}_{dryclay}$ is given by;

$$\rho^{*}_{dry\,clay} = \rho_{s,dryclay} + \frac{P_{Comp,dryclay}}{B_{El.Compr,dryclay}} \tag{5.6}$$

To account for the effect of sand in dry clay (specifically for the fact that the compressibility of sand particles is small in comparison to that of clay particles), the CU-ARL dry clay EOS model parameters are next generalized as:

$$\rho_{o,drySandyclay} = (1-\alpha_o)\rho_{s,drySandyclay} = (1-\alpha_o)\left[(1-\Omega)\rho_{s,dry\,clay} + \Omega\rho_{s,sand}\right] \tag{5.7}$$

$$P_{Comp,dry\,Sandyclay} = (1-\Omega)\,P_{Comp,dryclay} + \Omega\,P_{Comp,sand} \tag{5.8}$$

$$B_{Pl.Comp,drySandyclay} = \frac{P_{Comp,drySandyclay}}{\left(\rho^{*}_{drySandyclay} - \rho_{o,drySandyclay}\right)} \tag{5.9}$$

$$\rho^{*}_{drySandyclay} = \rho_{s,drySandyclay} + \frac{P_{Comp,drySandyclay}}{B_{El.Compr,drySandyclay}} \tag{5.10}$$

and

$$B_{El.Compr,drySandyclay} = (1-\Omega)B_{El.Compr,dryclay} + \Omega B_{El.Compr,Sand} \tag{5.11}$$

Saturated Sandy Clay: To account for the fact that under high deformation-rate conditions, intra- and inter-particle water are trapped within the soil (which prevents significant plastic compaction of soil), the EOS for saturated clay-based soil is defined using the following two-part piece-wise linear function:

$$P_{sat\,Sandyclay} = \begin{cases} 0 & \rho_{sat\,Sandyclay} \le \rho_{o,sat\,Sandyclay} \\ B_{sat\,Sandyclay}\left(\rho_{sat\,Sandyclay} - \rho_{o,sat\,Sandyclay}\right) & \rho_{sat\,Sandyclay} > \rho_{o,sat\,Sandyclay} \end{cases} \tag{5.12}$$

where $B_{sat\ sandyclay}$ is the compaction modulus of saturated sandy clay and is defined using the elastic compression modulus of dry sandy clay, $B_{El.Compr,\ drySandyclay}$ and the compaction modulus of water, B_w, and the fact that both the solid phase and the water-filled porosity form continuous networks, as:

$$B_{sat\,Sandyclay} = (1-\alpha_0)B_{El.Compr,dry\,Sandyclay} + \alpha_0 B_w \tag{5.13}$$

while $\rho_{o,\ sat\ Sandyclay}$is the initial density of saturated sandy clay and is defined in terms of the density of dry sandy clay, $\rho_{s,drySandyclay}$, and the density of water, ρ_w, as:

$$\rho_{o,sat\ Sandyclay} = (1-\alpha)\rho_{s,dry\ Sandyclay} + \alpha\rho_w \tag{5.14}$$

Unsaturated Sandy Clay: The pressure vs. density curve for unsaturated sandy clay is obtained as a linear combination of the pressure vs. density relations for the dry sandy and the saturated sandy clay, as:

$$P_{unsat,Sandyclay}(\alpha_o,\beta,\Omega) = \begin{cases} 0 & \rho_{unsat,Sandyclay} \le \rho_{o,unsat,Sandyclay} \\ B_{unsat,Sandyclay,low}\left(\rho_{unsat,Sandyclay} - \rho_{o,unsat,Sandyclay}\right); & \rho_{o,unsat,Sandyclay} \le \rho_{unsat,Sandyclay} \le \rho^*_{unsat,Sandyclay} \\ B_{unsat,Sandyclay,high}\left(\rho_{unsat,Sandyclay} - \rho^*_{unsat,Sandyclay}\right); & \rho_{unsat,Sandyclay} > \rho^*_{unsat,Sandyclay} \end{cases} \tag{5.15}$$

where

$$\rho_{o,unsat,Sandyclay} = (1-\beta)\rho_{o,dry\ Sandyclay} + \beta\rho_{o,sat\ Sandyclay} \tag{5.16}$$

$$\rho^*_{unsat,Sandyclay} = (1-\gamma_1)\rho^*_{dry\ Sandyclay} + \gamma_1\rho^*_{sa\,t\ Sandyclay} \tag{5.17}$$

$$B_{unsat,Sandyclay,low} = \frac{P_{Comp\ dry\ Sandyclay}}{\left(\rho^*_{unsat,Sandyclay} - \rho_{o,unsat,Sandyclay}\right)} \tag{5.18}$$

and

$$B_{unsat\ Sandyclay,high} = \left[\frac{1}{\frac{(1-\beta)}{B_{El.Compr,dry\ Sandyclay}} + \frac{\beta}{B_{sat\ Sandyclay}}}\right] \tag{5.19}$$

where

$$\gamma_1 = \beta\left[\frac{1-\dfrac{P_{Comp\,dry,Sandyclay}}{B_{Sat\,Sandyclay}\rho^{*}_{sat\,Sandyclay}}}{(1-\beta)\left(1-\dfrac{P_{Comp\,dry\,Sandyclay}}{B_{Pl.Comp,dry\,Sandyclay}\rho^{*}_{dry\,Sandyclay}}\right)+\beta\left(1-\dfrac{P_{Comp,dry\,Sandyclay}}{B_{sat\,Sandyclay}\rho^{*}_{sat\,Sandyclay}}\right)}\right] \tag{5.20}$$

Eq. (5.19) reflects the fact that the compaction modulus of the material residing in the intra- and inter-particle voids in sandy clay, consisting of dry air and water, is dominated by its more compliant phase (dry air).

Eqs. (5.8)-(5.20) define the pressure vs. density relation during loading which results in (irreversible) compaction of sandy clay. During unloading/elastic-reloading the pressure vs. density relationship is nearly linear with the slope being equal to the square of the (density-dependent) sound speed, C. Thus to fully define the CU-ARL sandy clay EOS model, a C vs. ρ relation must also be specified. The material sound speed is defined as a square-root of the ratio of the bulk modulus and the material mass density.

Dry Sandy Clay: The bulk modulus (in GPa) vs. density relationship for dry clay is given as [5.2]:

$$K_{dryclay} = \begin{cases} 0 & \rho_{dryclay} < \rho_{o,dryclay} \\ -22.01 + 0.01565\rho_{dryclay} & \rho_{o,dryclay} < \rho_{dryclay} \le 0.8407\rho_{s,dryclay} \\ -119.93 + 0.07358\rho_{dryclay} & 0.8407\rho_{s,dryclay} \le \rho_{dryclay} \le 0.9714\rho_{s,dryclay} \\ -979.94 + 0.5152\rho_{dryclay} & 0.9714\rho_{s,dryclay} < \rho_{dryclay} < \rho_{s,dryclay} \\ -4.4088 + 0.0306\rho_{dryclay} & \rho_{dryclay} > \rho_{s,dryclay} \end{cases} \tag{5.21}$$

To account for the effect of sand in CU-ARL dry sandy clay, the dry clay bulk modulus $K_{dryclay}$ given by Eq. (5.21) is modified as:

$$K_{dry,Sandyclay} = \left[\frac{1}{\dfrac{(1-\Omega)}{K_{dryclay}\left(\rho_{dry\,clay}\right)}+\dfrac{\Omega}{K_{sand}}}\right] \tag{5.22}$$

where K_{sand} is the bulk modulus of solid-sand particles (=21.97 GPa [5.26]).

Saturated Sandy Clay: The density-dependent bulk modulus in saturated sandy clay is derived following the same procedure as in the case of P vs. ρ relation as:

$$K_{sat,Sandyclay} = B_{sat,Sandyclay}\rho_{sat,Sandyclay} \tag{5.23}$$

Unsaturated Sandy Clay: In the same way, the density-dependent bulk modulus for unsaturated sandy clay is defined as:

$$K_{unsat,Sandyclay}(\rho_{unsat,Sandyclay}, \Omega, \alpha_o, \beta) = \left[(1-\beta)K_{dry,\,Sandyclay} + \beta K_{sat,\,Sandyclay}\right] \tag{5.24}$$

where

$$\rho_{dry,Sandyclay} = \rho_{unsat,Sandyclay} - \alpha_0 \beta \rho_{water} \tag{5.25}$$

and

$$\rho_{sat,Sandyclay} = \rho_{unsat,Sandyclay} + \alpha_0 (1-\beta)\rho_{water} \tag{5.26}$$

The effect of (0%, 50% and 100%) saturation on the P vs. ρ and C vs. ρ EOS relations in sandy clay with 10 vol.% sand is displayed in Figures 5-3(a)-(b), respectively.

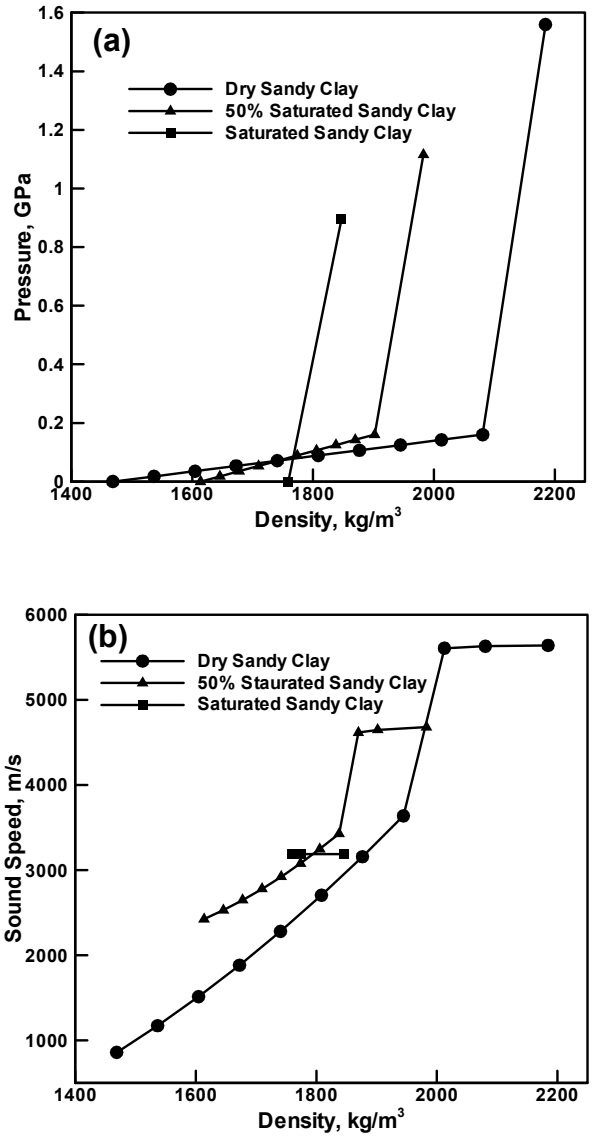

Figure 5-3. (a) Pressure vs. Density and (b) Sound Speed vs. Density Relation for Dry, Unsaturated and Saturated CU-ARL Sandy Clay (10vol. % sand) at Different Degrees of Saturation

CU-ARL Sandy-clay Strength Model

As discussed in Section 5.3.3, the yield strength (σ_y) of clay is not significantly affected by the magnitude of confining pressure, and to the first order of approximation, can be represented using a pressure-independent ideal-plastic constitutive law. The pressure-invariant yield stress is however a decreasing function of the degree of saturation and is assumed to vary linearly between its dry clay value (ca. 50kPa [5.21]) and its saturated-clay value (ca. 0.5kPa [5.21]). Minor additions of sand to the clay are modeled as the effect of rigid inclusions within a clay matrix. This effect is accounted for using a simple approach within which the yield strength of sandy clay, at any level of saturation, is obtained by multiplying the corresponding value for clay with a factor 1/(1-Ω) [5.2].

In addition to specifying the yield stress vs. pressure relationship, the strength model entails the knowledge of the shear modulus and its dependence on density and/or pressure. The shear modulus is used to define the relationship between the deviatoric stress and the deviatoric strain components during unloading/elastic reloading.

It is generally found that the shear modulus of dry clay is fairly independent of pressure but that it increases as mass density is increased. This increase is initially small and becomes larger and larger as the condition for full compaction is being reached. Once the full compaction condition is reached, shear modulus becomes essentially density independent. To account for this behavior, the following density-dependent relation for shear modulus of dry clay is proposed:

$$\begin{aligned} G_{dryclay} &= G^0_{dryclay} + G^1_{dryclay}\left(\rho_{dryclay} - \rho_{0,dryclay}\right)^n, \qquad \rho_{dryclay} \le \rho_{s,dryclay} \\ G_{dryclay} &= G^0_{dryclay} + G^1_{dryclay}\left(\rho_{s,dryclay} - \rho_{0,dryclay}\right)^n, \qquad \rho_{dryclay} > \rho_{s,dryclay} \end{aligned} \tag{5.27}$$

where $G^0_{dryclay}$ (=ca. 0.9GPa [5.28]), $G^1_{dryclay}$ (=$6.18\cdot10^{-9}$ GPa [5.28])and n (=ca. 3[5.29]) are the initial shear modulus, a shear modulus parameter and a shear modulus exponent, respectively.

Since water has a negligibly-small value of shear modulus, the effect of the degree of saturation on shear modulus in saturated and unsaturated clay is defined simply as:

$$G_{unsaturated,clay} = G_{saturatedclay} + (1-\beta)\left(G_{dryclay} - G_{saturatedclay}\right) \tag{5.28}$$

where $G_{saturatedclay}$ is the shear modulus of fully saturated clay (=ca. 0.12GPa [5.30]).

As in the case of yield strength, minor additions of sand cause elastic stiffening of clay and, hence, the shear modulus of sandy clay is obtained by multiplying the corresponding value for shear modulus for clay by a factor (1/1-Ω).

The effect of saturation on σ_y and on the G vs. ρ strength relation in sandy clay with 10 vol.% sand is displayed in Figures 5-4(a)-(b), respectively.

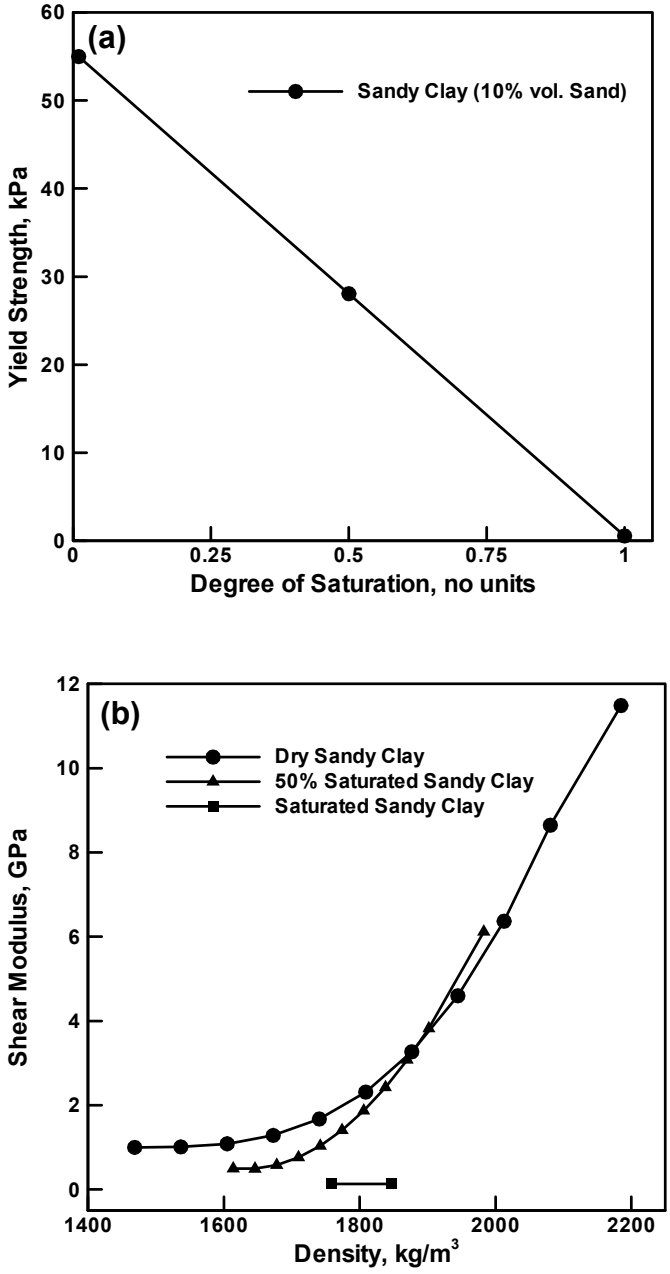

Figure 5-4. (a) Yield stress vs. Degree of Saturation and (b) Shear Modulus vs. Density Relation for Dry, Unsaturated and Saturated CU-ARL Sandy Clay (10vol. % Sand)

CU-ARL Sandy-clay Failure Model

In the suite of CU-ARL failure models for sand-based soils developed in our previous work [5.1-5.3], failure was assumed to occur when the negative pressure falls below a critical value, $P_{sand,fail}$ (i.e. a "*hydro*" type failure mechanism was adopted). After failure, the failed material element looses the ability to support tensile or shear loads while its ability to support compressive loads is retained. In dry sand-based soils, $P_{sand,fail}$ was set to $P_{drysand,fail}$ =0. [5.4]. In saturated sand-based soils, on the other hand, capillary-induced inter-particle cohesion causes the failure pressure to acquire a more negative value (=$P_{saturatedsand,fail}$ = -70kPa [5.31]). Furthermore, to account for the experimentally observed fact that the failure pressure in sand-based soils at the saturation level of 0.75 is around 15% of that in saturated sand (P_{fail}) [5.31], the following saturation-level dependent failure-pressure relation for unsaturated sand-based soils was proposed [5.1]:

$$P_{unsatclayeysand,fail} = \beta^5 P_{fail.sat} \tag{5.29}$$

The CU-ARL failure models for the sand-based soils presented above were developed in Refs. [5.1-5.3] to account for the fact that failure in these soils primarily takes place by negative-pressure induced decohesion. In clay-based, soils which are the subject of the present work, on the other hand, it is generally observed that failure can occur not only due to decohesion but also due to excessive shearing. Hence, a hybrid ("*hydro*" + "*shear*") failure model will be developed below for the clay-based soils. In addition, the hybrid failure model will account for the fact that, while in sand-based soils increased saturation leads to an increase in the failure resistance of the soil, the cohesion strength in clay-based soils initially sharply increases (from its dry-soil value of ca. 60kPa) with an increase in saturation until a peak value of ca. 225kPa [5.32] (at a saturation

level of ~40-50%) is attained and then sharply decreases to a value of ca. 10kPa in fully-saturated clay [5.33].

The *"hydro"* portion of the failure model is considered first. In dry clay-based soils, intra- and inter-particle cohesion gives rise to a non-zero value of the negative failure pressure, $P_{dryclay,fail}$ (ca. -60kPa [5.33]). In saturated clay-based soils, the cohesion strength is greatly deteriorated and the $P_{saturatedclay,fail}$ becomes substantially less negative (ca. -10kPa [5.33]). To account for the aforementioned effect of saturation on the cohesion strength of the unsaturated clay-based soils, $P_{unsaturatedclay,fail}$ is assumed to vary in accordance with the following relation with the degree of saturation as:

$$P_{unsaturatedclay,fail} = P_{dryclay,fail} - 720.8\beta + 770.8\beta^2 \tag{5.30}$$

The effect of sand particles in the clay-based soils on the cohesion-strength of these soils is not well understood [5.21]. More evidence in the literature points out towards the fact that clay/sand particle interfaces are most likely places for decohesion-induced failure and, hence, the presence of sand compromises the ability of clay-based soils to withstand negative pressures. However, based on the results of prior studies, this effect does not appear to be major and, given the lack of required quantitative data, will not be taken into account in the present rendition of the CU-ARL sandy-clay material model. Hence, Eq. (5.30) will be used in the "hydro" portion of the failure model of the sandy-clay soil under consideration.

Next, the shear-induced clay-based soil failure is considered. Failure is assumed to take place when the maximum shear stress reaches a critical level of saturation-level dependent shear-failure strength of the material. Increased saturation of the soil reduces the shear-failure strength of the soil and this reduction scales nearly linearly with the extent of saturation [5.34]. Hence, the shear-based portion of the failure model can be defined as:

$$\tau_{unsaturatedclay,fail} = \tau_{dryclay,fail} + \beta\left(\tau_{saturatedclay,fail} - \tau_{dryclay,fail}\right) \quad (5.31)$$

where $\tau_{dryclay,fail}$ (=ca. 50kPa [5.35]) and $\tau_{saturatedclay,fail}$ (=ca. 20kPa [5.35]) are the dry and the saturated clay shear failure strengths.

Since sand particles hamper shear in clay-based soils, they generally have a significant effect on the ability of the clay-based soils to withstand shear without failure. To account for this effect, a simple non deformable inclusion based hardening model is adopted according to which the failure strength of clay-based soils (at any level of saturation) is defined by multiplying Eq. (5.31) with a factor (1/1- Ω).

It should be noted that within the current hybrid failure model for clay-based soils, interactions between the hydro and the shear modes of failure is not considered. In other words, failure occurs when conditions for either of the two failure mechanisms are met.

The effect of saturation on $P_{fail}$and τ_{fail} in sandy clay with 10 vol.% sand is displayed in Figures 5-5(a)-(b), respectively.

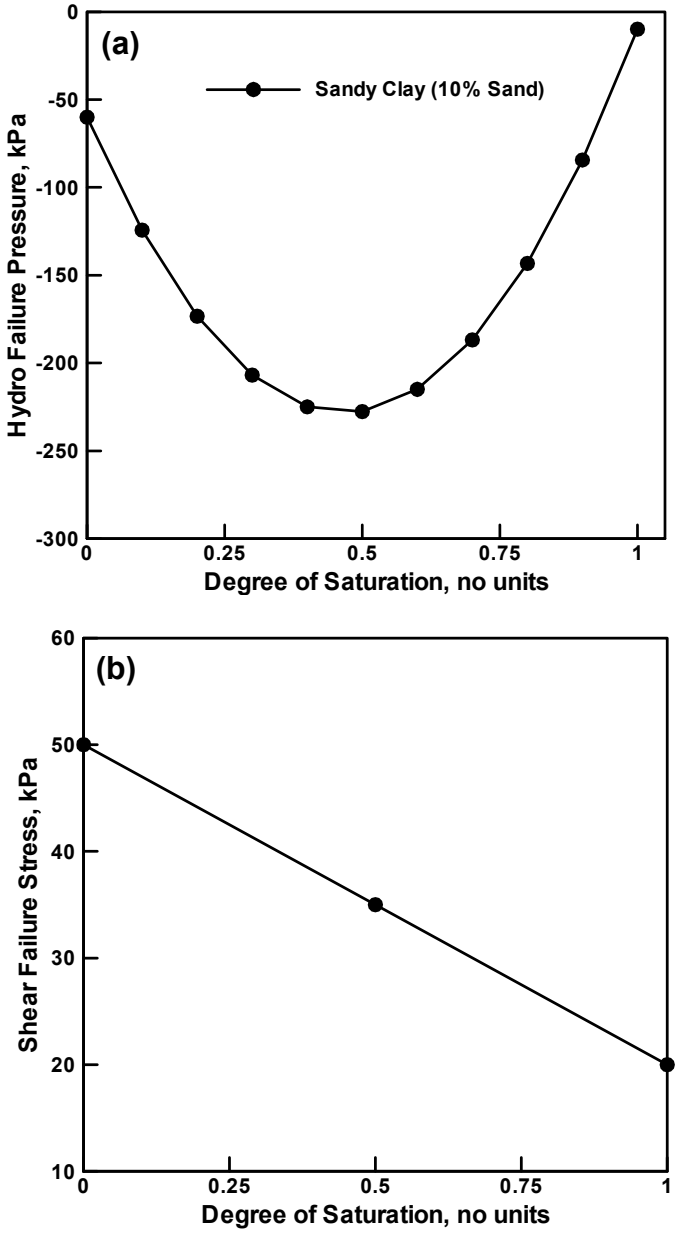

Figure 5-5. Variation in (a) Hydro failure pressure and (b) shear failure strength for CU-ARL sandy clay (10vol. % sand) with degrees of saturation.

CU-ARL Sandy-clay Erosion Model

Erosion of highly-distorted sandy-clay finite elements/cells is assumed to take place when the equivalent geometrical (i.e. elastic plus plastic plus damage/crack) instantaneous strain reaches a maximum allowable value. Our prior investigation [5.1-5.3], established that the optimal value for the equivalent geometrical instantaneous strain for soils of various types is ~1.0. When a material element is eroded, its nodes are retained along with their masses and velocities in order to conserve momentum of the system.

5.4. Validation of the CU-ARL Sandy-Clay Model

The CU-ARL sandy clay model presented in Section 5.3.4 was developed using simple physical arguments regarding the effects of moisture and minor sand contents on the dynamic mechanical behavior of clay-based soils. The model was next parameterized using various soil-testing experimental results and property-correlation analyses. The parameterizations of the CU-ARL sandy clay model for the dry, 50% unsaturated and saturated sandy clay with 10vol.% sand are given in Tables 5-1-5-3. To facilitate implementation of these parameterizations into the ANSYS/Autodyn material library, a piece-wise linear representation of the EOS and the strength models were used. In this section, an attempt is made to validate the CU-ARL sandy clay model by comparing the available open-literature field-test results pertaining to the detonation of shallow-buried landmines in sandy clay with their computational counterparts obtained in the present work. The latter results were obtained by carrying out a set of the transient non-linear dynamics simulations corresponding to the field tests in question. In order to assess the potential improvements in modeling soil behavior resulting from the use of the CU-ARL sandy clay model, simultaneous non-linear dynamics simulations were also carried out using the original Laine and Sandvik dry-sand compaction model [5.14] which is currently the soil material model most

widely used in shallow-buried landmine-detonation computational community. All the computational analyses carried in the present work were done using the commercial software ANSYS/Autodyn [5.4]. A brief description of the essential features of a typical transient non-linear dynamics analysis is discussed in the next section.

Table 5-1. Material Model Parameters for Dry Sandy Clay with Initial Porosity of 0.29 and with 10vol.% Sand

Field Dependent Variables	Units	Piece-wise Model Relations									
Reference Density, $\rho_{s,drysandyclay}$	kg/m^3	2080.5									
Equation of State											
Density, $\rho_{drysandyclay}$	kg/m^3	1468	1536	1604	1672	1740	1808	1876	1944	2012	2080
Pressure, $P_{drysandyclay}$	MPa	0	0.0178	0.0355	0.0533	0.0711	0.0889	0.106	0.124	0.146	0.1601
Sound Speed, $C_{drysandyclay}$	m/s	859	1214	1466	1663	2280	2842	3278	3637	5606	5629
Strength Model											
Yield Strength, $\sigma_{y,drysandyclay}$	kPa	55									
Density, $\rho_{drysandyclay}$	kg/m^3	1468	1536	1604	1676	1746	1806	1876	1946	2015	2085
Shear Modulus, $G_{drysandyclay}$	MPa	991.3	1001	1074	1271	1655.8	2289	3233	4552	6306	8559
Hybrid Hydro/Shear Failure Model											
Hydro Failure Pressure, $P_{drysandyclayfail}$	kPa	-60									
Shear Failure Pressure, $\tau_{drysandyclayfail}$	kPa	50.00									
Erosion Model											
Instantaneous Geometric Strain	-	2.0									

Table 5-2. Material Model Parameters for Unsaturated Sandy Clay (50% saturation) with Initial Porosity of 0.29 and with 10vol.% Sand

Field Dependent Variables	Units	Piece-wise Model Relations									
Reference Density, $\rho_{s,umsatsandyclay}$	kg/m^3	2080.5									
Equation of State											
Density, $\rho_{unsatsandyclay}$	kg/m^3	1613	1645	1677	1709	1741	1773	1805	1837	1869	1901
Pressure, $P_{unsatsandyclay}$	MPa	0	0.0178	0.0355	0.0533	0.0711	0.0889	0.106	0.124	0.146	0.1601
Sound Speed, $C_{unsatsandyclay}$	m/s	2424	2477	2526	2572	2783	3022	3234	3424	4594	4622
Strength Model											
Yield Strength, $\sigma_{y,unsatsandyclay}$	kPa	28									
Density, $\rho_{unsatsandyclay}$	kg/m^3	1613	1645	1677	1709	1741	1773	1805	1837	1869	1901
Shear Modulus, $G_{unsatsandyclay}$	MPa	566	571	608	708	902	1222	1699	2365	3251	4389
Hybrid Hydro/Shear Failure Model											
Hydro Failure Pressure, $P_{unsatsandyclayfail}$	kPa	-227.22									
Shear Failure Pressure, $\tau_{unsatsandyclayfail}$	kPa	35.00									
Erosion Model											
Instantaneous Geometric Strain	-	2.0									

Table 5-3. Material Model Parameters for Saturated Sandy Clay with Initial Porosity of 0.29 and with 10vol.% Sand

Field Dependent Variables	Units	Piece-wise Model Relations									
Reference Density, $\rho_{s,satsandyclay}$	kg/m^3	2080.5									
Equation of State											
Density, $\rho_{satsandyclay}$	kg/m^3	1758	1760	1762	1764	1765	1767	1769	1770	1772	1774
Pressure, $P_{satsandyclay}$	MPa	0	0.0178	0.0355	0.0533	0.0711	0.0889	0.106	0.124	0.146	0.1601
Sound Speed, $C_{satsandyclay}$	m/s	3189	3189	3189	3189	3189	3189	3189	3189	3189	3189
Strength Model											
Yield Strength, $\sigma_{y,satsandyclay}$	kPa	0.556									
Density, $\rho_{satsandyclay}$	kg/m^3	1758	1760	1762	1764	1765	1767	1769	1770	1772	1774
Shear Modulus, $G_{satsandyclay}$	MPa	133	133	133	133	133	133	133	133	133	133
Hybrid Hydro/Shear Failure Model											
Hydro Failure Pressure, $P_{satsandyclayfail}$	kPa	-10									
Shear Failure Pressure, $\tau_{satsandyclayfail}$	kPa	20.00									
Erosion Model											
Instantaneous Geometric Strain	-	2.0									

Table 5-4. Coordinates of the Pressure Transducers Located in air. The Origin of the Coordinate System is Located along the Line of Symmetry at the Sandy-clay/Air Interface

Transducer Designation	Transducer Coordinates, cm	
	X	Y
PT_30_0	-30.00	0
PT_30_22.5	-27.71	11.48
PT_30_45	-21.21	21.21
PT_70_0	-70.00	0
PT_70_30	-60.62	35.00
PT_110_0	-110.00	0

5.4.1. The Basics of Non-linear Dynamics Simulations

A transient non-linear dynamics problem is analyzed within ANSYS/Autodyn [5.4] by solving simultaneously the governing partial differential equations for the conservation of momentum, mass and energy along with the materials constitutive equations and the equations defining the initial and the boundary conditions. The equations mentioned above are solved numerically using a second-order accurate explicit scheme and one of the two basic mathematical approaches, the Lagrange approach and the Euler approach. Within ANSYS/Autodyn [5.4] these approaches are referred to as "*processors*". The key difference between the two basic processors is that within the Lagrange processor the numerical grid is attached to and moves along (and deforms) with the material during calculation while within the Euler processor, the numerical grid is fixed in space and the material moves through it. In our recent work [5.2], a brief discussion was given of how the governing differential equations and the materials constitutive models

define a self-consistent system of equations for the dependent variables (nodal displacements, nodal velocities, cell material densities and cell internal energy densities).

In the present work, both the Lagrange and Euler processors are used. The Lagrange processor was used to model the sand and various targets and structural components. High-energy explosives, gaseous mine-detonation products and the surrounding air are modeled using either a single-material FCT (Flux Corrected Transport) or a multi-material Euler processor. Different regions of the mine/air/target/sand model are allowed to interact and self-interact using the ANSYS/Autodyn [5.4] interaction options. A brief overview of the parts interactions and self interaction ANSYS/Autodyn algorithms can be found in our recent work [5.2]. Also a detailed description of the Lagrange, Euler-FCT and multi-material Euler processors as well as of the material models used for air, high explosives and metallic structural materials can be found in our recent work [5.1,5.2].

Throughout this manuscript, terms the "*Depth of Burial*" (DOB) and the "*Stand-off Distance*" (SOD) are used to denote distances between the mine top face and the sandy clay/air interface and between the sandy clay/air interface and the bottom face of the target structure, respectively.

In the next section, a comparison between the computational and experimental results is presented for the spatial and temporal evolution of the sandy clay overburden bubble and the associated pressure fields. Then, a comparison is made between the computational results regarding the total impulse captured by a witness plate obtained using the Laine and Sandvik dry-sand compaction model [5.14] and the present CU-ARL sandy clay model.

5.4.2. Temporal Evolution of Soil Oveburden Bubble and Pressure Fields

While a number of field-test studies of the detonation of landmines shallow-buried in sand-based soils exist in literature [5.9-5.11, 5.13], the authors of the present manuscript were

able to locate only one public-domain source of field-test data pertaining to the landmine detonation associated with clay-based soils [5.36]. Hence, the validation of the current CU-ARL sandy clay model will be done by comparing the experimental results obtained in Ref. [5.36] with the corresponding computational results obtained in the present work. In this section, a brief overview of the experimental set-up and the procedure used in Ref. [5.36] is first presented.

The experiments carried out in Ref. [5.36] can be briefly described as follows: A 1.27cm wall thickness cylindrical barrel with the outer-diameter of 81.6cm and the overall height of 71cm is filled with a clay-based soil up to its top. A 100g cylindrical-disk shape C4 high-energy explosive (6.4cm in diameter and 2cm in height) is buried into the clay-based soil along the centerline of the barrel with its faces parallel with the clay-based soil surface. A photograph of the experimental setup used in Ref. [5.36] is given in Figure 3-10. The Depth of Burial (DOB) (defined as the vertical distance between the top face of the explosive and the clay-based soil surface) is varied in a range between 0 and 8cm. Thus a 0cm DOB case corresponds to a flush-buried explosive. A set of six pressure transducers is utilized to monitor the pressure in the air following the detonation of the explosive. The designations and the position coordinates of the six transducers are given in Table 5-4. The first number in the Pressure Transducer (PT) designation represents the distance in centimeters of the transducer from the origin of the coordinate system (defined below), while the second number represents the angular relation in degrees between the position vector of the pressure transducer and the axis of symmetry. The location of the six pressure transducers is also shown in Figure 3-11. To be consistent with the definition of coordinate system for the 2D axi-symmetric problem used in ANSYS/Autodyn [5.4], the y coordinates are measured in the radial direction from the centerline of the barrel, while the x coordinates are measured along the axis of symmetry, with $x=0$ corresponding to the sand surface and $x<0$ denoting the air region above the ground.

The physical model displayed in Figure 3-11 has been represented using the computational multi-material Euler model shown in Figure 3-12. In Figure 3-12, various portions of the computational domain are filled with one or more of the attendant materials (air, clay-based soil, C4 gaseous-detonation products and AISI 1006 mild steel). Due to the inherent axial symmetry of the set-up used in Ref. [5.36], the mine detonation is analyzed as a 2D axi-symmetric problem. The left boundary in Figure 3-12 coincides with the axis of symmetry (x-axis). The horizontal direction (y-axis) corresponds to the radial direction.

The *"flow-out"* boundary conditions are applied to all the outer boundaries of the computational domain. In other words, the material at the outer boundary of the domain with a non-zero normal-outward component of the velocity is allowed to leave the computational domain. To mimic the detonation initiation conditions used in Ref. [5.36], detonation is initiated at the central circular portion of the explosive of radius 3.2cm, at the bottom face of the mine. To monitor the temporal evolution of pressure in air, six gage points are introduced whose locations coincide with those of the pressure transducers used in Ref. [5.36].

A standard mesh sensitivity analysis was carried out (the results not shown for brevity) in order to ensure that the results obtained are insensitive to the size of the cells used.

A comparison between the computational results obtained in the present work (using the Laine and Sandvik sand model [5.14] and the present CU-ARL sandy clay model) and their experimental counterparts [5.36] for the cases of dry and saturated clay-based soil are displayed in Figures 5-6(a)-(d) and 5-17(a)-(d), respectively. The results pertaining to the dry sandy clay will be discussed first.

Dry Sandy Clay

The variation of the peak side-on (static) pressure in air with the distance (along the vertical axis) from the sandy-clay/air interface at two (3cm and 8cm) DOBs is displayed in Figure

5-6(a). The results displayed in Figure 5-6(a) show that at 8cm DOB the two models reasonably well account for the observed experimental results. At 3cm DOB, on the other hand, the Laine and Sandvik model [5.14] greatly under predicts the side-on pressure, particularly at short distances of the pressure transducer from the Sandy-Clay/Air interface. What is even more troubling in the case of the Laine and Sandvik model [5.14] is that, in contrast to the experimental findings [5.36], it predicts lower values of side-on pressure at 3cm DOB at the lower values of pressure-transducer distance from sandy-clay/air interface.

The variation of the blast-wave time of arrival with the distance from the sandy-clay/air interface at the same two DOBs is displayed in Figure 5-6(b). The results displayed in Figure 5-9(b) reveal that, as in the case of Figure 5-6(a), the two sets of computational results are in good agreement with the experimental results in the 8cm DOB case. On the other hand, at 3cm DOB, the present CU-ARL sandy clay model continues to agree well with the experiments while the Laine and Sandvik [5.14] falls short, particularly at larger pressure-transducer distances from the sandy-clay/air interface.

The variation in the blast-wave time of arrival with offset angle (from vertical axis) at a fixed (30cm) distance from the sandy-clay/air interface is displayed in Figure 5-6(c). The results displayed in this figure show that the two models yield reasonably good agreement with the experiment in the case of 3cm DOB (not 8cm DOB), while in the case of 8cm DOB the CU-ARL sandy clay model clearly out-performs the Laine and Sandvik model [5.14].

The temporal evolution of the sandy clay bubble height for the cases of 3cm and 8cm DOB is displayed in Figure 5-6(d). The results displayed in this figure show that the Laine and Sandvik model [5.14] causes the sand bubble to burst earlier causing the venting of the detonation products in both the 3cm and 8cm DOB cases. The CU-ARL sandy clay model on the other hand, predicts substantially higher values of sand- bubble height at the moment of venting. Additional

computations carried out in the present work revealed that this short-coming of the CU-ARL sandy clay model can be readily eliminated by small adjustments to the hydrodynamic failure parameters.

Saturated Sandy Clay

A comparison between the computational results and their experimental counterparts in the case of saturated sandy clay are presented in Figures 5-7(a)-(d) and discussed next.

The results displayed in Figure 10(a) show that while both models yield reasonably good agreement with the experiment at 8cm DOB, the agreement is somewhat better in the case of the CU-ARL sandy clay model. In the case of 3cm DOB, the CU-ARL sandy clay model clearly outperforms the Laine and Sandvik model [5.14] at high values of the pressure-transducer distance from the sandy clay/air interface. However, at low values of this distance, where the Laine and Sandvik model [5.14] under-predicts the side-on peak overpressure, the CU-ARL sandy clay model yields higher values of this quantity. Unfortunately, this correction is too excessive making the agreement between the CU-ARL sandy clay model and the experiment less satisfactory.

The variation of the blast-wave time of arrival with the distance from the sandy clay/air interface at the same two DOBs is displayed in Figure 5-7(b). A simple analysis of the results displayed in this figure reveals that, at 8cm DOB, the CU-ARL sandy clay model does not significantly improve the agreement with the experiment and that both models reveal reasonable agreement with the experiment. However, a clear evidence of the improved agreement with the experiment [5.36] brought about by the present CU-ARL sandy-clay model is seen in the case of 3cm DOB.

The variation in the blast-wave time of arrival with offset angle (from vertical axis) at a fixed (30cm) distance from the sandy clay/air interface is displayed in Figure 5-7(c). The results

displayed in this figure show that at both 3cm and 8cm DOB the agreement between the model predictions is reasonably good and that the CU-ARL sandy clay model clearly out-performs Laine and Sandvik model [5.14].

The temporal evolution of the sandy clay bubble height for the cases of 3cm and 8cm DOB is displayed in Figure 5-7(d). The results displayed in this figure show that the Laine and Sandvik model [5.14] clearly under-predicts the maximum value of sand-bubble height (the height when bubble bursting takes place), while, the current CU-ARL sandy clay model over-predicts the same. As discussed earlier, this short-coming of the present CU-ARL sandy clay model can be eliminated by small adjustments in the hydrodynamic failure parameters.

Overall, it is found that, in the case of dry and saturated sandy clay, a significant improvements in model/experiment agreement are obtained when the widely used Laine and Sandvik sand model [5.14] is substituted with the present CU-ARL sandy clay model.

5.4.3. Total Momentum Transferred to the Target Structure

To assess the ability of the CU-ARL sandy clay model to account for the total momentum transferred to the target structure following detonation of a ground-laid or shallow buried mine at different soil saturation levels, a set of experimental field-tests is planned to be conducted in the near future. A Vertical Impulse Measurement Fixture (VIMF) will be used. The experimental test matrix to be used is displayed in Table 5-5 and the results to be obtained will be compared with their computational counterparts. In this section, in the absence of the experimental results, a comparison will be made between the computational results obtained using the Laine and Sandvik sand model [5.14] and the present CU-ARL sandy clay model. It is often found that the Laine and Sandvik sand model underpredicts the total momentum transferred to the target structure [e.g. 5.2]. Hence, it is interesting to learn if the present CU-ARL sandy clay model predicts higher values of this momentum.

The VIMF, Figure 5-8, is a structural mechanical device that enables direct experimental determination of the imparted blast-loading impulse via measurements of the vertical displacement of a known fixed-mass vertical guide rail that is capped with a witness plate, which serves as a momentum trap to capture the blast loading of the buried charge. The design and operation of the VIMF has been described in details by Taylor and Skaggs [5.37], Gniazdowski et al. [5.38], and Skaggs et al. [5.39] and will be only briefly discussed here. To create the required water-saturated soil condition, a cylindrical pit 3.65m in diameter and 1.32m deep is first constructed in the soil within the VIMF test area. To retain water in the soil pit and to keep the soil-water mixture separated from the rest of the soil, the walls of the pit are lined with 0.32cm thick poly-ethylene sheets and the pit floor is built using a commercial swimming pool liner. Once the pit liners are in place, a series of water hoses is placed in pit bottom to allow the introduction of water into the pit from the bottom. Next, approximately 14.2m^3 of soil is placed in the pit. The soil to be used in the planned experimental field tests and also used in the present computational work is clay-based and contains 10vol.% sand. In the case of saturated soil, water is allowed to fill the soil pit until standing water is observed on top of the soil.

The basic formulation of the computational problem dealing with the interactions between the detonation products, shell fragments and soil ejecta (all resulting from the explosion of a shallow-buried landmine) and the VIMF is presented next. The computational modeling of this interaction involved two distinct steps: (a) geometrical modeling of the VIMF along with the adjoining mine, air and soil regions, and (b) the associated transient non-linear dynamics analysis of the impulse loading (momentum transfer) from the detonation products, shell fragments and soil ejecta to the VIMF structure. The part (b) of this analysis was performed using a modified version of the technique developed by Fairlie and Bergeron [5.40]. This technique couples a multi-material Eulerian mesh to three Lagrangian meshes. The Eulerian mesh contained initially

a TNT mine (and after mine explosion the resulting high-pressure, high-internal energy-density detonation products) and the (initially stationary, atmospheric-pressure) air. The mesh was constructed in terms of eight node elements. One of the Lagrangian mesh was used to model the soil, the other to represent the VIMF witness plate while the third one was used to model the remainder of the VIMF structure. The soil and the VIMF structure were modeled using eight node solid elements, while the witness plate was modeled using four-node shell elements.

An advantage was taken of the inherent symmetry of the model. In other words, two mutually-orthogonal vertical planes of symmetry were placed along the axis of the VIMF as well as along the axis of the air, mine and sand regions which enabled only a quarter of the computational model to be analyzed. Representative models for various computational domains used in the present study are shown in Figure 3-9. It should be noted that the lower portion of the Eulerian domain contains the landmine, while the rest of the lower portion of the Eulerian domain is occupied by the Lagrangian soil mesh. Likewise, the upper portion of the Eulerian domain which extends above the soil contains initially air and is partially occupied by the Lagrangian VIMF witness-plate and vertical-base meshes.

At the beginning of the simulation, all the Lagrange and Euler domains were activated and the landmine detonated. The (circular-disk shape) mine was detonated over its entire bottom face at the beginning of the simulation.

A standard mesh sensitivity analysis was carried out (the results not shown for brevity) in order to ensure that the results obtained are insensitive to the size of the cells used.

A comparison between the two sets of computational results (one based on the use of the Laine and Sandvik sand model and the other based on the use of the present CU-ARL sandy clay model) pertaining to the total impulse transferred to the VIMF are shown in Table 5-5. The two cases of the depth of burial (3cm and 8cm) and two cases of stand-off distance (20cm and 40cm)

for both dry and saturated clay-based soils are considered. The results displayed in Table 5-5 suggest that the present CU-ARL sandy clay model predicts the total impulse values which, in the case of dry soil, are on average 30-50% higher than their counterparts obtained using the Laine and Sandvik sand model [5.14]. This increase is as high as 100% in the case of saturated soil. These findings are quite encouraging suggesting that the present model should also remove some of shortcomings of the Laine and Sandvik sand model [5.14] with respect to the ability to predict computationally the correct level of the total impulse transferred to a target structure.

Table 5-5. Computed Impulse (N-s) Transferred to the VIMF Witness Plate for the case of Cylindrical Disc-shaped TNT Charge (Diameter=0.254m, Height=0.056m and mass= 4.540kg)

DOB (cm)	SOD (cm)	Laine and Sandvik Sand Model (N-s)	CU-ARL Sandy Clay Model (N-s)
Dry Clay-based Soil			
3	20	15100	22100
8	20	18600	26200
3	40	11550	14200
8	40	13270	20750
Saturated Clay-based Soil			
3	20	15100	30700
8	20	18600	35470
3	40	11550	21100
8	40	13270	28750

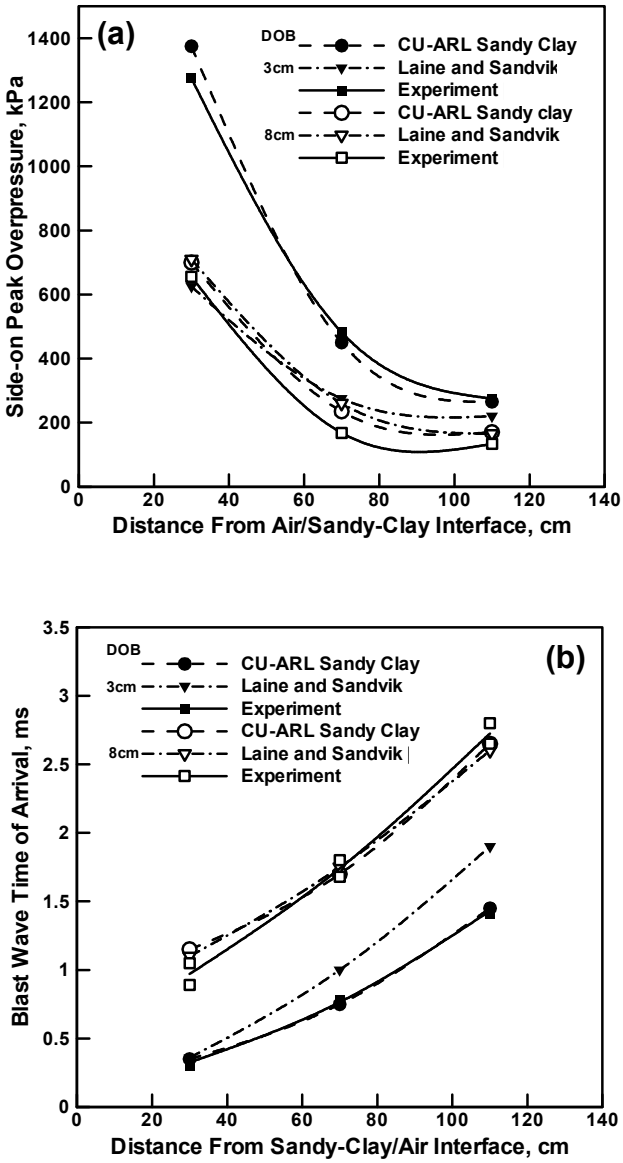

Figure 5-6. A comparison of the experimental [5.36] and computed (present work) results pertaining to various phenomena associated with landmine detonation in dry sandy clay: (a) Side-on overpressure vs. transducer distance from air/sandy clay interface; (b) Blast wave arrival time vs. transducer distance from air/sandy clay interface; (c) Blast wave arrival time vs. transducer offset angle from the symmetry axis and (d) Sand clay bubble height vs. landmine post-detonation time

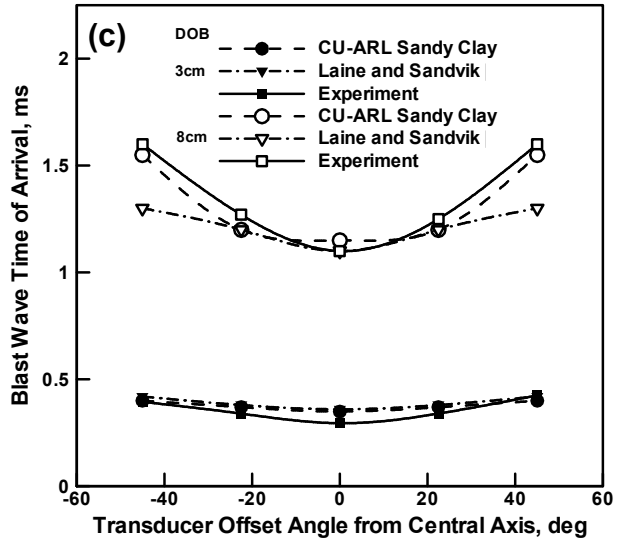

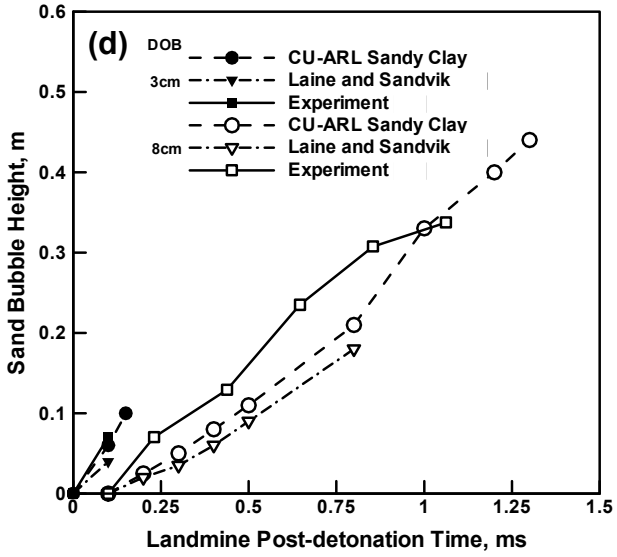

Figure 5-6. Contd…

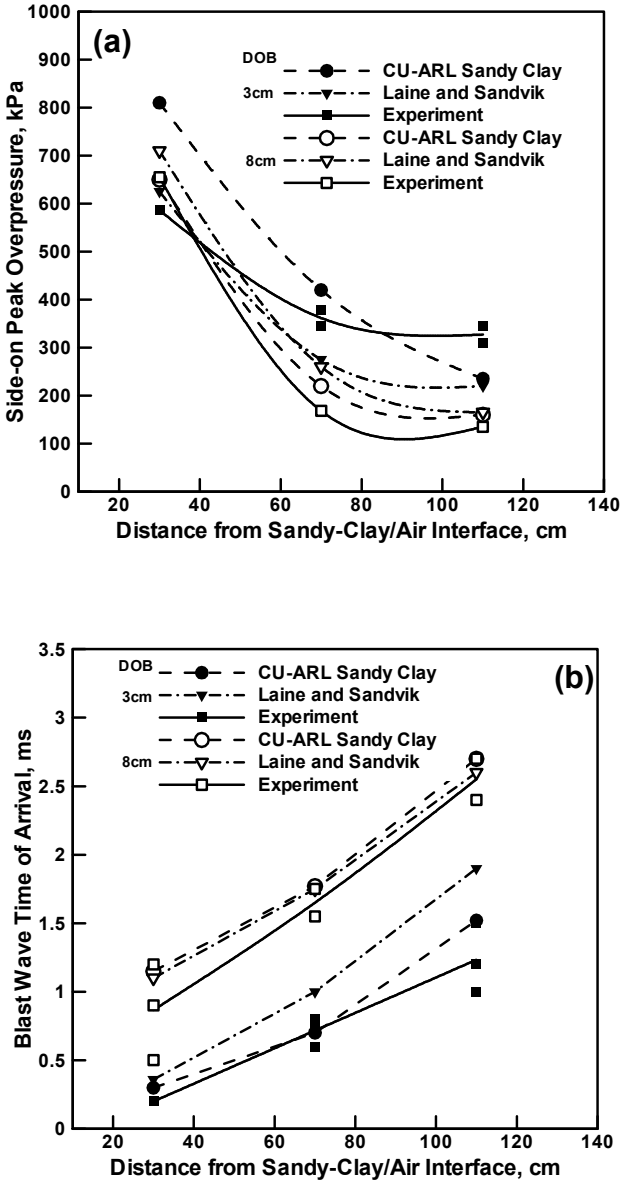

Figure 5-7. A comparison of the experimental [5.36] and computed (present work) results pertaining to various phenomena associated with landmine detonation in fully saturated sandy clay: (a) Side-on overpressure vs. transducer distance from air/sandy clay interface; (b) Blast wave arrival time vs. transducer distance from air/sandy clay interface; (c) Blast wave arrival time vs. transducer offset angle from the symmetry axis and (d) Sand clay bubble h1eight vs. landmine post-detonation time

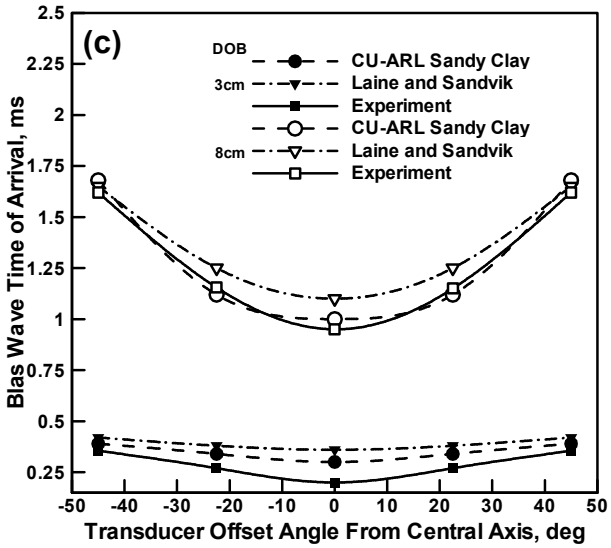

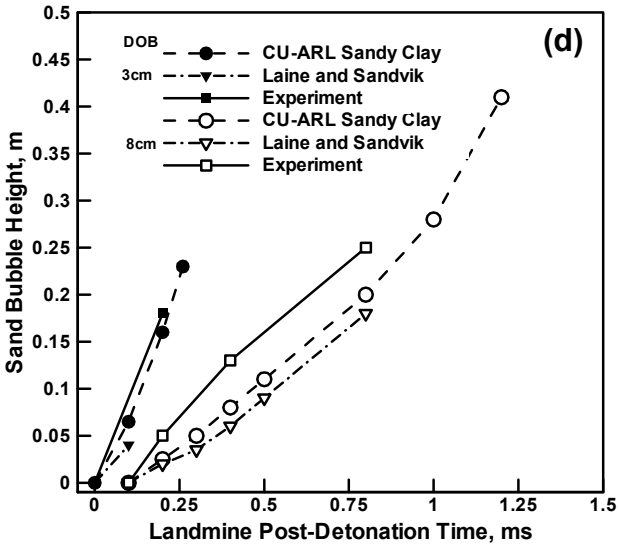

Figure 5-7. Contd…

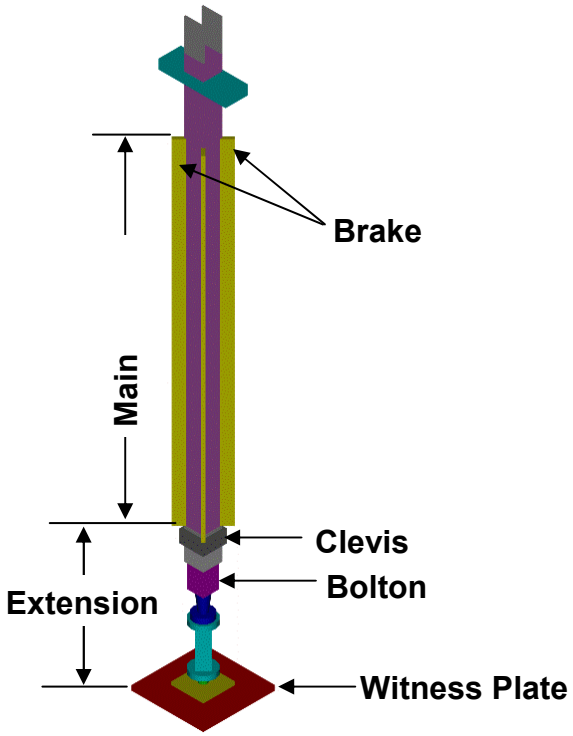

Figure 5-8. The Vertical Imp2ulse Measurement Fixture (VIMF)

5.5. Summary and Conclusions

Based on the results obtained in the present work, the following main summary remarks and conclusions can be drawn:

1. Using a simple procedure based on physical arguments and a property correlation analysis, a new material model for clay-based soils named CU-ARL sandy clay model has been developed and parameterized.

2. The resulting CU-ARL sandy clay model was validated by comparing the model predictions with their experimental counterparts for a number of scenarios involving detonation of a landmine (buried in sand) and the interactions of the mine fragments, detonation products and sand ejecta with various target structures.

3. The comparison between the experimental and the computational results (those based on the Laine and Sandvik sand model [5.14] and the CU-ARL sand clay model) revealed that the CU-ARL sandy clay model shows significantly better agreement with the experiment. .

5.6. References

5.1 M. Grujicic, B. Pandurangan and B. Cheeseman, *"The Effect of Degree of Saturation of Sand on Detonation Phenomena Associated with Shallow-buried and Ground-laid Mines*," Shock and Vibration, 13, 2006, 41-61.

5.2 M. Grujicic, B. Pandurangan, N. Coutris, B. A. Cheeseman, W. N. Roy and R. R. Skaggs, "*Derivation and Validation of a material model for clayey sand for Use in Landmine Detonation Computational Analysis*," Multidiscipline Modeling in Materials and Structures, accepted for publication, May 2007.

5.3 M. Grujicic, B. Pandurangan, N. Coutris, B. A. Cheeseman, W. N. Roy and R. R. Skaggs, "*Computer-simulations based Development of a High Strain-rate, Large-deformation, High-pressure Material Model for STANAG 4569 Sandy Gravel*," Soil Dynamics and Earthquake Engineering, accepted for publication, December 2007.

5.4 ANSYS/Autodyn-2D and 3D*, Version 11*, *User Documentation*, Ansys Inc., 2007.

5.5 J. Heffernan, *Pentagon announces specific plans to use mines in Iraq*, http://www.banminesusa.org/news/946_pentagon.htm, March 2003.

5.6 M. P. M. Rhijnsburger, "*Overview of the Use of LS-Dyna in Close-in Explosive Problems at TNO-PML*," 11th International Symposium on Interaction of Effects of Munitions with Structures, Manheim, Germany, May 2003.

5.7 Centers for Disease Control (CDC), Landmine Related Injuries, "*Morbidity and Mortality Weekly Report*," 46, 31, August 1997, 724-726.

5.8 K. A. Holsapple and K. R. Housen, *Crater Database and Scaling Tools* http://keith.aa.washinton.edu/craterdata, November 2004.

5.9 P. S. Westine, B. L. Morris, P. A. Cox and E. Polch, "*Development of computer program for floor plate response from landmine explosions*," Contract Report No. 1345, for U.S. Army TACOM Research and Development Center, 1985.

5.10 B. L. Morris, "*Analysis of Improved Crew Survivability in Light Vehicles Subjected to Mine Blast*," Final Report for Contract No. DAAK70-92-C-0058 for the U.S. Army Belvoir RDEC, Ft. Belvoir, VA, 1993.

5.11 D. Bergeron, S. Hlady and M. P. Braid, *Pendulum Techniques to Measure Landmine Blast Loading*, 17th International MABS Symposium, Las Vegas, USA, June 2002.

5.12 M. Grujicic, B. Pandurangan and B. Cheeseman, "*A Computational Analysis of Detonation of Buried Mines*," Multidiscipline Modeling in Materials and Structures, 2, 2006, 363-387.

5.13 D. Bergeron, R. Walker and C. Coffey, "*Detonation of 100-gram Anti-Personnel Mine Surrogate Charges in Sand-A Test Case for Computer Code Validation*," Suffield Report No. 668, Defence Research Establishment Suffield, Ralston, Alberta, Canada, April 1998.

5.14 P. Laine and A. Sandvik, "*Derivation of Mechanical Properties for Sand*," Proceedings of the 4th Asia-Pacific Conference on Shock and Impact Loads on Structures, CI-Premier PTE LTD, Singapore, November 2001, 361-368.

5.15 D. Bergeron, J. E. Tremblay, *"Canadian Research to Characterize Mine Blast Output,"* 16th International MABS Symposium, Oxford, UK, September 2000.

5.16 M. Grujicic, B. Pandurangan, B. A. Cheeseman, W. N. Roy and R. R. Skaggs, "*Impulse Loading Resulting from Shallow Buried Explosives in Water-saturated Sand*," Journal of Materials: Design and Applications, 221, 2007, 21-35.

5.17 A. M. Bragov, A. K. Lomunov, I. V. Sergeichev, K. Tsembelis and W. G. Proud, "*The Determination of Physicomechanical Properties of Soft Soils from Medium to High Strain Rates*," in process of submission, November 2005.

5.18 D. J. Chapman, K. Tsembelis and W. G. Proud, "*The Behavior of Water Saturated Sand under Shock-loading,*" Proceedings of the 2006 SEM Annual Conference and Exposition on Experimental and Applied Mechanics, 2, 2006, 834-840.

5.19 M. Grujicic, B. Pandurangan, B. A. Cheeseman, W. N. Roy, R. R. Skaggs and R. Gupta, "*Parameterization of the Porous-Material Model for Sand with Various Degrees of Water Saturation*," Soil Dynamics and Earthquake Engineering, 28, 2008, 20-35.

5.20 STANAG 4569- *Protection Levels for Occupants of Logistics and Light Armored Vehicles*.

5.21 G. Eisenstadt and D. Sims, "*Evaluating Sand and Clay Models: Do Rheological Differences Matter?*," Journal of Structural Geology, 27, 2005, 1399-1412.

5.22 J. Henrych, *"The Dynamics of Explosion and Its Use,"* Chapter 5, Elsevier Publications, New York, USA, 1979.

5.23 B. Loret, N. Khalili, *"A Three-phase Model for Unsaturated Soils,"* International Journal for Numerical and Analytical Methods in Geomechanics, 24, 2000, 893-927.

5.24 Z. Wang, H. Hao and Y. Lu, "*A Three-phase Soil Model for Simulating Stress Wave Propagation due to Blast Loading*," International Journal for Numerical and Analytical methods in Geomechanics, 28, 2004, 33-56.

5.25 A. Revil, D. Grauls and O. Brevart, "*Mechanical Compaction of Sand.Clay Mixtures*," Journal of Geophysical Research, 107, B11, 2002, ECV 11 1-15.

5.26 Y. M. Tien, P. L. Wu, W. S. Chuang and L. H. Wu, "*Micromechanical Model for Compaction of Bentonite-Sand Mixtures*," Applied Clay Science, 26, 2004, 489-498.

5.27 M. W. Lee, "*Geophysical Prospecting of the Biot Coefficient in Predicting Shear-wave Velocity in Water-saturated Sediments*," Geophysical Prospecting, 54, 2006, 177-185.

5.28 L. Laine, "*Numerical Simulation of Ground Shock Attenuation Layer for Swedish Rescue Centers and Shelters*," Proceedings of the 4th Asia Pacific Conference on Shock and Impact Loads on Structures, 2001, 1-8.

5.29 S. R. Cohen, *Measurement of Visco-elastic Properties of Water-saturated Clay Sediments*, Master's Thesis, Naval Postgraduate School, Monterey, CA, 1968.

5.30 A. Sanna and D. Penumadu, *Shear Modulus and Damping Variation During Consolidation of Clay,* Project Report, SURE Symposium, Clarkston University, 2000.

5.31 S. Stein and T. Kim, "*Effect of Moisture on Attraction Force on Beach Sand*," Marine Geosources and Geotechnology, 22, 2004, 33-47.

5.32 S. N. Abduljauwad and H. Rehman, "*Effect of Oil Contamination on the Behavior of Calcareous Expansive Clays*," Proceedings of the 12th Southeast Asian Geotechnical Conference, Malaysia, 1, 505-510, 1996.

5.33 N. A. Al-Shayea, "*The Combined Effect of Clay and Moisture Content on the Behavior of Remolded Unsaturated Soils*," Engineering Geology, 62, 2001, 391-342.

5.34 J. Kuwano, Y. Yoshida and K. Ishihara, "*Change in the Stability of Slopes with Degree of Saturation*," Fifth Australia-New Zealand Conference on Geomechanics, National Conference Publication (Institution of Engineers, Australia), 88/11, 1988, 465-469.

5.35 G. G. Moses and S. N. Rao, "*Behavior of Marine Clay Subjected to Cyclic Loading with Sustained Shear Stresses*," Marine Geosources and Geotechnology, 25, 2007, 81-96.

5.36 J. Foedinger, "*Methodology for Improved Characterization of Landmine Explosions*," SBIR Phase-II Plus Program, Technical Interchange Meeting, Material Science Corporation, June 2005.

5.37 L. C. Taylor, R. R. Skaggs and W. Gault, "*Vertical Impulse Measurements of Mines Buried in Saturated Sand*," Fragblast, 9, 1, 2005, 19-28.

5.38 N. Gniazdowski, "*The Vertical Impulse Measurement Facility Maintenance and Inspection Manual,*" ARL Technical Report (in submission) 2004.

5.39 R. R. Skaggs, J. Watson, T. Adkins, W. Gault, A. Canami and A. D. Gupta, "*Blast Loading Measurements by the Vertical Impulse Measurement Fixture (VIMF)*,"ARL Technical Report, in submission

5.40 G. Fairlie and D. Bergeron, "*Numerical Simulation of Mine Blast Loading on Structures,*" Proceedings of the 17th Military Aspects of Blast Symposium, Nevada, June 2002.

CHAPTER 6

CONCLUSIONS AND FUTURE WORK

6.1. General Discussion and Concluding Remarks

As stated in Chapter 1, the main objective of the present work was to develop, parameterize and validate dynamic material models for soil under blast loading conditions and glass under ballistic loading conditions. Towards the fulfillment of this objective, the expressions representing the various parts of the material model were derived and various computational analyses were carried out whose description and main findings are given below:

To begin with, the compaction material model for sand was presented and the modifications to the sand model arising from the extent of moisture content were discussed. The dependence of the material behavior on the rate of deformation was also discussed. It was found that water residing in the pores and the rate of deformation play a critical role in the dynamic material response of sand. In particular, the behavior of dry sand is essentially rate independent and dominated by irreversible energy-absorbing densification processes while the high deformation-rate behavior of saturated sand is predominantly elastic and controlled by incompressibility of water. The results of the computational analyses were compared with the experimental counterparts and it was seen that the results obtained after model modification were able to capture the behavior of sand under experimental blast loading conditions better than the compaction material model for dry sand.

Subsequently, the effect of the presence of clay (<15% vol.) on the behavior of dry and saturated sand was discussed and the representative material model was derived. It was assumed that clay essentially existed as a coating over the sand particles and thus did not affect the initial porosity or the initial degree of saturation of the sand-clay system. The effect of the presence of

clay was therefore more pronounced in the strength and the failure models while, its effect on the equation of state was considered negligible. The results of the computational analyses were compared with their experimental counterparts pertaining to the momentum transfer to the target structure and sand crater morphology. It was found there was a fairly better agreement between the computational results and the experimental results when the clayey-sand model was used as compared to the original compaction model.

Next, a material model for STANAG 4569 sandy-gravel was developed. Sieving curves were used to get the correct volume fractions of sand and gravel particles in the sandy-gravel model. The essential material property data for sandy gravel was obtained by performing some basic computational analyses. Due to the lack of public-domain data for experimental testing of sandy-gravel type of soil, recommendations were provided for future testing to be carried out at other universities.

Finally, a material model for a clay-rich type of soil containing minor amounts of sand was developed. The differences in the structures of sand and clay were discussed and the essential modifications were done to the model to account for the presence of intra-particle water in clay in addition to inter-particle water. The results of the computational analyses were compared with the experiments performed on clay-rich soil and a C4 charge. It was found that the model gave a significant improvement as compared to the original compaction model.

6.2. Suggestion for Future Work

In the present work, the experimental results used for comparison with the computational data are derived from open literature and therefore show considerable variation. The soil structure, the moisture content and other factors like the presence of organic matter in soil, environmental conditions etc. depend upon the place where the experiments were performed. It is therefore essential to obtain experimental results from soil found at a single location to eliminate

the variability associated with environmental conditions and the presence/absence of organic matter. In the future therefore, a set of such experiments should be conducted at a single location and the results compared to the computation. These experiments are to be conducted in the near future at the Weapons and Materials Research Directorate of the Army Research Labs at Aberdeen Proving Ground in Maryland.

APPENDICES

APPENDIX A

AN IMPROVED MECHANICAL MATERIAL MODEL FOR BALLISTIC SODA-LIME GLASS

A.1. Abstract

In our recent work [A.1], various open-literature experimental findings pertaining to the ballistic behavior of soda-lime glass were used to construct a simple, physically-based, high strain-rate, high-pressure, large-strain mechanical model for this material. The model was structured in such a way that it is suitable for direct incorporation into standard commercial transient non-linear dynamics finite-element based software packages like ANSYS/Autodyn [A.2] or ABAQUS/Explicit [A.3]. To validate the material model, a set of finite element analyses of the Edge-On-Impact (EOI) tests was conducted and the results compared with their experimental counterparts obtained in the recent work of Strassburger et al. [A.4, A.5]. In general, a good agreement was found between the computational and the experimental results relative to: (a) the front-shapes and the propagation velocities of the longitudinal and transverse waves generated in the target during impact and (b) the front-shapes and propagation velocities of a *"coherent-damage"* zone (a zone surrounding the projectile/target contact surface which contains numerous micron and sub-micron size cracks). However, substantial computational-analysis/experiment disagreements were found relative to the formation of **"***crack centers***"** i.e. relative to the presence and distribution of isolated millimeter-size cracks nucleated ahead of the advancing coherent-damage zone front. In the present work, it was shown that these disagreements can be substantially reduced if the glass model [A.1] is advanced to include a simple macro-cracking algorithm based on the linear elastic fracture mechanics.

A.2. Introduction

Ballistic glass is a material (or more often a system of materials) designed to be optically transparent while providing the necessary level of protection against blast and ballistic/fragmentation impacts. This class of materials is used in such diverse applications as protective visors for non-combat usage (e.g. riot control or explosive ordinance disposal) or as transparent-armor systems (to protect on-board instruments/sensors from fragments and debris, and to protect vehicle occupants from terrorist actions or other hostile conflicts). The critical importance of transparent armor has become evident by recent experiences of the U.S. military forces in the Operation Iraqi Freedom. With continuing escalations in the number and variety of threats, the needs for rapidly-deployable threat-specific weight/cost-performance-optimized transparent armor and armor systems have greatly increased. There are numerous efforts by the researchers in the U.S.A. and elsewhere around the world, to help accelerate the development of transparent armor systems. Traditionally, transparent armor is made of monolithic glass or transparent-elastomer inter-layered glass laminates. Among the new transparent-armor materials and technologies available today, the following have received most attention: crystalline ceramics (e.g. aluminum-oxinitride spinel, AlON [A.4]), new transparent polymer materials (e.g. transparent nylon [A.5]), and new interlayer technologies (e.g. polyurethane bonding layers [A.4]), and new laminate designs [e.g. A.6]. Due to their large size and curved shape, the majority of armor windows are still being constructed using glass. While ever increasing demands for reductions in weight and for improvements in ballistic-protection performance of transparent armor are calling for the use of new transparent materials (e.g. transparent crystalline ceramics, advanced transparent polymeric materials) and advanced technologies (e.g. multi-material functionally-graded laminated transparent armor), glass (as well as glass ceramics) continue to remain important material choice in ground-vehicle transparent armor applications.

Compositional modifications, chemical strengthening, and controlled crystallization have demonstrated to be capable of significantly improving the ballistic properties of glass [A.6]. Glass windshields and windows can also be produced in large sizes with curved geometries, and can be produced to provide incremental ballistic performance at incremental cost.

The development of new glass-based transparent-armor systems aimed at reducing the vulnerability of the military vehicle occupants and on-board instrumentation to various threats typically includes extensive experimental test programs. Such experimental test programs are critical for ensuring the utility and effectiveness of the transparent-armor systems. However, the use of experimental test programs is generally expensive, time-consuming and involves destructive testing. While the role of experimental test programs remains critical, they are increasingly being complemented by the corresponding computation-based engineering analyses and simulations. The knowledge of the armor-material response under high-deformation-rate/high-pressure loading conditions, as described by the corresponding material model, is one of the key components in such analyses greatly affecting their utility and fidelity. The main objective of the present chapter is to help advance the use of these computational engineering analyses and simulations in transparent-armor design applications by further developing and improving the simple, computationally-efficient, physically-based material model for soda-lime ballistic glass proposed in Ref. [A.1].

It is well established that glass exhibits quite different behavior under quasi-static (i.e. low deformation-rate) and dynamic (i.e. high deformation-rate) loading conditions. Under quasi-static loading conditions, pre-existing flaws/defects situated primarily in the surface regions of glass play a dominant role in the fracture process and fracture results in the formation of few large fragments [A.7-A.9]. In sharp contrast, under dynamic loading conditions, high-intensity stresses may cause the nucleation of bulk/volume defects so that the fracture process becomes

less surface-flaw controlled and results in the comminution (i.e. the formation of numerous fine fragments) [A.10,A.11]. Bulk cracks are seldom observed under quasi-static loading conditions except under very specific loading conditions (e.g. such as those encountered during high-temperature testing of glass fibers [A.12], compression testing of glass spheres [A.13], etc).

As mentioned above, brittle failure in ceramics and glasses is the result of nucleation (on pre-existing flaws) and propagation of the cracks, and it is accompanied by stress attenuation and fragments formation. Finite element analyses have been extensively used over the last dozen of years to elucidate the underlying mechanisms and quantify the ballistic performance of ceramic targets under high-velocity impact and penetration conditions. In these analyses, most of the effort was typically devoted to modeling the complicated post-failure initiation response of ceramic materials (i.e., the mechanical/structural response of these materials to impact loads in the presence of cracks). In general, all the existing brittle-fracture models reported in the literature, can be categorized as being either: (a) continuum based or (b) being of a discrete nature.

The continuum approaches [e.g. A.9, A.14] generally involve homogenization of a crack-laden (damaged) material into an equivalent crack-free continuum material with degraded stiffness and strength. The fundamental assumption in these models is that the elastic-stiffness degradation is the result of inelastic deformation caused by micron and sub-micron size cracks and that this degradation can be quantified using a so-called *"damage tensor"* whose evolution during loading can be formulated using a generalized Griffith-type crack initiation and propagation criteria for brittle materials. In addition, some of continuum models account for the interactions between the cracks, their coalescence, friction between fragments, etc. However, most of these phenomenological models have short-comings in that they cannot describe damage induced anisotropy and also, that their parameters are difficult to determine experimentally.

To overcome the aforementioned limitations of the continuum models, Espinosa and co-workers [A.15,A.16] proposed a multiple crack-plane (continuum) micro-mechanics constitutive model for brittle materials which can be parameterized by measuring experimentally the fundamental material properties (e.g. fracture toughness). Within the model, the dynamic growth of micro-cracks with different orientations is considered leading to damage induced anisotropy while the rate effects are naturally incorporated in the model. In spite of these improvements, the continuum models continue to be criticized because they require assumptions regarding the size and distribution of pre-existing crack-nucleating defects, and because they cannot be used to describe the growth of dominant cracks (the cracks which lead to failure), which, due to their size, cannot bee smeared-out/homogenized. On the computational side, the continuum models suffer from the problem that at very large deformations and under high strain rates, finite-element distortions may reduce the integration time steps below an acceptable level. One of the possible means to circumvent this problem is the application of adaptive meshing [e.g. A.3], a procedure in which a region containing highly distorted elements is re-meshed, in the course of an analysis, using regularly-shaped elements. However, repeated application of adaptive meshing during the analysis is also computationally quite costly.

The discrete models for brittle fracture [e.g. A.17] deal with the nucleation, propagation and coalescence of discrete (rather than smeared-out/homogenized) cracks during deformation. Among these models, the one proposed by Camacho and Ortiz [A.17] appears to be the most comprehensive. Within this model, conical and longitudinal cracks are allowed to nucleate at any node in a finite element mesh when the resolved normal or shear stress at that node reaches an effective fracture stress. Cracks are nucleated by duplicating nodes and propagated, along the element boundary, by continuing to duplicate nodes. Adaptive re-meshing is used to provide a rich enough set of possible fracture paths around the crack tip. The forces at the cracked surfaces

are brought to zero in accordance with the Griffith criterion accounting for unloading, before reaching the critical fracture opening. This enables the formation of fragments as cracks coalesce in a closed path. Thereafter, contact and friction between the fragments is accounted for. The major disadvantages of the discrete models, such as the one described above, are that they are extremely computationally intensive and become intractable as the number of cracks increases. In order to capture all possible crack nucleating sites, meshes with micron-size element are ultimately required.

The detailed review of the continuum and discrete material models (like the ones mentioned above) carried out in the present work clearly established that these models are capable of revealing complex intrinsic mechanisms and phenomena associated with fracture in brittle materials and are, hence, very important for gaining a better understanding of the behavior of these classes of materials. However, as argued in Ref. [A.1], it is the effect of these mechanisms/phenomena on the material response rather than their explicit analysis that is sufficient/needed when one is attempting to develop a computationally-efficient material model suitable for use in large-scale computational analyses of the multi-hit ballistic performance of geometrically-complex, multi-layered, functionally-optimized transparent-armor systems. In the present work, an effort is made to further advance the simple high strain-rate, high-pressure, large-strain material model for soda-lime ballistic glass proposed in Ref. [A.1] in order to improve the aspects of the model dealing with formation and growth of isolated millimeter-size cracks ahead of the advancing coherent-damage zone front. This was done by introducing in the model [A.1] a linear elastic fracture mechanics based algorithm for macro-cracking.

The organization of this chapter is as follows: In Section A.3.1, a brief overview is provided of the quasi-static and dynamic failure regimes observed in amorphous brittle materials like glass. A brief summary of the material model for ballistic soda-lime glass including its

physical foundation and the governing equations are presented in Sections A.3.2 and A.3.3. A newly proposed model for macro cracking is presented in Section A.3.4. Model parameterization and its implementation into a subroutine suitable for use with commercial finite element programs are presented in Sections A.3.5 and A.3.6, respectively. Details of a transient non-linear dynamics computational analysis of an Edge-on-Impact (*EOI*) test used to validate the material model for soda-lime ballistic glass are discussed in Section A.4. The main results obtained in the present work are presented and discussed in Section A.5. The key conclusions resulted from the present work are summarized in Section A.6.

A.3. Derivation of the Material Model

As discussed earlier, the main purpose of the present work is to improve the simple large-strain, high-deformation rate, high-pressure material model for soda-lime ballistic glass developed in our recent work [A.1] so that better agreement can be obtained between the model predictions and their experimental counterparts regarding the nucleation and growth of isolated millimeter-size cracks. The model in question was found to be computationally quite efficient while physical soundness of the model was retained by addressing within it the key underlying physical phenomena/processes controlling the mechanical response of soda-lime glass under ballistic loading conditions. In the remainder of this section, a brief account is first given of the essential features of the material model for soda-lime ballistic glass, the derivation procedure used to construct various components of the model and the approach used for parameterization of the model. Then, a brief discussion is presented of the modifications of the model introduced in the present work in order to better account for nucleation and growth of the isolated millimeter-size cracks.

A.3.1. Physical Foundation of the Model

Many experimental studies [e.g. A.4, A.5] have clearly established that the mechanical response of soda-lime glass is drastically different under low deformation-rate (i.e. quasi-static) and high deformation-rate (i.e. impact) loading conditions. Under quasi-static loading conditions, glass typically fails by the propagation of a single or a couple of discrete cracks and only a few fragments are created after complete fracture. In sharp contrast, under dynamic loading conditions, glass tends to undergo substantial damage (resulting from the formation of a large number of micron and submicron-size cracks) and tends to undergo comminution (i.e. forms a large number of sub-millimeter size fragments). In both cases, however, the failure is believed to be controlled by pre-existing flaws which, when subjected to sufficiently large stresses, can become cracks. A brief overview of the two failure regimes (i.e. the quasi-static coarse-fragmentation regime and the dynamic comminution regime) is presented below while more quantitative discussion of the same can be found in Ref. [A.1].

The occurrence of the two fracture regimes is believed to be the result of the two internal processes accompanying loading of glass: (a) crack formation at the pre-existing flaws and crack growth. The nucleation of cracks is accompanied by the formation of so-called "*shielding*" zones, i.e. the zones surrounding the cracks within which the stresses are highly relaxed and the probability for nucleation of additional cracks is very small; and (b) the increase in stress level which promotes the formation of additional cracks (at less potent pre-existing flaws). Since the crack formation process is typically associated with mechanical instability (i.e. once a crack is nucleated, it grows at a terminal velocity, until it reaches the free surface or another crack), low loading rates tend to promote the coarse fragmentation fracture regime. In other words, once a crack or a couple of cracks are formed, they can extend over the entire structure before the stress at other flaws has reached a high enough level to form additional cracks. Conversely, high

loading rates promote the formation of large number of cracks, i.e. the critical stress level for crack nucleation is reached at many pre-existing flaws before the previously-nucleated cracks have a chance to extend far enough and shield these flaws from the externally applied stress.

In the Edge-on-Impact (*EOI*) tests, reviewed in more details in Section A.4.1, it is also observed that both regimes of fragmentation take place, i.e. in the region of the glass-plate target surrounding the projectile-impacted surface, in which the loading rates are very high, fracture is dominated by the fine-scale (*"coherent"*) damage and the comminution (with occasional appearance of few coarse fragments). On the other hand, in target regions further away from the impact surface in which the loading rate is relatively low, isolated cracks ("*crack centers*") are formed and grow until they are swept by the advancing coherent-damage (i.e. the comminution) front.

A.3.2. Simplifying Assumptions and Basic Components of the Model

In this section, more details are provided regarding the physical foundation of the ballistic material model for glass developed in Ref. [A.1]. The following are the key simplifying assumptions and basic components of the model:

(a) The distribution of pre-existing flaws throughout the material was assumed to follow the Weibull-type distribution (discussed in next section). In order to account for the differences in the flaw distributions between the target surface and the bulk, different (typical) Weibull distribution parameters for soda-lime glass were used when dealing with surface and near-surface regions vs. the bulk region of the material (Table A-1);

(b) Both the nucleation of micro-cracks (which leads to comminution) and macro-cracks (which leads to coarse fragmentation) were postulated to be governed by the same stress-level based damage initiation criterion. Crack initiation was assumed to be controlled by the largest principal normal stress and only the normal mode (mode I) of cracking was considered;

(c) It was further assumed that it is the loading/stress rate at the moment of crack nucleation which determines if a crack will remain a single macro-crack within the given finite element resulting in the coarse-fragmentation failure mode of the element or the crack will be accompanied by the formation of many additional micro-cracks leading to progressive damage and ultimate multiple-fragmentation failure of the element. A single critical stress-rate value ($\dot{\sigma}_{crit}$, = ca. *1,000MPa/μs*, estimated using a simple constant stress-rate analysis) was introduced to separate these two regimes of fracture. At stress rates below this critical value, a single crack fracture regime was assumed while at stress rates above it a multiple-crack regime was assumed;

(d) When an element begins to fail via the single-crack mode, the (single) crack nucleated within that element was assumed to extend at the terminal velocity (defined in the next section) and the total time for element failure was obtained by dividing the characteristic element dimension by the terminal crack velocity. Once an element is fractured in a single-crack mode, it is removed from the model. In other words, multi-axial macro-cracking was not handled explicitly. When an element is undergoing fracture via the growth of the single-crack, stiffness and strength properties of this element were assumed to degrade linearly with the corresponding crack strain from the point of crack initiation to the point of complete traversal of the element by the crack;

(e) Once an element has started undergoing (*"coherent"*) damage due to the formation of multiple cracks, stress-shielding and path-crossing effects prevent, initially, the nucleation of macro-cracks. However, when the extent of coherent damage within a single element reaches a critical value, this element was assume to fracture by micro-crack coalescence and to lose most of its ability to support load. To account for the experimental observations that the resulting micro-fragments are typically confined by the surrounding non-fractured material and can support compressive and shear loads, the elements that failed in the multi-fragmentation regime were not

removed from the model. Instead, they were retained and assigned small residual normal and shear stiffness values. As shown in the next section, the critical level of coherent damage at which element failure takes place was found to be stress-rate invariant; and

When an element is subjected to coherent damage, the extent of damage was taken to be governed by a damage evolution equation and the extents of degradation of the corresponding stiffness and stress properties of the material were assumed to be governed by the appropriate damage-dependent stiffness and strength material constitutive relations (presented in the next section).

A.3.3. Mathematical Formulation of the Model

Course-fragmentation Quasi-static Failure Regime

As mentioned earlier, under low-rate (i.e. quasi-static) loading conditions, glass is typically observed to fracture in the coarse-fragmentation failure regime in which the failure of the complete structure is caused by the nucleation and propagation of a single crack or a few cracks. This observation has been rationalized as follows: Under low deformation rates, stresses are increasing slowly within the material. When the stresses become high enough, the first crack nucleates and begins to propagate at a terminal crack velocity. As the crack grows, so does its shielding zone within which stresses are relaxed and all flaws located within the shielding zone become impotent. Due to a low rate of stress increase in the remainder of the material, the stresses typically never reach a critical level needed to nucleate a large number of additional cracks and, consequently, the coarse-fragmentation regime ensues. Under such conditions, the fracture strength of the brittle material behaves as a stochastic quantity, i.e. the fracture resistance of a brittle material is not defined using a single (mean-value) fracture strength, but rather by a failure probability function. To derive an expression for the failure probability, the coarse-fragmentation fracture regime is analyzed using a Poisson point-process framework and the

resulting failure probability function, commonly referred to as the Weibull distribution function, was derived as:

$$P_F = 1 - \exp[\lambda_t Z] \tag{A.1}$$

The failure probability P_F in Eq. (A.1) defines the probability of finding at least one crack-nucleating flaw in the domain Z while the stress-dependence flaw-density λ_t is defined as:

$$\lambda_t = \lambda_0 \left(\frac{\sigma}{S_0} \right)^m \tag{A.2}$$

where λ_0 and S_0 are the reference density and a stress normalizing parameter, while the exponent m is generally referred to as the Weibull modulus.

Using the standard expressions for the mean value for a single-variate distribution function and Eqs. (A.1)-(A.2), the mean quasi-static fracture strength and its standard deviation can were derived as [A.18]:

$$\sigma_{f,static} = \frac{S_0}{\left(Z_{eff} \lambda_0 \right)^{1/m}} \Gamma\left(1 + \frac{1}{m} \right) \tag{A.3}$$

and

$$\sigma_{sd} = \sqrt{\frac{S_0^2}{\left(Z_{eff} \lambda_0 \right)^{2/m}} \Gamma\left(1 + \frac{2}{m} \right) - \sigma_{f,static}^2} \tag{A.4}$$

where Γ denotes the gamma function which is defined as:

$$\Gamma(x) = (x-1)! \tag{A.5}$$

where the probability distribution function for the fracture strength is obtained by combining Eqs. (A.1) and (A.2) and differentiating the resulting equation with respect to Γ.

Multiple Fine-fragmentation/Comminution Dynamic Failure Regime

As stated earlier, under high-rate (i.e. dynamic) loading conditions, it is generally observed that damage and the final failure occurs by nucleation, growth and interconnection of multiple micron- and millimeter-size cracks. The reason for the nucleation of multiple cracks is that, due to a high rate of stress increase within the material, stress levels at many defects become high enough to nucleate cracks before shielding zones of the previously nucleated nearby cracks can extend over these defects. Under such conditions, material damage is distributed and when the extent of damage becomes extensive, fine-scale fragmentation (often referred to as *"comminution"*) takes place.

To obtain more insight into the size and topology of the damage/fracture zone and the morphology and distribution of the cracks within such a zone, EOI tests are typically carried out. The following key aspects of the damage zone are generally observed: (a) In a region surrounding the place of impact, a *"coherent-damage"* zone is typically observed within which the damage is caused by micron and sub-micron size cracks. In addition, ahead of the coherent-damage zone front, multiple millimeter-size cracks are observed; (b) These cracks are typically aligned in radial directions with respect to the place of impact; (c) The cracks appear to be mainly of the mode-I opening and, hence, are caused by high tensile hoop stresses. The latter are most likely the result of target-material motion in the radial directions accompanying the projectile penetration into the target; (d) A crack is believed to form in a dynamic fashion as a result of high tensile stresses propagated by the stress wave (generated at the place of impact) and its growth ceases when the surrounding cracks cause significant stress reductions in the shielding zone of the crack in question; and (e) Crack distribution is highly non-uniform and anisotropic.

Following the original work of Denoual and Hild [A.18,A.19], Grujicic et al. [A.1] recently proposed a physically-based computationally-efficient material dynamic multiple-fragmentation fracture model for soda-lime glass. The key components of this model are as follows:

(a) When a defect is activated and the associated crack is nucleated, a shielding zone is created around the crack within which stress component responsible for crack nucleation is relaxed to zero. Consequently, any defect residing in such a zone will become impotent (i.e. will no longer represent the potential nucleus for a crack). As a crack grows, its shielding zone also grows but in a self-similar fashion. Consequently, the size of the shielding zone at a time t associated with a crack which was nucleated at the time τ was defined by the following relation:

$$Z_{sh}(t,\tau) = S\left[kC(t-\tau)\right]^n \tag{A.6}$$

where $C = \left[E/\rho\right]^{0.5}$ is the speed of sound (i.e. the speed of the impact-generated stress wave), E the Young's modulus, ρ the mass density, k=0.2-0.4, a ratio of the crack speed and the sound speed, n a defect-distribution dimensionality factor (=2, for surface-flaw dominated failure and =3, for bulk flaw dominated failure) and S is a shielding zone shape factor ($=4\pi/3$, for a spherically shaped bulk shielding zone);

(b) Under quasi-static loading conditions, as discussed above, once a crack is nucleated, it can traverse the entire structure (while it's shielding zone spreads over the entire surface/volume of the structure) before the stress on other defects can become sufficiently high to cause the nucleation of additional cracks. Under dynamic loading, on the other hand, the condition for crack nucleation will be met at many flaws leading to a multiple-cracking fracture mode. However, the neighboring cracks with compatible opening modes and orientations, via their shielding zone, will mutually terminate each other's growth, giving rise to relatively short cracks;

(c) Due to the shielding effects discussed above, one can distinguish between the non-shielded and shielded defects and the total defect density can be decomposed as:

$$\lambda_t = \lambda_{non-sh} + \lambda_{sh} \tag{A.7}$$

where both $\lambda_{non\text{-}sh}$ and λ_{sh} are defined by dividing the corresponding number of defects by the total domain size;

(d) The extent of defect shielding is controlled by the competition between the expansion of the shielding zone(s) (which promote defect shielding) and higher rates of loading (which promote activation of new defects in the regions outside the shielding zones). As the rate of loading is decreased, a larger number of defects will become shielded and, in the limit of quasi-static loading, all defects (except for the one which nucleated the first crack) will be shielded leading to the coarse-fragmentation failure mode; and

(e) As the loading rate increases, the density of shielded defects will decrease, (at a given level of stress, i.e. at a given level of total defect density). This, in turn, will give rise to higher fracture-strength levels, as a larger portion of the domain will remain unshielded (i.e. undamaged) and could support the applied load.

The (mean) fracture strength for a brittle material in the single-fragmentation failure mode is defined by Eq. (A.3) and is rate-independent. The failure strength for the multiple-fragmentation failure mode is derived in the remainder of this section and, as argued in point (e) above is expected to be an increasing function of the loading rate.

During derivation of the multiple-fragmentation brittle-fracture model [A.1], the case of uniform loading at a constant stress rate ($\dot{\sigma}$.) was considered first and a distinction was made between the externally-applied macroscopic stress, Σ, and an internal stress $\sigma = \dot{\sigma}t$, where t is the time of loading. Due to the formation of cracks and their shielding zone (within which the

internal stress is relaxed), only non-shielded portions of the brittle-material structure was assumed to support σ. Next, a damage variable, D, was defined as a ratio of the union of all shielding-zone volumes and the structure volume, yielding the following relations exist between Σ and σ:

$$\Sigma = \sigma(t)(1 - D(\sigma)) = \dot{\sigma}t(1 - D(\dot{\sigma}, t)) \tag{A.8}$$

where D is implied to depend on $\dot{\sigma}$ and t, since these quantities affect the density/number of cracks via $\sigma = \dot{\sigma}t$ and Eq. (A.2) while t affects the size of the shielding zones via Eq. (A.6).

According to Eq. (A.8), as the loading time increases, the $\sigma(t)$ increases while the $(1 - D(\sigma))$ term decreases. The macroscopic multiple-fragmentation fracture strength is then defined as the peak value of Σ, i.e. $\sigma_{f,\,dynamic} = \Sigma_{max}$, and is obtained from the relation:

$$\frac{d\Sigma}{d\sigma} = 0 \tag{A.9}$$

Following Denoual and Hild [A.18,A.19], D was next set equal to the probability of defect shielding, P_{sh}, which is then defined using Eq. (A.1) as:

$$D = P_{sh} = 1 - \exp(-\lambda_t Z_{sh}) \tag{A.10}$$

where Z_{sh} is the average size of the shielding zone defined as:

$$\lambda_t(t) Z_{sh}(t) = \int_0^t \left. \frac{d\lambda_t}{dt} \right|_\tau \left[kC(t - \tau)\right]^n d\tau \tag{A.11}$$

Eq. (A.11) states that, in order to compute Z_{sh} at time t, when the total defect density is $\lambda_t(t)$, one must take into account that cracks may have nucleated at a time, $0 \le \tau \le t$, and that their shielding-zone size is, hence, $\left[kC(t - \tau)\right]^n$. Furthermore, the probability that a crack present at time t was nucleated at time τ is expected to be proportional to the rate of activation of the flaws

at time □, i.e. to scale with $\frac{1}{\lambda_t(t)}\left.\frac{d\lambda_t}{dt}\right|_\tau$. while $\int_0^t \lambda_t(t)\left.\frac{d\lambda_t}{dt}\right|_\tau d\tau = 1$.

In the case of uniform loading under constant stress rate conditions and via Eq. (A.2), the term $\left.\frac{d\lambda_t}{dt}\right|_\tau$ becomes:

$$\left.\frac{d\lambda_t}{dt}\right| = \frac{\lambda_0 m \dot{\sigma}^m t^{m-1}}{{S_0}^m} \tag{A.12}$$

When Eq. (A.12) is substituted into Eq. (A.11) and, in turn, in Eq. (A.10), and integrated, the following expression for the damage extent is obtained:

$$D = 1 - \exp\left(- \frac{m!n!\left(\frac{\sigma}{\sigma_c}\right)^{m+n}}{(m+n)!} \right) \tag{A.13}$$

where σ_c is a characteristic stress defined as:

$$\sigma_c = \dot{\sigma} t_c = \left[\frac{S_0^m \dot{\sigma}^n}{\lambda_0 S (kC)^n} \right]^{\frac{1}{m+n}} \tag{A.14}$$

After substituting Eq. (A.13) into Eq. (A.8) and after differentiating the resulting equation in accordance with Eq. (A.9) one obtains:

$$\sigma|_{\Sigma_{\max}} = \left(\frac{S_0^m \dot{\sigma}^n}{\lambda_0 S (kC)^n} \right)^{\frac{1}{m+n}} \left(\frac{(m+n-1)!}{m!n!} \right)^{\frac{1}{m+n}} \tag{A.15}$$

and

$$\sigma_{f,dynamic} = \Sigma_{\max} = \sigma_c \left[\frac{1}{e} \frac{(m+n-1)!}{m!n!} \right]^{\frac{1}{m+n}} \tag{A.16}$$

Then Eqs. (A.15) and (A.13) are combined to get:

$$D\big|_{\Sigma_{\max}} = 1 - \left(\frac{1}{e} \right)^{\frac{1}{m+n}} \tag{A.17}$$

Likewise, $\sigma = \dot{\sigma} t$ and Eq. (A.15) are combined to get:

$$t\big|_{\Sigma_{\max}} = \left(\frac{S_0^m}{\lambda_0 S (kC)^n \dot{\sigma}^m} \right)^{\frac{1}{m+n}} \left(\frac{(m+n-1)!}{m!n!} \right)^{\frac{1}{m+n}} \tag{A.18}$$

An example of the relationship between the expressions for the quasi-static and dynamic fracture strengths, (Eqs. (A.3) and (A.16), respectively), for soda-lime glass in the case when brittle fracture is controlled by bulk flaws is displayed in Figure A-1. To help interpret fracture strength vs. stress rate plot displayed in Figure A-1, a second horizontal axis, Z_{eff}/Z_c, is introduced. The relevant mechanical property parameters used in the construction of Figure 1 are listed in Table A-1 while Z_{eff} was set to a representative fixed value of 10^{-4}m^3. It should be noted that in Figure A-1, the two expressions for the (mean) fracture strength, Eqs. (A.3) and (A.16), are valid only over a limited range of stress rates and that the ranges are different for the two relations. That is, at high stress rates, defect shielding is limited and, hence, the static course-fragmentation fracture strength relation, Eq. (A.3), which assumes complete shielding of all flaws by the first nucleated crack is not valid. Likewise, Eq. (A.16) is not valid in the low stress rate range (i.e. at lower values of Z_{eff}/Z_c), since in this case, a shielding zone must grow beyond the total structure volume before a single defect is shielded. Thus the multiple cracking fracture mode is not feasible. The results displayed in Figure 1 further show that, as expected, the fracture strength

increases with an increase in stress rate in the multiple-fragmentation regime at high stress rates, while it is essentially stress-rate independent in the single-fragmentation fracture mode at low stress rates.

As mentioned earlier, coherent damage causes degradation of the material strength and stiffness and, in order to assess the temporal evolution of this degradation, a damage evolution equation is needed. This was obtained in Ref. [A.1], by differentiating Eq. (A.13) for the extent of damage, D, with respect to stress, σ, to get:

$$dD/d\sigma = \frac{m!n!(m+n)\sigma^{m+n-1}}{(m+n)!{\sigma_c}^{m+n}}(1-D) \tag{A.19}$$

It should be noted that, as implied by Eqs. (A.13) and (A.19), damage is assumed to be isotropic and, hence, degraded glass, like the virgin glass, is considered as an isotropic material. Degradation of the Young's modulus of the glass is then defined by the following relation:

$$E = E_0(1-D) \tag{A.20}$$

where subscript *0* is used to denote a quantity pertaining to glass in its initial condition.

One of the key features of the soda-lime glass multiple-fragmentation model [A.1] is that, in accordance with Eq. (A.19), the evolution of coherent damage is controlled by the *"internal"* stress, σ (i.e. the stress residing in the non-shielded portion of the finite element in question, while the overall stress state of that element is defined by a *"macroscopic"* stress, $\Sigma = \sigma(1-D(\sigma))$. Thus, the internal-stress level is controlled by the initial stiffness of soda-lime glass while the macroscopic-stress level is controlled by the degraded-material stiffness.

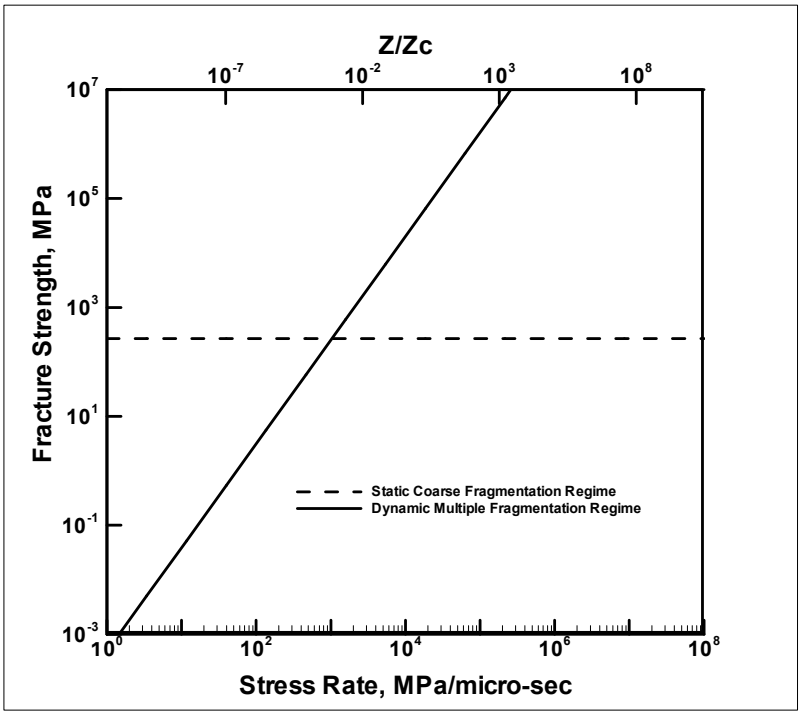

Figure A-1. The Transition between the Static Coarse Fragmentation and the Dynamic Fine-fragmentation Brittle-fracture Modes as a Function of an Increase in Stress Rate

Table A-1. Mechanical Property Parame1ters for Soda-lime Glass Used in the Present Work

Property	Symbol	Value	Unit
Young's Modulus	E	70.0	GPa
Poisson's Ratio	υ	0.22	N/A
Density	ρ	2500	kg/m^3
Mean Fracture Toughness	K_{IC}	0.75	$MPa \cdot m^{1/2}$
Surface Controlled Fracture			
Weibull Modulus	m	7	N/A
Mean Static Fracture Strength	$\sigma_{f,static}$	50	MPa
Effective Surface	Z_{eff}	0.024	m^2
Volume Controlled Fracture			
Weibull Modulus	m	30	N/A
Mean Static Fracture Strength	$\sigma_{f,static}$	230	MPa
Effective Volume	Z_{eff}	10^{-4}	m^3

A.3.4. Macro-cracking Fracture Model

As discussed earlier, the ballistic glass model developed in Ref. [A.1] handled the phenomenon of macro cracking using a very simple approach. That is, only a stress-based crack nucleation criterion was considered which typically resulted in the formation of single element long isolated cracks (crack centers). Since the edge-on impact results of Strassburger et al. [A.4,A.5] revealed the presence of significantly longer cracks, a good computation/experiment agreement could not be attained. To overcome this shortcoming of the ballistic glass model [A.1], the stress based crack-nucleation criterion is complemented with a fracture toughness-based crack growth criterion in the present work. This is accomplished as follows:

(a) Adjacent failed elements aligned in a particular direction are used to define the associated crack length in that direction;

(b) For an element located at a crack tip, the stress intensity factor K_I is calculated by multiplying its maximum principal stress with a factor $\sqrt{\pi a}$, where a is the crack half-length;

(c) Then, crack extension occurs by failure of an element described in (b) when the following condition is satisfied: $K_I > K_{IC}$, where K_{IC} is the stress intensity factor of the ballistic glass; and

(d) For simplicity, only five crack propagation directions were considered. Three of these were aligned with the edges of the cube shaped finite element, while the remaining two are aligned at a ±45 degree angle in the 2-3 plane.

A.3.5. Parameterization of the Model

As discussed earlier, brittle failure of glass in either of the coarse-fragmentation or fine-fragmentation mode is assumed to be controlled by pre-existing flaws and to comply with the Weibull distribution. However, to account for the fact that surface regions can contain higher density of flaws, different Weibull-distribution parameters were used for the finite elements

residing on the target faces, Table A-1. Table A-1 also contains the values for the linear elastic properties for soda-lime glass. As stated earlier, transition between the coarse-fragmentation and fine-fragmentation brittle-fracture modes is assumed to take place at a constant stress-rate, which, based on Figure A-1 was set to *1,000MPa/μs*. A typical value of 0.3 was assigned to the ratio between the crack terminal velocity and the sound speed, *k*. The crack shielding zones are assumed to be circular or spherical depending on whether the failure is controlled by surface or volume flaws.

The macro-cracking growth model proposed in Section A.3.4 is associated with a single material parameter, i.e. the critical mode-I stress intensity factor, K_{IC}. In accordance with the macro-cracking initiation criterion, the critical Mode-I stress intensity factor was taken to be a stochastic quantity given by the same Weibull-distribution parameters as the corresponding fracture strength. Also, the same mean value of 0.75 $MPa \cdot m^{1/2}$ [A.20] was used for the critical mode-I stress intensity factor in both the surface and bulk regions of the material.

A.3.6. Implementation of the Material Model in the User-material Subroutine

The brittle-fracture material model for soda-lime glass developed and parameterized in the previous sections is next implemented in a *VUMAT Material User Subroutine* of the commercial finite element program ABAQUS/Explicit [A.3]. This subroutine is compiled and linked with the finite element solver and enables ABAQUS/Explicit to obtain the needed information regarding the state of the material and the material mechanical response during each time step, for each integration point of each element.

The essential features of the coupling between the ABAQUS/Explicit finite-element solver and the VUMAT Material User Subroutine at each time increment at each integration point of each element can be summarized as follows:

(a) The corresponding previous time-increment stresses and material state variables as well as the current time-step strain increments are provided by the ABAQUS/Explicit finite-element solver to the material subroutine. In the present work, the strain components, the extent of coherent damage and a variable defining the deletion status of the element in question are used as state variables; and

(b) Using the information provided in (a), and the soda-lime glass material model presented in Section A.3.4, the material stress state as well as values of the material state variables at the end of the time increment are determined within the VUMAT and returned to the ABAQUS/Explicit finite-element solver. It should be also noted that in order to implement the new algorithm for macro-cracking, global three-dimensional matrices containing the location, the failure status and the direction of cracking (where appropriate) had to be assembled and used during each call of the VUMAT subroutine.

A.4. Validation of the Material Model

The material model for soda-lime glass developed and parameterized in the previous section is validated in this section by carrying out a series of transient non-linear dynamics analyses of the Edge-on-Impact tests of a glass target and by comparing the computational results with the experimental results obtained recently by Strassburger et al. [A.4, A.5]. In the remainder of this section, a brief description of the EOI test and the nature of the results obtained in this test are presented. This is followed by the description of the computational procedure used to simulate the test.

A.4.1. Edge-on Impact Test

Test Set-up and Procedure

Edge-on Impact (*EOI*) tests are frequently used to study the deformation and damage of

(non-transparent) conventional structural-ceramic armor systems and involves real-time, reflection-mode, optical monitoring of the armor deformation and damage during impact. In the recent work of Strassburger et al. [A.4,A.5], the EOI set-up is coupled with a high-speed 0.10μs-resolution Cranz-Schardin camera and utilized in a number of studies to visualize damage propagation and dynamic fracture in structural ceramics. Strassburger et al. [A.4,A.5] also reconfigured the EOI test set-up in order to record photographically the evolution of damage in transparent-armor systems using the plane-light shadow-graphs transmission mode (*"the shadow-graphs mode"*). In addition, the test set-up was modified by adding crossed polarizers to visualize the propagation of stress waves using a dynamic photo-elasticity technique (*"the photo-elasticity mode"*). A schematic of the EOI test set-up with the added crossed polarizers is displayed in Figure A-2. A close-up view of the projectile/target interaction and a schematic of the resulting damage and wave-swept zones are provided in Figure A-3.

In the work of Strassburger et al. [A.4,A.5], a projectile is used to strike one side face (generally referred to as an "*edge*") of a plate-like specimen/target and damage formation and fracture propagation is recorded by photographing (in transparent mode) the broad faces of the target during the first 20μs following the impact. Plate-shape 100 x 100 x 10 mm test specimens/targets are typically impacted using either solid right circular cylinder-shape steel projectiles (30 mm diameter, 23 mm length) or using 16mm-diameter solid sphere-shaped projectiles. The impact velocities used are normally in a range between 270 and 925 m/s. In the shadow-graph mode of the optical set-up, the target is placed between the condensing lens and the camera. In the photo-elasticity mode of the optical set-up, two sheet polarizers (one on each side of the target) are attached to the transparent sides of the target chamber so that broad polarizers' faces are parallel with the broad target faces, Figure A-2.

To help clarify the nature of the shadow-graph type and the photo-elasticity type EOI

results, simple schematics of these results are provided in Figures A-4(a)-(b), respectively. Schematics shown in A-4(a)-(b) both pertain to the corresponding photographic positives i.e. due to the damage induced, the coherent damage zone as well as the isolated crack centers appear as dark regions in the shadow-graphs. Differences in the light intensity associated with the longitudinal-wave and transverse-wave swept regions in the case of shadow-graph mode are dominated by stress-induced birefringence effects (in the case of the longitudinal wave) and by surface reflection phenomena (in the case of the transverse wave). In the case of the photo-elastic imaging mode, stress-induced birefringence in the target material gives rise to a 90^{o} switching in the beam polarization vector producing bright regions in the stressed areas.

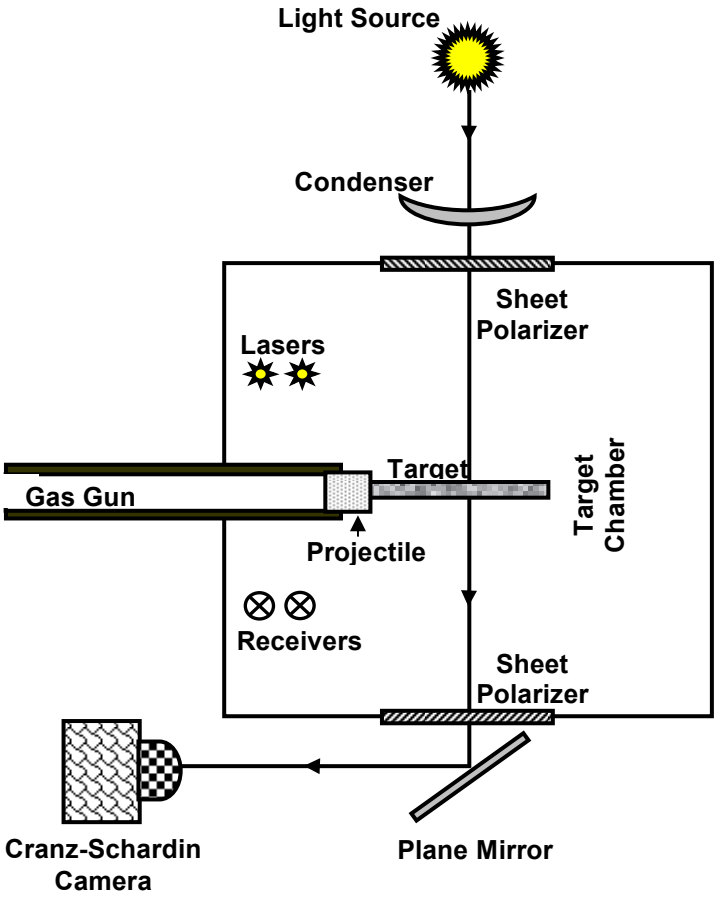

Figure A-2. A Schematic of the Edge-On-Impact (EOI) Experimental Set-up with two Cross Polarizers and a Single Cranz-Schardin Camera

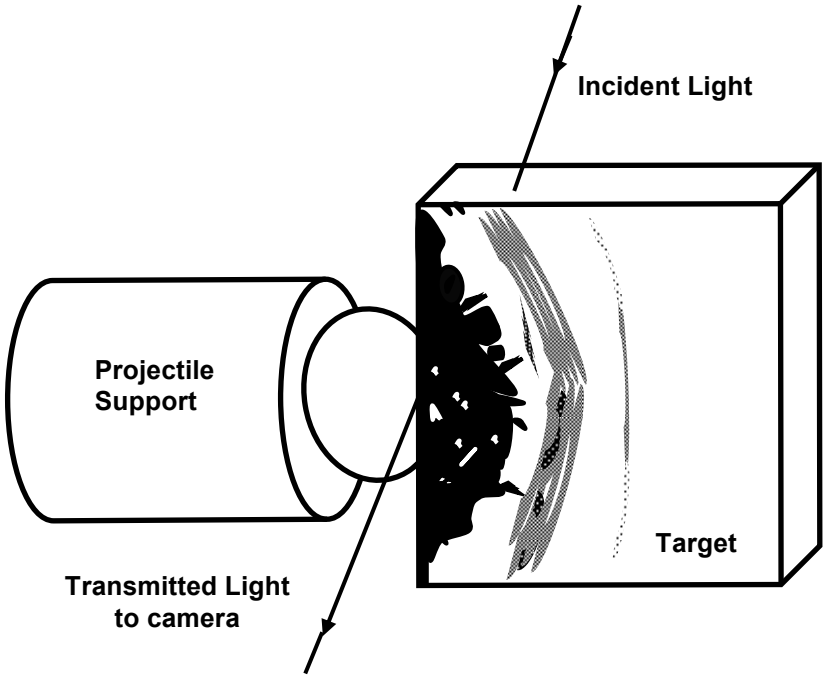

Figure A-3. A Close-up View of the Projectile/target Interaction in an EOI set-up

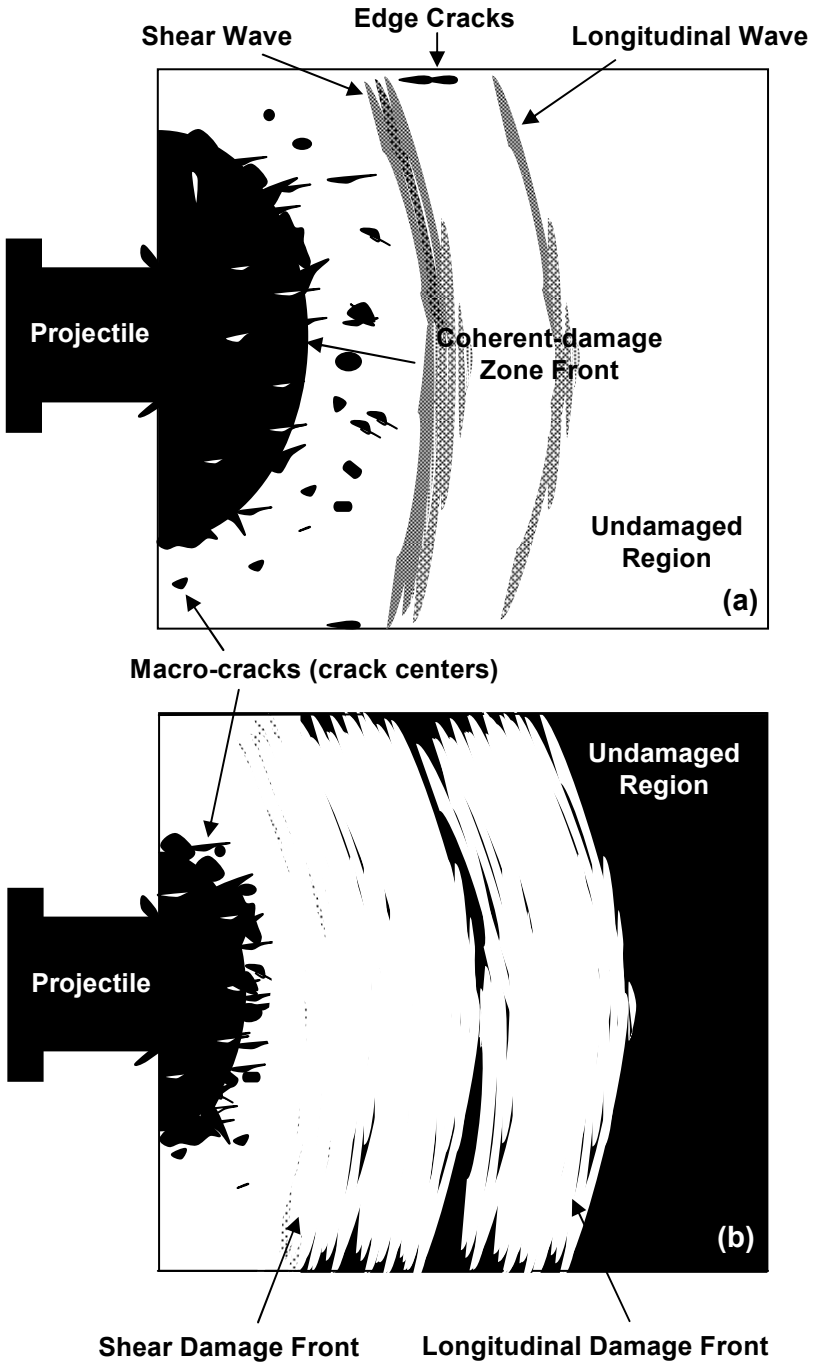

Figure A-4. Schematic of the Typical (a) Shadowgraph and (b) Birefringence Results obtained in the work by Strassburger et al. [A.4, A.5]

Typical EOI Test Results for Soda-lime Glass

As discussed in the previous section, two different optical configurations were employed in the work of Strassburger et al. [A.4,A.5]: A regular transmitted plane-light shadow-graph set-up was used to observe wave and damage propagation, while a modified configuration, in which the specimens were placed between crossed polarizers to create a photo-elastic effect, was used to visualize the stress-wave propagation. Pairs of impact tests at approximately identical velocities were conducted in transmitted plane (shadow-graphs) and crossed polarized light. The two sets of results were next compared to establish the extent of wave and damage propagation and to establish correlation between damage initiation and the stress components most likely responsible for the observed damage.

The main observations made by Strassburger et al. [A.4, A.5], during the EOI testing of soda-lime glass can be summarized as follows:

(a) Damage appears to be in two distinct forms: (i) as a coherent, continuous (damage) zone emanating from the impacted target edge and (ii) as discrete crack centers located at some distance from the advancing coherent-damage zone front. To overcome the limitations of the *"side-view"* shadow-graph optical set-up that always provides photographic images with superimposed bulk-damage and surface-damage contributions, Strassburger et al. [A.4, A.5] also carried out a simultaneous top-view shadow-graph imaging of the target-damage process. The results obtained revealed that the material damage initiates both in the bulk of the target and on the side faces. The advancement of damage from the impacted edge of the specimen was found to be greater in the case of bulk damage. This finding was somewhat surprising since, in the case of glass, it is generally postulated that damage-inducing flaws are primarily concentrated in the surface regions of the sample;

(b) While both the shadow-graph optical mode and the photo-elastic mode revealed the

positions of the advancing longitudinal and shear waves, the positions of the wave front revealed by the two optical set-ups were somewhat different. This discrepancy was explained to be the result of differences in the physical phenomena responsible for the light-intensity differences (contrast) in the two cases. That is, in the case of plain-light shadowgraph optical set-up, the transmitted light intensity is controlled by the second derivative of the refractive index while in the case of cross-polarizers set-up, the transmitted-light intensity is controlled by the underlying photo-elastic effect;

(c) The longitudinal-wave velocity was found to be around 5760m/s while the propagation velocity of the transverse waves was found to be ca. 3520m/s. Both of these velocities are consistent with their counterparts (5708m/s and 3224m/s) computed using the Young's modulus of 73GPa, a shear modulus of 29GPa and a density of 2240kg/m^3 for glass [A.1,A.21]; and

(d) The damage propagation velocity (defined as the velocity at which new crack centers are nucleated ahead of the advancing coherent-damage zone front) was found to be ca. 3270m/s and thus quite close to the transverse wave velocity. This finding suggests that the most likely mechanism for damage initiation is mode I cracking induced by the tensile hoop stresses at pre-existing material flaws.

A.4.2. Transient Non-linear Dynamics Analysis of the EOI test

In this section, a brief description is provided regarding the construction of the geometrical model and the computational procedure used to simulate the Edge-on-Impact tests on soda-lime glass as carried out by Strassburger et al. [A.4, A.5].

Plate-like soda-lime glass targets with LxWxH=100mmx100mmx10mm dimensions are used and one of their edges is impacted with either a 4340-steel spherical projectile (diameter=16mm) or a 4340-steel cylindrical projectile (diameter=30mm, height=23mm). For

brevity and due to the fact that experiment/computation agreement was similar for two types of projectiles, only the results pertaining to the case of the spherical projectile will be presented in this chapter. The projectile was meshed using four-node reduced integration tetrahedron solid elements. Since initial work showed that no plastic deformation takes place in the projectile during impact, 4340 steel was modeled as a linear elastic material with a Young's modulus E=210GPa and a Poisson's ratio ν =0.3. To enable easy determination of the relative location of the elements (needed in the present formulation of the macro-cracking model), the target was meshed using equal size cube-shaped eight-node reduced integration brick elements. The soda-lime glass target was modeled using the high-deformation-rate, high-pressure, large strain model presented in the previous section. Also, since only the normal impact of the projectile on the target is analyzed, advantage is taken of the inherent symmetry of the model, i.e. only one quarter of the model is analyzed. Typically the spherical projectile was divided into ~8,000 elements, while the target contained 200,000 elements. An Example of the typical meshed model used in the present work is displayed in Figure A-5. The mesh size was varied initially in order to validate that the results are not significantly mesh-size dependent.

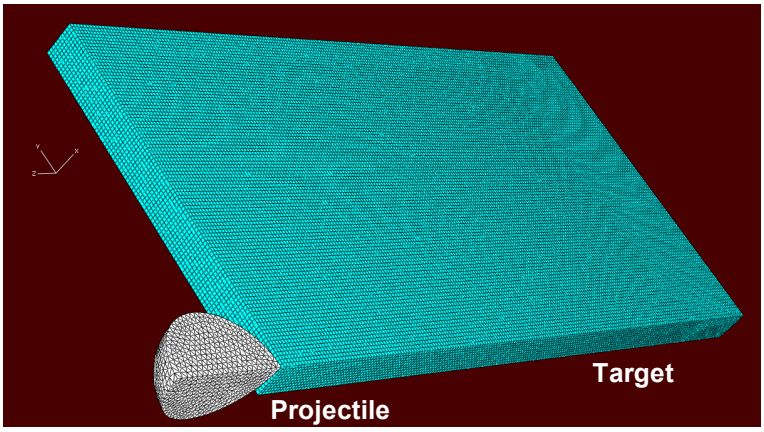

Figure A-5. A Typical (quarter) Meshed Model used for the Projectile and the Target

All the calculations were carried out using ABAQUS/Explicit computer program [A.3]. The material model for the soda-lime glass was implemented into a *VUMAT* User Material Subroutine and linked with ABAQUS/Explicit before the model could be used.

Interactions between the projectile and the target as well as between different fragments of the target are modeled using the "*Hard Contact Pair*" type of contact algorithm. Within this algorithm, contact pressures between two bodies are not transmitted unless the nodes on the "*slave surface*" contact the "*master surface*". No penetration/over closure is allowed and there is no limit to the magnitude of the contact pressure that could be transmitted when the surfaces are in contact. Transmission of shear stresses across the contact interfaces is defined in terms of a static, μ_{st}, and a kinematic μ_{kin}, friction coefficient and an upper-bound shear stress limit, μ_{slip} (a maximum value of shear stress which can be transmitted before the contacting surfaces begin to slide).

The impact of the projectile with the target is modeled by assigning an initial (translational) velocity to the projectile ("*the initial condition*"). The initial velocity of the target was set to zero and, during the impact simulation, the narrow side face of the target normal to the impacted face was kept at a fixed position ("*the boundary conditions*").

To prevent hour-glassing effects which may arise due to the use of reduced-integration elements, a default value of hour-glass stiffness was used. No mass-scaling algorithm was used to increase the maximum stable time increment. Computational analyses were run on a machine with a single 2.79GHz dual-core Intel Pentium D processor with 3GB of RAM. A typical 20μs impactor/target computational analysis would require five minutes of (wall-clock) time.

A.5. Results and Discussion

A.5.1 Edge-on Impact Analysis

In Section A.4.2, a detailed description was provided regarding the transient non-linear dynamics finite element analysis of the EOI tests of plate-like soda-lime glass targets with a spherical projectile as reported in Refs. [A.4, A.5]. In the present section, the main results of the EOI computational analysis are presented and discussed.

A.5.1.1. Propagation of Longitudinal and Transverse Stress waves

To verify that the pre-damage initiation elastic portion of the material model for soda-lime glass was implemented correctly into the VUMAT User Material Subroutine and correctly linked with the ABAQUS/Explicit finite-element solver, the propagation of the (elastic) longitudinal stress waves and transverse (more specifically, the maximum principal) stress waves were investigated first. The contour plots displayed in Figures A-6(a) and A-7(a) show respectively the positions of the longitudinal and transverse stress-wave fronts 7.7μs after the impact with the spherical projectile (propelled with an initial velocity of 440m/s). For comparison, the corresponding results obtained experimentally in Ref. [A.4] (using a cross-polarization photo-elastic experimental technique), are shown in Figures A-6(b) and A-7(b), respectively. It is evident that both the computed shape of the stress-wave fronts and their locations are in fairly good agreement with their experimental counterparts. The same conclusion is reached after analyzing the results displayed in Figures A-8(a)-(b) and A-9(a)-(b). In these figures, a comparison is made between the computed and experimental results pertaining to the position of the longitudinal and transverse stress-wave fronts 15.7μs after the impact with the same spherical projectile propelled with the same initial velocity.

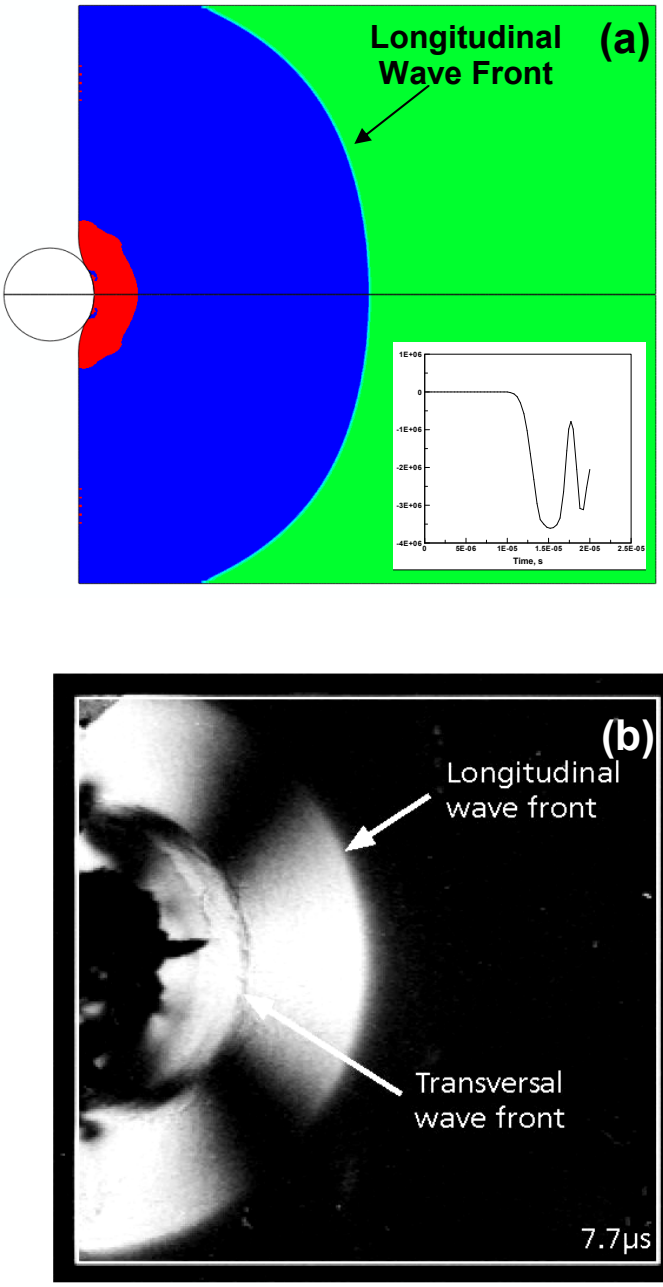

Figure A-6. A Comparison of the Longitudinal-stress Wave Fronts obtained (a) Computationally and (b) Experimentally (in Refs. [A.4,A.5]) for the case of a Spherical Impactor with an Initial Velocity of 440m/s and a Post-impact time of 7.7μs. The Inset in (a) shows a Typical Longitudinal-wave Trace

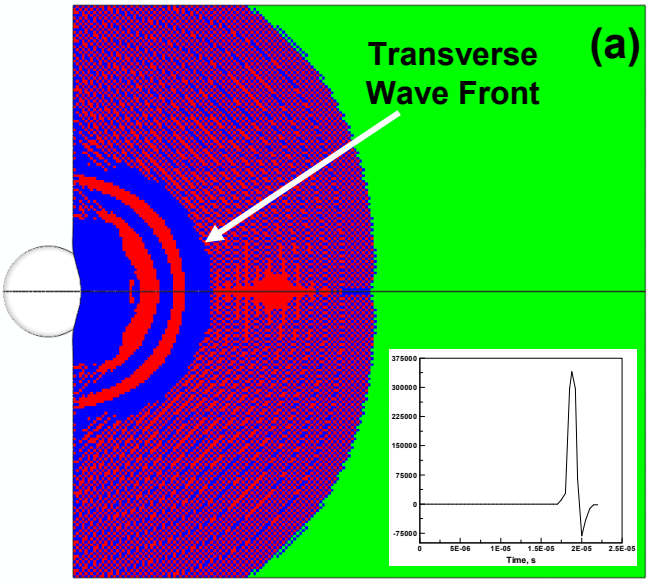

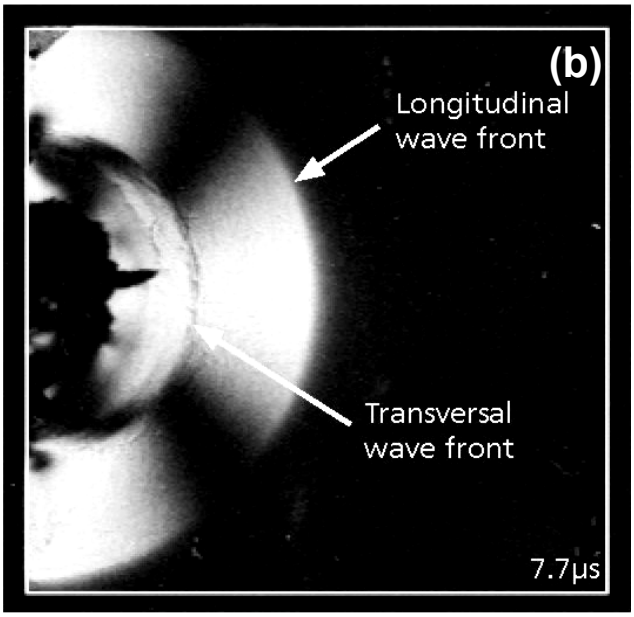

Figure A-7. A Comparison of the Transverse-stress Wave Fronts obtained (a) Computationally and (b) Experimentally (in Refs. [A.4, A.5]) for the case of a Spherical Impactor with an Initial Velocity of 440m/s and a Post-impact time of 7.7μs. The Inset in (a) shows a Typical Transverse-wave Trace

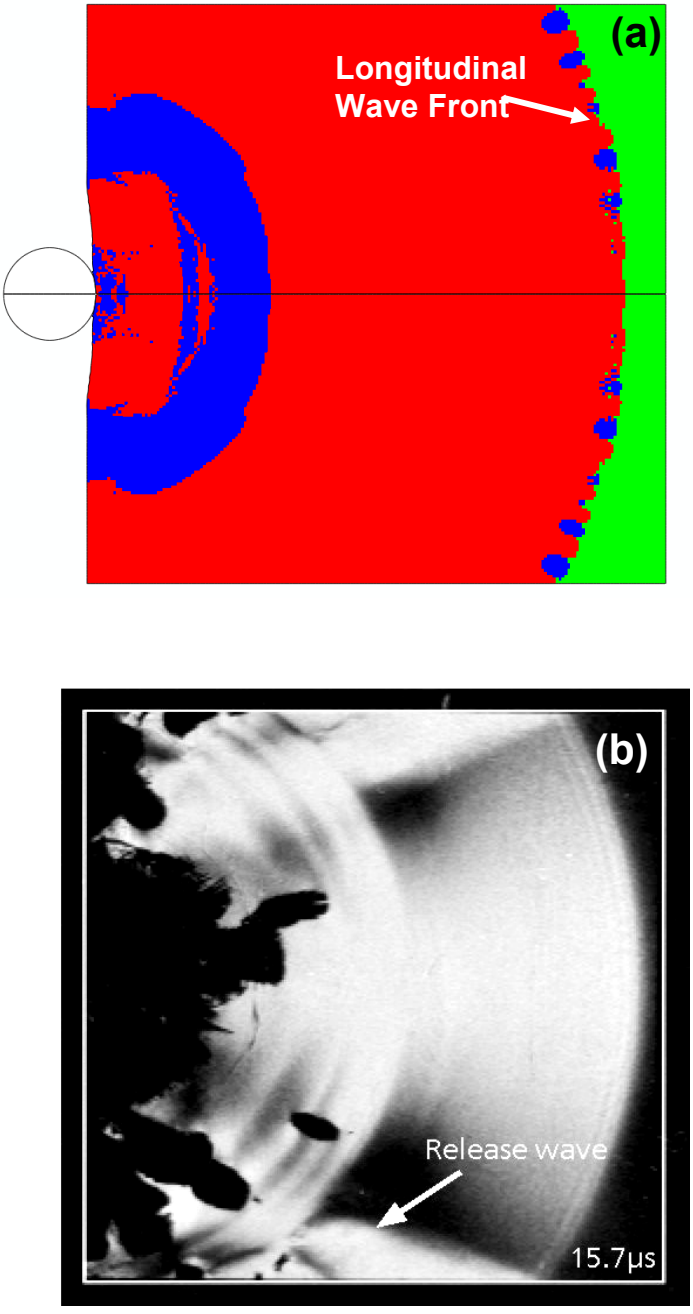

Figure A-8. A Comparison of the Longitudinal-stress Wave Fronts obtained (a) Computationally and (b) Experimentally (in Refs. [A.4, A.5]) for the case of a Spherical Impactor with an Initial Velocity of 440m/s and a Post-impact time of 15.7μs. The Inset in (a) shows a Typical Longitudinal-wave Trace.

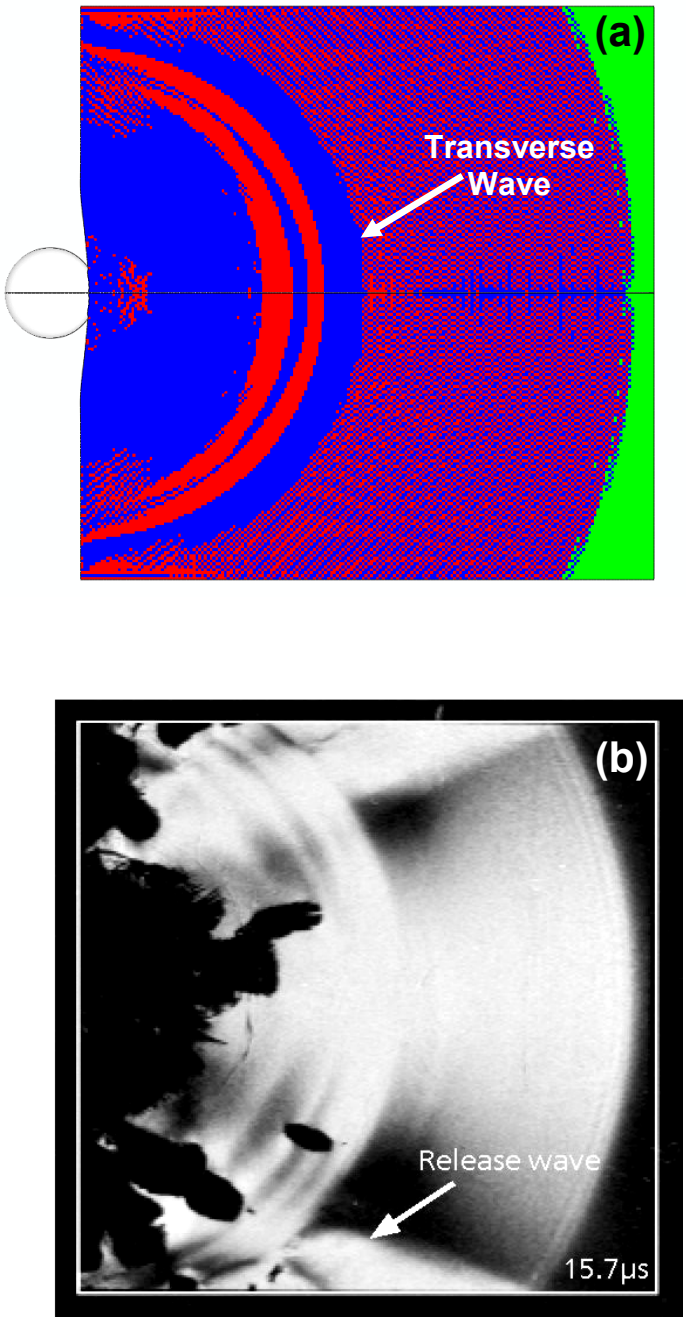

Figure A-9. A Comparison of the Transverse-stress Wave Fronts obtained (a) Computationally and (b) Experimentally (in Refs. [A.4,A.5]) for the case of a Spherical Impactor with an Initial Velocity of 440m/s and a Post-impact time of 15.7μs. The Inset in (a) shows a Typical Transverse-wave Trace

As mentioned earlier, a similar agreement between the computed and the experimental results pertaining to the positions of the longitudinal and transverse stress-wave fronts was obtained in the case of the cylindrical projectile (the results are not shown for brevity).

To further validate the implementation of the elastic part of the material model, a number of gage points were placed along the centerline of the target (in the direction of propagation of projectile motion) and the moment of arrival of the longitudinal and transverse stress-wave fronts recorded. Typical stress vs. time traces obtained are shown (as insets) in Figures A-6(a) and A-7(a). From the distances between the gage points and the time-of-arrival of the stress waves to the gage points, the average longitudinal and transverse stress-wave velocities were obtained as v_{long}= 5890±100m/s and v_{trans}= 3410±70m/s. These results are in quite good agreement with their experimental counterparts (5763m/s and 3518m/s) and the ones obtained by using the Young's and shear moduli and the material density (5407m/s and 3413m/s), respectively. This finding suggests that the transverse normal stress wave (i.e. the wave associated with the maximum principal stress) travels at a speed which is comparable to that of the corresponding shear wave. This could be justified by the fact that due to mutual normality of the wave vector and the polarization vector in the case of transverse normal stress wave, the propagation of this wave relies on shear-like coupling between the material particles just ahead and just behind the wave front.

Based on the results obtained and discussed in this section, it can be concluded that the elastic portion of the soda-lime glass material model is appropriate, correctly implemented in the VUMAT user material subroutine and properly linked with the ABAQUS/Explicit solver.

A.5.1.2. Temporal Evolution of the Coherent Damage/ Comminution Zone

As discussed in Section A.4.1, the region surrounding the target face impacted by the

projectile suffers damage (and ultimately fine-fragmentation fracture) due to formation of the micron and sub-micron size cracks. The extent of this *"coherent"* damage at a given material point is represented in the present work by a scalar material state variable, D. While in many brittle-fracture material models existing in the literature damage is represented using a tensorial quantity (in order to account for the anisotropic nature of the damage), the extent of such anisotropy within the coherent-damage zone is generally quite small. Since very small differences in the computational results were obtained in the present work when the anisotropic nature of the coherent damage was taken into account while the computational cost was more than doubled, the use of a damage tensor was deemed unwarranted.

To test the ability of the present material model for soda-lime glass to account for the temporal evolution of size and shape of the coherent-damage zone, a comparison is made in Figures A-10-A-11 between the computational results pertaining to the size and shape of the coherent-damage zone (obtained in the present work) and their experimental counterparts (obtained in the shadow-graph technique in Refs. [A.4,A.5]). In Figures A-10-A-11, part (a) contains the computational results while part (b) contains the corresponding experimental results.

The results displayed in Figures A-10 and A-11 pertain to the case of a spherical projectile (the initial velocity = 440m/s and the post-impact times of 7.7μs and 15.7μs, respectively). It should be noted that while the computational results can reveal detailed spatial distribution of damage within the coherent-damage zone, similar details cannot be obtained using the shadow-graph technique. Consequently, only the size and the shape of the coherent-damage zone are used for comparison of the computational and the experimental results.

A careful examination of the results displayed in Figures A-10(a)-(b) shows that at a post-impact time of 7.7μs: (a) there is a reasonably good agreement between the computational and the experimental results pertaining to the shape of the coherent-damage zone and its depth along the

impact direction; (b) there is also a reasonably good agreement between the computational and the experimental results pertaining to the extent of the coherent-damage zone along the target face impacted by the projectile. It should be recalled that the extent of the coherent-damage zone along the target face impacted by the projectile is controlled by surface flaws while the evolution of damage in the remainder of the target is controlled by bulk flaws; and (c) both the computation and the experiment provide no evidence of coherent damage along the clamped top and bottom edges of the target.

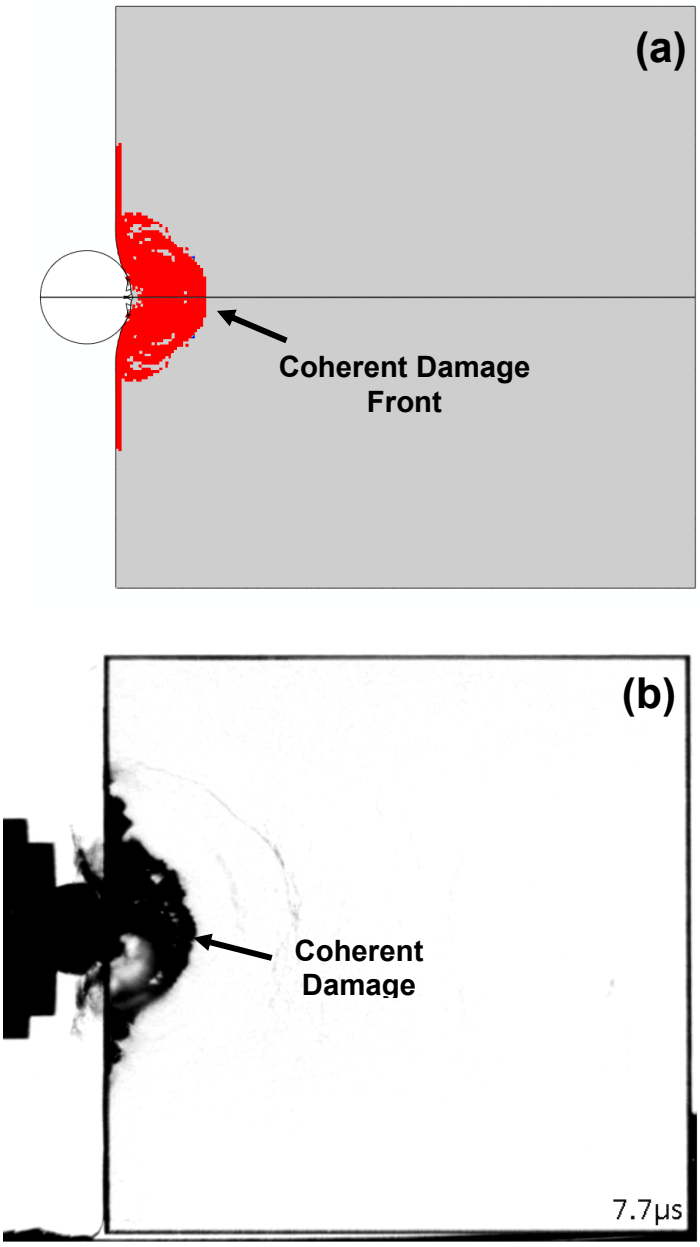

Figure A-10. A Comparison of the Coherent-damage Zone Fronts obtained (a) Computationally and (b) Experimentally (in Refs. [A.4, A.5]) for the case of a Spherical Impactor with an Initial Velocity of 440m/s and a Post-impact time of 7.7μs

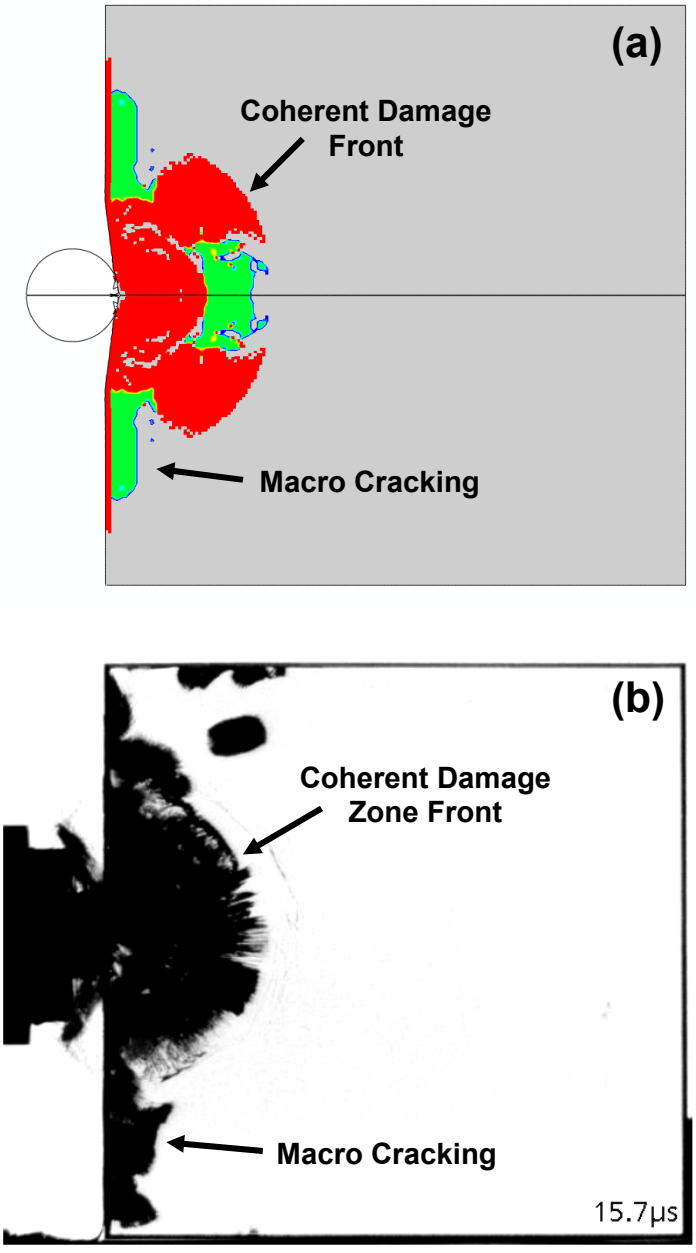

Figure A-11. A Comparison of the Coherent-damage Zone Fronts obtained (a) Computationally and (b) Experimentally (in Refs. [A.4, A.5]) for the case of a Spherical Impactor with an Initial Velocity of 440m/s and a Post-impact time of 15.7μs

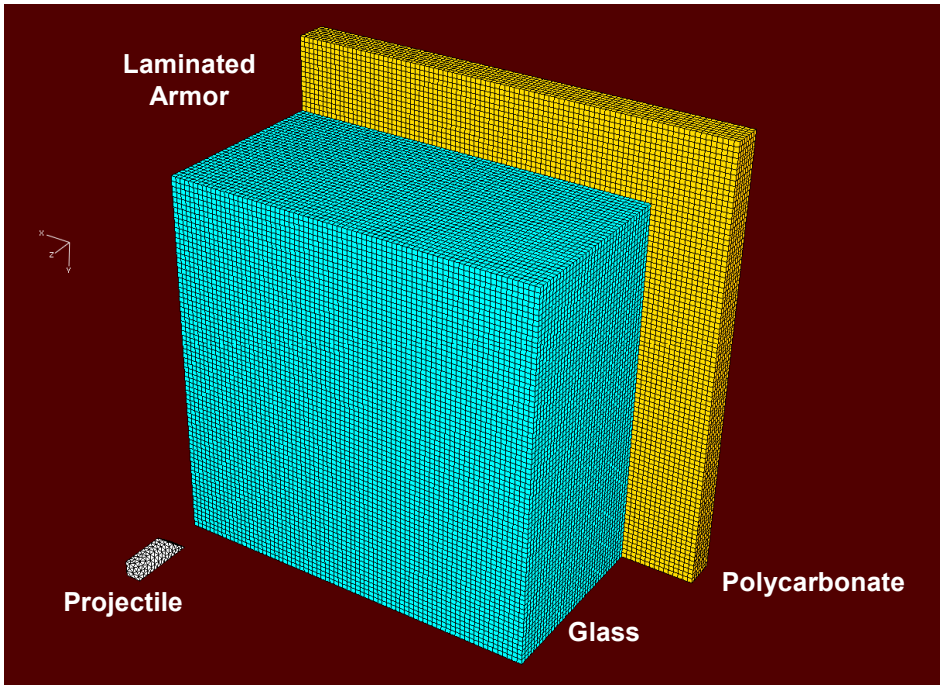

Figure A-12. A Typical (quarter) Meshed Model used for the Projectile and the Laminated Transparent Armor System used in the work by Bless and Chen [A.22]

A careful examination of the results displayed in Figures A-11(a)-(b) reveals that at a post-impact time of 15.7μs: (a) there is a reasonably good agreement between the computational and the experimental results pertaining to the extent of coherent damage along the target strike-face; (b) on the other hand, the overall size and depth of the computed coherent damage zone is significantly smaller than the experimental damage zone counterparts from the work of Strassburger et al. [A.4,A.5]. However, if the size and depth of the entire (coherent-damage and macro-cracking) computed damage zone (Figure A-11(a)) is compared with the corresponding experimental results in Figure A-11(b), a reasonably good agreement is obtained. It should be noted that the shadow graph technique used by Strassburger et al. [A.4,A.5] has limitations in fully distinguishing between the coherent-damage and macro-cracking failure modes. Thus, the overall computation/experiment agreement pertaining to the size and shape of the coherent-damage zone obtained in the present work may be better than the one suggested by comparing the coherent damage zone displayed in Figure A-11(a) with the overall experimentally observed damage zone displayed in Figure A-11(b); and (c) the onset of damage along the (top and bottom) clamped faces of the target observed experimentally is not predicted computationally (e.g. Figure A-11(b) vs. Figure A-11(a)). There are several potential reasons for this discrepancy. Two most likely reasons are: (i) the fixtures used to hold the target during impact introduce stresses into the target which, when superimposed with the impact-induced stresses, can cause an early damage initiation in the regions near the target top and bottom surfaces; and (ii) cutting and grinding of the side faces of the target used during the target manufacturing process may have changed the distribution and potency of surface flaws relative to those corresponding to the surface-flaw Weibull distribution parameters listed in Table A-1. Both of the aforementioned hypotheses were tested in the present work. The first hypothesis was tested by adding compressive-normal and shear tractions to the top and bottom target faces, while the second hypothesis was investigated

by reducing the mean fracture strength for the finite elements which reside on the impacted as well as the top and bottom clamped faces of the target. The results obtained (not shown for brevity) suggest that both of the hypothesized reasons may account for the observed discrepancy between the computed and experimental shapes of the coherent-damage zones. Thus, additional experimental investigation is needed to help resolve this uncertainty. Such experimental investigation may involve the use of chemical polishing which can reduce considerably the amount of damage induced by cutting/grinding.

To summarize, based on the results presented in this section, it appears that the proposed material model for soda-lime glass can capture the essential features of the spatial distribution and temporal evolution of the coherent-damage zone at shorter post impact times. On the other hand, a good agreement between the computational and the experimental results at longer post impact times pertaining to the damage zone size and shape can be obtained only if the computed total (coherent-damage and macro-cracking) damage zone is compared with the experimentally-observed overall damage zone. It is also found that more experimental work is needed to establish if target fixturing or cutting/grinding-induced surface flaws alter the stress/microstructural state of the surface regions. Either of these effects can be readily included as fixturing-induced loads (i.e. through the changes in boundary conditions) or through changes in the values of the surface-flaw Weibull distribution parameters used in the present material model for soda-lime glass.

A.5.1.3. Temporal Evolution of the Discrete Damage

As discussed earlier, the experimental investigations carried out by Strassburger et al. [A.4,A.5] revealed the formation of millimeter-size discrete cracks (i.e. *"crack centers"*) at a small distance ahead of the advancing coherent-damage zone front. To allow for the formation of discrete cracks, as discussed in Sections A.3.3 and A.3.4, a stress-rate and a linear fracture

mechanics based criteria were proposed to control the mode of damage initiation and ultimate failure of the ballistic soda-lime glass under impact loading conditions. That is, material points residing within the finite elements which reach the stress-based damage-initiation condition at a stress-rate higher than a critical stress-rate are assumed to undergo coherent damage and to fail in a "*dynamic-type*" multiple-fragmentation mode. This was justified by the fact that at high stress rates and the associated high stress levels, the criterion for crack nucleation is met at many points within the element. Conversely, material points residing within the finite elements which reach the stress-based damage-initiation condition at a stress rate lower than the critical stress-rate are assumed to fail in a "*static-type*" coarse-fragmentation failure mode, to reflect the fact that the first crack to form in these elements would traverse the entire element before additional cracks can nucleate. As discussed in Section A.3.4, when an element is located at a tip of a crack, its stress level is enhanced so that it is more likely to fail by the extension (growth) of the crack. Thus, in this case, despite the fact that the stress level (and perhaps the stress rate) may be high throughout the entire element in question, the static single-fragmentation fracture mode is assumed to take place.

The results obtained in the present work, Figures A-10(a)–(b) and A-11(a)–(b), can be used to carry out a comparison between the computational results obtained in the present work and their experimental counterparts in Ref. [A.4,A.5] with respect to temporal evolution and spatial distribution of macro-cracking. A comparison of the results displayed in Figures A-10(a)–(b) reveals a good computation/experiment agreement, i.e. no clear evidence of macro-cracking is seen at the post impact time of 7.7μs. On the other hand, at a post impact time of 15.7μs, the computed results (Figure A-11(a)) reveal that a substantial portion of the overall damage zone is associated with macro-cracking and that macro-cracking primarily takes place in the regions ahead of the advancing coherent-damage zone front. These observations are fully consistent with

the ones made by Strassburger et al. [A.4,A.5] and, as pointed out earlier, one must recall that the experimental technique employed in their work had serious limitations concerning the discrimination between the two modes of damage. Consequently, the predictions made by the current material model for soda-lime glass regarding the spatial distribution and temporal evolution of macro-cracking can be considered as encouraging.

In passing, it should be noted that the computational results obtained in the present work reveal that formation of macro-cracks does not significantly affect the ability of the glass to absorb the kinetic energy of the projectile. In other words, macro-cracking does not seriously compromise the ballistic protection performance of soda-lime glass. However, the formation of a large macro-cracking zone surrounding the central coherent damage zone during the frontal impact of a soda-lime glass based transparent armor can seriously degrade the functional performance of the armor by reducing its transparency/clarity.

A.5.2. Crack Morphology in the Frontal Impact of a Transparent-Armor

In an attempt to further validate the present material model for ballistic glass, a comparison was made between the computational results obtained in the present work and the corresponding experimental findings pertaining to the spatial distribution of damage and cracking during frontal impact of the glass panel by a hard projectile.

A review of the public-domain literature carried out in the present work was unsuccessful in identifying the appropriate experimental investigation involving frontal impact of monolithic glass panels. Instead, a comprehensive investigation carried out by Bless and Chen [A.22], pertaining to the frontal impact of glass-polyurethane-polycarbonate laminated transparent armor system was located. Despite the fact that the transparent armor system studied in the work of Bless and Chen [A.22] included other materials (polyurethane and polycarbonate) it was selected for the validation of the present material model for ballistic glass due to its completeness and

relevant range of projectile velocity (ca. 1000m/s). A brief summary of the relevant experimental findings reported by Bless and Chen [A.22], of the computational procedure used in the present work to study the frontal impact of the transparent armor system and of the material models used in the present computational analysis for polyurethane and polycarbonate is provided below. A more detailed account of the above will be reported in our future communication [A.23].

In the work of Bless and Chen [A.22], the glass strike face of a nine-layer (seven 300mm × 300mm glass layers backed by two 360mm × 360mm polycarbonate layers) laminate with a total thickness of 88.7mm was impacted with a 0.5 caliber chisel-nosed circular cylindrical projectile at a nominal velocity of 1000 m/s. Adjacent glass layers were separated by 0.6mm polyurethane adhesive films. The armor laminate was placed in a vertical position and fixed along its two vertical sides using straps and a wooden block during impact. A post-mortem visual micrographic analysis was conducted on the partially penetrated armor plates and on the glass fragments. The main findings obtained in the work of Bless and Chen [A.22] which are relevant to the present investigation can be summarized as follows:

(a) The projectile managed to fully penetrate only the front-most A.4mm-thick glass lamina and to partially penetrate the second 12.7mm-thick glass lamina. The resulting crater radius was found to be ca. 31mm. In the process of penetration, the projectile was compressed from its initial 18mm length to a length of 8mm;

(b) While the remaining glass laminae were not penetrated by the projectile, they all experienced substantial damage. The damaged region surrounding the tip of the projectile was composed of very fine (sub-millimeter size) cracks (coherent damage) while in the region farther away from the projectile tip millimeter-size, isolated radial cracks, and fan-shaped and bow-tie shaped crack bundles were observed. The extent of damage region in the radial direction at the

bottom of the crater was ca. 70mm, while at the back face of the last glass lamina was ca. 150mm;

(c) At the strike face of the armor, coherent damage was observed in a 20mm-thick circular band region around the crater. At larger radial distances up to ca. 100mm from the crater, isolated radial cracks and crack bundles were observed; and

(d) No evidence of deformation/damage in the two back-most polycarbonate layers was observed.

To test the ability of the present material model for ballistic glass to correctly account for the aforementioned experimental findings of Bless and Chen [A.22], a transient nonlinear dynamic analysis of the frontal impact of the laminated transparent armor system was carried out in the present work. An example of the finite element mesh used in this portion of the work is shown in Figure A-12. To take advantage of the inherent symmetry of the problem, only a quarter of the model is analyzed, while the appropriate symmetry-plane boundary conditions are applied. Due to a very low thickness of the polyurethane films, the films were not modeled explicitly. Rather, their contribution was included through the use of the appropriate cohesive-zone interfaces. A derivation for the cohesive-zone material model for polyurethane was previously reported in Ref. [A.24]. The polycarbonate laminae were represented using an elastic/strain-rate-dependent plastic material model [A.25] with a plastic strain-based damage initiation and a total plastic displacement-based failure criterion. Typically, the projectile was meshed using 500 tetrahedron elements, while the laminated transparent armor was meshed using 250,000 cubic/near-cubic eight-node reduced-integration solid elements. The projectile was initially assigned a velocity of 1118m/s, while the top and bottom nodes of two opposing lateral faces of the armor were kept fixed during the analysis. As mentioned earlier, a more detailed account of the geometrical model of the laminated transparent armor, of the material models for

polyurethane and polycarbonate and of the computational analysis will be presented in our future communication [A.23].

A comparison between the computational results obtained in the present work and the corresponding experimental results obtained in the work of Bless and Chen [A.22] is shown in Figures A-13(a)-(b) and A-14(a)-(b). The results displayed in Figures A-13(a)-(b) pertain to the post-mortem spatial distribution of damage over the vertical center cut-plane passing through the glass portion of the transparent armor system. The results displayed in Figures A-14(a)-(b), on the other hand, show the spatial distribution of damage over the armor strike face. For both Figures A-13 and A-14, the part (a) shows the computed results, while the part (b) displays the corresponding experimental results. Due to copyright restrictions, only schematics of the experimental results from Ref. [A.22] could be displayed in Figures A-13(b) and A-14(b).

A careful comparison of the computational results displayed in Figure A-13(a) and the corresponding experimental results displayed in Figure A-13(b) pertaining to the post-mortem spatial distribution of damage along a vertical center cut-plane reveals that:

(a) The computed depth of armor penetration by the projectile closely matches its experimental counterpart (to within 5%);

(b) The extent and shape of the total damage region (coherent-damage and macro-cracking) in the transparent armor found in the experimental work is reproduced with reasonable accuracy by the computation. However, the extent of coherent-damage is somewhat over-estimated while the macro-cracking is under-predicted;

(c) In good agreement with the experiment, the computational results predict the formation of more extensive coherent damage at the back face of the last glass lamina. This damage was found to be caused by the release tensile stress waves generated by reflection of the incident compressive stress waves at the glass/polycarbonate interface; and

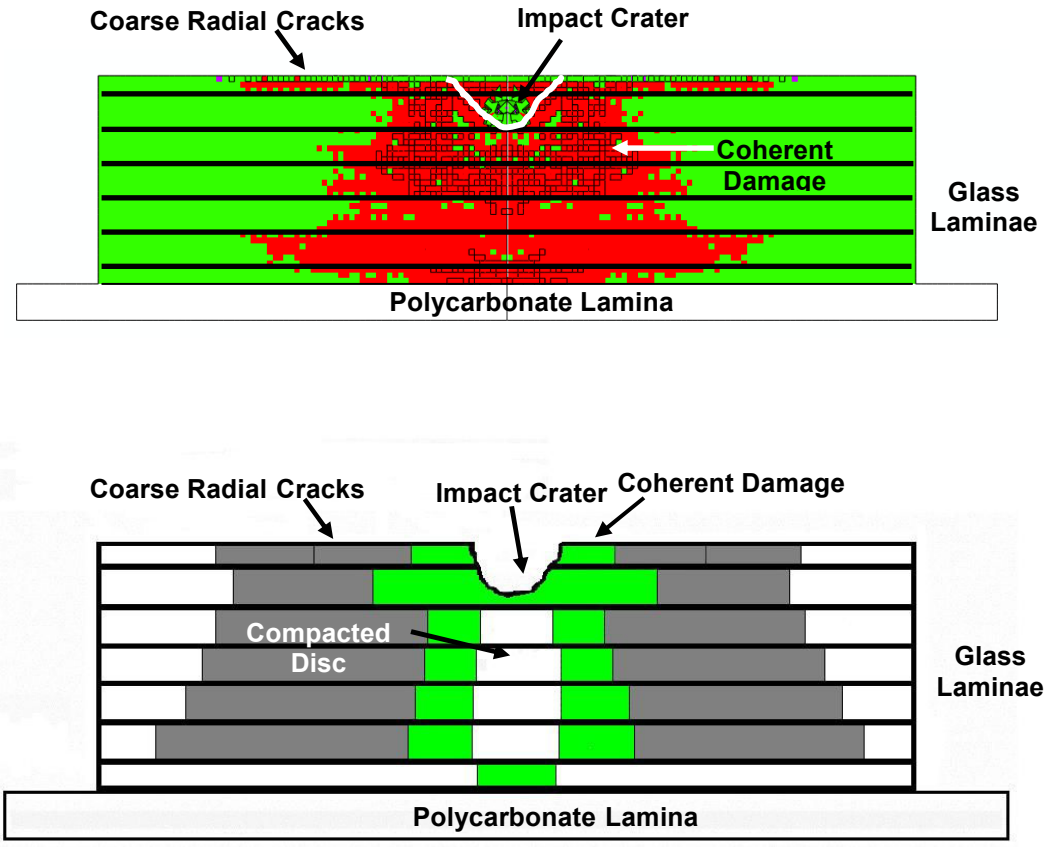

Figure A-13. Distribution of Coherent-damage and Macro-cracking over the Vertical Center Cut-plane of a Frontally Impacted Tran1sparent-armor System: (a) Computational Results obtained in the Present Work; and (b) Experimental Results obtained in the Work by Bless and Chen [A.22]

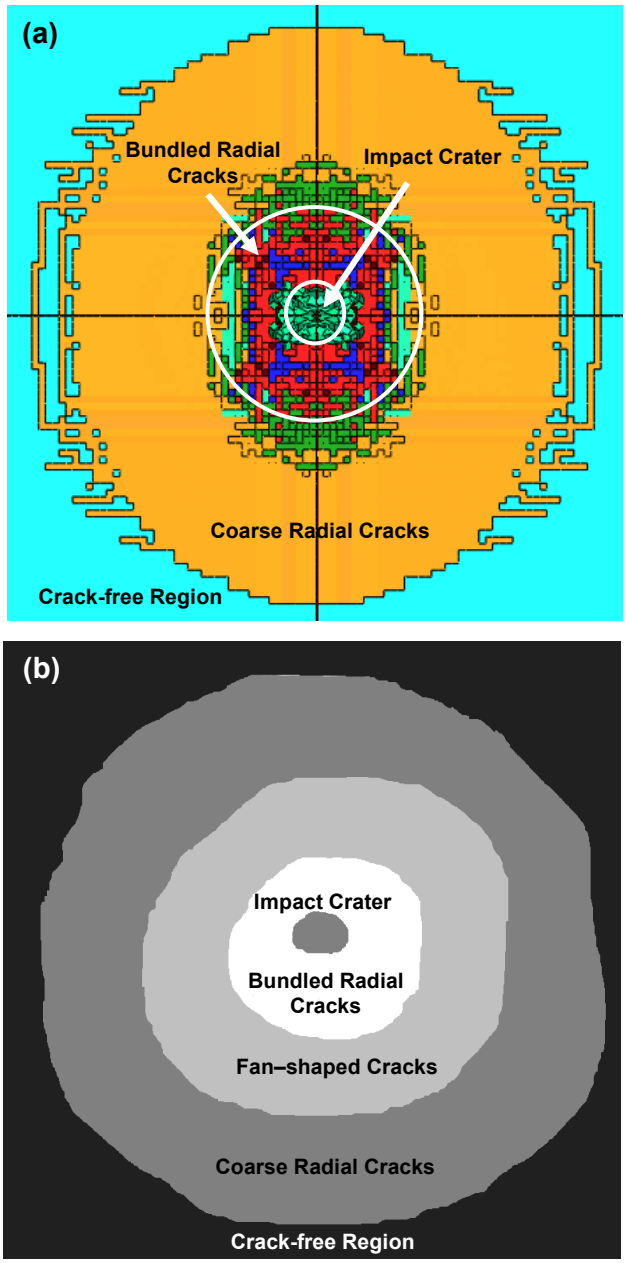

Figure A-14. Distribution of Coherent-damage and Macro-cracking over the Strike Face of a Frontally- impacted Transparent-armor System: (a) Computational Results; and (b) Experimental Results obtained in the work by Bless and Chen [A.22]

(d) The experimental results displayed in Figure A-13(b) show the presence of a coherent-damage free region (denoted as the *"compacted disk"* region) ahead of the projectile extending over four glass laminae. The computed results also reveal the presence of a coherent-damage free region, but this region is confined to within only two glass laminae.

A careful comparison between the computational results displayed in Figure A-14(a) and the corresponding experimental results in Figure A-14(b) pertaining to the post-mortem spatial distribution of damage over the transparent armor strike face, yielded the following findings: While, the experimental results indicate five distinct zones (central circular impact crater, the inner-most circular ring region containing very fine bundled radial cracks, the intermediate circular ring region containing fan shaped crack bundles, the outer circular ring region containing well-spaced coarse radial cracks and outer-most crack free region listed from the center of impact outward), four of these regions except for the intermediate region with fan-shaped cracks are reproduced well computationally. In addition, the size of the central circular impact crater, the inner-most circular ring region containing very fine bundled radial cracks and the outer circular ring region containing well-spaced coarse radial cracks are matched within 10-30%. The intermediate central circular ring region containing fan-shaped crack bundles (not observed computationally), was postulated in Ref. [A.22] to form by the release stress waves reflected from the target's free lateral surfaces. Although, stress wave reflection was observed in the present work, the stress magnitudes were not sufficiently high to nucleate cracks. Another possible reason for the lack of the formation of fan-shaped crack bundles is that the number of possible macro-crack growth directions (five on the strike face surface) was highly limited.

In summary, the overall computation/experiment agreement regarding the spatial distribution of coherent-damage and macro-cracking both over the transparent armor vertical

center cut-plane and the strike face can be deemed as reasonable.

A.6. Summary and Conclusion

Based on the material-model development procedure utilized and the results of the subsequent computational analyses, the following main summary remarks and conclusions can be drawn:

1. The simple, physically-based, high strain-rate, high-pressure, large-strain mechanical model for ballistic soda-lime glass originally proposed in Ref. [A.1] has been extended to include a linear fracture mechanics-based model for macro-cracking. This extension enables modeling of the formation and growth of millimeter-size isolated cracks and crack bundles.

2. To test the model, a series of transient non-linear dynamics analyses pertaining to the edge-on-impact of plate-like monolithic soda-lime glass targets with a spherical projectile and frontal impact of laminated glass/polycarbonate transparent-armor system with a chisel-nosed cylindrical projectile was conducted and the results obtained compared with their experimental counterparts as reported by Strassburger et al. [A.3,A.4] and Bless and Chen [A.22], respectively.

3. A comparison between the computed and experimental edge-on-impact results revealed that the proposed model fairly well accounts for the propagation of the elastic (longitudinal and transverse) waves in the target following impact and that the predicted speeds of these waves are quite comparable with their experimental counterparts. Likewise, a good agreement between the computed and experimental results is obtained relative to the temporal evolution of size and the shape of the coherent-damage and macro-cracking zones. The observed computation/experiment disagreements were attributed to the effect of clamping-induced contact stresses and/or cutting/grinding-induced flaw-population changes along the lateral faces of the target.

4. A comparison between the computed and the experimental frontal impact results revealed a reasonably good agreement with respect to spatial distribution and the extent of coherent-damage and macro-cracking both along the transparent-armor strike face and along a vertical center cut-plane. Minor computation/experiment discrepancies were observed relative to the absence of fan-shaped crack bundles over the transparent-armor strike-face in the computational results and these were attributed to the low intensity of the release tensile stress waves and a limited number of possible crack-growth directions.

A.7. References

A.1 M. Grujicic, B. Pandurangan, N. Coutris, B. A. Cheeseman, C. Fountzoulas, P. Patel and E. Strassburger, "*A Simple Ballistic Material Model for Soda-Lime Glass*," International Journal of Impact Engineering, accepted for publication, August 2008.

A.2 ANSYS/Autodyn version 11.0, User Documentation, Century Dynamics Inc., a subsidiary of ANSYS Inc., 2007.

A.3 ABAQUS version 6.7, User Documentation, Dessault Systems, 2007.

A.4 E. Strassburger, P. Patel, J. W. McCauley, C. Kovalchick, K. T. Ramesh and D. W. Templeton, "*High-Speed transmission Shadowgraphic and Dynamic Photoelasticity Study of Stress Wave and Impact Damage Propagation in Transparent Materials and Laminates Using The Edge-on Impact Method*," Proceedings of the 23rd International Symposium on Ballistics, Spain, April 2007.

A.5 E. Strassburger, P. Patel, W. McCauley and D. W. Templeton, "*Visualization of Wave Propagation and Impact Damage in a Polycrystalline Transparent Ceramic- AlON*," Proceedings of the 22nd International Symposium on Ballistics, November 2005, Vancouver, Canada.

A.6 AMPTIAC Quarterly: *Army Materials Research*: *Transforming Land Combat Through New Technologies*, 8, 4, 2004.

A.7 D. Z. Sun, F. Andreiux, A. Ockewitz, "*Modeling of the Failure Behavior of Windscreens and Component Tests*," 4th LS-DYNA Users' Conference, Bamberg, Germany, 2005.

A.8 T. Zarzycky*, Glasses and the Vitreous State*, Cambridge University, Cambridge, UK, 1991.

A.9 B. Nghiem, *PhD thesis*, University of Paris 6, France, 1998.

A.10 X. Brajer, P. Forquin, R. Gy and F. Hild, "*The Role of Surface and Volume Defects in the Fracture of Glass under Quasi-static and Dynamic Loadings*," Journal of Non-Crystalline Solids, 316, 2003, 42-53.

A.11 C. Guillemet in: C. R. Kurkjian (Ed.), *Strength of Inorganic Glass*, Plenum, New York, 1985.

A.12 R. Gy, C. Guillemet, in: L. D. Pye, W. C. La Course, H. J. Stevens (Eds.), *The Physics of Non-Crystalline Solids*, Taylor and Francis, London, 1992.

A.13 B. A. Kshinka, S. Perrela, H. Nguyen and R. C. Bradt, "*Strengths of Glass Spheres in Compression*," Journal of American Ceramic Society, 69, no.6, 1986, 467-472.

A.14 M. Yazdchi, S. Valliappan and W. Zhang, "*A Continuum Model for Dynamic Damage Evolution of Anisotropic Brittle Materials*," International Journal of Numerical Methods in Engineering, 39, 1996, 1555-1583.

A.15 H. D. Espinosa, P. D. Zavattieri and S. K. Dwivedi, "*A Finite Deformation Continuum/Discrete Model for the Description of Fragmentation and Damage in Brittle Materials*," Journal of Mechanics and Physics of Solids, 46, 10, 1998, 1909-1942.

A.16 P. D. Zavattieri and H. D. Espinosa, "*Grain Level Analysis of Crack Initiation and Propagation in Brittle Solids*," Acta Materialia, 49, 2001, 4291-4311.

A.17 G. T. Camacho and M. Ortiz, "*Computational Modeling of Impact Damage in Brittle Materials*," International Journal of Solids and Structures, 33, 20-22, 1996, 2899-2938.

A.18 C. Denoual and F. Hild, "*Dynamic Fragmentation of Brittle Solids: A Multi-scale Model*," European Journal of Mechanics of Solids A, 21, 2002, 105-120.

A.19 F. Hild, C. Denoual, P. Forquin and X. Brajer, "*On the Probabilistic and Deterministic Transition Involved in a Fragmentation Process of Brittle Materials*," Computers and Structures, 81, 2003, 1241-1253.

A.20 G. Geandier, S. Denis and A. Mocellin, "*Float Glass Fracture Toughness Determination by Hertzian contact: Experiments and Analysis*," Journal of Non-Crystalline Solids, 318, 2003, 284-295.

A.21 M. Grujicic, B. Pandurangan, N. Coutris, B. A. Cheeseman, C. Fountzoulas, P. Patel and E. Strassburger, "*A Ballistic Material Model for Starphire®, a Soda-Lime Transparent-Armor Glass*," Materials Science and Engineering-A, 491, 2008, 397-411.

A.22 S. Bless, and T. Chen, "*Impact Damage in Layered Transparent Armor*," to be submitted for publication, 2008.

A.23 M. Grujicic, B. Pandurangan, N. Coutris, B. A. Cheeseman, C. Fountzoulas and P. Patel, "*A Computational Investigation of the Multi-Hit Ballistic-Protection Performance of Laminated Glass-Polycarbonate Transparent Armor Systems*," to be submitted for publication, September 2008.

A.24 M. Grujicic, V. Sellappan, B. Pandurangan, G. Li, N. Seyr, M. Erdmann and J. Holzleitner, "*Computational Analysis of Injection-Molding Residual-Stress Development in Direct-Adhesion Polymer-to-Metal Hybrid Body-In-White Components*", Materials Processing Technology, 203, 2008, 19-36.

A.25 T. Bjerke, Z. Li and J. Lambros, *"Role of Plasticity in Heat Generation during High Rate Deformation and Fracture of Polycarbonate,"* International Journal of Plasticity, 18, 2002, 549-567.